AD-A168 005 DEVELOPMENT OF FRACTURE MECHANICS MAPS FOR COMPOSITE MATERIALS VOLUME 4(U) DEUTSCHE FORSCHUNGS- UND VERSUCHSANSTALT FUER LUFT- UND RAUMF.. H W BERGMANN 1/3

UNCLASSIFIED DEC 85 AFWAL-TR-85-4150-VOL-4 F/G 11/4 NL

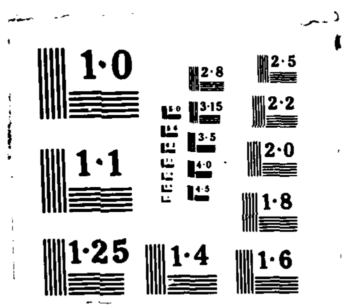
1·0
2·8
2·5
3·15
2·2
3·5
1·1
4·0
2·0
4·5
1·8
1·25
1·4
1·6

AFWAL-TR-85-4150
Volume 4

DEVELOPMENT OF FRACTURE MECHANICS MAPS FOR COMPOSITE MATERIALS

Dr. H. W. Bergmann

DFVLR - Institute for Structural Mechanics
Braunschweig, West Germany

December 1985

Final Report for Period January 1982 - January 1985

Approved for public release; distribution unlimited.

MATERIALS LABORATORY
AIR FORCE WRIGHT AERONAUTICAL LABORATORIES
AIR FORCE SYSTEMS COMMAND
WRIGHT-PATTERSON AIR FORCE BASE, OHIO

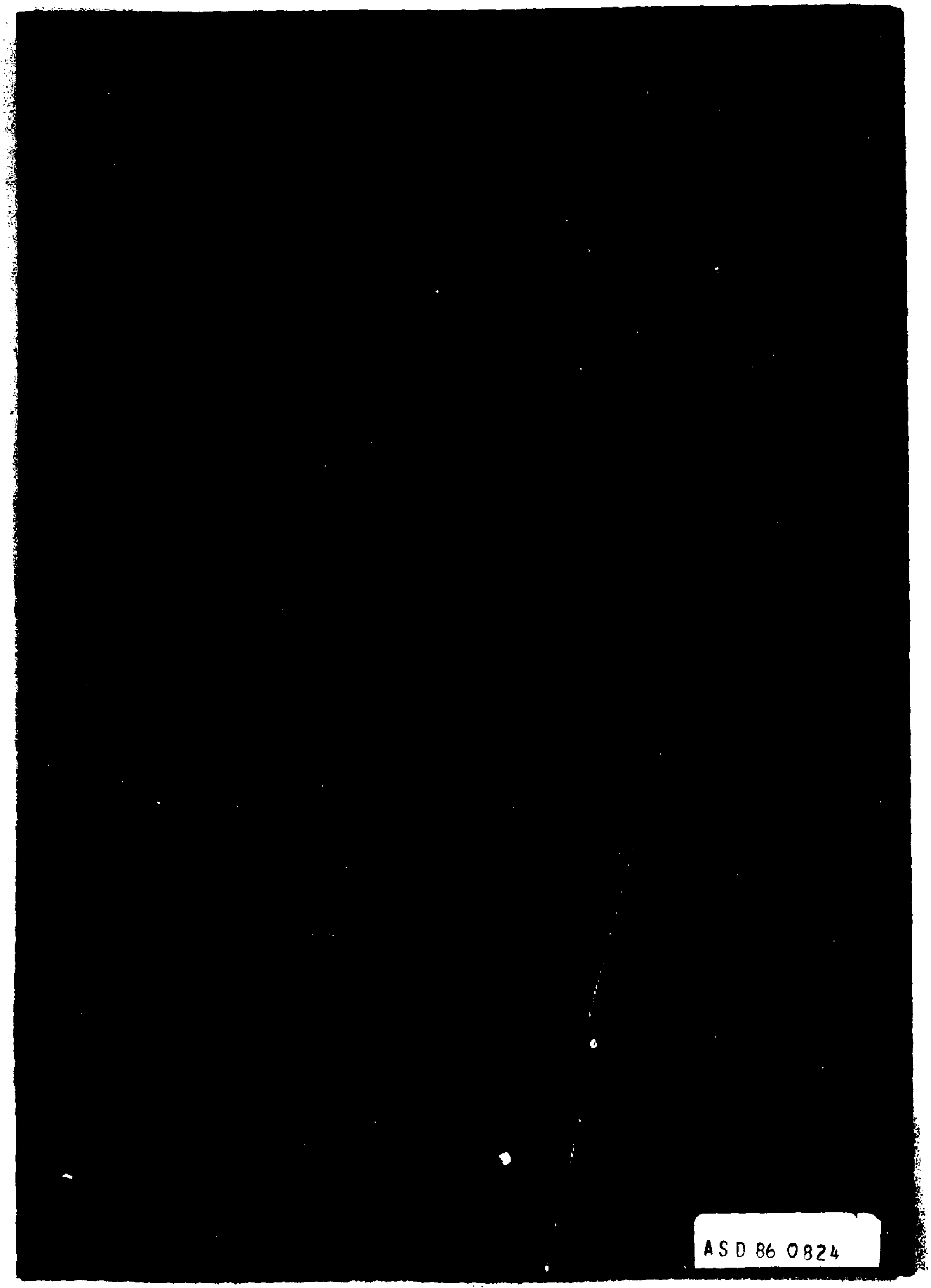
ASD 86 0824

NOTICE

When Government drawings, specifications, or other data are used for any purpose other than in connection with a definitely related Government procurement operation, the United States Government thereby incurs no responsibility nor any obligation whatsoever; and the fact that the government may have formulated, furnished, or in any way supplied the said drawings, specifications, or other data, is not to be regarded by implication or otherwise as in any manner licensing the holder or any other person or corporation, or conveying any rights or permission to manufacture use, or sell any patented invention that may in any way be related thereto.

This report has been reviewed by the Office of Public Affairs (ASD/PA) and is releasable to the National Technical Information Service (NTIS). At NTIS, it will be available to the general public, including foreign nations.

This technical report has been reviewed and is approved for publication.

FOR THE COMMANDER

Theodore J Reinhart

THEODORE J. REINHART, Chief
Materials Engineering Branch
Systems Support Division

UNCLASSIFIED

SECURITY CLASSIFICATION OF THIS PAGE

REPORT DOCUMENTATION PAGE

1a. REPORT SECURITY CLASSIFICATION: UNCLASSIFIED	1b. RESTRICTIVE MARKINGS: NONE
2a. SECURITY CLASSIFICATION AUTHORITY: N/A	3. DISTRIBUTION/AVAILABILITY OF REPORT: Approved for Public Release Distribution unlimited
2b. DECLASSIFICATION/DOWNGRADING SCHEDULE: N/A	
4. PERFORMING ORGANIZATION REPORT NUMBER(S): None	5. MONITORING ORGANIZATION REPORT NUMBER(S): AFWAL-TR-85-4150, Vol 4
6a. NAME OF PERFORMING ORGANIZATION: DFVLR - Institute for Structural Mechanics; 6b. OFFICE SYMBOL (If applicable): N/A	7a. NAME OF MONITORING ORGANIZATION: AFWAL/Materials Laboratory (AFWAL/MLSE)
6c. ADDRESS (City, State and ZIP Code): Braunschweig, West Germany	7b. ADDRESS (City, State and ZIP Code): Wright-Patterson AFB, OH 45433
8a. NAME OF FUNDING/SPONSORING ORGANIZATION: European Space Technology Committee; 8b. OFFICE SYMBOL (If applicable): N/A	9. PROCUREMENT INSTRUMENT IDENTIFICATION NUMBER: ESTEC/Contract No 4825/81/ML/AK(SC)
8c. ADDRESS (City, State and ZIP Code): Brussels, Belgium	10. SOURCE OF FUNDING NOS.: PROGRAM ELEMENT NO. N/A; PROJECT NO. N/A; TASK NO. N/A; WORK UNIT NO. N/A
11. TITLE (Include Security Classification): Development of Fracture Mechanics Maps for Composite Materials	
12. PERSONAL AUTHOR(S): Editor (Dr. H. W. Bergmann)	
13a. TYPE OF REPORT: Final; 13b. TIME COVERED: FROM Jan 82 TO Jan 85	14. DATE OF REPORT (Yr., Mo., Day): 1985 Dec; 15. PAGE COUNT: see below (16)
16. SUPPLEMENTARY NOTATION: Vol 1 (216) Vol 2 (204) Vol 3 (265) Vol 4 (192)	

17. COSATI CODES

FIELD	GROUP	SUB. GR.
11	04	
01	03	

18. SUBJECT TERMS (Continue on reverse if necessary and identify by block number): Fiber Reinforced Composites, Dynamic Test, Thermal Cycling, Quality Control, Static Test, Stress Concentrations

19. ABSTRACT (Continue on reverse if necessary and identify by block number)

The Institute for Structural Mechanics of the German Aerospace Research Establishment (DFVLR) has conducted a research program aimed at the characterization of the fracture behavior of carbon-fiber-reinforced epoxy resins. The research effort encompassed a comprehensive experimental and analytical investigation of the response of test specimens under a broad range of material, loading and environmental parameters. By combining an evaluation of global laminate properties with an investigation of micro- and macroscopic modes of failure, the understanding of the fracture and fatigue behavior of carbonfiber-reinforced composites was enhanced. It is expected that the results of the research program and their representation in the form of tables, figures, graphs and maps will assist the design engineer and lead to improved engineering concepts. This Volume includes the following Appendices:

20. DISTRIBUTION/AVAILABILITY OF ABSTRACT: UNCLASSIFIED/UNLIMITED ☒ SAME AS RPT. ☐ DTIC USERS ☐	21. ABSTRACT SECURITY CLASSIFICATION: UNCLASSIFIED
22a. NAME OF RESPONSIBLE INDIVIDUAL: THEODORE J. REINHART	22b. TELEPHONE NUMBER (Include Area Code): 513/255-3691; 22c. OFFICE SYMBOL: AFWAL/MLSE

DD FORM 1473, 83 APR EDITION OF 1 JAN 73 IS OBSOLETE.

A

SECURITY CLASSIFICATION OF THIS PAGE

DEVELOPMENT OF FRACTURE MECHANICS MAPS

FOR COMPOSITE MATERIALS

Final Report
- Volume 4 -

APPENDICES F - K

B

VOLUME 4 - CONTENTS

APPENDIX F

Fatigue Response of Notched Graphite-Epoxy Laminates

Gerald Kress

DFVLR
Institut für Strukturmechanik
Braunschweig-Flughafen

DEUTSCHE FORSCHUNGS- UND VERSUCHSANSTALT FÜR LUFT- UND RAUMFAHRT E.V.
INSTITUT FÜR STRUKTURMECHANIK

Interner Bericht
IB-131-84/04

Fatigue Response of Notched Graphite-Epoxy Laminates

Gerald Kress

Braunschweig, Januar 1984

Der Bericht umfaßt:
18 Seiten
18 Bilder

Institutsleiter:
Dr.-Ing. H.W.Bergmann

Bearbeiter:
M.s. G.R.Kress

Abstract

Changes in the stiffness and strength of notched quasi-isotropic graphite-epoxy laminates were recorded and related to the fatigue damage. Two different laminates were considered and the effects of stacking sequence were compared. Nondestructive testing techniques such as X-radiography, moire technique, acoustic emission, deply technique, and stiffness change were performed to observe damage development. Results show that the mechanical response and the fatigue damage depend strongly on the stacking sequence of laminates. In general, residual strength increased remarkably for both laminates due to stress redistributions while the continuous stiffness change curve is typical for each laminate and reflects damage characteristics. Buckling effects as well as matrix cracking and delaminations contribute to stiffness changes.

CONTENTS

LIST OF ILLUSTRATIONS

1. INTRODUCTION

The study of hole related fatigue damage in materials is motivated by the need to include holes into structures. For example, in an airplane, even a critical plate or shell may have to provide access from one side to another for electric lines, fuel pipes, or other supplementary equipment.

As of to-date, the knowledge of the fatigue response of notched composite laminates is much less complete than that of unnotched laminates. The main reason is that fatigue damage, residual strength, and stiffness predicting models [1,2] for the unnotched situation are based on uniformities of damage that are reflected by terms such as 'characteristic damage state (CDS)', for instance. These uniformities of damage do not apply, however, for notched specimens. An idea of the complexity of the fatigue behaviour of notched specimens may be given by studying an X-ray photo of damage around the hole of a notched specimen after high fatigue loading.

The objectives of the present work are to determine the nature of damage induced in graphite epoxy composite laminates with center holes by cyclic tensile loading and to establish the influence of such damage on the strength, stiffness and life of laminates.

The complexity of damage in composite materials requires different techniques for complementary insight. Sendeckyj [3] found that the X-ray technique makes damage, namely matrix cracks and delaminations, visible but restricted to observing the x-y distribution of damage only. The deply technique complements the X-ray photography because of its ability to identify specific planes of delamination. X-ray photography and the deply technique are also opposite in the sense that the former is a non-destructive test (NDT) method while the latter inevitably destroys the test specimen.

The advantage of the ultrasonic C-scan technique, compared with X-ray photography, is that its sensitivity is not dependent on a contrast medium, thus enabling it to detect delamination-like flaws surrounded by undamaged material. Damage events during the loading process can be detected by acoustic emission recording. It yields, in combination with the simultaneously recorded load-strain curve, information on the sequence and the interactive effects of subsequent damage events.

Since the strain field in notched specimens is nonuniform, it is difficult to decide what strain measurement technique gives the most valuable information. However, the moire technique [4] provides insight into the complete nonhomogeneous in-plane strain field.

A recently established investigative method is the use of stiffness change recording as an indicator for damage state or strength values [5].

E.T. Camponeschi and W.W. Stinchcomb [6] pointed out that a quasi-isotropic laminate exhibits a different response than its constituent sublaminates. For instance, the response of a [0,90,+45,-45]s laminate cannot be predicted by knowing the behaviour of the [0,90]s and of the [45,-45]s laminate. Static strength predicting models for notched specimens were developed that do not require a laminate stress analysis. Instead, the notched and the unnotched situation are compared. J.M. Whitney and R.Y. Kim [7] published the results of a test series which exhibit that notched failure mechanisms differ from the unnotched situation. They investigated the influence of two different stacking sequences, one of them producing tensile, the other producing compressive interlaminar normal stress throughout the thickness of the straight edge on both notched and unnotched specimens. The data indicate that unnotched tensile strength is reduced by the straight edge effects and is strongly dependent on the stacking sequence; while the strength of notched specimens is independent of the straight edge effects since tensile failure

is initiated by the stress concentration at the notch before straight edge delamination comes into effect.
Other investigations of the fatigue behaviour of notched specimens were conducted by Sendeckyj [3], Stinchcomb and co-workers [2], and Whitcomb [8]. The work most comparable to the present one is that of Whitcomb, who described the damage state and the mechanical response of four different notched laminates after tension-tension-fatigue loading and related delamination onset to the results of a FEM stress analysis. The load levels of two-thirds of the initial strength of the laminates, respectively, were low enough to let the specimens survive a lifetime of ten million cycles. At this point, the damaged specimens were investigated using destructive and nondestructive methods. The residual strength of all laminates was equal to or higher than the initial strength of specimens, respectively. Stiffness degradations were found to be in the range from zero to minus 10 percent. Whitcomb also shows figures comparing initial stress distributions with delaminations at different locations through the thickness on the hole that suggest that interlaminar normal stress and shear stress distributions govern the locations of first fatigue delaminations. Later in the lifetime, the direction of delamination growth can be changed by an altered stress distribution.
In the present study, two laminates with relatively little straight edge initiated damage were chosen in order to isolate notch effected damage from straight edge driven damage as much as possible.
The damage induced by static and by fatigue loading was observed by nondestructive inspection and other methods. Quasi-static tests were performed to compare the development of damage under cyclic with that under static loading. Experimentally observed data were interpreted.

2. EXPERIMENTAL PROCEDURES

2.1 Material and Specimens

The material in this study is T300-5208 graphite epoxy. The Specimens were ten inches long, 1.5 inches wide and had a 0.375 inch diameter hole in the center. The two stacking sequences were:

[0, 90,+45,-45]s type A
[+45, 90,-45, 0]s type B

For comparison, static strength tests were also performed on unnotched specimens with the stacking sequence:

[+45,-45, 0, 90]s type C

2.2 Fatigue Tests

All fatigue tests were run in the tension-tension mode with a load ratio of R=0.1 and a frequency of 10 Hertz.
Specimens were tested at several different load levels evaluated as percentages of the mean tensile strength of five samples. The load levels spanned

the range from 70 to 95 percent; i.e., from long-life-load levels to short-life-load levels.
Several specimens were run to failure to obtain lifetime-over-load (s-n) curves, others were monotonically loaded to failure after a certain number of cycles to obtain the typical strength versus loading-history curves. Many of these specimens were subjected to nondestructive inspections, such as X-radiography or moire tests, at selected numbers of cycles.

3. RESULTS

3.1 Initial Tensile Strength

Tensile strength tests were performed on five specimens of each type of laminate, including the unnotched laminate.
In Figure 1, the failure load of each specimen is represented by the length of a vertical line. The average failure loads of A, B and C specimens were 2620, 2240, and 4680 lbs., respectively as indicated by the solid horizontal lines.
The lower, dashed horizontal lines indicate the averaged load levels for which major discontinuities in the strain-load curves, as well as the first strong acoustic emissions during the loading process, occurred.

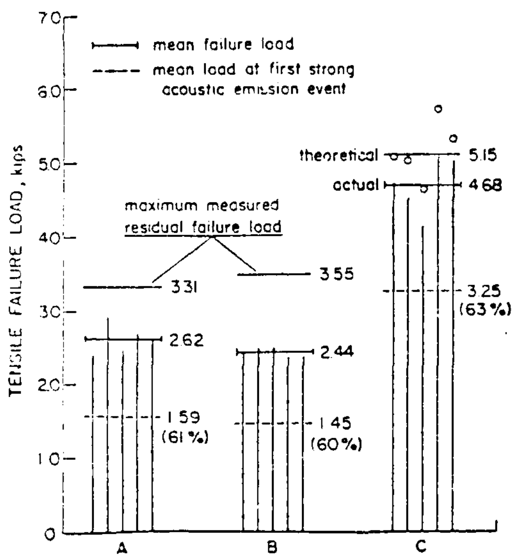

Figure 1. Static Strength

The percentages refer to the average failure load of each type of laminate. The large difference between the strength values of notched and unnotched specimens is due to the stress concentrating effect of the hole. Yet, it must be noted, that the strength of the C-specimens is also reduced by straight,

free edge effects. But the strength values indicate that a strength reduction factor for the hole must be much larger than one for the straight edge. Furthermore, since edge effects in general (whether for curved or straight edges) decrease rapidly with increasing distance from the edge, the effects of the straight edge and the curved edges of the notched laminates are independent. In other words, we may assume that for the notched specimens used in this study, the effects of the straight edge do not yield an additional contribution to the reduction of static strength caused by the hole.
It is important to note that the highest measured residual strengths, related to the notched cross-section, of A- (66.5 ksi) and B- (71.4 ksi) specimens approach the tensile strengths of C-specimens, thus indicating that fatigue damage redistributes local stresses to the extent of reducing the stress concentration to the hole.

3.2 Initial Stiffness

Stiffness data were taken from the linear part of the load-strain curves recorded during the tensile strength tests by means of a 1.0 in. extensometer centered with respect to the hole. Each vertical line in Figure 2 represents the stiffness of a specimen. Average stiffness values, based on the area of the unnotched section, are indicated by the horizontal lines.

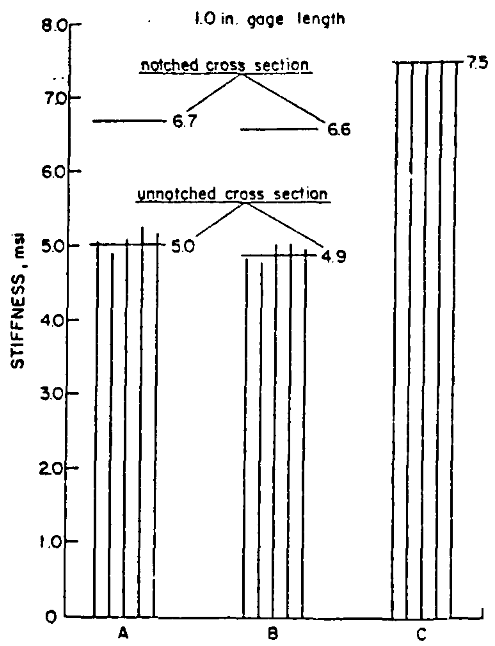

Figure 2. Static Stiffness

The stiffness values of A- and B-specimens, based on the cross-sectional area, are lower than the stiffness values determined for unnotched C type specimens. This demonstrates the large, local deformation field associated with the local stresses due to the hole.

3.3 S-N Data

A lifetime of more than one million cycles under the condition of a sinusoidal load with a ratio σmin/σmax = 0.1 and a frequency of 10 Hertz can be expected at an 80 percent load level (2093 kips) for A-specimens and a 70 percent load level (1707 kips) for B-specimens. Load-log life curves for the two laminates are shown in Figure 3. A-specimens, cycled on a 95 percent load level (2485 kips), and B-specimens, cycled on an 85 percent load level (2093 kips) will survive hundred thousand cycles.

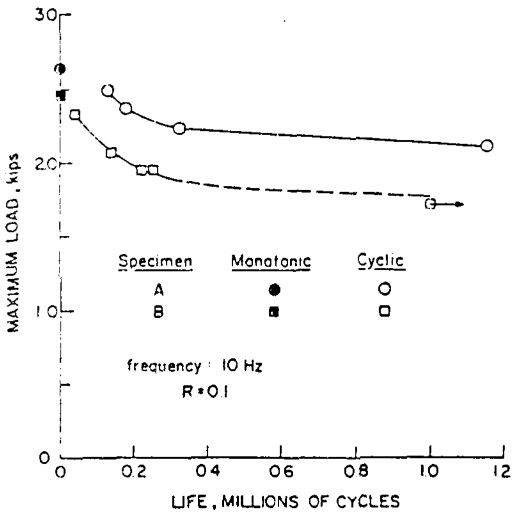

Figure 3. S-N Curves

Two A-specimens had an average lifetime of 1.1 million cycles at the 80 percent load level while the B-specimen, cycled at the 70 percent level, had a residual strength of 137 percent of the virgin strength after one million cycles. The residual strength data for type B laminates suggest that residual strength values of this magnitude occur during the final decade of logarithmic life.

3.4 Stiffness Degradation

Figure 4 on page 6 shows stiffness data for type B laminates cycled at the 85 percent level.
The two stiffness curves show the effect of gage length on the stiffness values. A clip type gage extensometer centered over the hole was used to measure displacement over a 1.0 in. gage length. A DCDT extensometer centered over the hole measured displacement over a 3.625 in. gage length. The stiffness

change values based on the short extensometer data are larger. However, if the damage zone spreads outside the 1.0 gage length, the stiffness change values determined from the short extensometer are inaccurate.

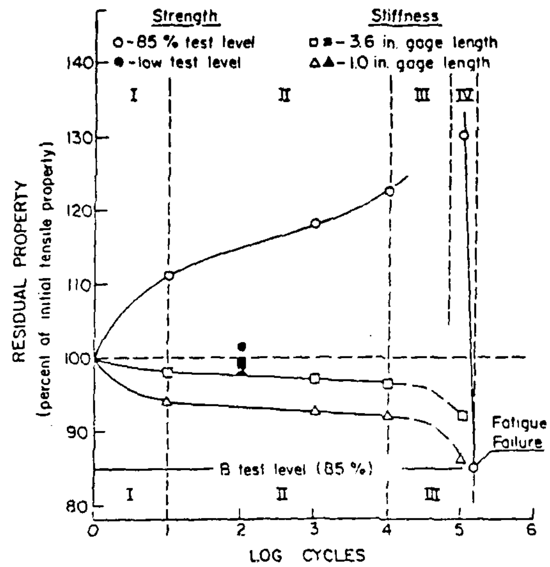

Figure 4. Stiffness and Residual Strength Versus Life

The process of damage development around the hole of a type B laminate is indicated by the stiffness curves shown in Figure 4. The limits of the regions I, II, and III are somewhat arbitrary, but are chosen to reflect transitions in the damage growth process as represented by stiffness change. In region I, the stiffness decreases at a decreasing rate as small matrix cracks develop near the hole. In region II, the stiffness degrades linearly with log cycles and the matrix cracks in the zero and 45 deg. plies extend away from the hole and delaminations form in the region damaged by matrix cracks. Region III begins as the stiffness degradation rate increases. In this region, the sharp decrease in stiffness is associated with further extension of the cracks in the 45 deg. plies, and growth of delamination along the 45 deg. matrix cracks. Early in the life of the laminate (region I) the damage is confined to the approximate zone of stress concentration around the hole. In later stages of life, the stresses around the hole are redistributed and the stress concentration around the hole is changed due to the growth of the damage zone away from the hole. Radiographs of damaged type A and type B specimens are shown Figure 9 on page 11 and Figure 10 on page 11. The data in Figure 4 are presented in terms of percent change in stiffness because the exact values of stiffness are not repeatable in situations where the cyclic test is stopped, the extensometer is removed from the specimen, and the specimen is removed from the grips for nondestructive evaluation at various cyclic intervals. However, if the stiffness values are determined at the beginning and end of each interval, or are recorded throughout a cyclic interval by the data aquisition system, the change in stiffness during the cyclic interval can be determined. The total change is then computed as the sum of the stiffness changes for all intervalls.

3.5 Continuous Stiffness Recording

The plots of the results of the peak detector program on a logarithmic life-time scale confirm the estimated stiffness curves based on quasi-static tests. The suggestion of a five percent stiffness loss after 100 cycles at a 90 percent cycling load for both laminates was taken into account by multiplying the first stiffness value, received by the peak detector after 200 cycles, by the factor 0.95.
Figure 5 shows the regions II and III of the stiffness degradation due to fatigue loading at the 90 percent level of failure load of each specimen, respectively. The time axis is logarithmically scaled. In this representation, region II appears as an almost linear line leading into a sharp knee which connects region II with region III. Immediately behind the knee, the degradation rate appears to be highly increased. At the end of region III, the stiffness decay accelerates again until failure.

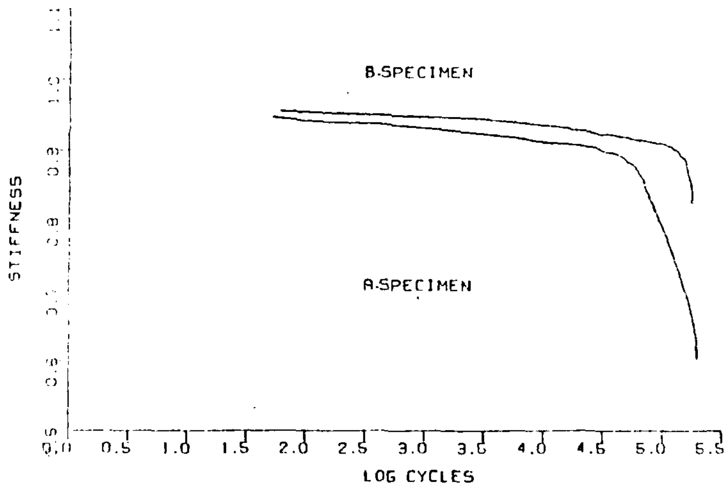

Figure 5. Stiffness Degradation Versus Logarithmic Cycles

Comparing the two curves shown in Figure 5, we find the B-laminate showing a lower stiffness degradation before the knee, a later and more distinct forming of the knee, and a higher degradation rate after the knee than the A-laminate. The stiffness loss at the end of fatigue life is 18 percent for the B-specimen and 40 percent for the A-specimen.
The data have been replotted using a linear scale for the life axis, Figure 6 on page 8. Throughout the lifetime, the A-specimen has a lower stiffness than the B-specimen. Between 10 K and 50 K cycles, the degradation rates of both curves are similar; after that the A-specimen looses stiffness more rap-

idly than the B-specimen. Although the total stiffness loss during its lifetime is lower for the B-specimen, the stiffness degradation rate shortly before failure is very high. Both laminates exhibit three sudden stiffness changes during the fatigue life: the first one occurs during the very first cycles of loading; the second one occurs within the first half of the lifetime for the A-specimen and well before failure of the B-specimen, and the third, sudden stiffness lossed leads into the failure of the specimens. The A-specimen has its second sudden stiffness loss at 70 K cycles and the B-specimen at 157 K cycles. Both events coincide with the onset of the knee in the logarithmic-scale stiffness representation and are generally followed by an increased degradation rate. It should be mentioned here that locally confined buckling effects were seen during cyclic loading of the A-specimen.

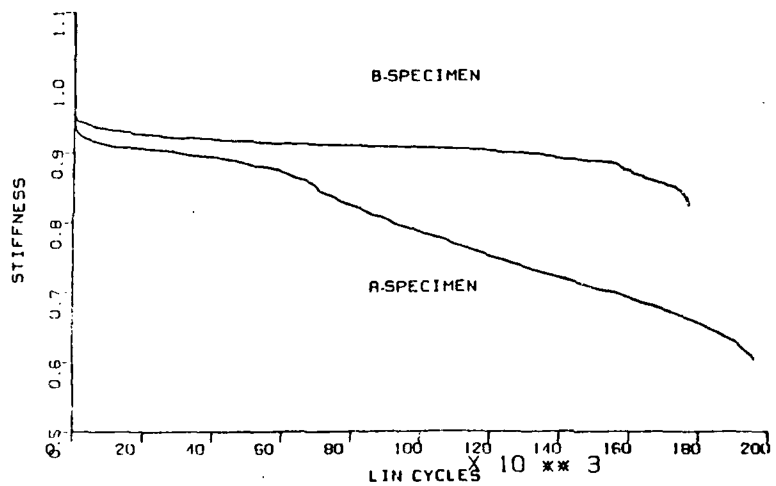

Figure 6. Stiffness Degradation Versus Linear Cycles

On both sides of the specimen, the zero-deg and the 90-deg plies, as a sublaminate, delaminated from the inner [45,-45]s block at locations governed by compressive circumferential stresses and buckled outwards. It could be hypothesized that the forming of these delaminations and in company the stiffness degradation is being rapidly accelerated after reaching a critical delamination size which facilitates buckling. The sudden stiffness change at 70 K for the A-specimen could then be related to the observed buckling effects. By eye inspection, no buckling effects were visible for the B-specimen. However, at the end of the fatigue life, it seemed to be obvious by eye observation that the surface 45-deg ply contributed only little or nothing to the load transfer, since around the hole matrix cracks were formed and some of the surface material confined by those cracks was almost completely delaminated. The matrix cracks prevent the in-plane-load transfer and the delaminations make load transfer through interlaminar shear stresses impossible. These effects were visible at the end of the lifetime of the B-specimen, thus suggesting the possibility of a relationship between them and the sudden stiffness change at 157 K cycles. Finally it should be recalled that the 90 percent load levels for the A- and the B-specimens are represented by the absolute values of 2354 lbs and 2195 lbs, respectively.

3.6 Residual Strength

A number of the cyclic tests were halted at various stages of the loading history for nondestructive inspection of the damage zone and residual strength measurements. This series of tests provided a characteristic and repeatable curve of the change in residual strength throughout the loading history.

During the first few (ten) cycles, the damage, primarily matrix cracks, reduces the effect of the stress concentration at the hole and the residual strength increase is on the order of ten percent. The actual strength increase does depend on the cyclic stress level, with the higher stress levels corresponding to slightly higher strength increases than the lower stress levels.

Stiffness change and residual strength data for a type B laminate after 100 cycles at a low cyclic stress amplitude are also shown in Figure 4. Both the increase in residual strength and the decrease in stiffness are less than those for the same type specimen cycled at the 85 percent stress level. The second region of the residual strength curve, approximately ten percent of the fatigue life, is characterized by a slow, but constant increase in residual strength over a logarithmic cycles scale. At the end of the second region, the increase in residual strength is 115 to 120 percent. The limits of regions I and II for residual strength are approximately the same as observed for stiffness change.

The third region of the residual strength curve is marked by a further increase in residual strength. Although the data in this region is incomplete, it appears that the maximum residual strength is reached between 50 and 80 percent of the lifetime. The largest increases in residual strength are 26 and 42 percent for the type A and B laminates, respectively. During the final region of the fatigue life, the residual strength decreases until the strength equals the level of maximum cyclic stress, as shown in Figure 4 and Figure 7.

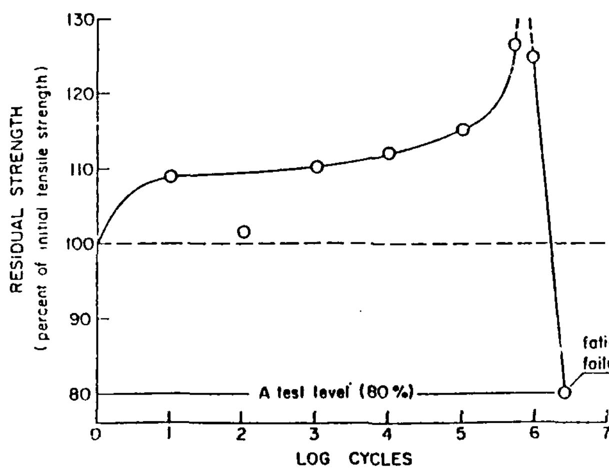

Figure 7. Residual Strength of an A-Specimen

The last two regions of the residual strength-log cycles curve correspond to the third region of the stiffness reduction curve where the stiffness change shows a sharp decrease on the log cycles plot. The logarithmic scale used to represent the lifetime may cause some confusion in interpreting these results. The residual strength data have been replotted in Figure 8 using a linear scale to represent cycles.

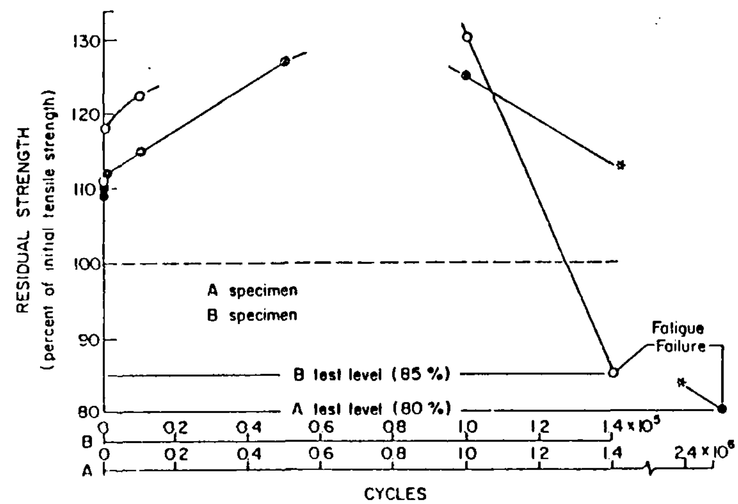

Figure 8. Residual Strength Versus Linear Cycles

3.7 Damage Patterns

Static damage starts with matrix cracks usually in the surface plies at 1570 lbs load for the A-laminate and 1220 lbs load for the B-laminate. At higher load levels, cracks appear in all directions. The A-laminate develops more well defined zero-deg cracks tangent to the hole while the B-laminate develops more well defined 45-deg cracks. Note that these are the directions of the surface layers, respectively. In both laminates, 45-deg and zero-deg cracks already exist. Zero-deg cracks in the A-laminate grow to a length of more than five hole diameters. When the tangent zero-deg cracks approach their maximum length, cracks in 45-deg and 90-deg direction are also initiated on the straight edge. In the final stages of lifetime, a regular pattern of matrix cracks is formed between the tangent zero-deg cracks and the straight edges. The uniformity of these cracks is similar to damage patterns of unnotched laminates, so-called characteristic damage states (CDS).
The delamination zone visible on an X-ray photo, Figure 9 and Figure 10, consists of the superimposed images of the delaminations on the various laminate interfaces. It seems as if the tangent zero deg cracks in both the A- and the B-laminates cause delaminations on adjacent interfaces. Those delaminations have the largest continuously connected area of all delaminations in the lam-

Figure 9. X-Radiograph of a Damaged A-Specimen

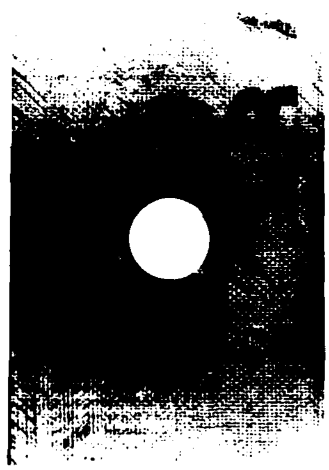

Figure 10. X-Radiograph of a Damaged B-Specimen

inates. In general, while the A-laminate develops a much larger delamination along its tangent zero-deg cracks, the more confined delaminations of the B-laminate spread along the 45-deg direction and reach the straight edge. It is emphasized that Figure 11 or page 12 gives the spatial distributions and the characteristic shapes as well as the proper magnitude of the delamination zones. Noting that the area of delaminations on all interfaces is higher for the A-laminate than for the B-laminate, we recall that the A-specimen experienced much higher stiffness losses during their fatigue life than the B-specimens.

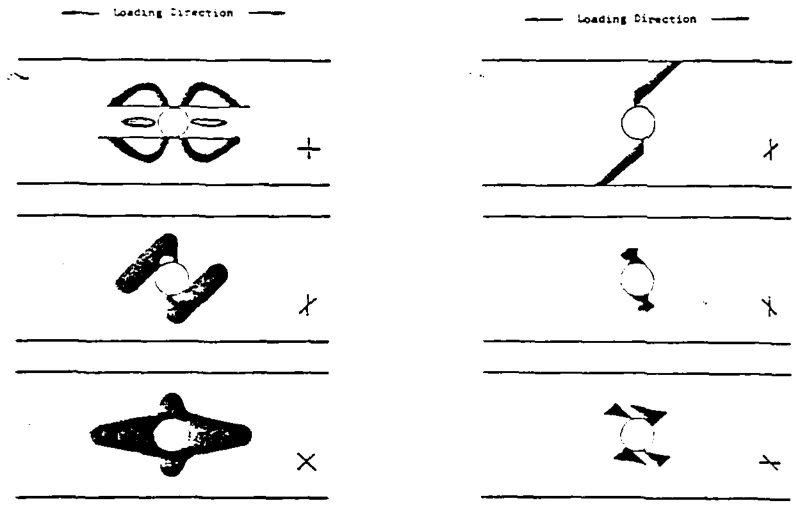

Figure 11. Delamination Areas on Interfaces

3.8 Damage and Mechanical Response

Figure 12 on page 13 shows that the tangent zero-deg cracks have a strong redistributing effect on the strain field near the hole, reducing the maximum strain concentration in x-direction. Except at the crack tips, the strain distribution along the cracks is almost uniform.
Figure 13 on page 14 presents the average strain concentrations as a function of the length of the tangent cracks at various fatigue stages for the A-specimen. After 600K cycles, which is estimated as being 50 percent of the expected lifetime the strain concentration is reduced to K=1.46.
Figure 14 on page 14 shows the decrease of strain concentration versus the logarithmically scaled number of cycles. The rate of decrease is very high during the first cycles of fatigue loading.
Recalling that the rate of increase of residual strength of both laminates is also very high at the beginning of fatigue life, it seems very likely that the tangent zero-deg cracks are a main factor influencing residual strength.

Figure 12. Undamaged Versus Low Damage Situation

Figure 15 on page 15 shows the results of two strength tests performed on an A-specimen and a B-specimen versus the length of the tangential cracks obtained from X-ray photos taken after applying the fatigue load.
We note that cracks of equal length in A- and B-specimen seem to influence the strength increases of A- and B-specimens differently. As a result of a linear curve fit for the data points we find an increase-in-strength rate of 44 percent per inch for the B- and 23 percent per inch for the A-laminate. A residual-strength versus strain-concentration curve (Figure 16 on page 15) was constructed from the data used in Figure 14 on page 14 and Figure 15 on page 15 by eliminating the crack length.
Figure 17 on page 16 and Figure 18 on page 17 show the increase of cracks in the zero-deg plies with the number of cycles under fatigue load. The crack

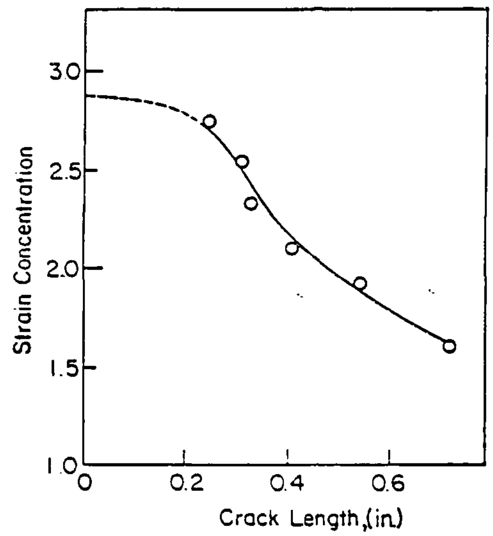

Figure 13. Strain Concentration Versus Length of Tangent Zero-Deg Cracks

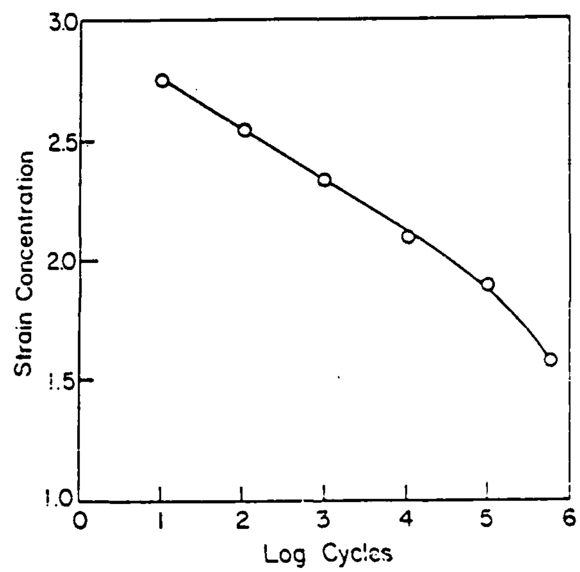

Figure 14. Strain Concentration Versus Logarithmic Number of Cycles

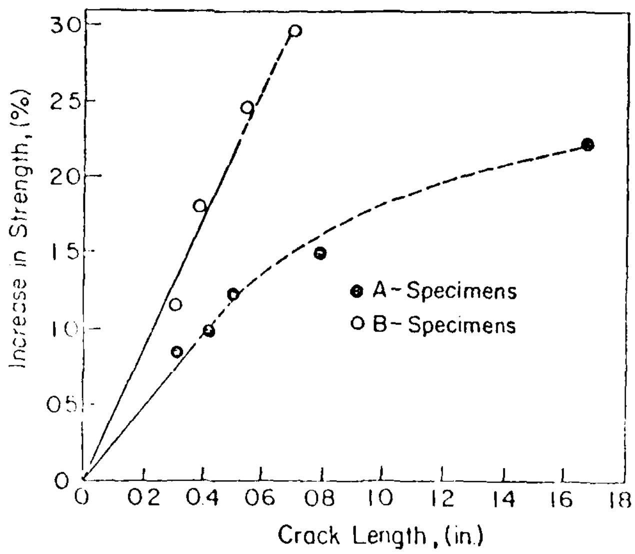

Figure 15. Strength Versus Length of Tangent Zero-Deg Cracks

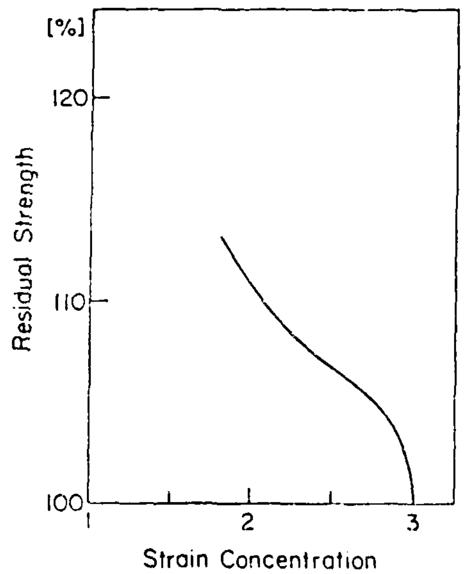

Figure 16. Residual Strength Versus Strain Concentration

lengths are the average values of the length of the two cracks visible on X-ray photos. For two reasons it is difficult, however, to measure average crack lengths exactly. First, the length of the dark line on a X-ray matches the actual crack length only in the case of complete penetration with zinc iodide. Second, it is difficult to decide what the length of a crack is since a dark line on a X-ray is the superimposed image of actually two cracks on each side of the laminate midplane. If these two actual cracks are shifted in different directions, one might observe a longer crack than actually exists. Since the data for the B-laminate is more complete, Figure 18 provides also information on the influence of the load parameter on the growth rate of those cracks. Figure 17 takes the initial crack length due to static load into account, so the crack length starts with the value indicated.

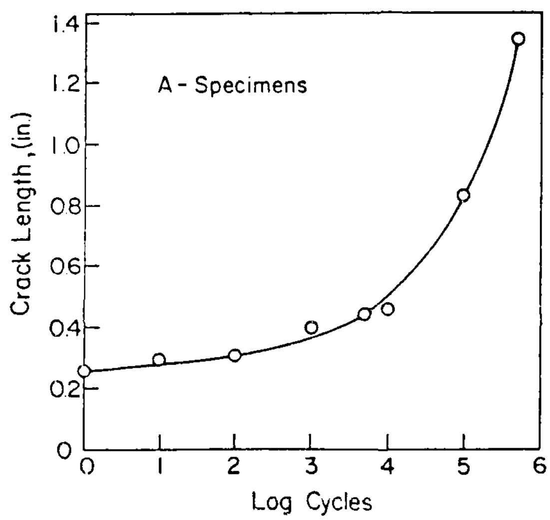

Figure 17. Zero-Deg-Crack Growth of an A-Specimen

The phenomenon of widely scattered fracture surfaces for specimens with high loading histories can be related to the shift of high strain concentrations away from the hole. Since those strain concentrations are presumably highest at the tips of the cracks, we conclude that catastrophic failure can be initiated right there. Many zero-deg fibers broke at a distance from the hole of 6 to 7 hole diameters or from 2.25 inches to 2.2625 inches. As for the phenomenon of stiffness degradation, we note that the A-laminate exhibits much larger delaminations than the B-laminate. These delaminations and also the buckling described in the section on continuous stiffness recording contribute to higher stiffness losses in the A-laminate than in the B-laminate.

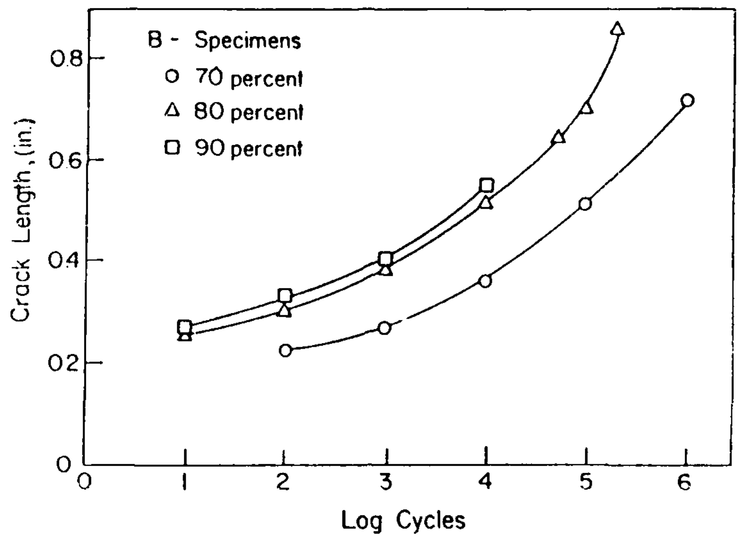

Figure 18. Zero-Deg-Crack Growth of B-Specimens

4. REFERENCES

1. W.W. Stinchcomb, K.L. Reifsnider, Fatigue Damage Mechanisms in Composite Materials: A Review, J.T. Fong, Ed., ASTM STP 675, American Society for Testing and Materials, 1979, pp. 762-787

2. W.W. Stinchcomb, K.L. Reifsnider, P. Yeung, J. Masters, Effect of Ply Constraint on Fatigue Damage Development in Composite Material Laminates, Fatigue of Fibrous Composite Materials, ASTM STP 723, American Society for Testing and Materials, 1981, pp. 64-84

3. G.P. Sendeckyj, G.E. Maddux, E. Porter, Damage Documentation in Composites by Stereo Radiography, Damage in Composite Materials, ASTM STP 775, K.L. Reifsnider, Ed., American Society for Testing and Materials, 1982, pp. 16-26

4. Daniel Post, Optical Interference for Deformation Measurements -- Classical Holographic and and Moire Interferometry, Mechanics of Non= destructive Testing, Editor W.W. Stinchcomb, Plenum Press, New York, 1980

5. T.K. O'Brien, Stiffness Change as a Nondestructive Damage Measurement, Mechanics of Nondestructive Testing, Editor W.W. Stinchcomb, Plenum Press, New York 1980

6. E.T. Camponeschi, W.W. Stinchcomb, Stiffness Reduction as an Indicator of Dama= ge in Graphite/Epoxy Laminates, Composite Materials: Testing and Design (sixth Confe= rence), ASTM STP 787, I.M. Daniel, Ed., American Society for Testing and Materials, 1982, pp. 225-246

7. J.M. Whitney R.Y. Kim, Effect of Stacking Sequence on the Notched Strength of Laminated Composites, Composite Materials: Testing and Design (Fourth Con= ference), ASTM STP 617, American Society for Testing and Materials, 1977, pp. 229-242

8. J.D. Whitcomb, Experimental and Analytical Study of Fatigue Damage in Notched Graphite/Epoxy Laminates, Fatigue of Fibrous Composite Materials, ASTM STP 723, American Society for Testing and Materials, 1981, pp. 48-63

APPENDIX G

Influence of Simulated Space
Environment on Carbon Fiber Reinforced
Plastic (CFRP)

W. Hartung

Institute for Structural Mechanics
Braunschweig-Airport

Contents

1. Introduction

In future spacecraft application satellite structures in the form of antennas or platforms will become increasingly important. Because of their attractive structural properties graphite/epoxy or graphite/polymide composites are the prime material candidates for such applications. Besides their specific strength and stiffness properties they offer low coefficients of thermal expansion. So that deformations of the structure under temperature exposure can be held to a minimum. However, on the microscopic level, the large differences in thermal expansion coefficients between the resins and the fibers lead to thermally induced stresses of substantial magnitude when the material undergoes thermal cycling as a consequence of sun and shadow phases in an earth orbit. The corresponding upper and lower temperature limits depend on the surface coating of the structure and on the attitude angle relative to the sun. They may range from -160°C in deep shadow to +100°C and even more when exposed to the sun. Depending on orbit height, inclination and service time 3000 to 5ooo thermal cycles may occur during the life of a typical vehicle and thereby introduce thermal fatigue problems in the material. Additionally, electronmagnetic and particle irradiation may degrade the properties of the organic matrix.

In order to assess the effects of severe thermal cycling and of electron radiation on the mechanical properties of various carbon fiber composites a test program was conducted with emphasis on a comparison of their initial and residual material properties.

2. Thermal Properties of Carbon-Fiber Reinforced Plastics (CFRP)

The thermal expansion coefficient of graphite fibers in the axial direction is nearly zero. It decreases as the modulus increases to a point where high modulus fibers exhibit negative axial thermal expansion coefficients [1]. Epoxy resins, however, have thermal expansion coefficients in the order of

2 times that of aluminum. The thermal expansion of cured laminates depends both on the material choice and the stacking order. Table 1 gives thermal expansion coefficients of several laminates prepared from different materials. All measurements were performed over a 60K temperature range (30°C to 90°C) using a quartz-tube dilatometer having an accuracy of about 10^{-8} m. The specimens were preconditioned at 70°C for 14 days in dry air to minimize moisture effects. The values shown in Table 1 are average values of 4 or 5 specimens. The thermal expansion coefficients of all unidirectional laminates are negative in the fiber direction. In accordance with ref. [1] the contraction is greater in laminates with high modulus fibers than in those with high tension fibers. Perpendicular to the fiber direction the thermal expansion coefficients of the laminates which contain 60% fibers by volume correspond to that of aluminum.

The data in Table 1 supplement the publicly available information on expansion coefficients of CFRP in the above mentioned temperature range. Extrapolations beyond this range especially into very low temperature regimes encountered in space, are hardly possible because thermal expansions do not depend linearly on temperature. Thermally induced stresses are initated in a laminate during the curing process when it reaches a temperature at which the resin changes from a rubbery gel to a glassy solid and the cross-linking reactions slow down. At this temperature no stress exists between the fibers and the matrix. It is slightly below the final cure temperature of the resin and is called the lock-on temperature.

When the laminate is cooled down to ambient temperature the different thermal expansion coefficients of fibers and matrix generate tensile stresses in the matrix and compressive stresses in the fibers along the fiber axes in each lamina. In addition to longitudinal stresses depending on the fiber volume fraction the transverse thermal expansion coefficient of the fibers and the mismatch of the Poisson's ratios of the fibers and matrix, radial and circumferential stresses can be generated. [2,3] Beyond this in cross/plied laminates shear stresses and tensile stresses transverse the fiber directions will be generated by the constraint of the different fiber directions. Because of the dependence of the stress state on the difference between curing temperature (respectively lock-on temperature) and ambient temperature it may be concluded that resins requiring low curing temperatures should be favoured for space applications. But nonlinearity of the thermomechanical properties of the laminates and / or the admissible strain of the matrix without crack formation may repress the influence of the curing temperature.

3. Material Selection

For the evaluation of the thermal properties of CFRP as discussed in chapter 2 different materials were selected including systems with high tension fibers as well as high modulus fibers. The curing temperatures are ranging from 120°C to 210°C. All of them were epoxy systems except for one polymide system identified as PJ. A survey of these materials is given in Table 2. The volume fraction of fibers and resin, respectively, was equal in all Materials.

4. Laminate Fabrication

Of each material at least one laminate was prepared with the size 380x380mm and numbered corresponding to Table 2. The curing cycles used in fabrication process met the instructions of the resin producers in all points with the exception that a pressclave was used instead of an autoclave.

The only polyimide system, laminate PJ, was prepared by Dornier System, Friedrichshafen. The laminates 164, 168, 169, 175, 246, and 247 were manufactured from industry supplied unidirectional prepregs in the own laboratory. The prepreg of laminate 170A was self/prepared by impregnating the carbon fibers and winding them on a drum.

The laminates consisted of 8 plies with the stacking sequence [2(+45°, -45°)]S, only laminate 247 was composed of 4 plies because of its double prepreg thickness. The total thickness of all laminates was 1mm. The mechanical properties of laminates with the selected stacking order are highly matrix controlled. Therefore, damages of the matrix as matrix cracks or delinations will substantially reduce the residual strength making the discovery of such damages possible by simple strength tests.

Four specimens were cut from the laminates 164, 168, 169. 175 and PJ respectively. One was for reference purposes while the others had to sustain different numbers of thermal cycles. The number of cycles reached by one specimen of each material respectively were 1170, 2295, and 3480.

5. Stress Calculation in [2(+45°, -45°)]S Laminates

The calculation of thermally induced stresses in a + 45°, -45° symmetrical 8-layer laminate was conducted on the basis of the classical lamination theory. The lock-on temperature was chosen to be 180°C, while thermal expansion coefficients of fibers and matrix and the elastic properties corresponded to those of 914 C-TS-5. The laminate was considered to extend infinitely in both directions. The calculation provided the compressive and tensile stresses in the individual layer parallel and normal to the fiber direction respectively as well as the shear stresses when the laminate is cooled down to -155°C.

For each layer the calculation indicated a tensile stress in the matrix perpendicular to the fibers of at least 71 MPa while the breaking strength of the resin is only 65 MPa. Severe cracking parallel to the fibers should be the consequence when exposed to very low temperatures encountered in space provided that the thermo-elastic properties of the material is linear. The shear stresses are of the same magnitude as the tensile stresses, i.e. 71 MPa. This is well below the 92 MPa shear strength of 914 C.

6. Thermal Cycling Tests

The thermal cycling tests were conducted in a vacuum test facility of the DFVLR. Inside a vacuum chamber of approximatly 100cm diameter a rotatable cage was located. The specimens were mounted on support provisions attached to the outer surfaces of two opposite sides of the cage (Fig. 1).By automatic rotation in 90° intervals the specimens were exposed, alternately, to infrared heaters and LN_2 - cooled plates simulating solar heating or energy dissipation by deep space effects (Fig. 2). The rear sides of the specimens were facing the walls of the cage whose inside was permanently cooled by LN_2. In this fashion a test specimen temperature of 95°C was realized during hot phase, and of -155°C during cold phase. The upper and lower temperature limits were controlled by the exposure time of 9 min during the hot phase and of 41 min during the cold phase resulting in a cycle time of 50 min. A chamber pressure of 10^{-4} Pa was maintained throughout the test. A typical thermal cycle is shown in Fig. 3.

Because of the viscoelastic behavior of the specimens matrix realistic thermal stresses will only be obtained when the simulation of the temperature-time gradients are as realistic as possible. This was accomplished in a nearily perfect fashion by the test arrangement.

7. Electron Irradiation Tests

Space structures, in general, are subject to electron and proton irradiation. The effects of electron irradiation on the laminates 168, 246, 247, and PJ (Table 2) were investigated by exposure of several specimens to electron beam irradiation of $3x10^8$ rads, at 100°C, and in 10^{-4} Pa vacuum. The beam current was held at 165μA for the required run time of twenty/seven (27) hours. The test was conducted in a Van der Graaf accelerator at the University of Illinois, USA.

8. Evaluation of Environmental Effects

The extent of damage caused in the laminates by environmental conditions was investigated by means of

- Ultrasonic inspections to detect delaminations generated by shear stresses
- Radiographs for the detection of matrix cracks due to tensile stresses perpendicular to the direction of the fibers
- Electron-beam micrographs to detect microcracks and debonding of fibers and matrix
- Measurements of the natural frequency and the logarithmic decrement of damping in transverse oscillation
- Measurements of the spectral reflection properties of the laminate surface
- Comparison between initial and residual strength and stiffness properties.

All of the test methodes were applied before and after increasing numbers of thermal cycles. Strength and stiffness tests were established both at room temperature and at 100°C. In order to obtain reproducible results the specimens were dried prior to testing. With respect to the irradiated specimens the tests were performed prior and after completion of the electron beam irradiation.

8.1 Ultrasonic Inspections

In Fig. 4 to 7 amplitude scans are shown of the laminates 164, 169, 170A, and 175 before and after 1170 thermal cycles. The laminate numbers and the corresponding material designations are contained in Table 2. Within the accuracy limits of ultrasonic techniques, the laminates 164, 169, and 175 are free of defects. The amplitude scans of laminate 170A show minor disturbances probably caused by pores progressing in the fiber directions as it was detected by scanning electron beam investigations. In contrast to the other laminates effects of thermal cycling, if they occured cannot be found by comparison of the two scans of Fig. 6 because prior to cycling ultrasonic inspection was only applied to the reference specimen.

Laminate 168 was prepared with artificially introduced delaminations at the center of each specimen for investigation of shear effects on the growth of such a damage. As evidenced by Fig. 8 no growth due to thermally induced stresses was experienced after 3480 thermal cycles.

In contrast to the epoxy based laminates, laminate PJ exhibited a rather smooth amplitude scan prior to cycling but, according to Fig. 9, indicated pores and extend delaminations after 1170 thermal cycles. The higher curing temperature of this material raises the thermally induced stresses by 6 to 7% over those of the former discussed graphite/ epoxy laminates and might have contributed to these damages.

8.2 Radiographs

Without special provision radiographs of thin CFRP laminates exhibit poor contrast. In order to raise the quality of the radiographs high-density fluids like Tetrabromethan (TBE) may be used. After penetration of the contrasting agent into cracks and pores in a TBE-bath, those defects become visible because the fluid absorbs X-rays to a higher degree than the sorrounding CFRP.

At the beginning of the program no experience existed wether this technique would affect the structural integrity of CFRP. Therefore, X-ray photographs of untreated epoxy/based laminates were taken before thermal cycling. During the thermal cycling test detailed investigations showed that the fluid can be removed by vacuum and heat without detectable defects in + 45°, - 45° laminates. Therefore, all radiographs taken after thermal cycling were contrast-lifted by TBE.

The photographs in Fig. 10 show no or little cracking in the TBE-treated laminates 164, 169, and 175 after cycling. The photograph of laminate 170A in the right of Fig. 11 indicates substantial damage, however. From the matching pattern of the striations in the photograph on the left it appers that damage existed already before the thermal cycling commenced. The reversal of the contrast is a consequence of the fact that for this photograph no TBE was used. Subsequent investigations with an electron beam microscope demonstrated that the damage existed in the form of extended internal pores in the fiber direction of the individual plies rather than of microcracks. Evidently, the majority of the damage was caused by faulty fabrication.

Severe matrix cracking as predicted by lamination theory could not be observed in any of the epoxy-based laminates. This indicates that the use of linear constitutive laws leads to unrealistic stress states.

The two radiographs in Fig. 12 of a polyimide based laminate PJ were also taken before and after thermal cycling. While the laminate seems to be initially free of any defects, a multitude of thin dark lines are visible after thermal cycling. Subsequently taken electron beam micrographs revealed that these lines do not represent internal pores as observed previously, but rather microcracks emanating from the surface of the specimen (Fig. 18).

As was expected no damage was found by ultrasonic inspections due to electron irradiation.

8.3 Scanning Electron Beam Micrographs

The effects of thermal cycling on all of the material systems were investigated also by scanning electron beam microscopy. In several specimens prepared from laminate 164 no defects were detected prior to cycling. After thermal cycling only a few short cracks extending through the thickness of one ply were visible. Its discovery was possible only after removal of the dust particles covering the polished surfaces by ionic etching. As can be seen in Fig. 13 the cracks were not confined to the matrix material but sometimes affected the fibers as well. This observation was made in 914C-TS-5 and T3T F178 laminates. It must be recognized, however, that the irregular distribution of such defects and the limited field of vision of the microscope make it difficult to establish reliable correlations.

Fig. 14 and 15 show accumulations of voids along the ply interface in samples cut from laminates 169 and 170A. No significant differences could be detected in the charakter of defects observed before and after thermal cycling. However, in laminate 169 the voids are limited to small local areas whereas in laminate 170A the voids seem to run together and extend over the whole laminate. Sometimes even indicating the formation of delaminations. This observation is consistent with the evaluation of the ultrasonic records in Fig. 6 and X-ray photographs in Fig. 11.

Samples from laminate 175 (Fig. 16) show similarity to those of laminate 164 except that more plies seem to be affected by crack formation. Again only a few cracks were created by thermal cycling.

Fig. 17 show a cross section and a surface view of the T3T F178 laminate PJ. They appear smooth and free of defects before thermal cycling, corroborating the previously obtained ultrasonic C-scans and radiographs. The photographs in Fig. 18 taken after 1170 thermal cycles exhibit comparatively large cracks forming a regular pattern on the surface (top photo). After progression of the cracks through the first ply a tendency toward formation of small delaminations along the interface with the adjecent ply could be observed (photo at bottom).

Fig. 19 to 22 show scanning electron beam micrographs of the fracture areas of laminates from 914C-TS-5 (Fig. 19 and 20) and from HYE-2034 D (Fig. 21 and 22), before and after thermal cycling. The fracture areas of the 914C-laminates show only a few broken fibers in both cases. Failure is obviously initiated by matrix cracks occuring parallel to the fibers in the inidividual layers of the laminate. The increasing peeling and shear stresses tend to create subsequently cracks in the plane of the interface between adjecent layers which lead to final rupture.

Fig. 20 shows the same secimen area as in Fig. 19 but taken at a higher magnification. The photos exhibit a distinct weakening of the bonding strength between fibers and matrix due to thermal cycling. When strength tested before thermal cycling the fracture surfaces of the individual plies were rough with some broken fibers visible. After thermal cycling they showed smooth traces of fiber pull out.

In the case of the laminate 175 the failure mechanism was different from that of the laminate 164 before thermal cycling. Lower strength of the pitch fibers and a high bonding strength between fibers and matrix tended to create ruptures transvers all plies where fracture of fibers was a normal mode of failure. After thermal cycling the failure mechanism was similar to that of laminate 164. As Fig. 22 indicates no significant change in bonding between fibers and matrix took place. No change of appearance was defected after electron irradiation.

8.4 Natural Frequencies and Decrements of Damping

Table 3 shows experimentally determinded natural frequencies and decrements of damping of the candidate materials after different numbers of thermal cycles. In all cases the natural frequency decreases with increasing numbers of thermal cycles. However, as shown in Fig. 23 and 24, the major change took place soon after the beginning of cycling, probably during the first few cycles. This may correspond to the development of initial cracks which ought to be expected during the same time frame. Because of the stress relaxation further cracking and crack extension will be slower with increasing numbers of thermal cycles.

The decrease of the natural frequency of the polyimide-bases laminate was three or more times larger than tnat of the other materials as is apparent in Fig. 24. This may be a consequence of the severe cracking observed in these samples. As indicated by Fig. 23 and 24 the decrement of damping of laminates 164, 169, and 170A increases with increasing numbers of thermal cycles indicating growing internal friction. The continous increase of friction is not only caused by matrix cracking since the formation of cracks, as previously described, tends to diminish because of stress relaxation. It is probable that the molecular structure of the resins is affected by fatigue, or the interface properties between fibers and matrix.

For the contradictory behavior of laminates 175 and PJ no physically reasonable explantion can be offered at this time.

With respect to electron irradiation, only minor effects on frequencies and damping characteristics were observed. However, these departures from the non-irradiated specimens, shown in Table 4, are so small that they may be due to the limited accuracy of the test equipment. As only one sample of each laminate was available a confirmation of these results by statistical means was not possible so their physical significance is questinable.

Table 4: Change of Natural Frequencies and Damping Decrements due to Electron Irradiation

Laminate No.	Material	Frequency f %	Damping %
168	914 C - TS - 5	--	-6,6
246	HYE - 2034 D	+2,4	-6,7
247	T6T 262 - 12 F 550	+1,0	-3,7
PJ	T3T F 178	-1,9	+4,5

8.5 Relative Spectral Reflection

Both the thermal cycling and the electron irradiation caused brownish discolorations of the specimen surfaces. Therefore, measurements were made of the relative spectral reflection of environmentally tested and of virginal laminates. Fig. 25 shows typical results of these investigations.

All the thermally cycled laminates experienced a decrease of relative spectral reflection. The formation of surface cracks, as observed by electron beam microscopy, can only be a partial explanation for this phenomenon because it also occured in two laminates which were exposed to electron irradiation without experiencing crack formation (Fig. 26). On the other hand, simulated sun irradiation for 150 hours with an intensity

comparable to that of a low earth orbit caused a substantial increase of spectral reflection (Fig. 25), which may be traceable to an increasing interlinking of the molecular chains of the matrix. This is a normal event due to energy transmission to the laminate. During longer exposure times the high energy photons of the ultra violet region of sun's light spectrum damage the molecular chains consequently leading to a blunt laminate surface. Very similar effects must be expected as a result of dense fluxes of high energy electrons.

Furthermore the fatigue stresses caused by thermal cycling might also have affected the molecular structure of the matrix as it was supposed in chapter 8.4. This is strongly supported by indications that the decrease of spectral reflection corresponded continously to the increase of the number of thermal cycles while the formation of cracks which are observable by micrography slowed down as discussed earlier.

8.6 Residual Strength

Tables 5 and 6 present mean values and their standard deviations of the static strength of test specimens obtained after various numbers of thermal cycles. For the determination of the orginal strength of the laminates six specimens were tested, whereas only 3 specimens were available for the residual strength tests after 1170, 2295, and 3480 cycles respectively.

Fig. 27 to 30 show the ratio of residual to initial strength against the number of thermal cycles. After 1170 thermal cycles all materials exhibited a reduction of residual strength regardless of their curing temperatures, consistent with the predictable formation of the microcracks due to discrepant thermal strains. In the high temperature curing materials the reduction ceased after 1170 thermal cycles. The strength of the low temperature curing materials decreased further after 2295 and 3480 cycles. Considering the higher intensity of prestress in the high temperature curing laminates, it is surprising that the reduction of tension and compression strength is only 3% and 10% in laminates 164 and 175. While the materials with lower curing temperatures deteriorated more both at 23°C and 100°C testing temperatures. Notable is the drastic strength reduction of the polyimide-based specimens after only 1170 thermal cycles, requiring additional testing of this material.

A comparison of initial and residual tensile strength of some materials subjected to electron irradiation is given in Fig. 31. Again the degradation of the polyimide-based laminate was the most severe, although no kind of defect was detectable by the applied techniques including measurements of spectral reflection. On the other hand, the epoxy-based laminates especially the 914C show small degrations of their tensile strength. Paradoxically, the T6T 262-12-F550 laminate 247 which had been phased out of the thermal cycling test because of poor fabrication shows an increase of tensile strength after electron irradiation.

8.7 Stress/Strain Relations

Fig. 32 to 39 show sress-strain plots of all materials tested after different numbers of thermal cycles and at two different temperatures. With increasing number of thermal cycles the stiffness of the specimens decreased in most cases especially during testing at 100°C indicating a higher toughness especially for the high curing temperature materials due to the small strength reduction. in contrast to the formation of cracks which took place at the beginning of thermal cycling and than ceased the reduction of stiffness progressed continually with increasing number of thermal cycles. Changes of the molecular structure as already supposed former more likely may be a satisfactory explanation for this phenomenonthan matrix cracking.

9. Conclusion

All epoxy-based materials exhibited only small effects due to thermal cycling and electron irradiation. The very small strength reduction especially of the laminates with high curing temperatures does not restrict the qualification for space applications of these materials at all. Only the continous decrease of the stiffness with increasing number of thermal cycles may be critical because of increasing deformations as far as the application for large structures with very long service times is considered. But this shall only be valid for such highly matrix controlled laminates as the tested $[2(+45° -45°)]_S$ laminates were.

The only polyimide based laminate in the test showing severe damage after thermal cycling should be further investigated to verify the observations made until now.

10. References

[1.]	J.L. Camahost E.H. Rennhack W.C. Coons	Effects of Thermal Cycling Environment on Graphite/epoxy Composites, Environmental Effects on Advandced Composite Materials, 1976, ASTM STP 602
[2.]	V.F. Mazzio	Effects of Thermal Cycling on the Properties of Graphite/Epoxy Composites, Composite Materials: Testing and Design, ASTM STP 617 Properties of Graphite/Epoxy
[3.]	D.H. Woolstencroft A.R. Curtis	Interface Stresses in Unidirectional Carbon Fibre Composites, PLASTICS AND RUBBER Inst., Interfaces in Composite Materials, Univ. of Liverpool, England, Apr.1,2 1981, 29p.

Table 1: Thermal Expansion Coefficients of Different CFRP-Materials

m/m · K

Measurement Direction	914 C - TS - 5 Laminate 164	HY-E 1548 A 1 B 169	HY - E 2034 D 175	914 C - MS - 5 177	T6T 262 - 12 F 550 247
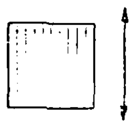	$-0{,}66 \cdot 10^{-6}$ $s = \pm 0{,}19 \cdot 10^{-6}$	$-0{,}98 \cdot 10^{-6}$ $s = \pm 0{,}14 \cdot 10^{-6}$	$-1{,}75 \cdot 10^{-6}$ $s = \pm 0{,}08 \cdot 10^{-6}$	$-1{,}23 \cdot 10^{-6}$ $s = \pm 0{,}2 \cdot 10^{-6}$	$-0{,}53 \cdot 10^{-6}$ $s = \pm 0{,}11 \cdot 10^{-6}$
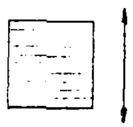	$+22{,}4 \cdot 10^{-6}$ ---	$+28{,}6 \cdot 10^{-6}$ $s = \pm 0{,}24 \cdot 10^{-6}$	$+23{,}2 \cdot 10^{-6}$ $s = \pm 0{,}64 \cdot 10^{-6}$	$+22{,}3 \cdot 10^{-6}$ ---	$+24{,}4 \cdot 10^{-6}$ $s = \pm 0{,}55 \cdot 10^{-6}$
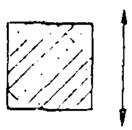	$+1{,}43 \cdot 10^{-6}$ $s = \pm 0{,}32 \cdot 10^{-6}$		$-1{,}20 \cdot 10^{-6}$ $s = \pm 0{,}17 \cdot 10^{-6}$	≈ 0 ---	$+2{,}16 \cdot 10^{-6}$ $s = \pm 0{,}14 \cdot 10^{-6}$

Table 2 List of Materials for Thermal Cycling and Electron Irradiation Tests

Laminate No.	Material Designation	Type of Fiber	Type of Resin	Curing Temperature
164 and 168	914 C - TS - 5	high tenacity Toray T 300	Ciba 914	190^{o} C
169	HY - E 1548 A 1 B	high modulus Celion GY - 70	Fiberite 948 A1	120^{o} C
170A	LY 556 / HY 917 / XB 2692 / T 300	high tenacity Toray T 300 - 6000	Unmodified Epoxy	140^{o} C
175 and 246	HY - E 2034 D	high modulus Thornel Pitch	Fiberite 934	180^{o} C
PI	T3T F 178	high tenacity Union Carbide T 300 - 3000	Hexcel F 178	210^{o} C
247	T6T 262 - 12 F 550	high tenacity Union Carbide T 300 - 6000	Hexcel F 550	120^{o} C

Stacking Sequence of the Laminates $(2[\pm 45^{o}])_s$

Laminate Thickness 1mm

Table 3 Change of Natural Frequencies and Logarithmic Decrements of Damping of Different CFRP Materials with Stacking Sequence $[\pm 45^{0}{}_{2}]_{s}$ due to Thermal Cycling

Laminate No. Material	0 Cycles		1170 Cycles		2295 Cycles		3480 Cycles	
	f 1/s	-	f 1/s	-	f 1/s	-	f 1/s	-
164 914C-TS-5	580	0,02283	566	0,02309	554	0,0259	560,5	0,0283
169 HY-E 1548 A1B	696,7	0,01084	677	0,01189	675	0,0125	675	0,0143
170A LY556/HY917/XB 2629/ T300-6000	585	0,0127	563	0,0136	568,5	0,0160	559,5	0,0154
175 HY-E 2034 D	634	0,02415	622	0,0229	617,5	0,0229	617	0,0234
PI T3T F 178	637	0,01383	565	0,01253	564	0,0127		

Table 5 Mean Values and Standard Deviations of Ultimate Strengths after Various Thermal Cycles; Stacking Sequence $[\pm 45^{o}_{2}]_{s}$

Laminate No. Material	Tensile Strength N/mm² Test Temperatur 23°C 0 Cycles	1170 Cycles	2295 Cycles	3480 Cycles	Compressive Strength N/mm² Test Temperatur 23°C 0 Cycles	1170 Cycles	2295 Cycles	3480 Cycles
164 914C-TS-5	156,6 6,6	148,8 4,7	153,5 3,7	151,9 2,5	163,0 9,6	159,1 1,5	163,5 6,9	159,7 4,6
169 HY-E 1548 A1B	122,9 8,1	112,7 2,2	106,1 0,4	94,4 3,3	122,2 7,5	106,2 3,5	108,4 4,0	100,5 0,9
170 A LY556/917/XB2692	204,2 11,8	183,1 6,5	190,3 8,7	172,8 16,6	188,9 11,8	167,1 4,7	169,2 11,4	178,7 1,8
175 HY-E 2034 D	69,9 3,9	61,3 1,9	63,9 0,7	64,3 0,8	68,5 6,8	58,3 0,9	66,1 2,0	61,6 9,3
PI T3T F 178	145,7 1,3	84,3 0,4			165,6 3,1	85,0 5,7		

Table 6 Mean Values and Standard Deviations of Ultimate Strengths at Various Thermal Cycles; Stacking Sequence $[\pm 45^{o}{}_{2}]_{s}$

Laminate No. Material	Tensile Strength N/mm^2 Test Temperature 100°C 0 Cycles	1170 Cycles	2295 Cycles	3480 Cycles	Compressive Strength N/mm^2 Test Temperature 100°C 0 Cycles	1170 Cycles	2295 Cycles	3480 Cycles
164 914C-TS-5	143,1 4,9	128,6 1,3	134,6 2,0	130,6 1,5	143,5 3,7	134,4 7,6	135,7 4,9	140,7 5,5
169 HY-E 1548 AlB	115,5 2,0	94,6 1,7	83,1 1,0	84,3 2,2	97,9 2,0	91,5 2,0	80,9 1,3	80,7 1,3
170 A LY556/917/XB2692 T300	119,5 5,2	112,5 12,0	97,8 3,5	87,8 7,9	115,3 5,7	105,4 6,1	97,8 0,7	111,1 2,3
175 HY-E 2034 D	58,5 1,9	51,9 4,1	54,5 2,6	51,2 1,1	57,0 4,6	53,2 2,0	53,3 3,5	57,1 7,3
PI T3T F 178	121,5 0,3	69,0 4,2			139,1 3,9	73,9 3,8		

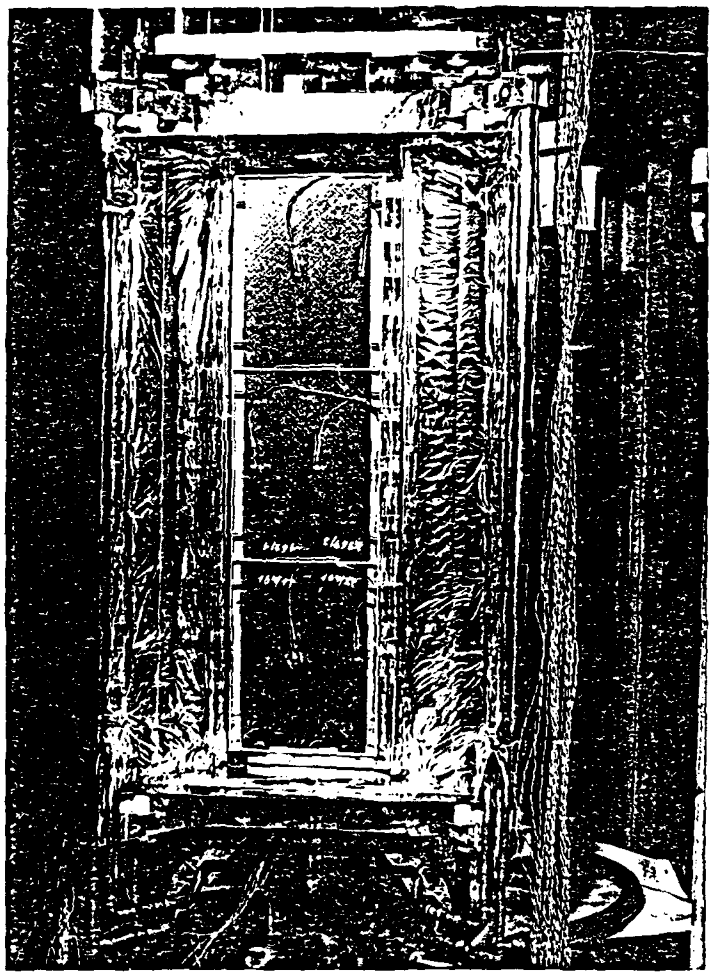

Fig. 1   Sample Support with Mounted Samples

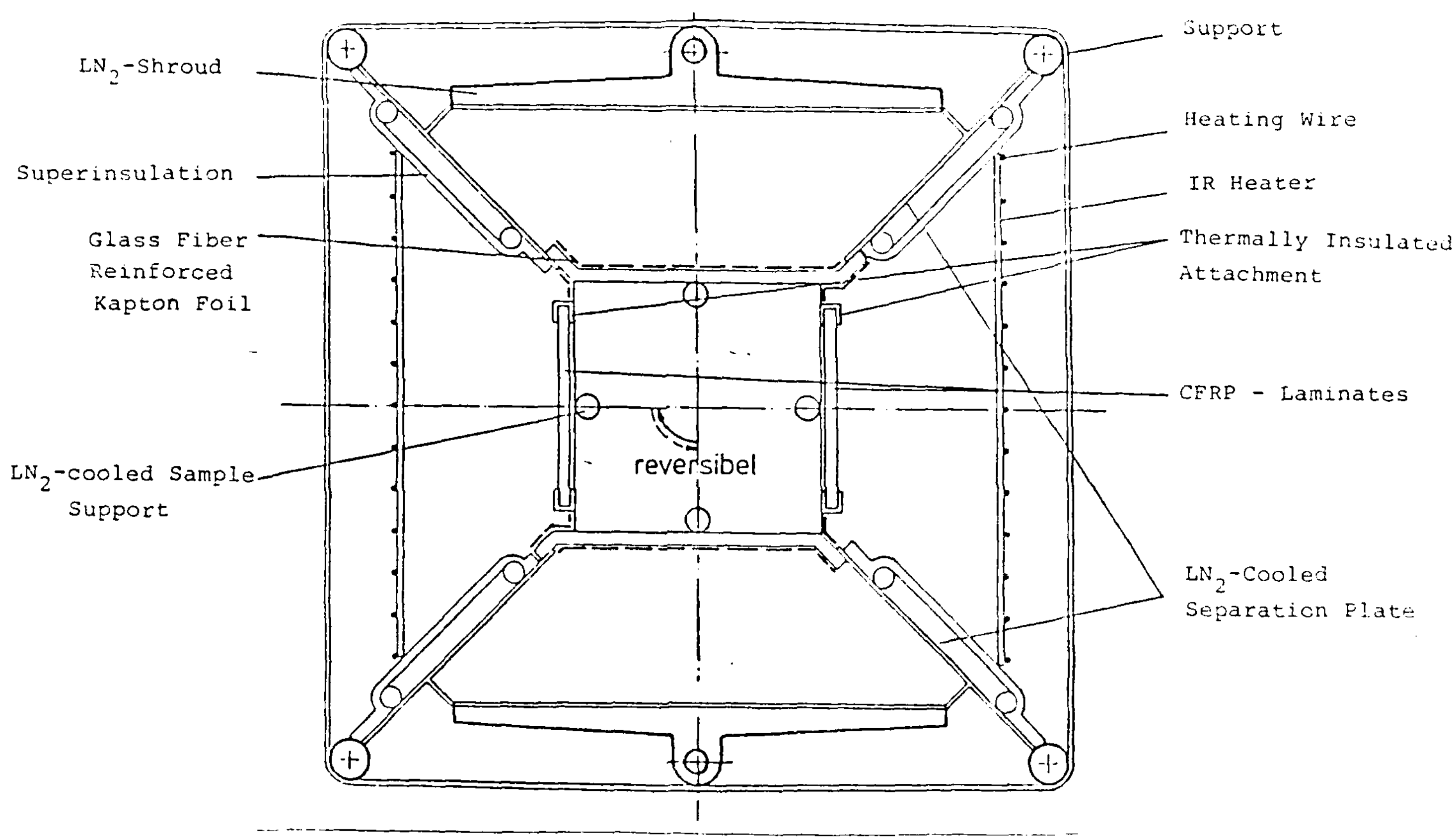

Fig. 2 Cross Section of Test Facility - Hot Phase Mode

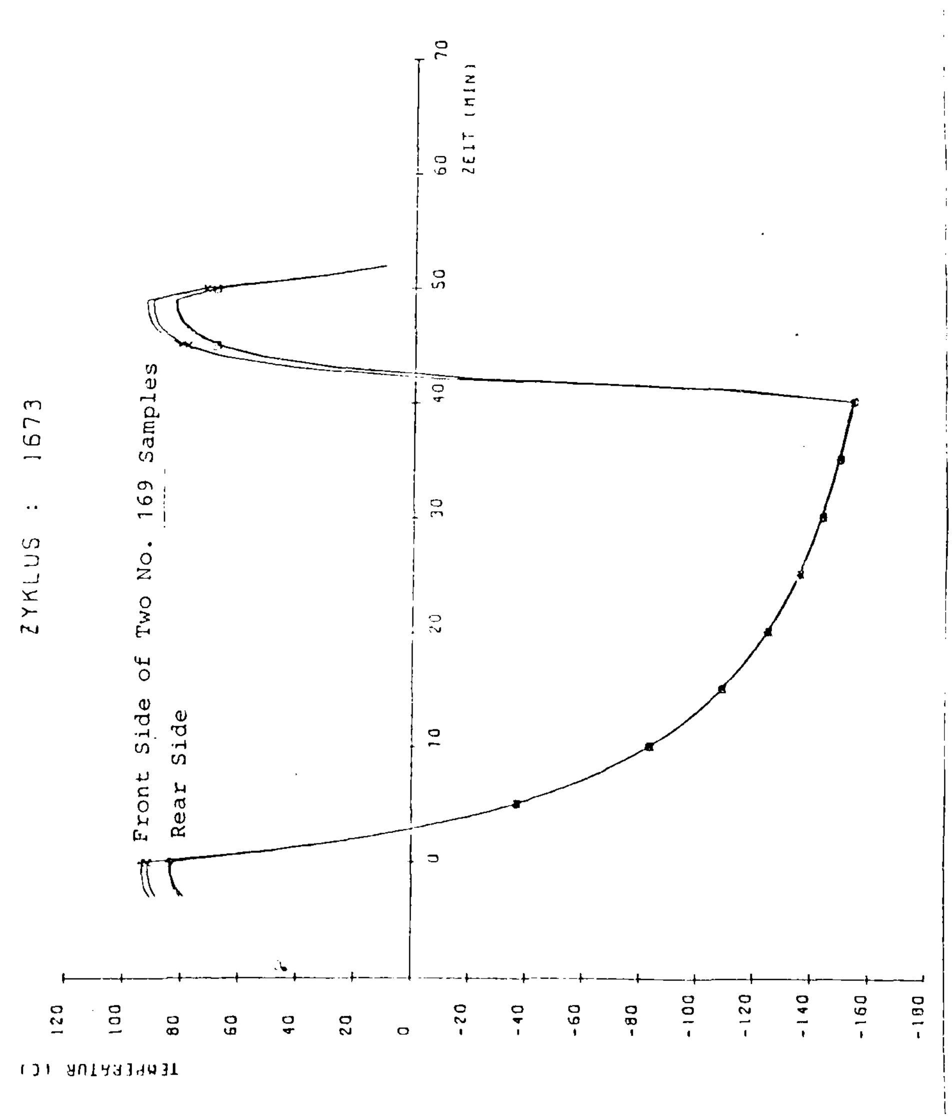

Fig. 3 Temperature Versus Time Curve
of a Typical Thermal Cycle

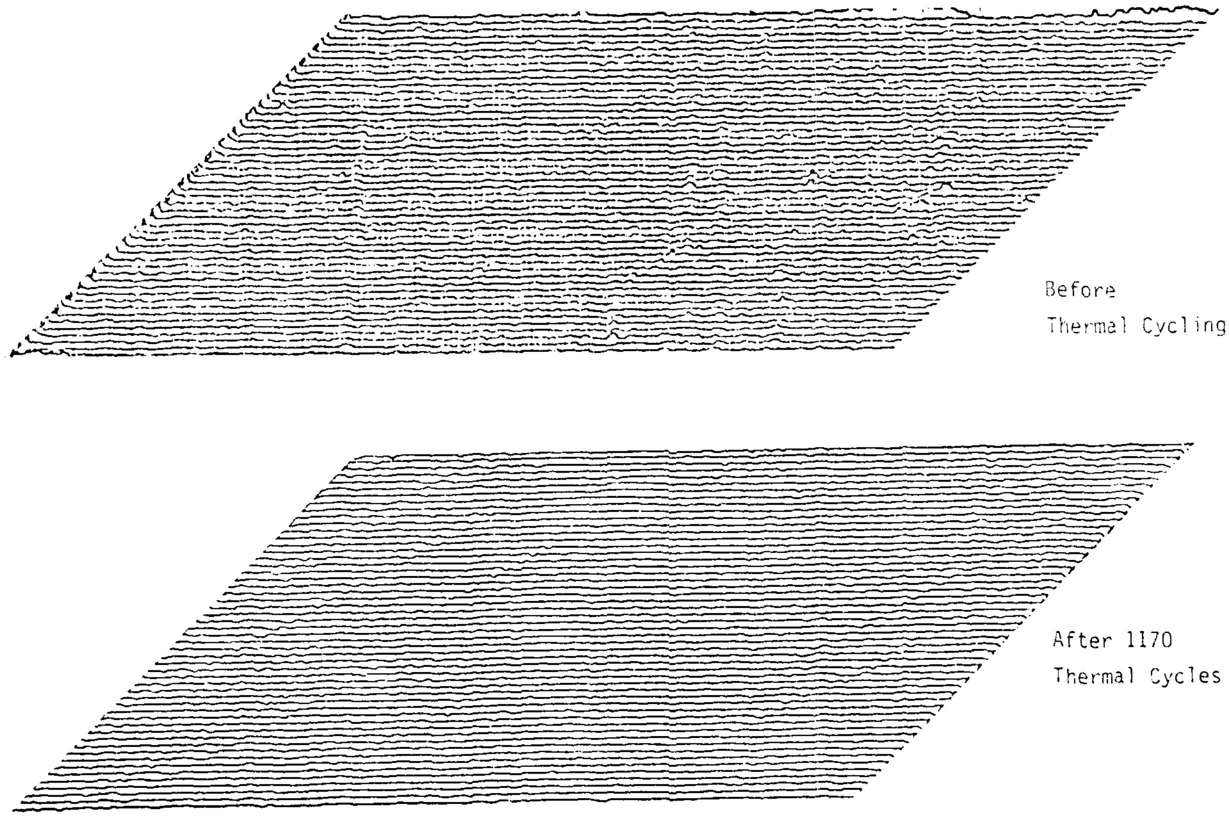

Fig. 4 Amplitude Scans of 914 C-TS-5 Laminate (164) Before and After Thermal Cycling

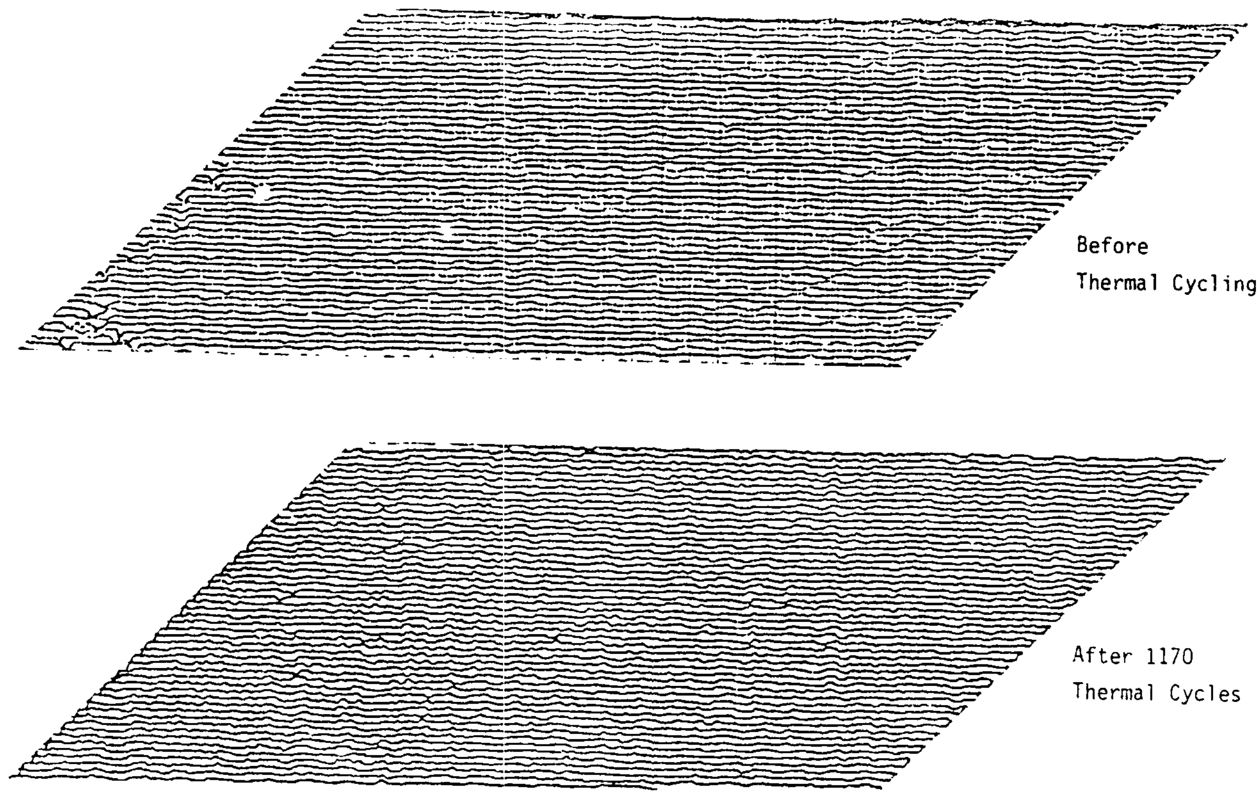

Fig. 5 Amplitude Scans of HY-E 1548 A1B Laminate (169) Before and After Thermal Cycling

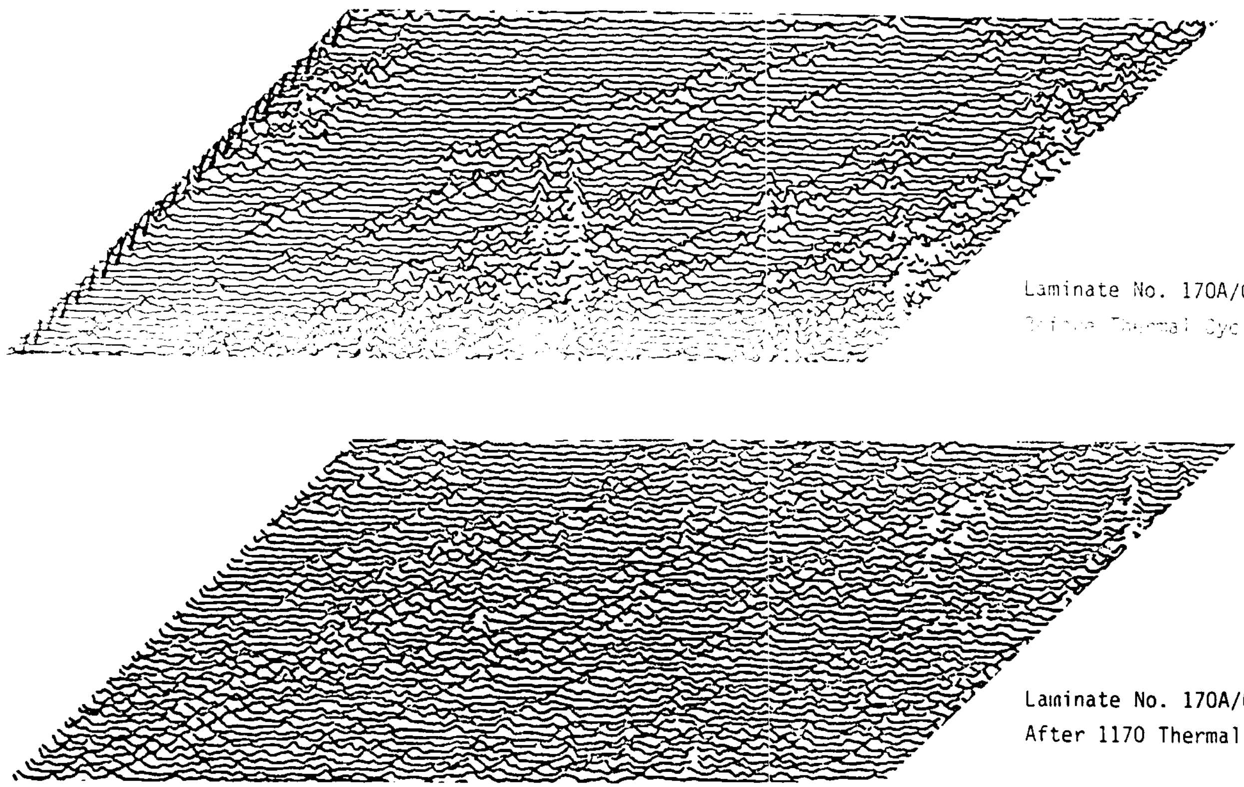

Laminate No. 170A/0
Before Thermal Cycling

Laminate No. 170A/0
After 1170 Thermal Cycles

Fig. 6 Amplitude Scans of LY 556/T 300 Laminate (170A) Before and After Thermal Cycling

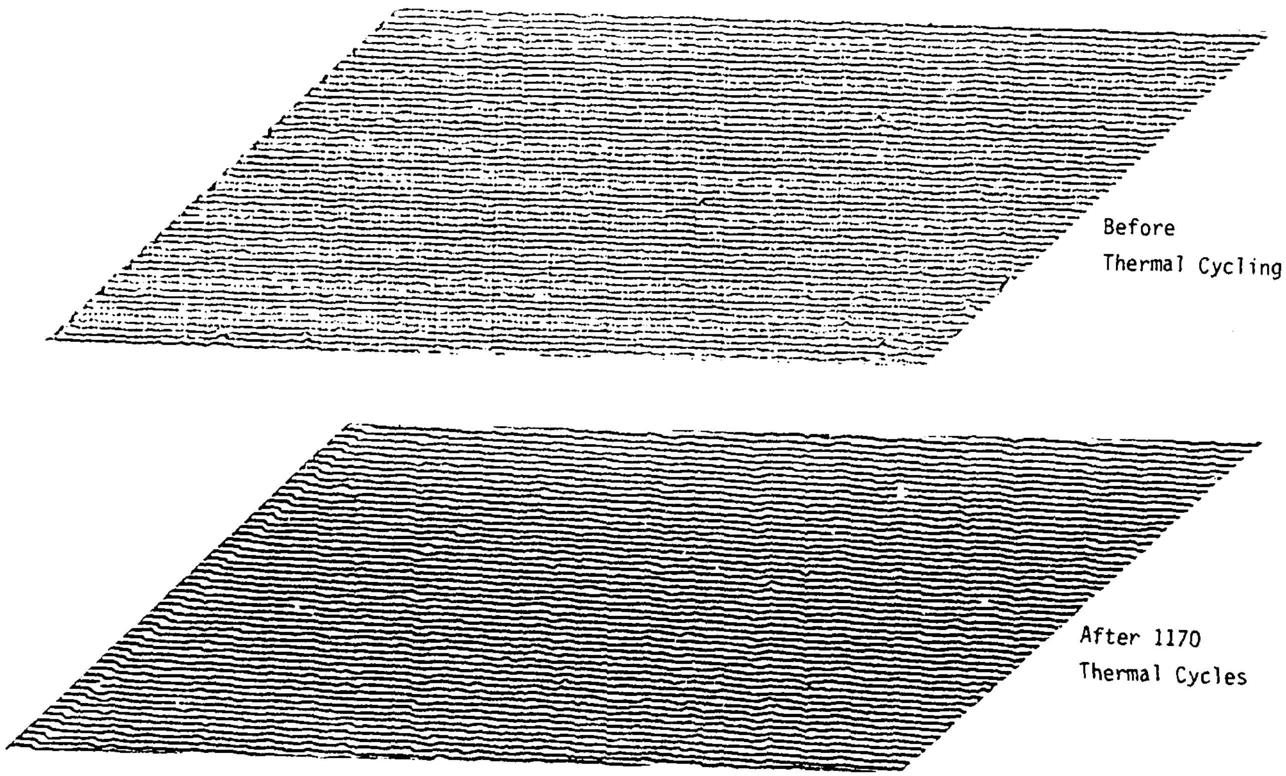

Fig. 7 Amplitude Scans of HY-E 2034 D Laminate (175)
Before and After Thermal Cycling

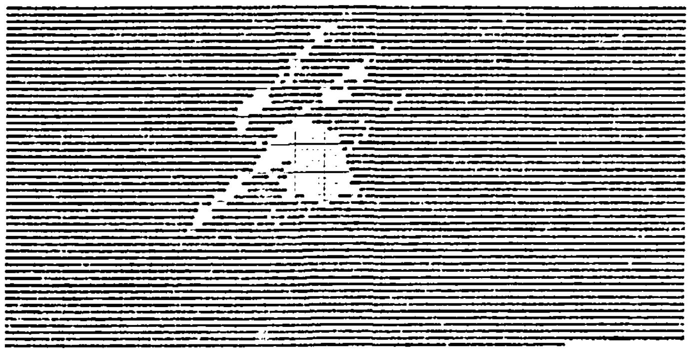

C - Scan Before Thermal Cycling

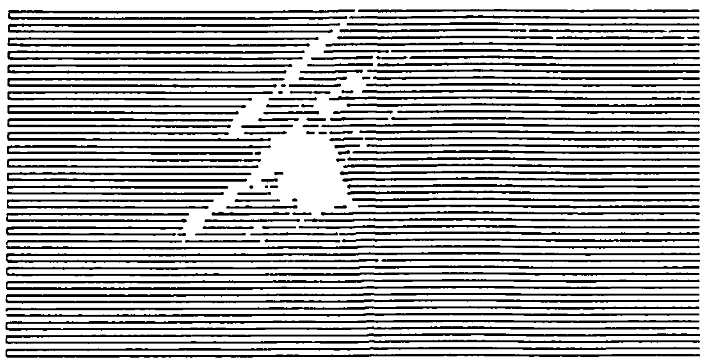

C - Scan

X-ray Photograph

After 3480 Cycles

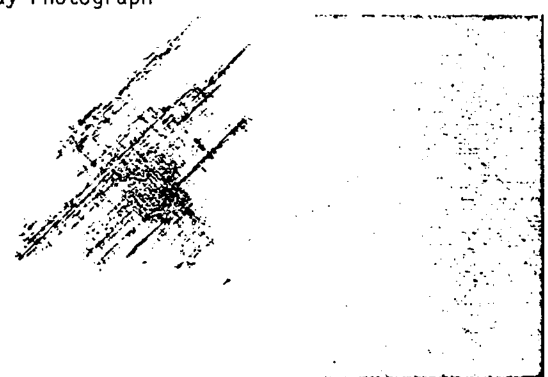

Figure 8. Effect of Thermal Cycling on Artificial Delaminations in 914C - TS - 5 Laminates

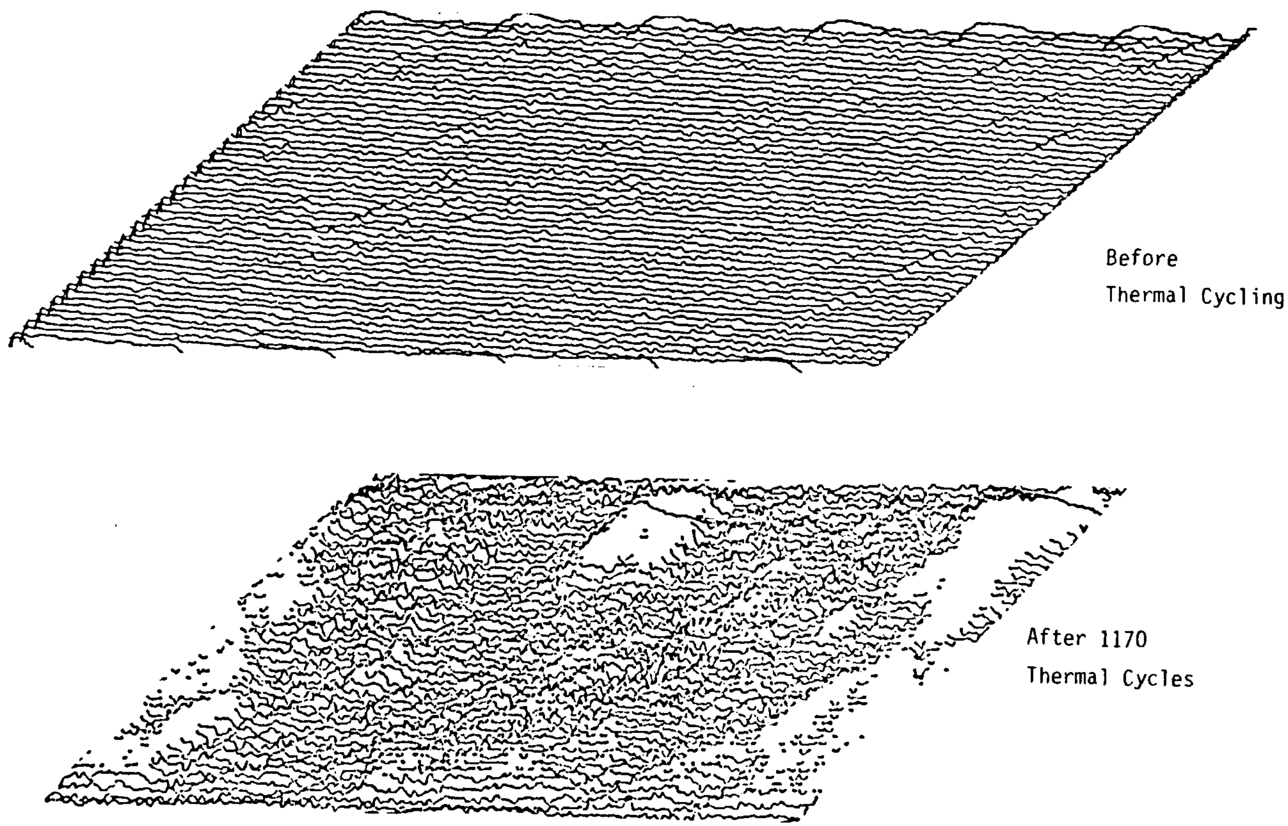

Fig. 9 Amplitude Scans of T3T F 178 Laminate (PI) Before and After Thermal Cycling

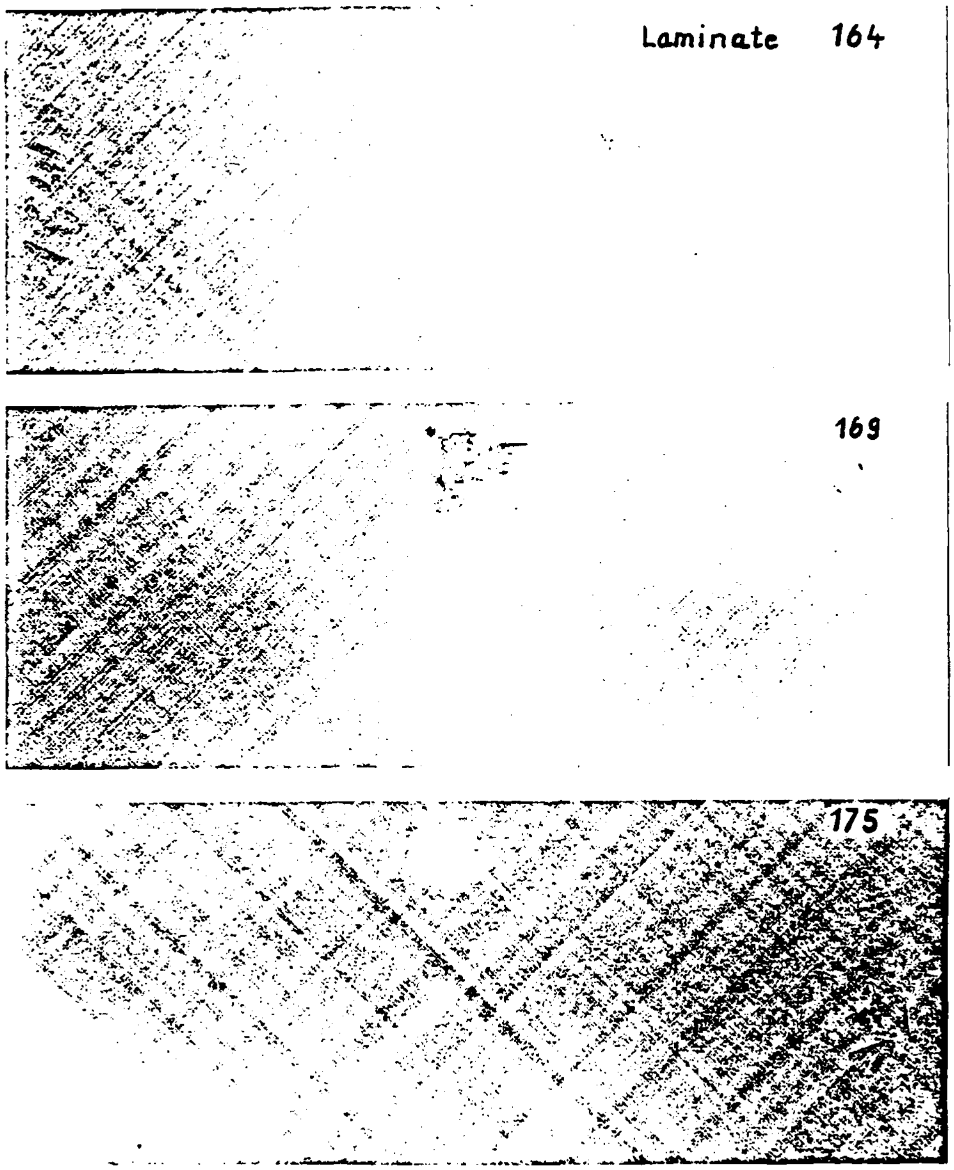

Fig. 10 X-ray Photographs of Three Different Materials After 3480 Cycles

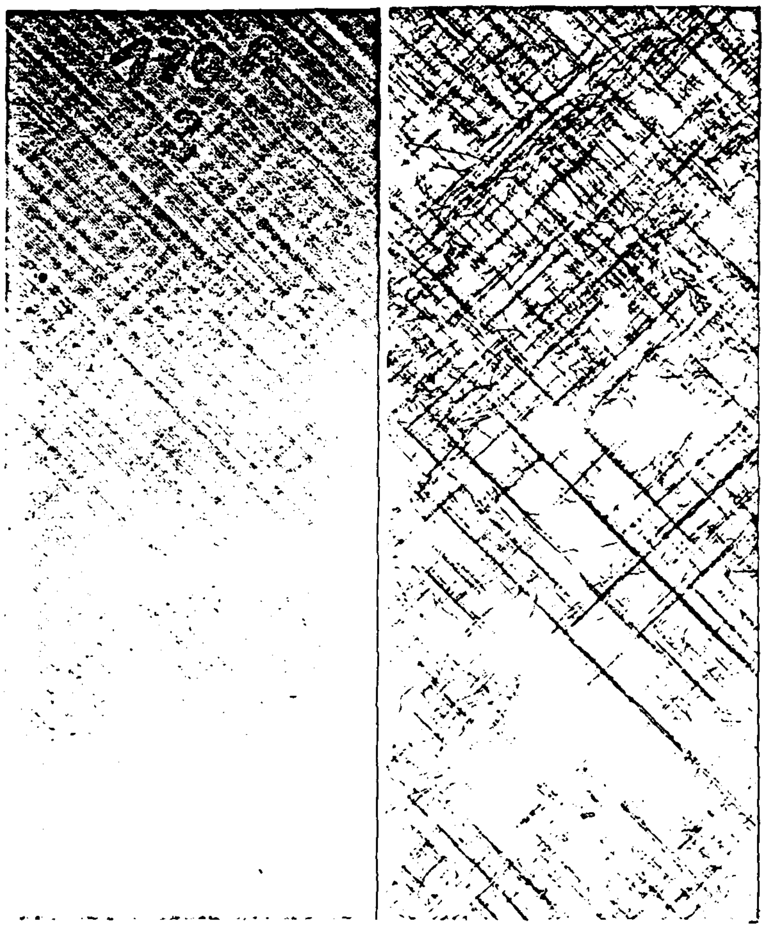

Before Thermal
Cycling
Without TBE

After 2295
Thermal Cycles
With TBE

Fig. 11 X-ray Photographs of LY 556/T300 Before and After Thermal Cycling

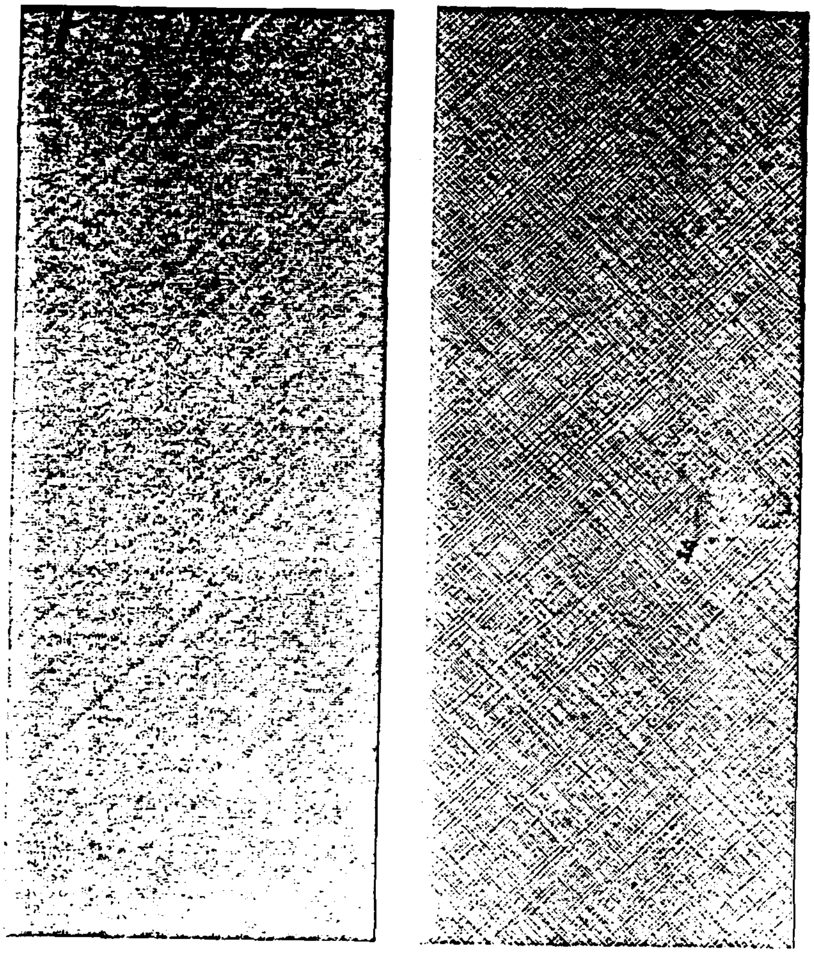

Before Thermal
Cycling

After 3480
Thermal Cycles

Fig. 12 X-ray Photographs of T3T F 178 Laminate Before and After 3480 Thermal Cycles

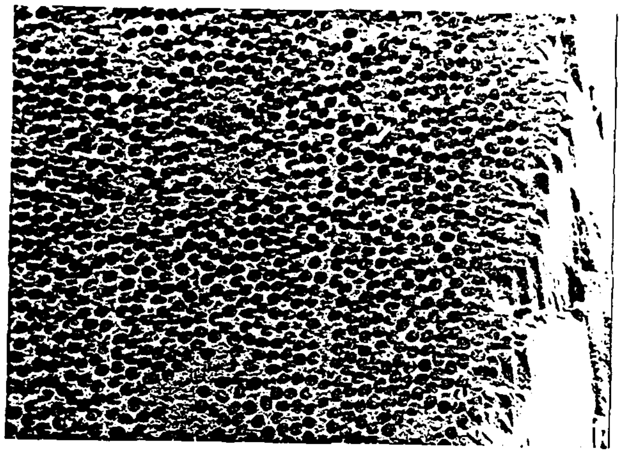

Before Thermal Cycling (400x)

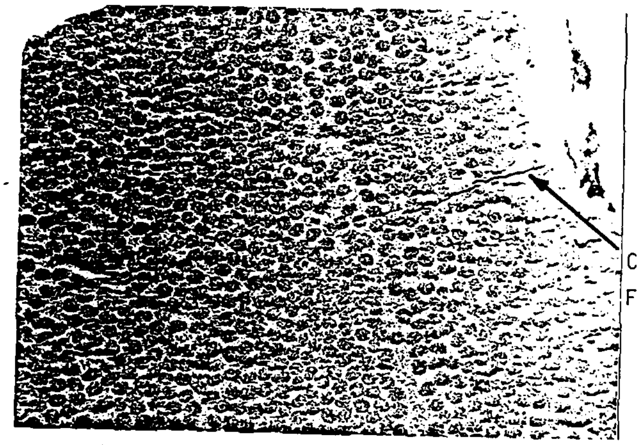

After 1170 Thermal Cycles (400x)

Fig. 13 Photomicrographs of the Cross Section of a 914C-TS-5 Sample Before and After Thermal Cycling

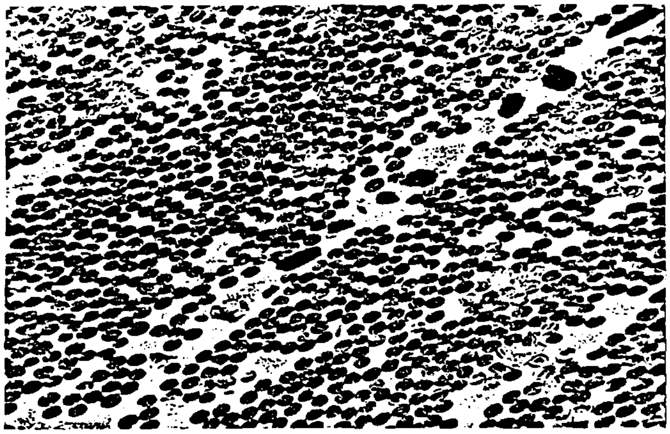

Before Thermal Cycling (400x)

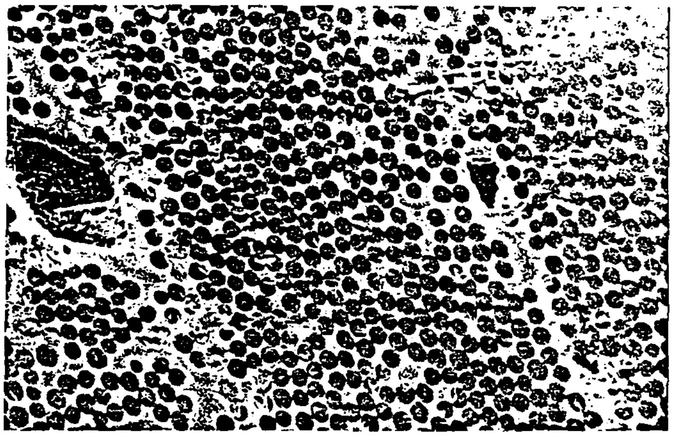

After 1170 Thermal Cycles (400x)

Fig. 14 Photomicrographs of the Cross Section of a HY-E 1548 AlB-Sample Before and After Thermal Cycling

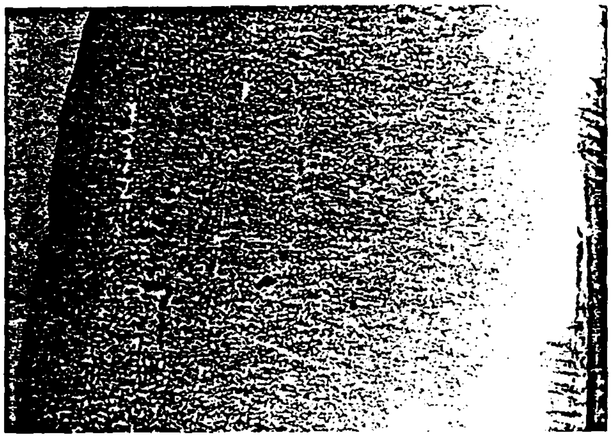

Before Thermal Cycling (100x)

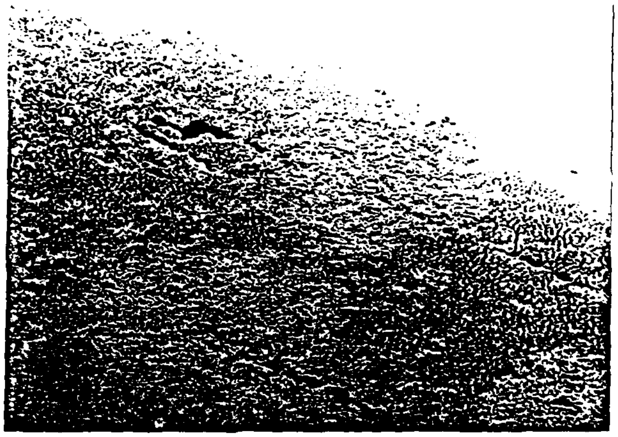

After 1170 Thermal Cycles (100x)

Fig. 15 Photomicrographs of the Cross Section of a LY 556/T300 Sample Before and After Thermal Cycling

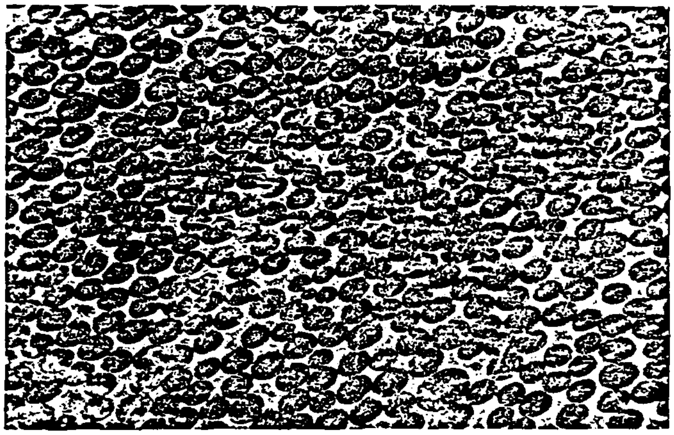

Before Thermal Cycling (400x)

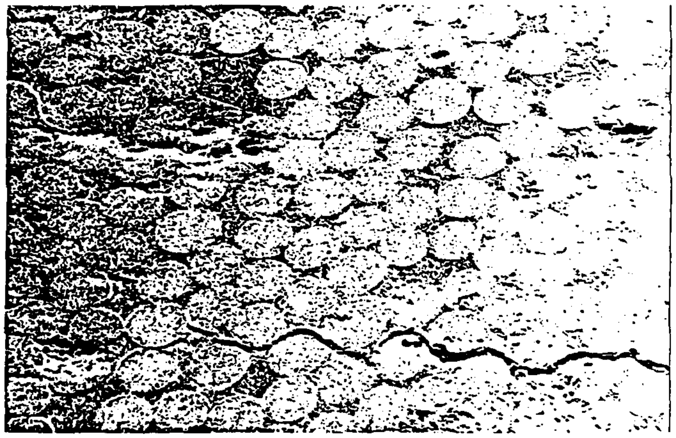

After 1170 Thermal Cycles (700x)

Fig. 16 Photomicrographs of the Cross Section of a HY-E 2034 D Sample Before and After Thermal Cycling

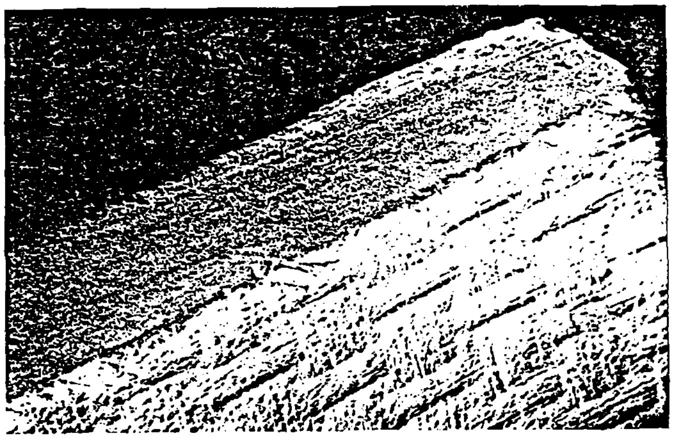

Surface and Cross Section (30x)

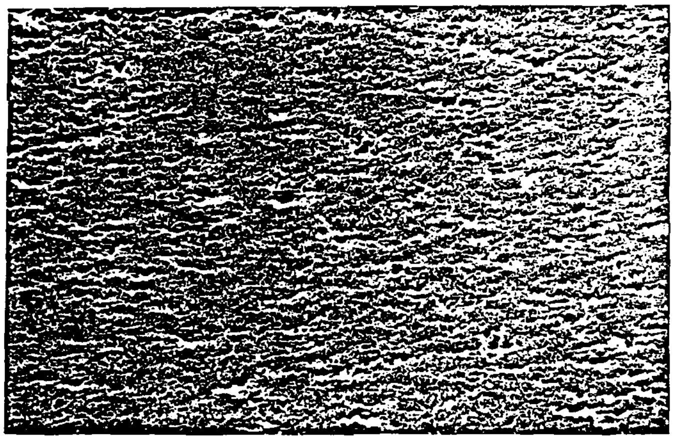

Cross Section (400x)

Fig. 17 Sample of T3T F 178 Before Thermal Cycling

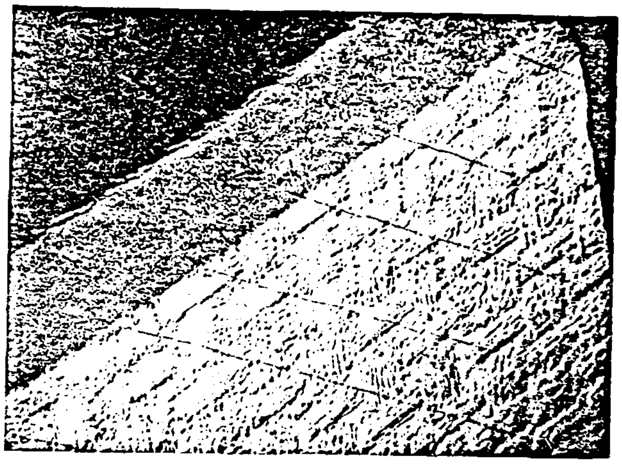

Surface and Cross Section (30x)

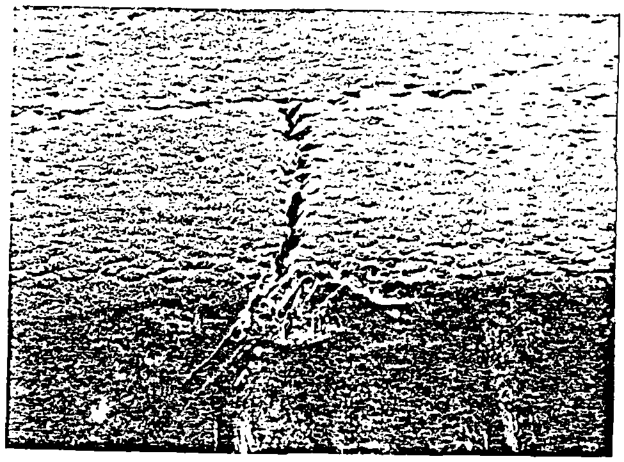

Cross Section (400x)

Fig. 18 Sample of T3T F 178 After 1170 Thermal Cycles

Prior to Cycling 186x

After 3480 Thermal Cycles 186x

Fig. 19 Typical Fracture Areas of 914C - Specimens Before and After Thermal Cycling

Prior to Thermal Cycling 655x

After 3480 Thermal Cycles 655x

Fig. 20 Fracture Areas of 914C - Specimens Before and After Thermal Cycling

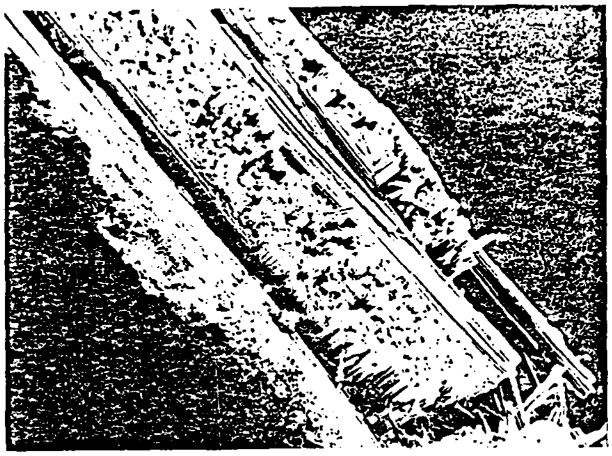

Prior to Thermal Cycling 50x

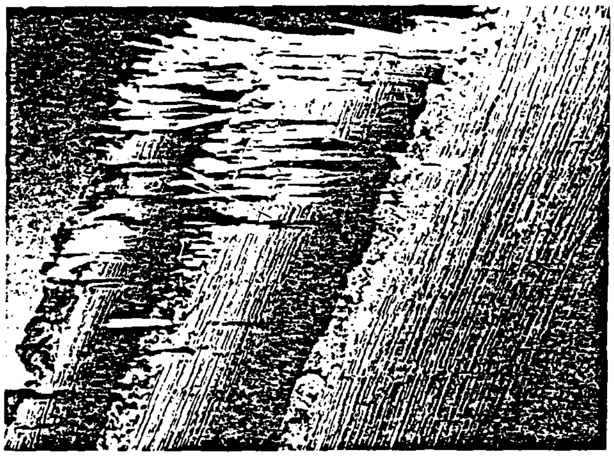

After 1170 Thermal Cycles 50x

Fig. 21 Typical Fracture Areas of HYE-2034 D - Specimens Before and After Thermal Cycling

As Fabricated 700x

After 1170 Thermal Cycles 700x

Figure 22 Fracture Areas of HYE 2034 D - Specimens Before and After Thermal Cycling

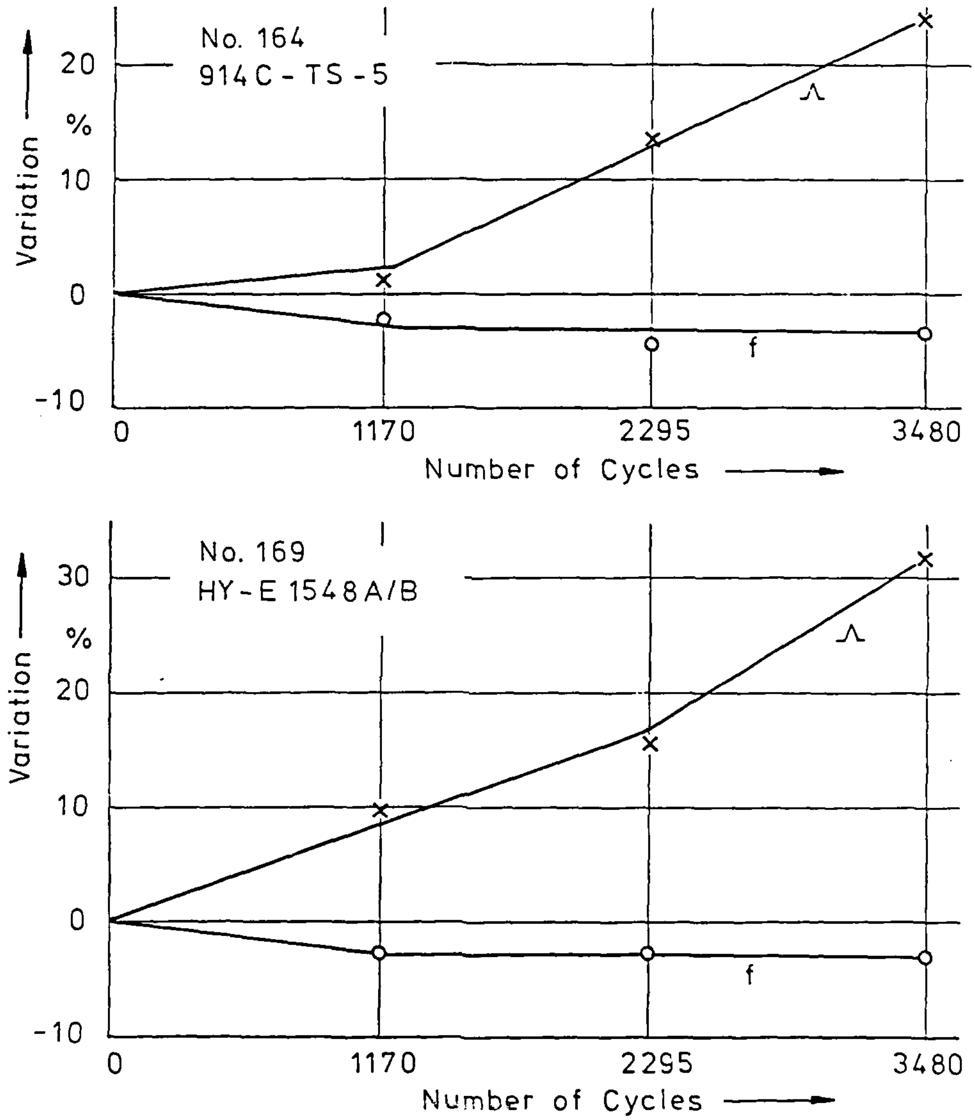

Fig. 23 Change of Natural Frequencies and Damping Characteristics in Percentages of Original Values as a Result of Thermal Cycling

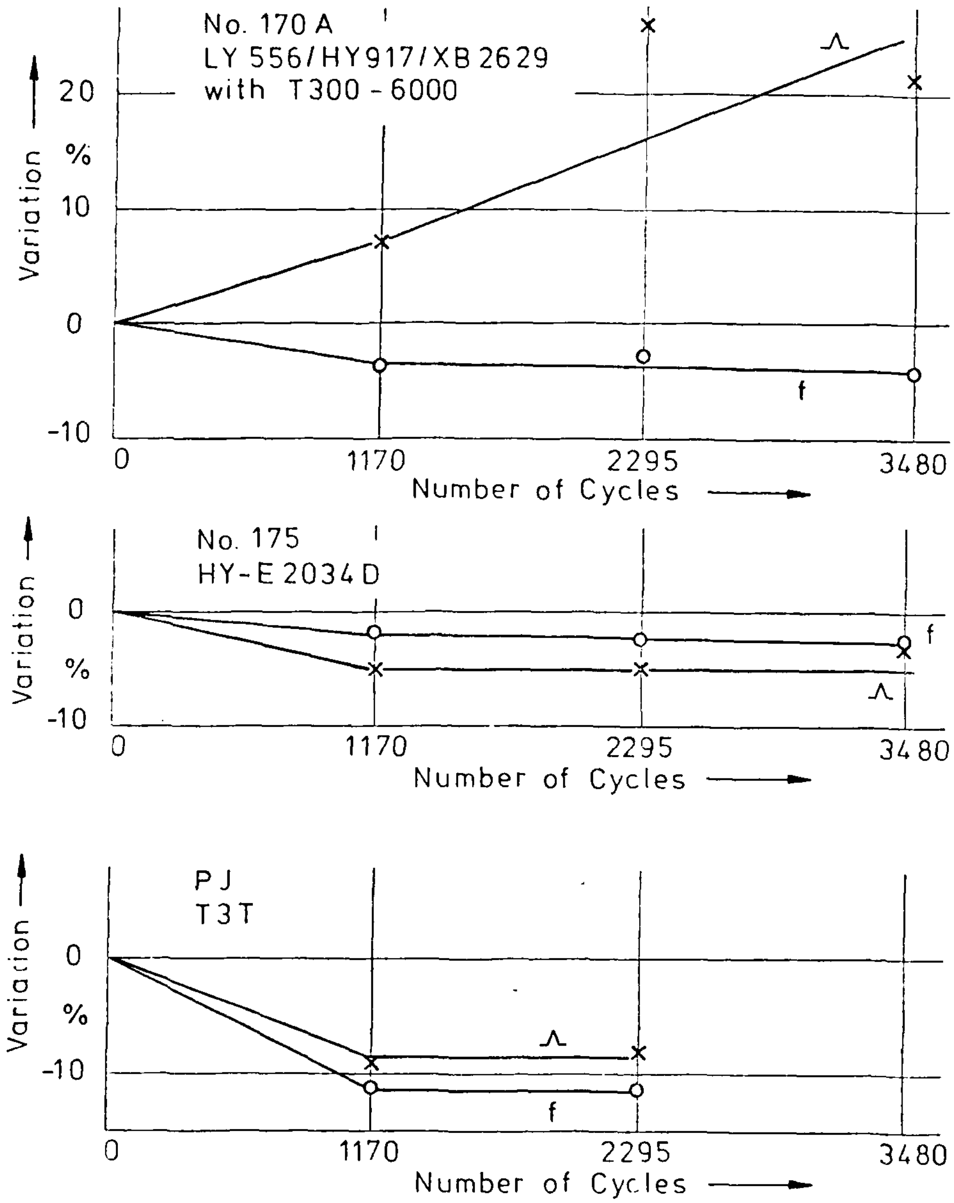

Fig. 24 Change of Natural Frequencies and Damping Characteristics in Percentages of the Orginal Values as a Result of Thermal Cycling

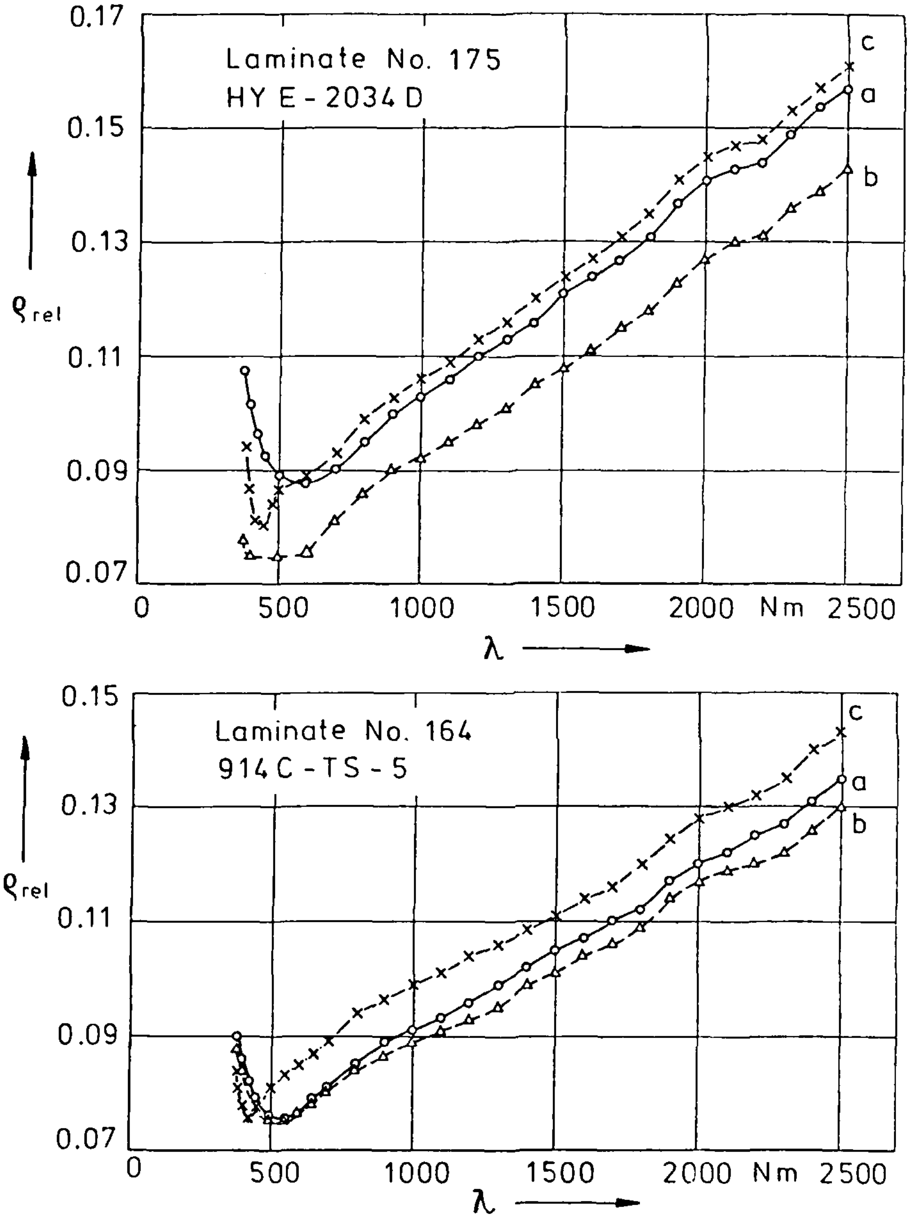

Fig. 25 Relative Spectral Degree of Reflection of CFRP-Laminate Surfaces

a: Prior to Environmental Testing

b: After Thermal Cycling

c: After Exposure to UV-Light

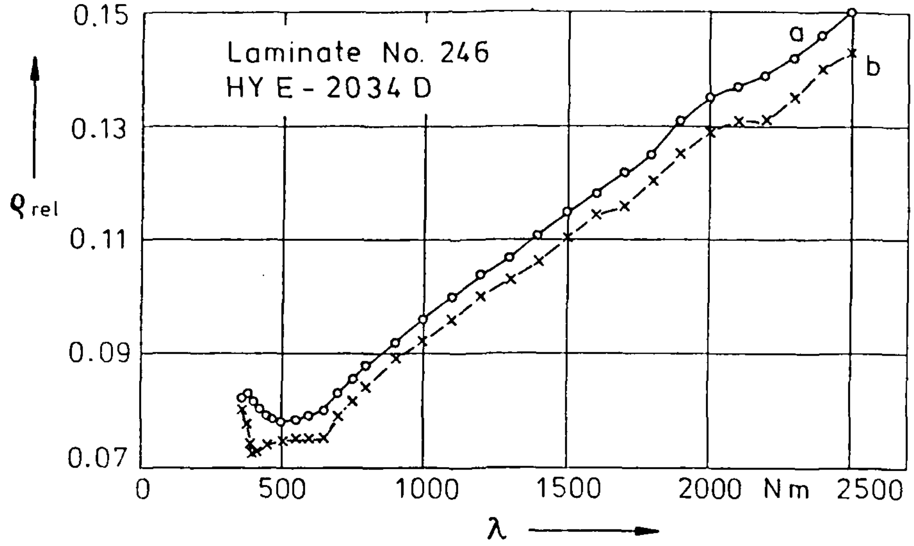

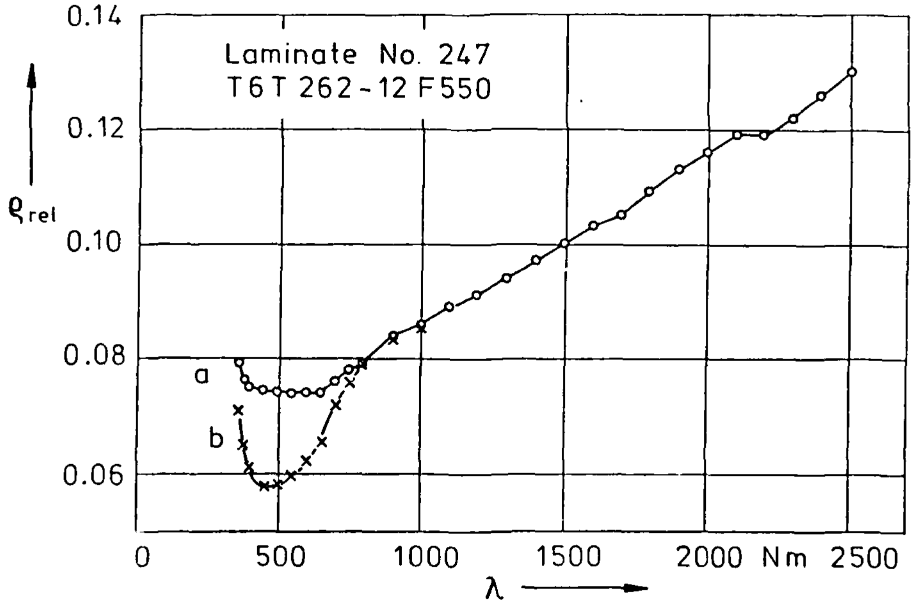

Fig. 26 Relative Spectral Degree of Reflection of CFRP-Laminate Surfaces
a: Prior to Environmental Testing
b: After Electron Beam Irradiation

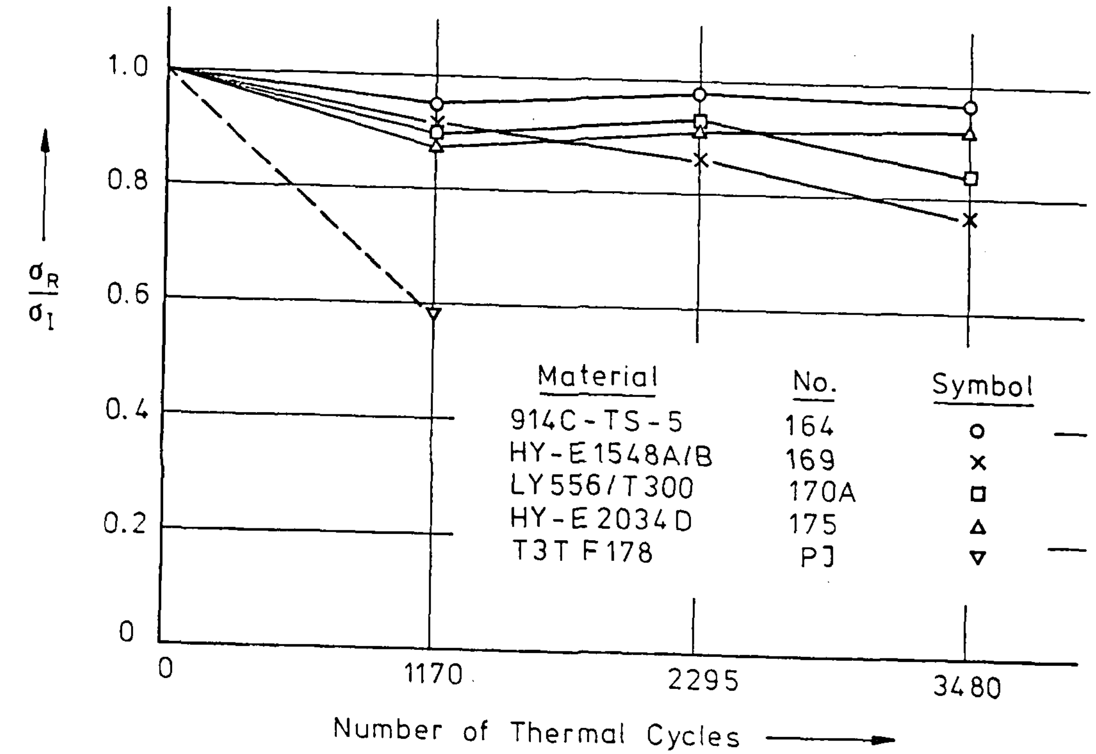

Fig. 27 Degradation of Tensile Strength due to Thermal Cycling
Test Temperature 23°C

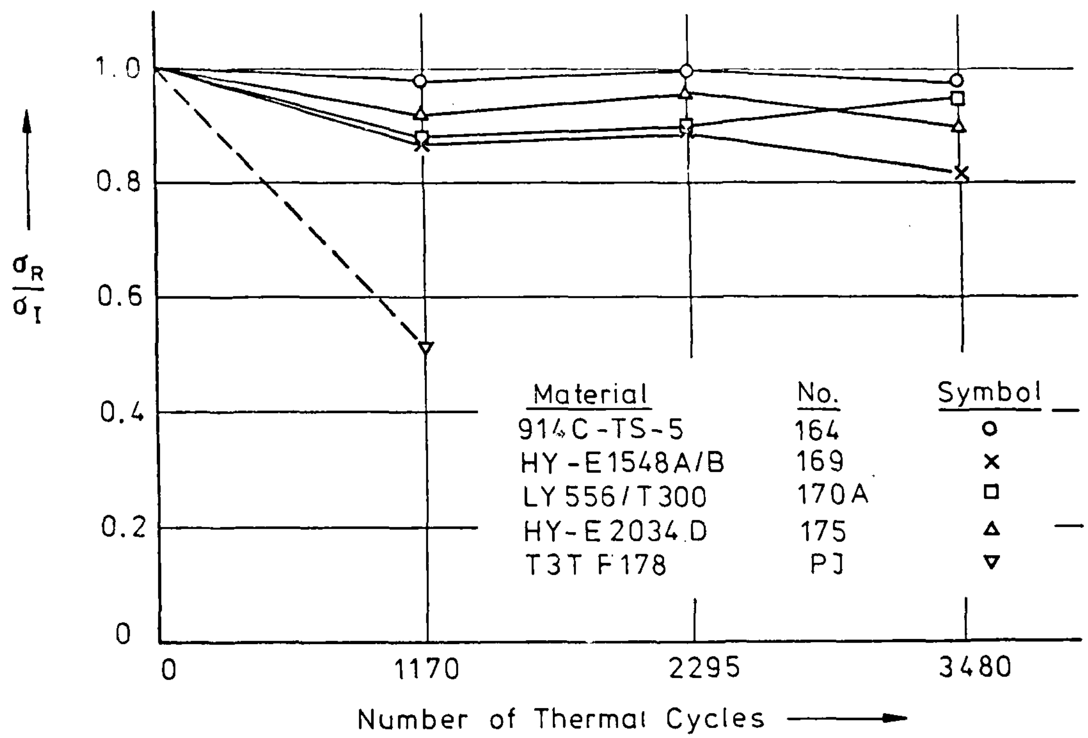

Fig. 28 Degradation of Compression Strength due to Thermal Cycling
Test Temperature 23°C

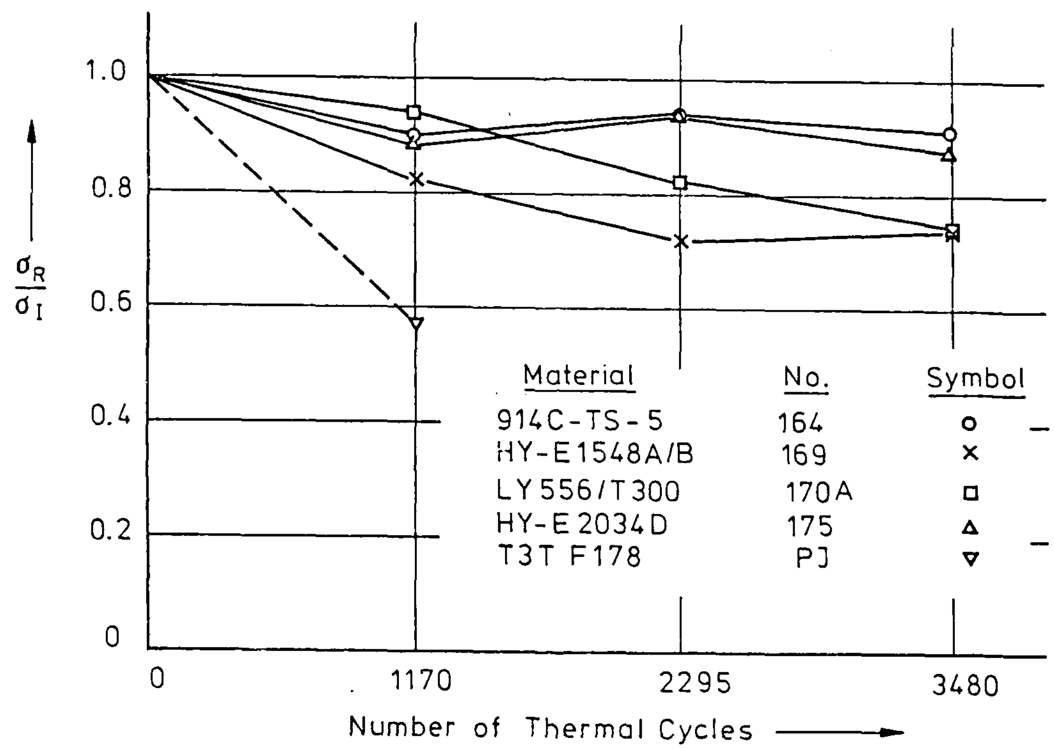

Fig. 29 Degradation of Tensile Strength due to Thermal Cycling
Test Temperature 100°C

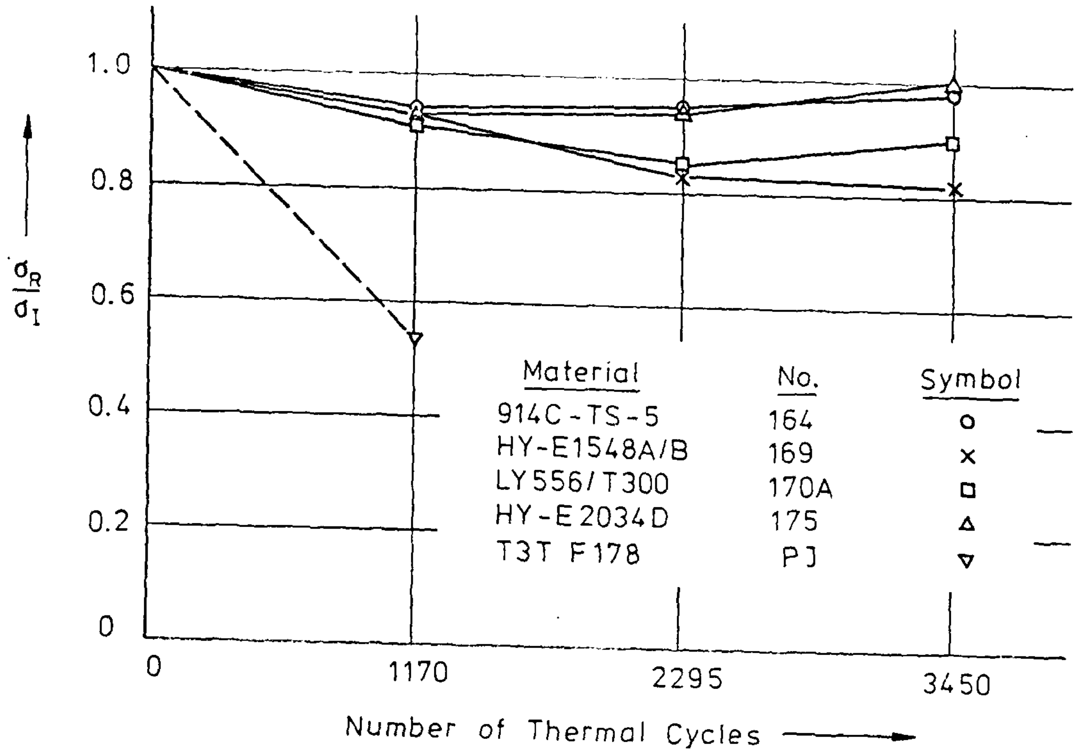

Fig. 30 Degradation of Compression Strength due to Thermal Cycling
Test Temperature 100°C

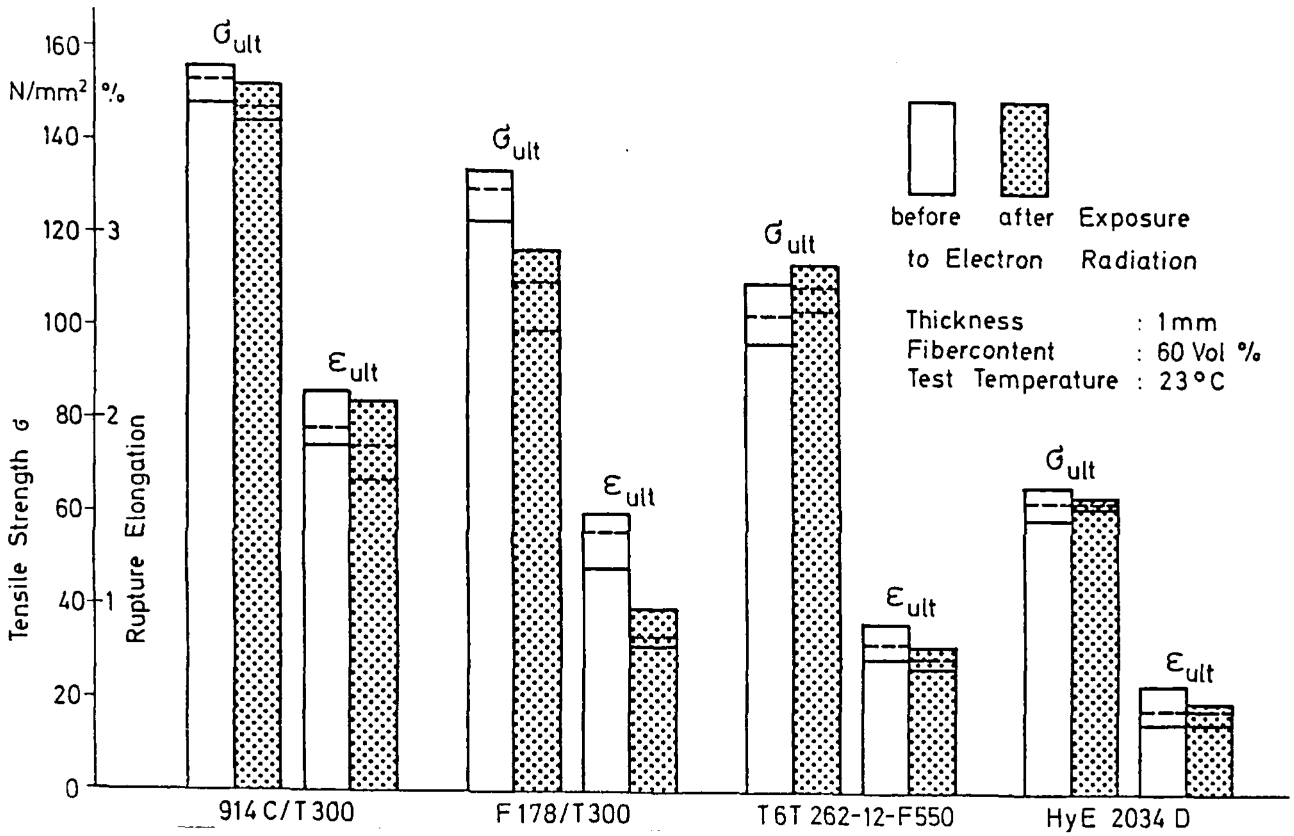

Fig. 31 Tensile Strength of ± 45° CRP-Laminates exposed to Electron Radiation

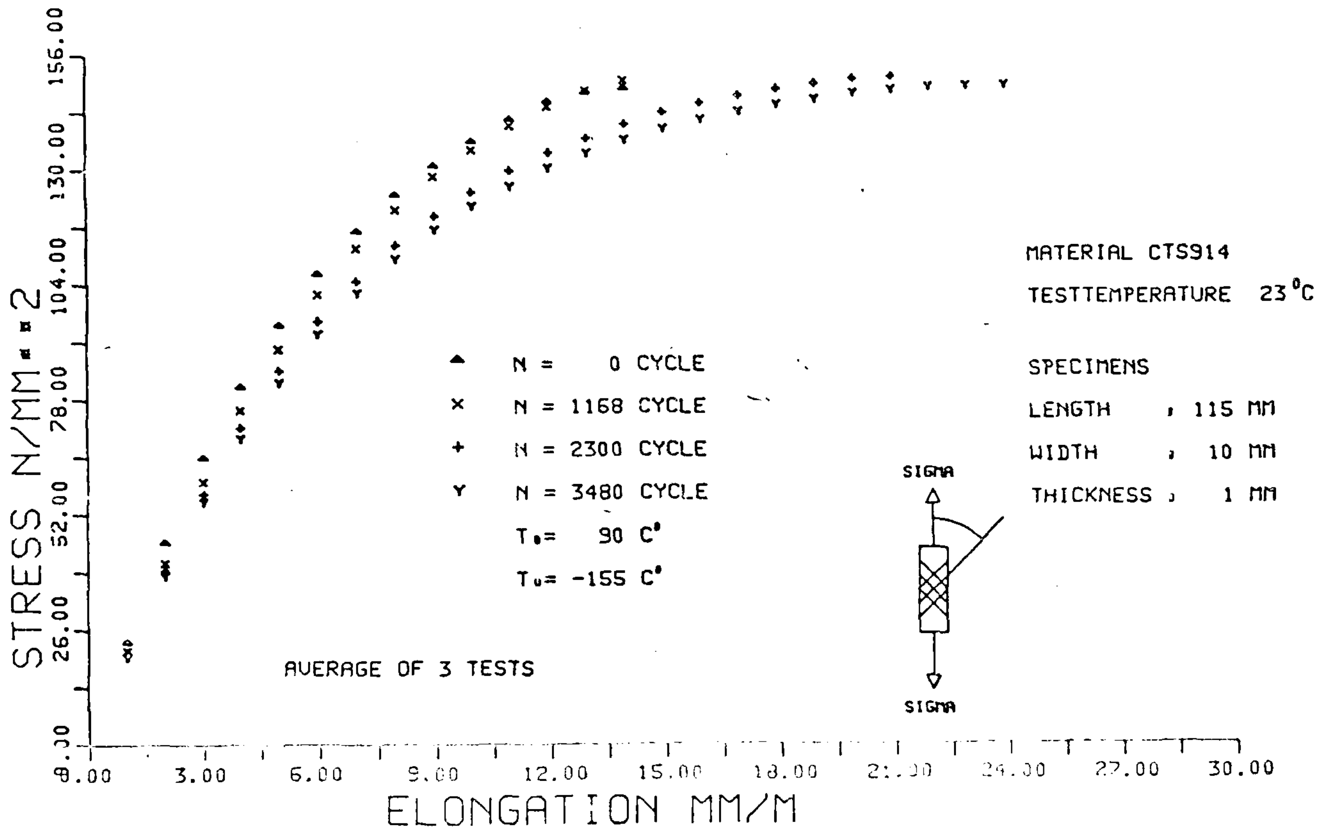

Fig. 32 Stress-Strain Slope From Tension on ± 45° CRP After Thermal Cycling

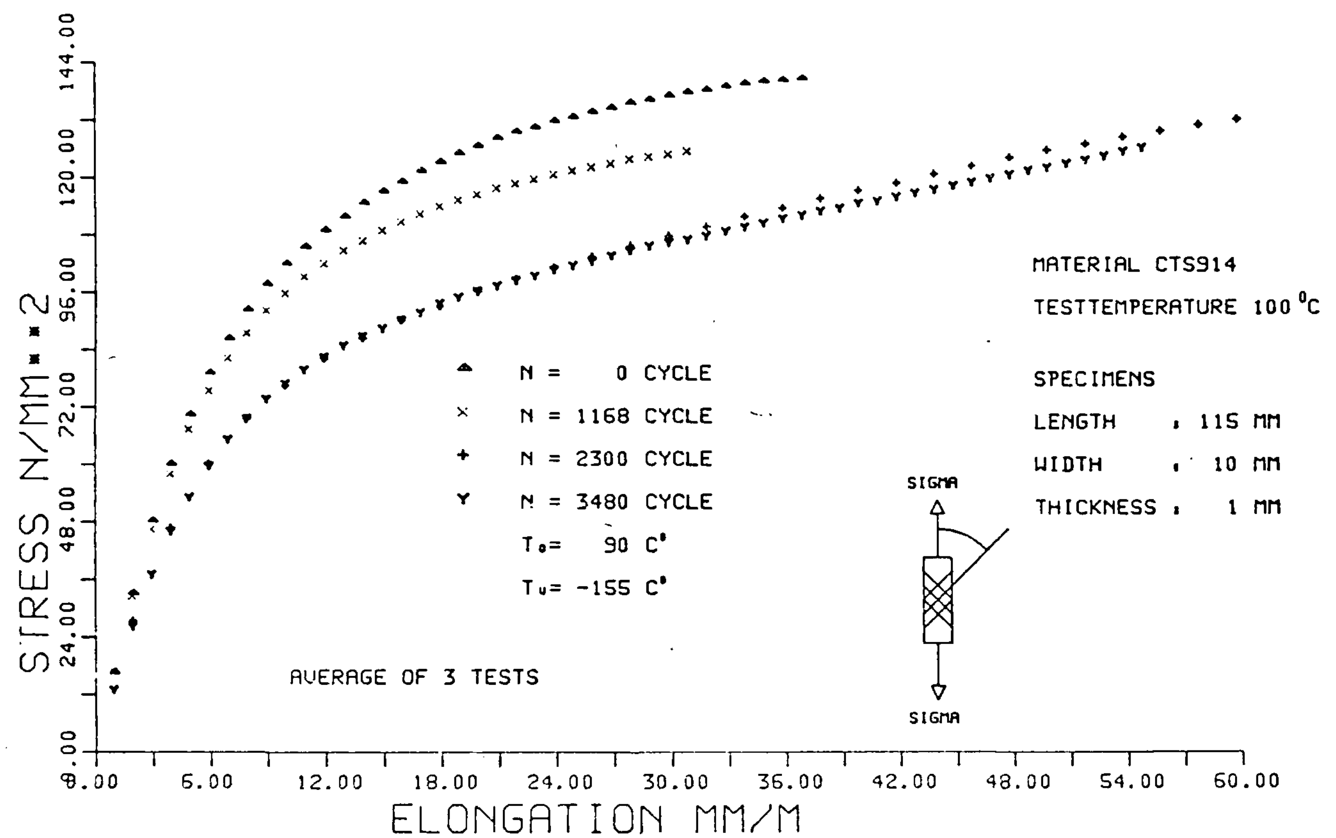

Fig. 33 Stress-Strain Slope From Tension on ± 45° CRP After Thermal Cycling

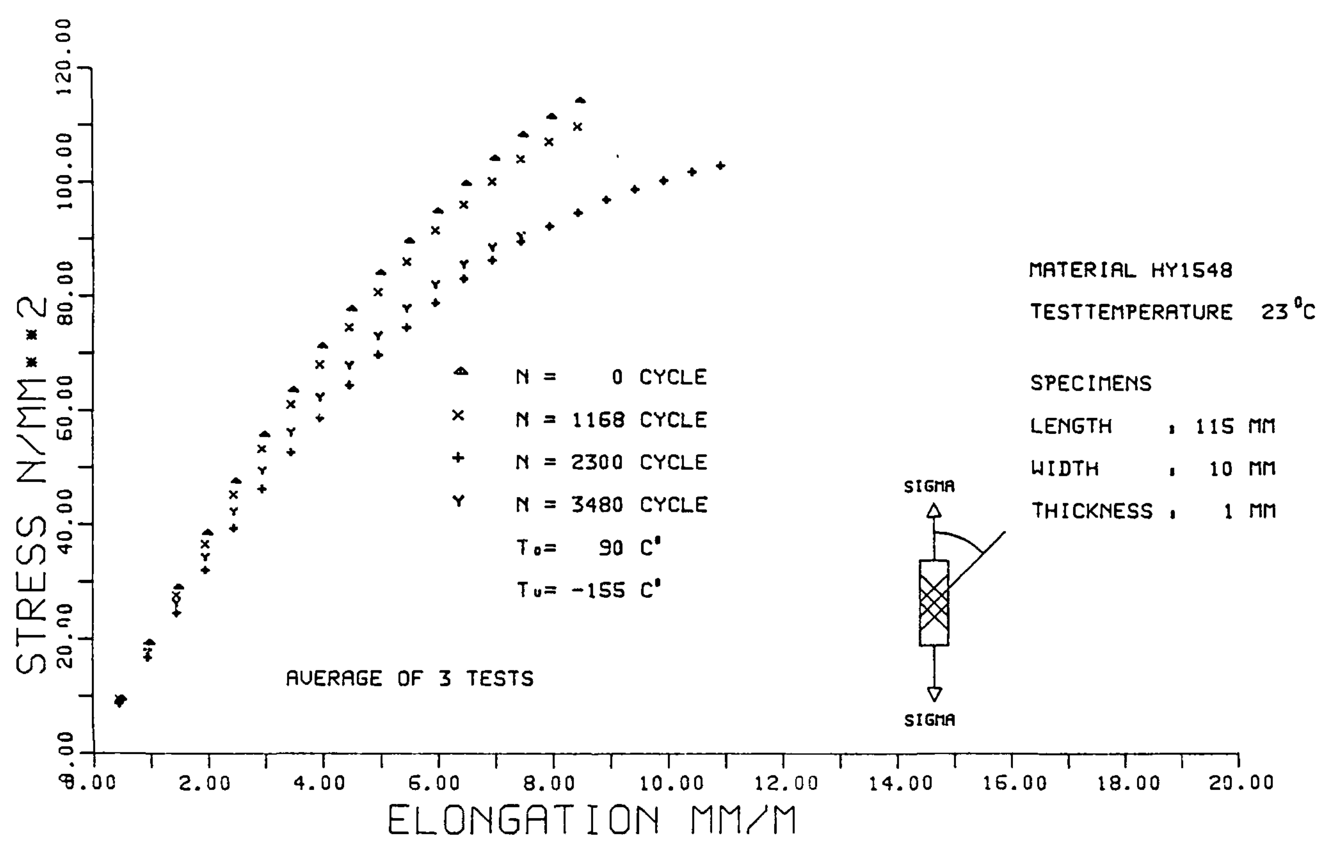

Fig. 34 Stress-Strain Slope From Tension on $\pm$ 45° CRP After Thermal Cycling

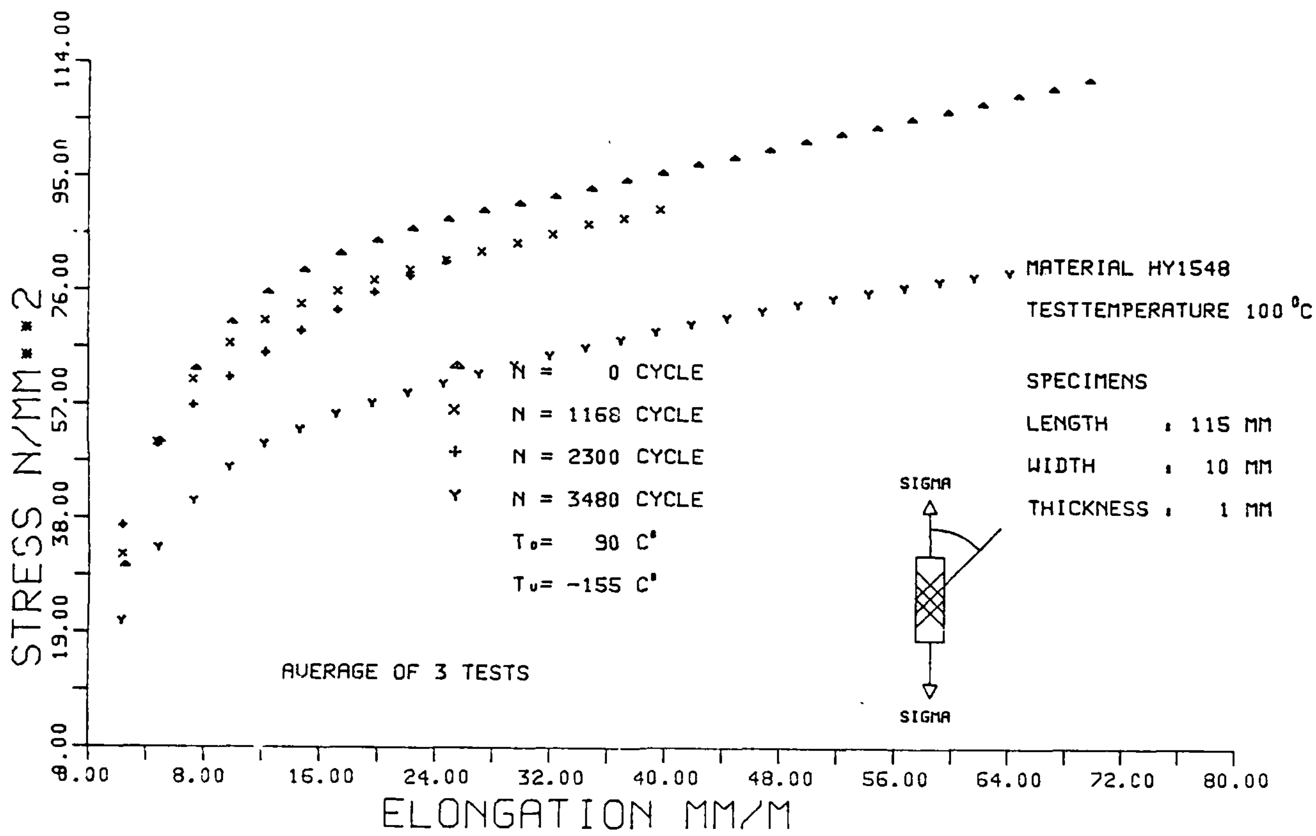

Fig. 35 Stress-Strain Slope From Tension on $\pm$ 45^{0} CRP After Thermal Cycling

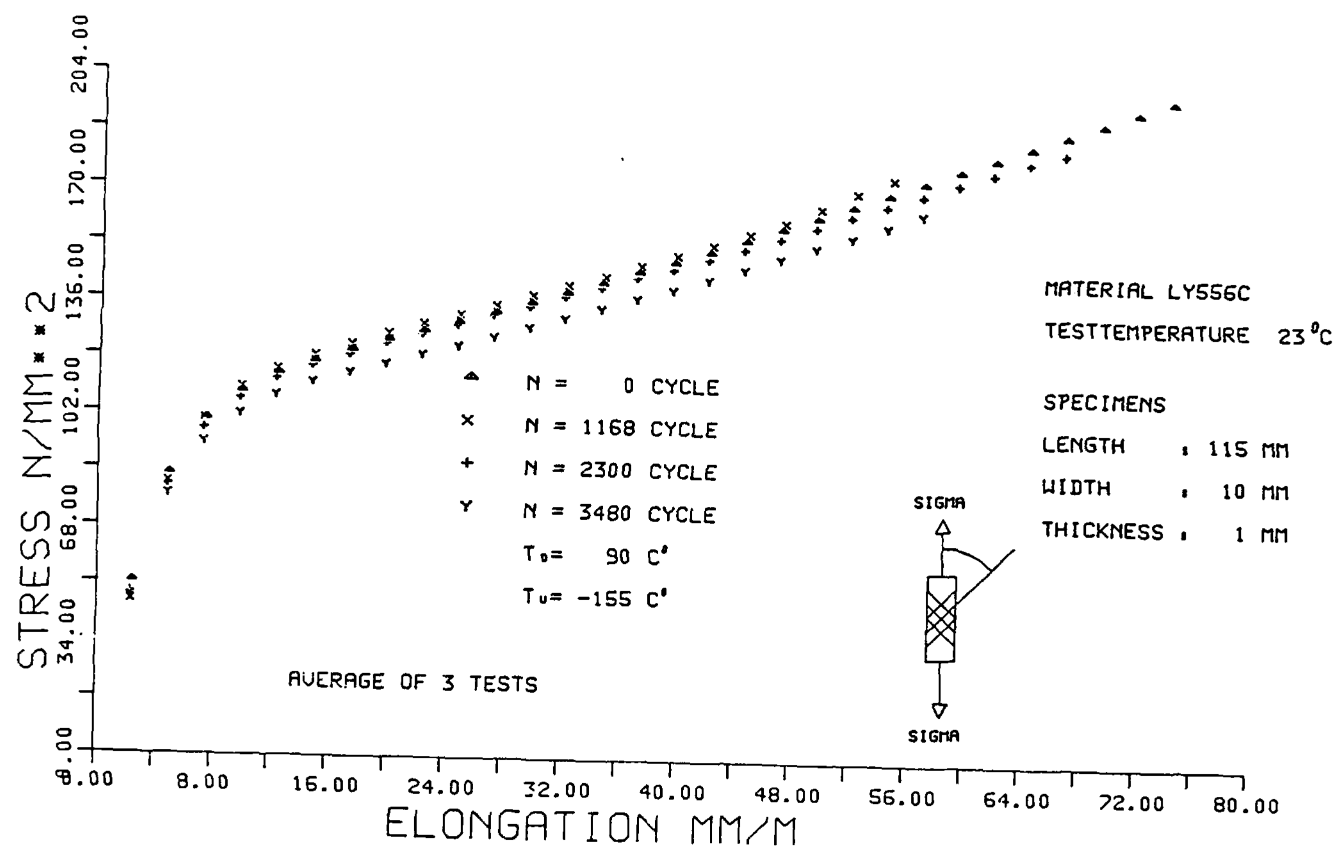

Fig. 36 Stress-Strain Slope From Tension on ± 45° CRP After Thermal Cycling

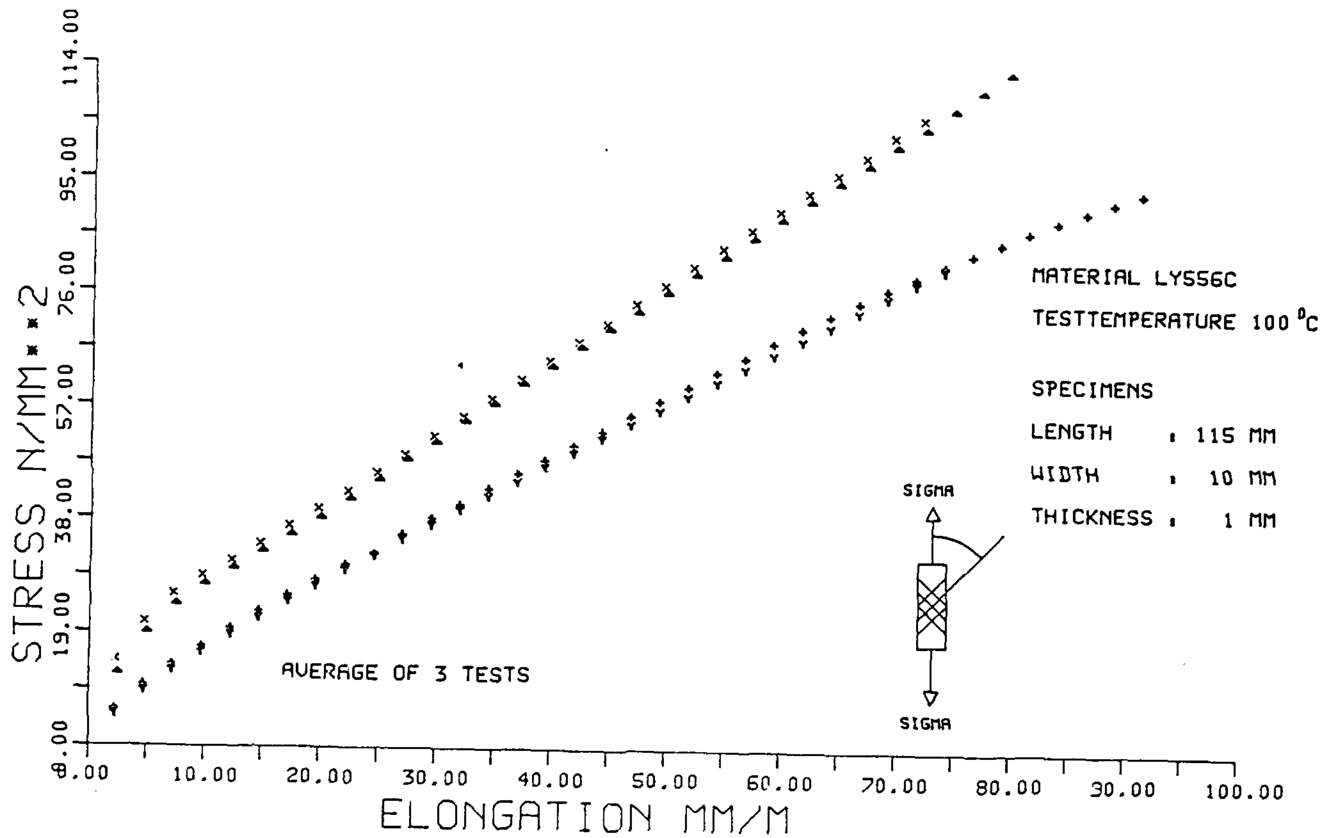

Fig. 37 Stress-Strain Slope From Tension on ± 45° CRP After Thermal Cycling

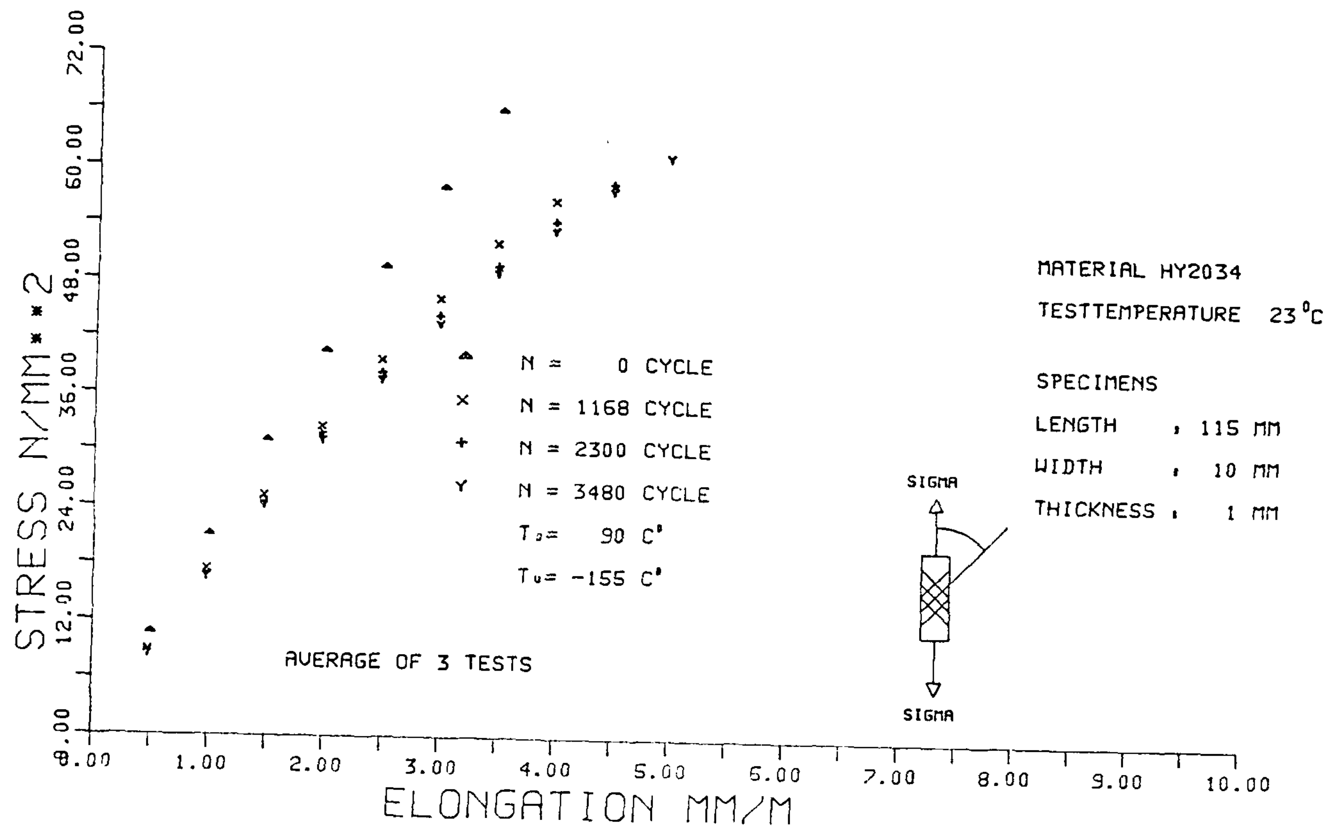

Fig 38 Stress-Strain Slope From Tension on ± 45° CRP After Thermal Cycling

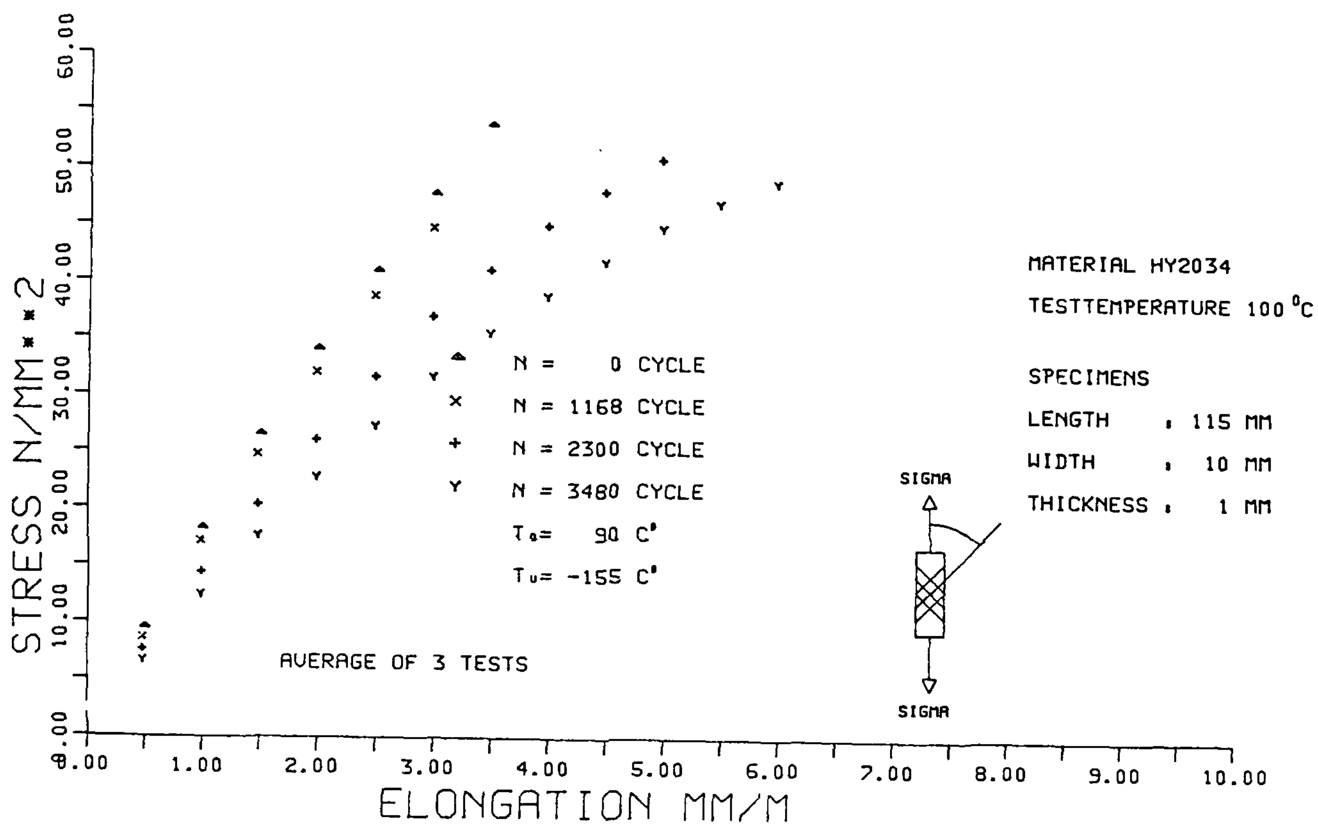

Fig. 39 Stress-Strain Slope From Tension on $\pm$ 45° CRP After Thermal Cycling

APPENDIX H

Notched Strength of Composite Laminates

J. Awerbuch

Dept. of Mechanical Engineering and Mechanics
Drexel University
Philadelphia, Pennsylvania 19104

DEUTSCHE FORSCHUNGS- UND VERSUCHSANSTALT
FÜR LUFT- UND RAUMFAHRT E.V.
INSTITUT FÜR STRUKTURMECHANIK

Interner Bericht
IB 131-85/04

Notched Strength of Composite Laminates

Submitted to the
Institute for Structural Mechanics
German Aerospace Research Establishment (DFVLR)
Braunschweig, Fed. Rep. of Germany
by

Dr. Jonathan Awerbuch
Associate Professor
Dept. of Mechanical Engineering an. Mechanics
Drexel University, Philadelphia, Pennsylvania 19104,
U S A

Braunschweig, den 14. 01. 1985

Der Bericht umfaßt :

141 Seiten mit
135 Bildern

Institutsleiter:

Dr.-Ing. H.W. Bergmann

Der Bearbeiter:

Dr. J. Awerbuch

FOREWORD

This document is a compilation of the more voluminous report

"Notched Strength Predictions of Graphite-Epoxy Laminates"
(Part I + II + 6 Appendices, DFVLR IB 131-83/21)

on research into the applicability of fracture models for predicting the notched strength of graphite/epoxy laminates.

The work was conducted from June, 1982, to September, 1983, sponsored jointly by the Institute for Structural Mechanics of the German Aerospace Research Establishment (DFVLR) and in-house research at Drexel University in Philadelphia. A Drexel University support group comprised of graduate and undergraduate students and various technical assistants participated in different phases of the program The principal investigator was Dr. Jonathan Awerbuch; Dr. H.W. Bergmann acted as the monitor of the German Aerospace Research Establishment (DFVLR).

NOTCHED STRENGTH OF

COMPOSITE LAMINATES

Jonathan Awerbuch

Department of Mechanical Engineering and Mechanics
Drexel University
Philadelphia, Pennsylvania 19104

Presented in the Composite Materials Workshop, Katholieke Universiteit, Leuven, June 4-8, 1984.

INTRODUCTION

Extensive research has been performed in recent years on the fracture behavior and toughness of composite systems containing artificially induced circular holes or cracks.* These studies focus on subjects such as initiation of crack tip damage growth, critical crack tip damage zone size, notch sensitivity, fracture toughness, failure modes on the micro and macro scales, crack arrest mechanisms, etc., using various theoretical and experimental techniques. There are several reasons for employing a variety of techniques to the study of fracture mechanics in composites. First, different composite systems demonstrate different failure modes and damage mechanisms and may require correspondingly different analytical tools and experimental techniques. Second, there is not yet a consensus regarding the proper set of criteria for failure. Furthermore, due to the multiplicity of failure modes and the corresponding complexity of failure processes and damage progression in laminated composites, a variety of analytical techniques have been developed ranging from comprehensive numerical methods to simplified semi-empirical fracture models. This situation is undesirable in light of the importance of understanding the fracture mechanisms of composites before they can be applied to primary aerospace structures. Continuing research is of the utmost importance because the aerospace applications of composites are designed with mechanical fasteners, and they are subjected to many types

* The terms 'crack', 'notch' and 'slit' are used interchangeably in the literature of composites to define artificially induced notches. It should be noted that the typical crack which forms in metals under cyclic loading (and for which stress analyses have been formulated) does not form in composites. Consequently, the artificially induced cracks (slits) should be termed 'notches', having a finite notch tip radius. In this report, however, the term 'crack' has been adopted since it is the term being used by most researchers. It should not be confused with the actual cracking which appears at the tip of these artificially induced 'cracks' (notches) under loading.

of impact damage (such as dropped tools, runway stones, etc.) under various loading functions and environmental conditions. A critical look at the current application of fracture mechanics in composites is given in [1].

There is a difference of opinion whether linear elastic fracture mechanics (LEFM) is also applicable to composites containing discontinuities. Initially, research has been directed toward the applicability of LEFM to composites, however, results so far indicate that LEFM can only be applied in limited cases. Several fracture models have been proposed in the past decade extending LEFM from metals to composites, primarily where the critical stress intensity factor (i.e. fracture toughness) is being compared to that of traditional structural metals. Also, the introduction of these fracture models was motivated by the desire to introduce simplified, easy to operate predictive tools for the notch sensitivity of composites. It must be emphasized, however, that all these semi-empirical fracture models which attempt to predict the notched strength of composites do not address, but rather by-pass, the micro and macrofailure associated with the crack extension process. The details of the actual crack-tip damage zone are very complex and vary among the different laminate configurations and material systems. In the great majority of cases, no self-similar crack growth is observed, as would be the case in metals.

As mentioned previously LEFM can only be applied directly to composites in limited cases. Wu [2] determined that only when very specific conditions are satisfied can the techniques of isotropic fracture mechanics be directly applied to anisotropic plates. The stated conditions are [2]:

1. The orientation of the flaw with respect to the principal axis of symmetry must be fixed;

AD-A168 005 DEVELOPMENT OF FRACTURE MECHANICS MAPS FOR COMPOSITE MATERIALS VOLUME 4(U) DEUTSCHE FORSCHUNGS- UND VERSUCHSANSTALT FUER LUFT- UND RAUMF.. H W BERGMANN 2/3

UNCLASSIFIED DEC 85 AFWAL-TR-85-4150-VOL-4 F/G 11/4 NL

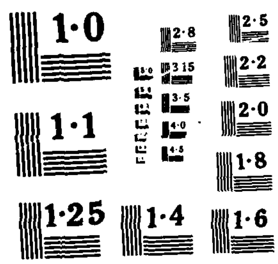
1·0
1·1
1·25
1·4
1·6
1·8
2·0
2·2
2·5
2·8

2. The stress intensity factors defined for anisotropic cases must be consistent with the isotropic case in stress distribution and in crack displacement modes; and

3. The critical orientation coincides with one of the principal directions of elastic symmetry.

The experimental results obtained by Wu [2] for unidirectional fiberglass reinforced Scotchply with centrally located cracks in the direction of the fibers (loaded in tension, pure shear, and combined tension and shear) indicated that for this particular case, fracture mechanics is adaptable to orthotropic materials. The use of unidirectional materials in actual structural applications is limited, however; and when general multidirectional laminates are concerned, the complexity of damage growth at the crack tip, e.g. Figure 1, raises serious questions as to the applicability of classical fracture mechanics to composites. On the microscopic level the actual failure modes occurring within the crack tip damage zone appear in the form of fiber pull-out, matrix micro-cracking, fiber-matrix interfacial failure, matrix serrations, and/or cleavage, fiber failure, etc. On the macroscopic level the major failure modes are delamination and matrix cracking along the fiber direction in the individual plies initiating at the crack tip, and failure of individual plies. An example of a typical crack tip damage in $[0_2/+45/0_2/-45/0/90]_s$ Gr/Ep laminate at two different load levels is shown in the radiographs of Figure 1. Matrix cracking (or fiber-matrix interfacial failure) along the 0°, 90°, and ±45° plies is clearly seen as well as the delamination emanating from the free edges at the crack tips. It should be noted that the failure process, type of damage and its progression strongly depends on intrinsic material parameters such as laminate configurations, material systems, etc., and on loading functions

SPECIMEN NO. 273/1 : NOTCH LENGTH = 12.51 mm

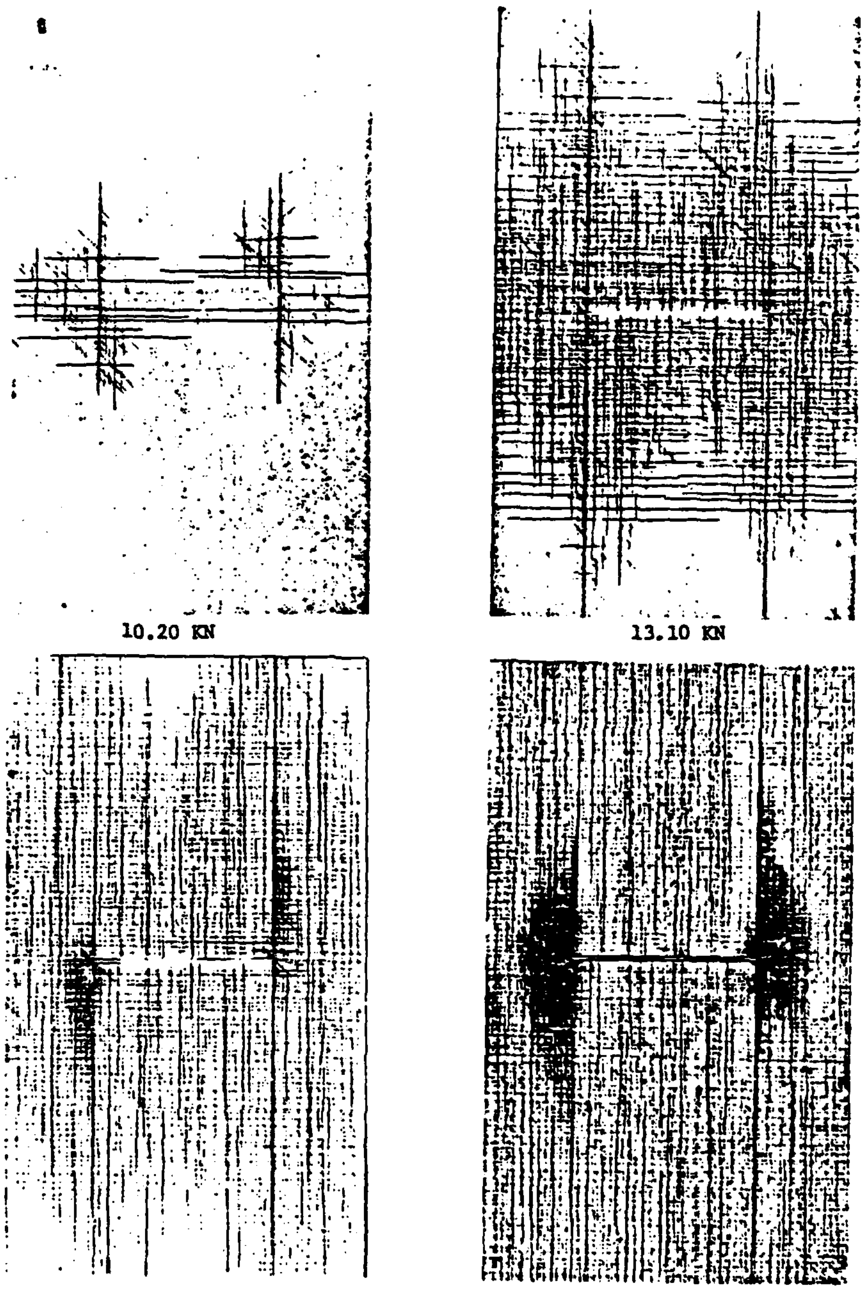

Figure 1. X-ray radiographs of center-cracked graphite/epoxy $[0_2/+45/0_2/-45/0/90]_s$ laminate, 25 mm wide.

and environmental conditions. Numerous researchers studied the type of damage progression ahead of the crack tip and provided insight regarding the different material variables affecting the crack tip damage zone.

The presentation is a brief summary of a comprehensive review conducted by the authors* on the notch sensitivity of composite laminates containing centrally located circular holes and straight cracks, and subjected to uniaxial loading. The complete review includes a detailed evaluation of several of the most commonly used fracture models for predicting the notched strength of composites, and of the experimental results published, including all the relevant available information regarding material system, laminate configuration and geometry, testing procedure, notched strength data, material mechanical properties, etc. The review of both the fracture models and experimental data is sufficiently detailed so that the comprehensive report is self-contained and the reader does not have to refer to the original publication. All the notched strength data reviewed were compared with all the fracture models reviewed and the various material constants associated with these fracture models were determined. For this purpose, special computer programs were developed for analyzing all the data through a variety of procedures. The applicability of the various fracture models and their associated material constants as well as the parameters affecting the notch sensitivity of composite laminates are discussed in detail.

In this presentation the highlights of each of the fracture models will be briefly reviewed, samples of experimental notched strength data will be presented, comparison between predictions and experiments will be shown, and a summary of the major material variables affecting notch sensitivity will be outlined.

---

* The complete review can be obtained from Dr. J. Awerbuch, Department of Mechanical Engineering and Mechanics, Drexel University, Philadelphia, Pennsylvania 19104.

PREDICTIONS OF NOTCH SENSITIVITY

OBJECTIVES

- EVALUATE ALL EXISTING SEMI-EMPIRICAL FRACTURE MODELS TO PREDICT NOTCHED STRENGTH OF COMPOSITES (ELEVEN MODELS).

- COLLECT AND REVIEW NOTCHED STRENGTH DATA OF Gr/Ep, B/Al AND Gr/PI LAMINATES CONTAINING CIRCULAR HOLES AND STRAIGHT CRACKS.

- COMPARE NOTCHED STRENGTH DATA WITH THE FRACTURE MODEL PREDICTIONS.

- CORRELATE THE VARIOUS PARAMETERS ASSOCIATED WITH THE DIFFERENT FRACTURE MODELS WITH NOTCH SENSITIVITY OF COMPOSITE LAMINATES AND EVALUATE THEIR APPLICABILITY AS MEASURES OF NOTCH SENSITIVITY.

- DETERMINE EFFECT OF MATERIAL PARAMETERS (E.G. STACKING SEQUENCE, CONSTITUENTS, ETC.) ON NOTCH SENSITIVITY.

LIST OF FRACTURE MODELS

AUTHORS	REF.	ABBRV.	CRITERION	HOLE	SLITS
M.E. WADDOUPS J.R. EISENMANN B.E. KAMINSKI	3	WEK	LEFM	✓	✓
J.M. WHITNEY R.Y. NUISMER	4,5	WN	POINT STRESS AVERAGE STRESS	✓ ✓	✓ ✓
R.F. KARLAK	6	K	POINT STRESS	✓	-
R.B. PIPES R.C. WETHERHOLD J.W. GILLESPIE	7,8,9	PWG	POINT STRESS	✓	✓
J.W. MAR K.Y. LIN	10,11	ML	$n \neq -0.5$	✓	✓
C.C. POE J.A. SOVA	12	PS	STRAIN	✓	-

WEK FRACTURE MODEL

(CIRCULAR HOLES)

- Application of Linear Elastic Fracture Mechanics (LEFM)
- Experimental results indicated that:

  1. Post-fatigue residual strength is equal to or greater than the static strength.

  2. "hole size effect" on notched strength, Figure 2.

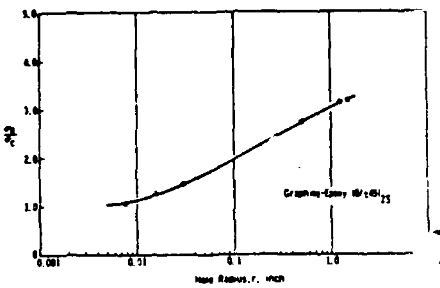

Figure 2. Stress concentration study [3].

- From Irwin [13]:

  (1) $G_I = \frac{(1-\nu^2)\pi}{E} K_I^2$

- From Bowie [14] solution for symmetrical cracks emanating from a circular hole

  (2) $K_I = \sigma_N^\infty \sqrt{\pi a}\ \ f(a/R)$

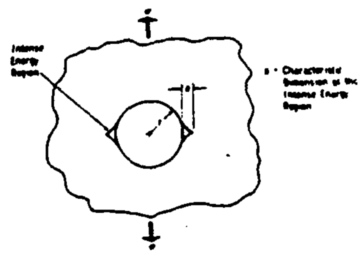

Figure 3. Fracture model [3].

- Values of f(a/R) can be found in [15]

  (3) $\sqrt{G_I} = [\pi\sqrt{a(1-\nu^2)/E}\ ]\ \sigma_N^\infty\ f(a/R)$

  (4) $\sqrt{G_I}\ /[\pi\sqrt{a(1-\nu^2)/E}] = \sigma_N^\infty\ f(a/R) = \text{constant}$

- At failure, from Eq. (2):

  (5) $\sigma_N^\infty = K_{IC}/[\sqrt{\pi a}\ f(a/R)]$

- For unnotched specimen:

  (6) $\sigma_o = \sigma_N^\infty|_{a/R\to\infty} = \frac{K_{IC}}{\sqrt{\pi a}(1.00)}$

  Thus:

  (7) $\sigma_o/\sigma_N^\infty = f(a/R)$

  See comparisons in Figure 5.

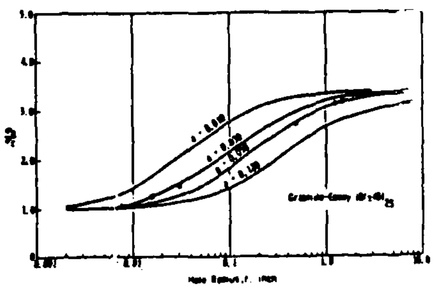

Figure 4. Parametric study [3].

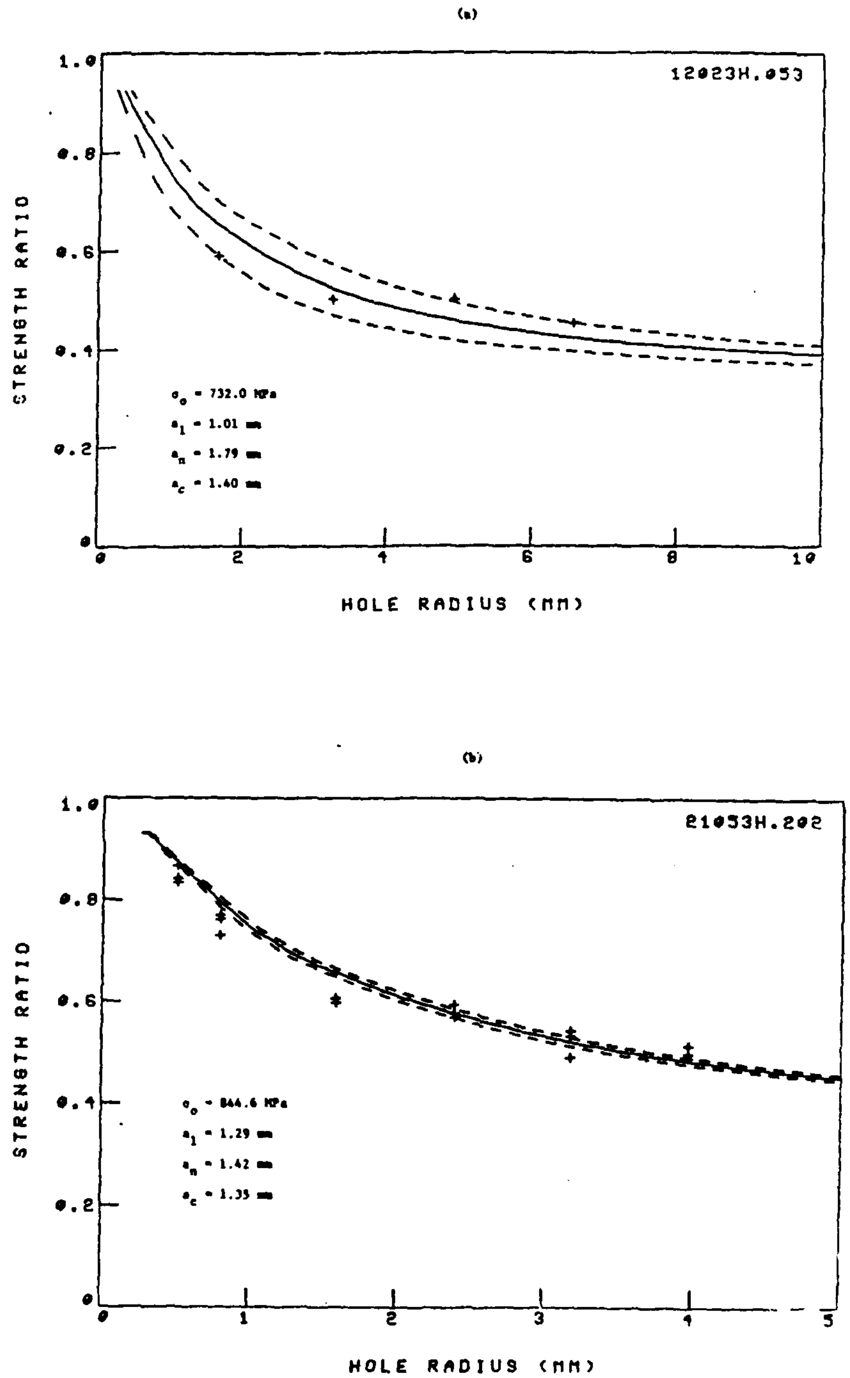

Figure 5. Comparison between experiments and predictions (WEK-fracture model for: a. graphite/epoxy $[\pm 45/0]_s$ laminate; b. boron/aluminum $[\pm 45/0_2]_s$ laminate.

WEK FRACTURE MODEL (STRAIGHT CRACKS)

The concept of an intense energy region at the tip of the crack has been applied by WEK for the case of composite laminates containing a straight crack of length 2c.

From Griffith [16]:

(8) $K_{IC} = \sigma_N^\infty \sqrt{\pi c}$

Similar to the Irwin's plastic zone correction [13]:

(9) $K_{IC} = \sigma_N^\infty \sqrt{\pi(c + a_c)}$

a_c...crack tip damage zone size at failure, i.e., $(c + a_c)$ is an "effective" half-crack length.

When c = 0:

(10) $K_{IC} = \sigma_o \sqrt{\pi a_c}$

The notch sensitivity becomes:

(11) $\dfrac{\sigma_N^\infty}{\sigma_o} = \sqrt{\dfrac{a_c}{c + a_c}}$

Data Analysis:

(12) $c = a_c[(\sigma_o/\sigma_N^\infty)^2 - 1]$

See comparisons in Figures 8 and 9 for Eqs. (11) and (12), respectively.

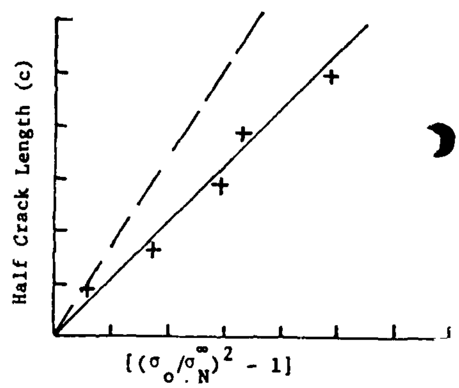

Figure 6. Schematic presentation of least squares fit of a_c.

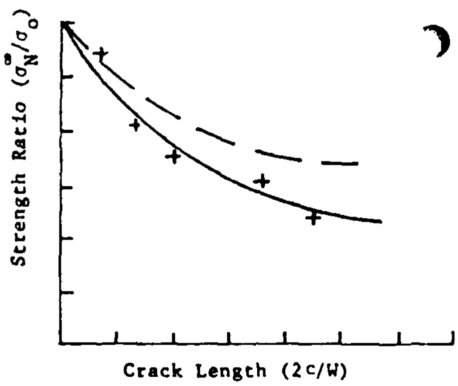

Figure 7. Schematic presentation of notched strength.

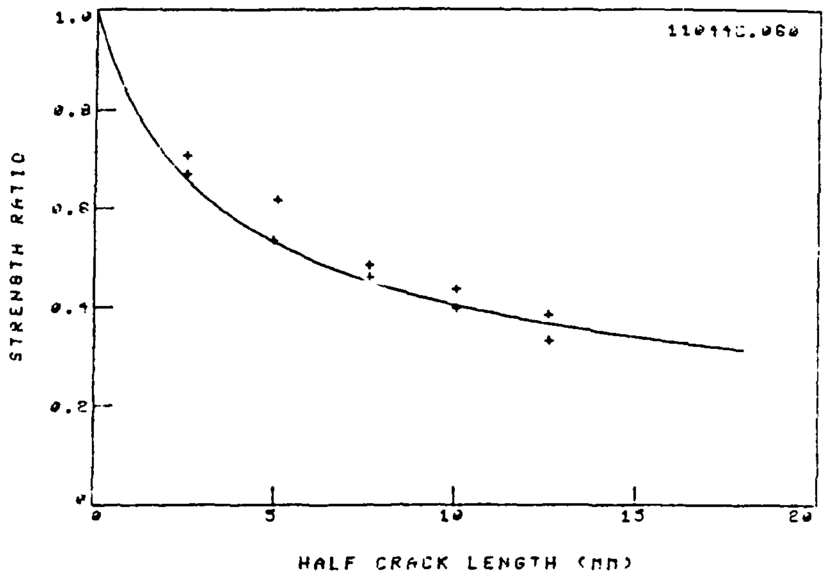

Figure 8. Comparison between experiments and prediction (WEK-fracture model) for graphite/epoxy $[0/90/\pm45]_s$ laminate (σ_o = 454.3 MPa, a_c = 1.02 mm).

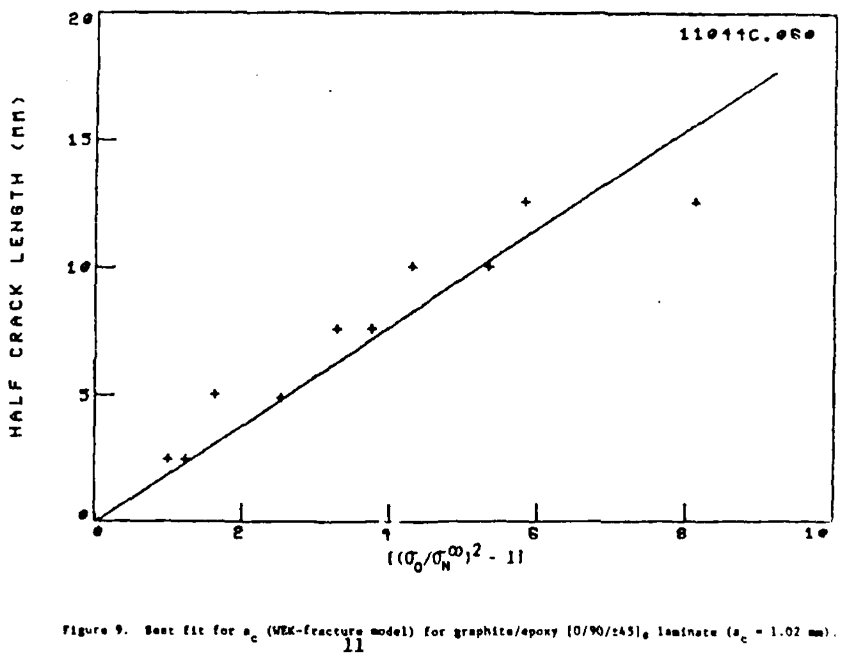

Figure 9. Best fit for a_c (WEK-fracture model) for graphite/epoxy $[0/90/\pm45]_s$ laminate (a_c = 1.02 mm).

WN-FRACTURE MODEL

I. STRESS CRITERIA

Point Stress Criterion: Assumes that failure occurs when the stress, σ_y, over some distance, d_o, away from the discontinuity is equal to or greater than the strength of the unnotched laminate [4]:

(13) $$\sigma_y(x,o)\Big|_{x=R+d_o} = \sigma_o \qquad \text{(See Figure 10)}$$

Average Stress Criterion: Assumes that failure occurs when the average stress, σ_y, over some distance, a_o, equals the unnotched laminate strength [4]:

(14) $$\sigma_o = \frac{1}{a_o}\int_R^{R+a_o} \sigma_y(x,o)\,dx \qquad \text{(See Figure 11)}$$

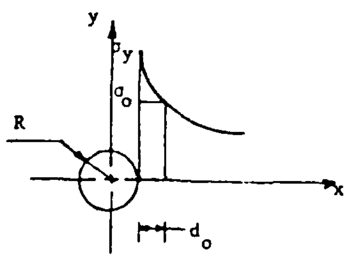

Figure 10. Schematic representation of the "point-stress" criterion [5].

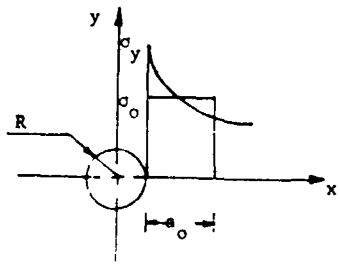

Figure 11. Schematic representation of the "average-stress" criterion [5].

II. STRESS DISTRIBUTIONS

For an infinite orthotropic plate subjected to a uniform stress, σ^∞, applied parallel to the y-axis at infinity, the normal stress, σ_y, along the x-axis ahead of the notch can be expressed by:

- Circular Hole of radius R; an approximate distribution is given in [21]:

$$\sigma_y(x,o) = \frac{\sigma^\infty}{2}\{2+(\frac{R}{x})^2+3(\frac{R}{x})^4 - (K_T^\infty-3)[5(\frac{R}{x})^6-7(\frac{R}{x})^8]\} \quad x > R \tag{15}$$

where K_T^∞ is the stress concentration factor for an infinite plate, expressed by [20].

$$K_T^\infty = 1 + \left\{\frac{2}{A_{22}}\left(\sqrt{A_{11}A_{22}} - A_{12} + \frac{A_{11}A_{22}-A_{12}^2}{2A_{66}}\right)\right\}^{\frac{1}{2}} \tag{16}$$

And A_{ij} are the orthotropic in-plane stiffnesses of the laminate [22-26].

In terms of effective elastic moduli, Eq. (16) can be written in the following form:

$$K_T^\infty = 1+\{2\cdot[(\bar{E}_{11}/\bar{E}_{22})^{\frac{1}{2}} - \bar{\nu}_{12} + \bar{E}_{11}/\bar{G}_{12}\}^{\frac{1}{2}} \tag{17}$$

Using the standard reference system adapted for composites:

$$K_T^\infty = 1+\{2\cdot[(E_y/E_x)^{\frac{1}{2}} - \nu_{yx} + E_y/G_{yx}]^{\frac{1}{2}}\} \tag{18}$$

where E_x, E_y, ν_{yx}, and G_{yx} are the effective elastic moduli of the laminate for the reference system shown in Figure 12.

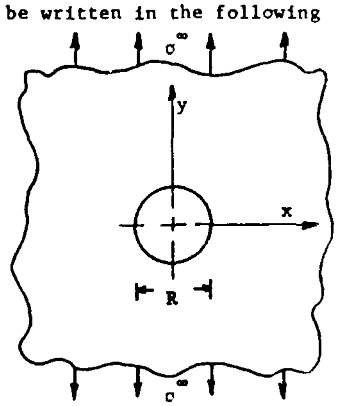

Figure 12. Circular hole in an infinite plate subjected to uniaxial tension.

• Straight Cracks of length 2c; an approximate distribution is given in [18,19] as:

$$\sigma_y(x,o) = \frac{K_I}{\sqrt{2\pi(x-c)}} = \sigma^{\infty}\sqrt{\frac{c}{2(x-c)}} \tag{19}$$

where the mode I stress intensity factor is defined by:

$$K_I = \sigma^{\infty}\sqrt{\pi c} \tag{20}$$

The exact elasticity solution has been formulated in [20]:

$$\sigma_y(x,o) = \frac{K_I x}{\sqrt{\pi c(x^2-c^2)}} = \frac{\sigma^{\infty} x}{\sqrt{x^2-c^2}} \tag{21}$$

For large cracks the approximate expression of Eq. (19) yields predictions similar to the exact solution of Eq. (21). However, for smaller cracks the exact solution should be applied. The approximate solution, Eq. (19), is independent of crack length while the exact solution, Eq. (21), does depend on crack length [4,5]. The "notch size effect" on the stress distribution is shown in Figures 13 and 14.

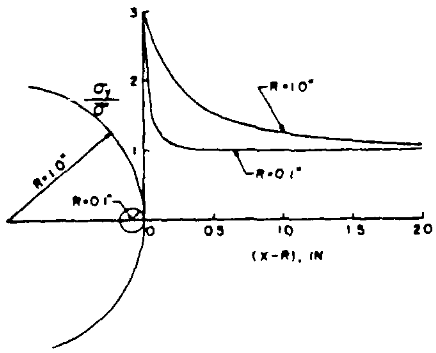

Figure 13. Normal stress distribution for a circular hole in an infinite isotropic plate [5].

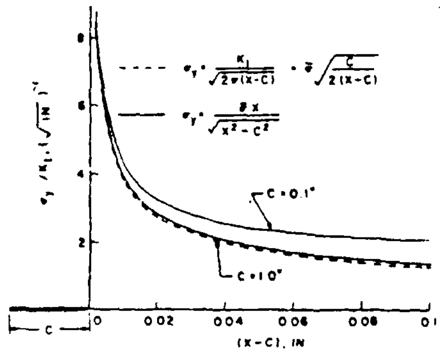

Figure 14. Normal stress distribution for a center crack in an infinite anisotropic plate [5].

III. NOTCHED STRENGTH PREDICTIONS:

A. Circular Holes:

a. Point Stress Criterion:

Applying the "point-stress" criterion, Eq. (13), in conjunction with Eq. (15):

$$\sigma_N^\infty/\sigma_o = 2/\{2+\xi_1^2+3\xi_1^4 - (K_T^\infty-3)(5\xi_1^6-7\xi_1^8)\} \tag{22}$$

where

$$\xi_1 = R/(R+d_o) \tag{23}$$

- when $R \to \infty$ (large holes): $\sigma_N^\infty/\sigma_o = 1/K_T^\infty$
- when $R \to o$ (small holes): $\sigma_N^\infty/\sigma_o = 1.0$
- when $K_T^\infty = 3.0$ (isotropic and quasi-isotropic materials):

$$\sigma_N^\infty/\sigma_o = 2/\{2+\xi_1^2 + 3\xi_1^4\} \tag{24}$$

- when $R \to \infty$ (large holes): $\sigma_N^\infty/\sigma_o = 1/3$
- when $R \to o$ (small holes): $\sigma_N^\infty/\sigma_o = 1.0$

See comparison in Figure 15.

b. Average Stress Criterion:

Applying the "average-stress" criterion, Eq. (14), in conjunction with Eq. (15):

$$\sigma_N^\infty/\sigma_o = 2(1-\xi_2)/\{2-\xi_2^2-\xi_2^4 + (K_T^\infty-3)(\xi_2^6-\xi_2^8)\} \tag{25}$$

where:

$$\xi_2 = R/(R+a_o)$$

when $K_T^\infty = 3.0$ (isotropic and quasi-isotropic materials):

$$\sigma_N^\infty/\sigma_o = 2(1-\xi_2)/(2-\xi_2^2-\xi_2^4) \tag{26}$$

See comparison in Figure 16.

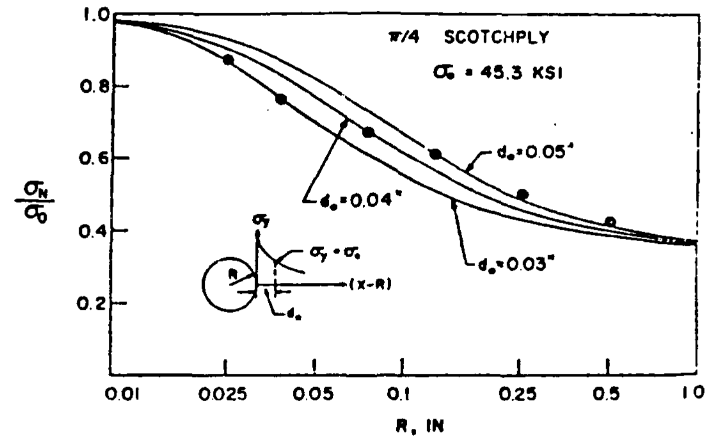

Figure 15. Stress reduction in quasi-isotropic glass/epoxy laminates due to the presence of a circular hole, point stress criterion [4].

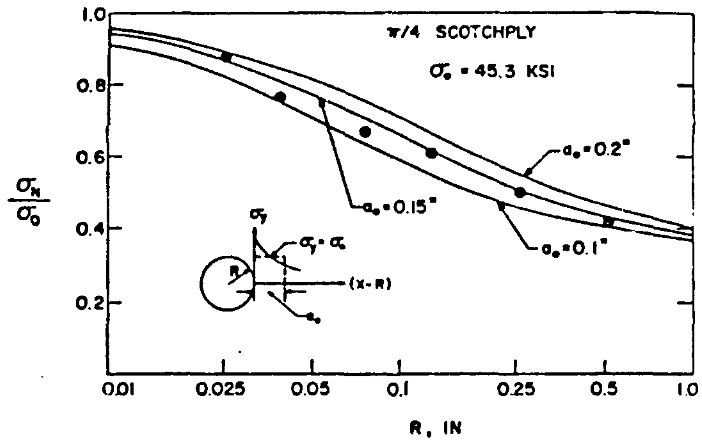

Figure 16. Stress reduction in quasi-isotropic glass/epoxy laminates due to the presence of a circular hole, average stress criterion [4].

- Since $K_T^{\infty} = 3.0$ Eqs. (24) and (26) could be used.
- The use of constant values of $d_o = 1.02$ mm and $a_o = 3.81$ mm yield very good agreement.

B. Straight Cracks

a. Point Stress Criterion

Applying the "point-stress" criterion, Eq. (13), in conjunction with Eq. (21):

(27) $$\sigma_N^\infty/\sigma_o = (1 - \xi_3^2)^{1/2}$$

where

(28) $$\xi_3 = c/(c + d_o)$$

Noting that for an infinite plate:

(29) $$K_Q = \sigma_N^\infty \sqrt{\pi c}$$

The critical stress intensity factor becomes:

(30) $$K_Q = \sigma_o \sqrt{\pi c(1 - \xi_3^2)}$$

which is a function of crack length. (From Eq. (19): $K_Q = \sigma_o\sqrt{2\pi d_o}$ = const.).

b. Average Stress Criterion:

Applying the "average-stress" criterion, Eq. (14), in conjunction with Eq. (21):

(31) $$\sigma_N^\infty/\sigma_o = [(1 - \xi_4)/(1 + \xi_4)]^{1/2}$$

where

(32) $$\xi_4 = c/(c + d_o)$$

The critical stress intensity factor, Eq. (29), becomes:

(33) $$K_Q = \sigma_o \sqrt{\pi c(1 - \xi_4)(1 + \xi_4)}$$

which is a function of crack length (From Eq. (19): $K_Q = \sigma_o \sqrt{\pi a_o/2}$ = const.)

From Eqs. (31) and (32):

(34) $$\sigma_N^\infty/\sigma_o = \sqrt{(a_o/2)/(c+a_o/2)}$$

Similar to WEK-fracture model, Eq. (11), i.e. $a_o = 2a_c$.

The effect of hole or crack size on the stress distribution ahead of the hole edge or crack tip is shown in Figures 17 and 18, respectively.

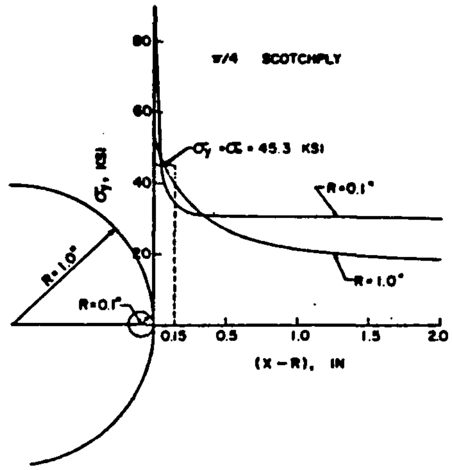

Figure 17. Stress distribution at failure, average stress criterion, quasi-isotropic glass/epoxy laminates with circular holes [4].

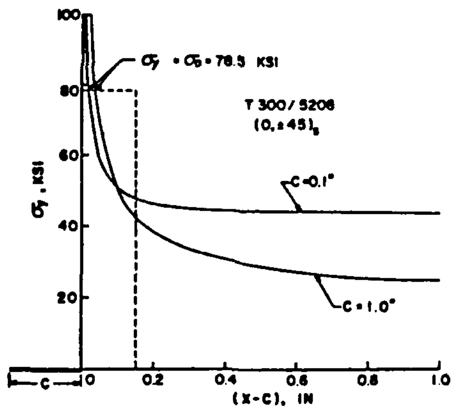

Figure 18. Stress distribution at failure, average stress criterion, graphite/epoxy laminates with center cracks [4].

- Significant differences in the stress distributions between the two holes and crack sizes, using Eqs. (26) and (21,33), respectively, (a_o=3.81 mm) are obtained.

- The results clearly demonstrate the "hole (crack) size effect" in composite laminates.

Comparisons between experimental values of K_Q (Eq. (29)) and predictions according to the "point stress" (Eq. (30)) and "average stress" (Eq. (33)) criteria are shown in Figures 19 and 20, respectively.

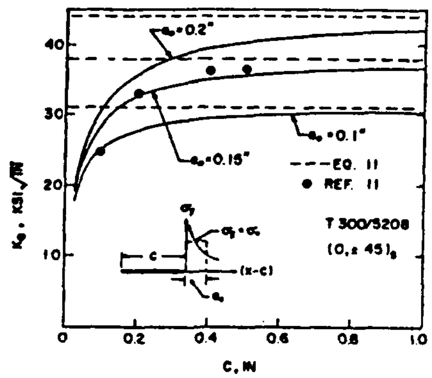

Figure 19. Critical stress intensity factor as a function of crack length for graphite/epoxy laminates, point stress criterion [4]. Data taken from [28].

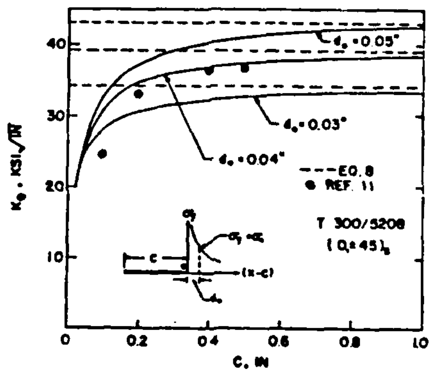

Figure 20. Critical stress intensity factor as a function of crack length for graphite/epoxy laminates, average stress criterion [4]. Data taken from [28].

- The use of constant values of d_o = 1.02 mm and a_o = 3.81 mm yield very good agreement.

- K_Q depends on crack length and asymptotically approaches a constant value (dashed lines in Figures 19 and 20), equal to that obtained by using the approximate solution, Eq. (19), as given by: $\sigma_o \sqrt{2\pi d_o}$ and $\sigma_o \sqrt{\pi a_o/2}$ for point and average stress criteria, respectively.

IV. DATA ANALYSES

The values of the characteristic distances d_o and a_o are determined through error analyses to best fit the experimental notched strength data.

- Linear Regression: Can be applied in the following cases.

  a. Circular Holes, "point-stress" criterion; For laminates having $K_T^\infty = 3.0$

  From Eq. (25):

$$R = d_o\{\sqrt{6}\ [-1 + \{1-24(1 - \sigma_o/\sigma_N^\infty)\}^{\frac{1}{2}}]^{-\frac{1}{2}} - 1\}^{-1} \tag{35}$$

  b. Straight Cracks, "point-stress" criterion; From Eq. (27):

$$c = d_o\ \{[1 - (\sigma_N^\infty/\sigma_o)^2]^{-\frac{1}{2}} - 1\}^{-1} \tag{36}$$

  c. Straight Cracks, "average-stress" criterion; From Eq. (31):

$$c = a_o\ \tfrac{1}{2}[(\sigma_o/\sigma_N^\infty)^2 - 1] \tag{37}$$

- Apply linear regression to the set of data pairs R (or c) and the parenthetical terms in Eqs. (35-37). Graphically, d_o and a_o are represented by the slope of the line, e.g. Figure 21.

- Error Minimization Techniques: For laminates containing circular holes and having $K_T^\infty \neq 3.0$ neither criteria, Eqs. (22) or (25) yields a closed-form expression for d_o and a_o. For such cases apply any of the classical error minimization techniques to determine the best fit of d_o and a_o.

- Comparison between experiments and predictions according to the "point stress" and "average stress" criteria for graphite/epoxy and boron/aluminum laminates containing holes, Figure 22, and straight cracks, Figure 23, show excellent agreement. Similarly, experimental results of K_Q (Eq. (29)) agree very well with predictions according to both criteria, Figure 24. The characteristic dimensions, d_o and a_o, seem to be independent of hole radius, Figure 25, and crack length, Figure 26.

(a)

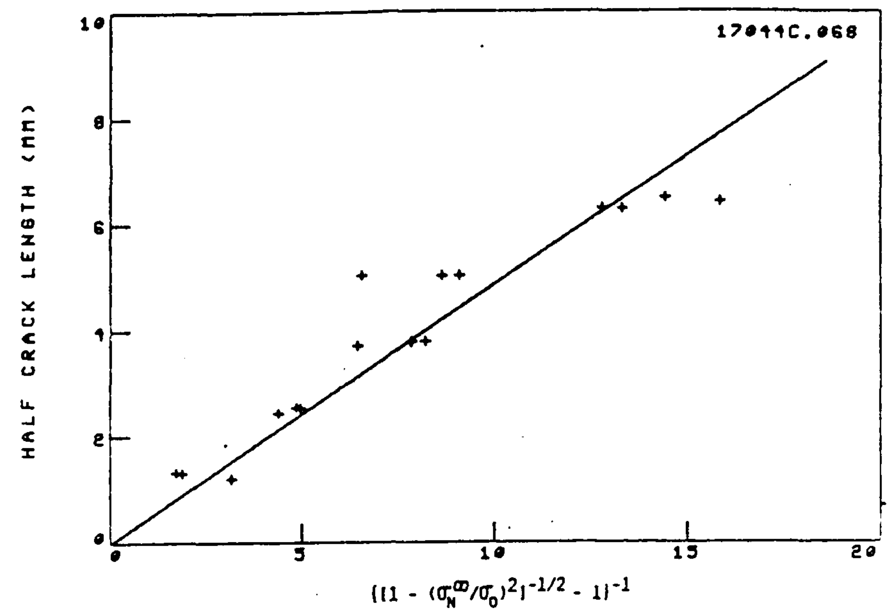

(b)

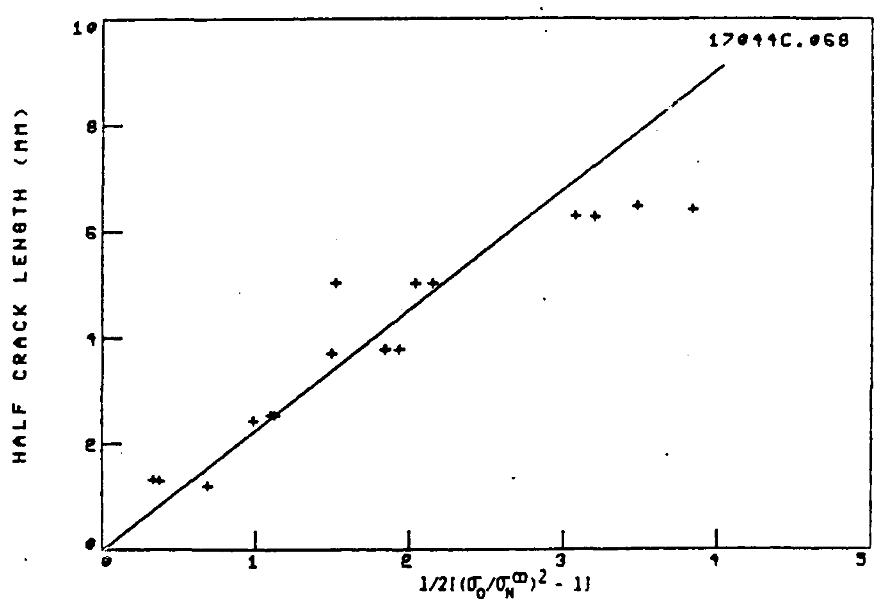

Figure 21. Best fit of: a. d_o ("point stress" criterion); b. a_o ("average stress" criterion) for graphite/epoxy $[0/90/\pm45]_s$ laminate (d_o = 0.51 mm, a_o = 2.26 mm).

(a)

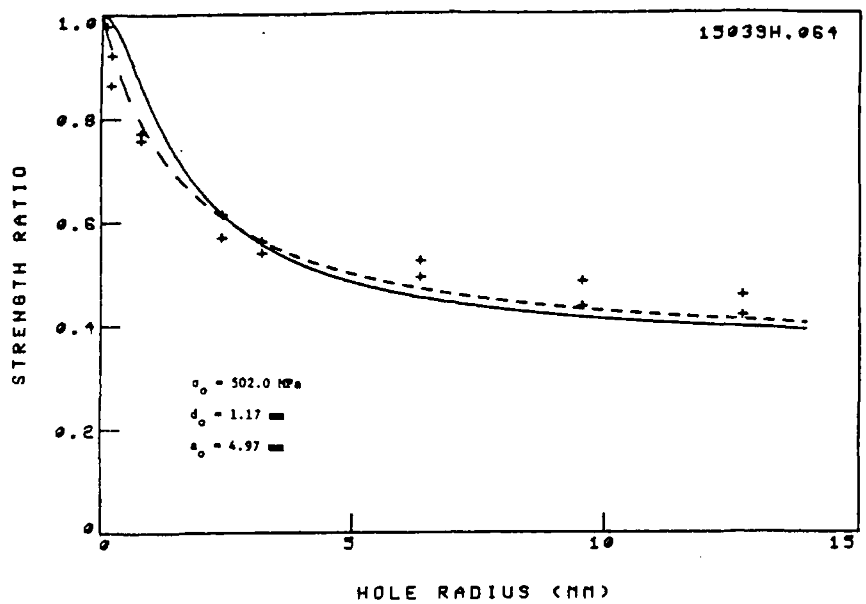

(b)

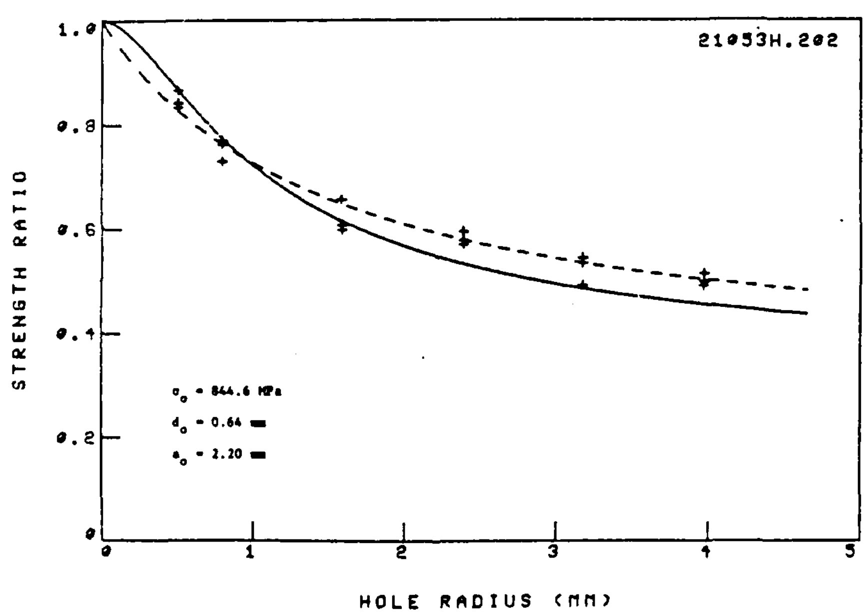

Figure 22. Comparison between experiments and predictions (WN-fracture model) for: a. graphite/epoxy $[0/\pm45/90]_s$ laminate; b. boron/aluminum $[\pm45/0_2]_s$ laminate (—— "point stress" criterion; - - - "average stress" criterion).

(a)

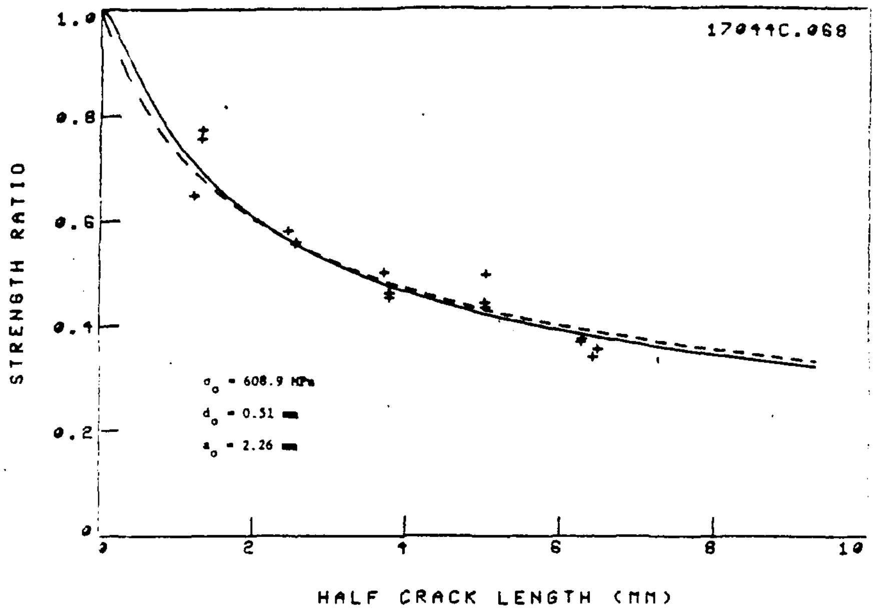

(b)

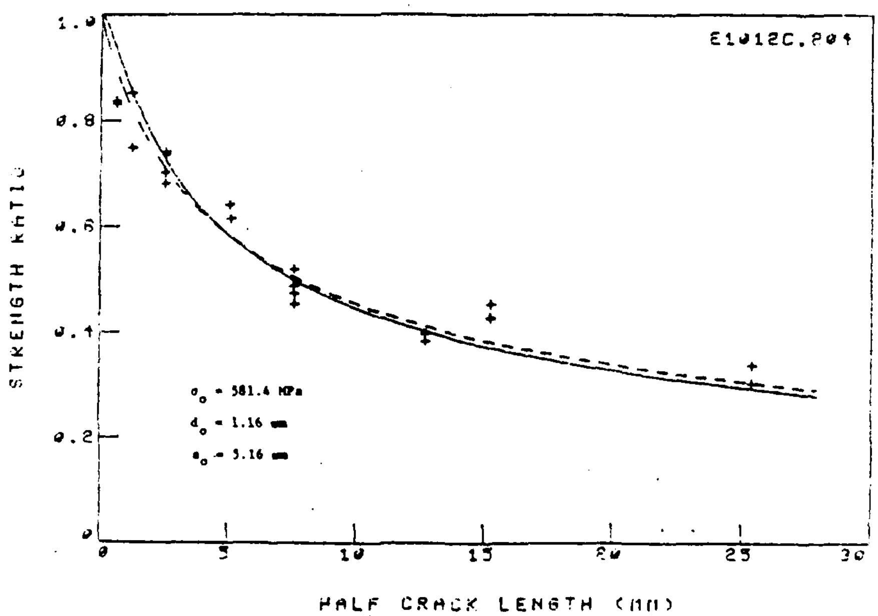

Figure 23. Comparison between experiments and predictions (WN-fracture model) for: a. graphite/epoxy $[0/90/\pm45]_s$ laminate; b. boron/aluminum $[0/\pm45]_s$ laminate. (——— "point stress" criterion; - - - "average stress" criterion).

(a)

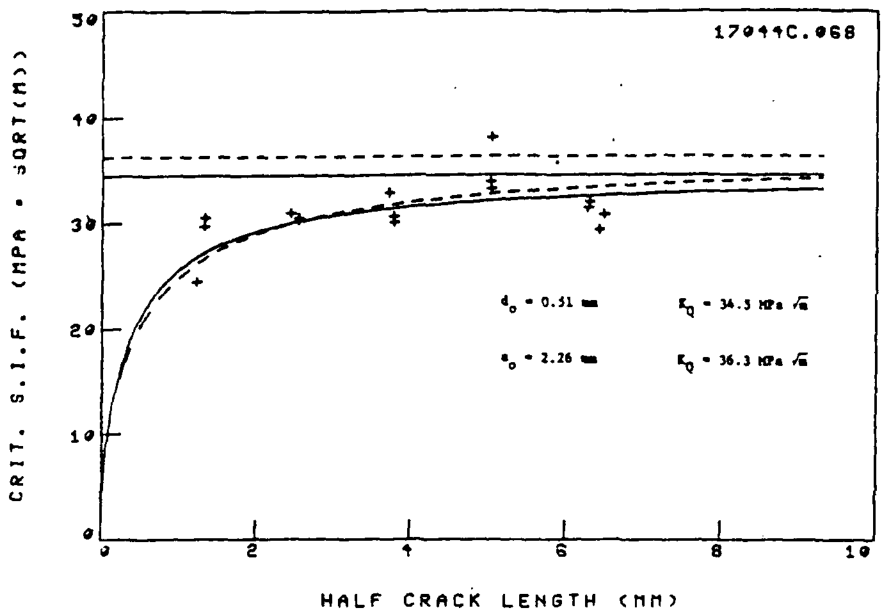

(b)

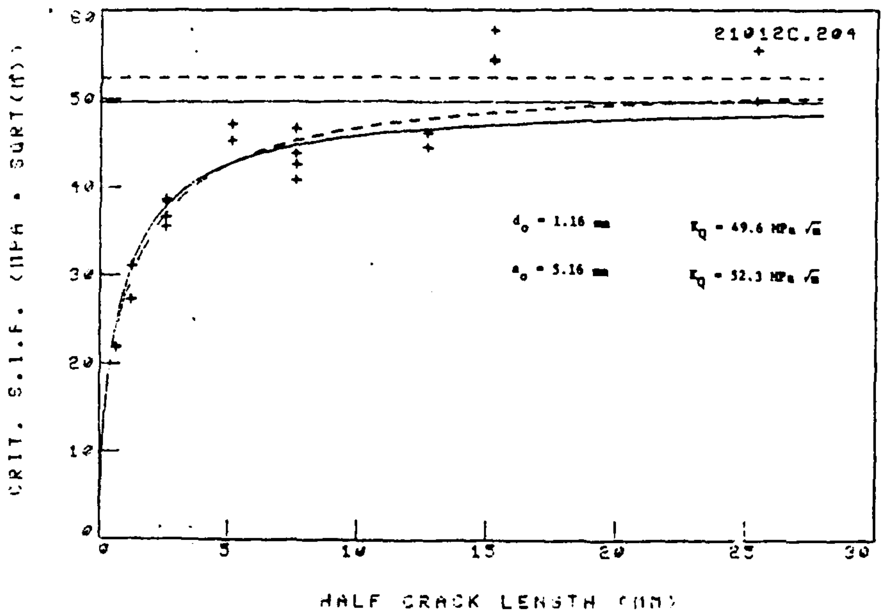

Figure 24. Critical stress intensity factor for: a. graphite/epoxy $[0/90/\pm45]_s$ laminate; b. boron/aluminum $[0/\pm45]_s$ laminate (—— "point stress" criterion, - - - "average stress" criterion).

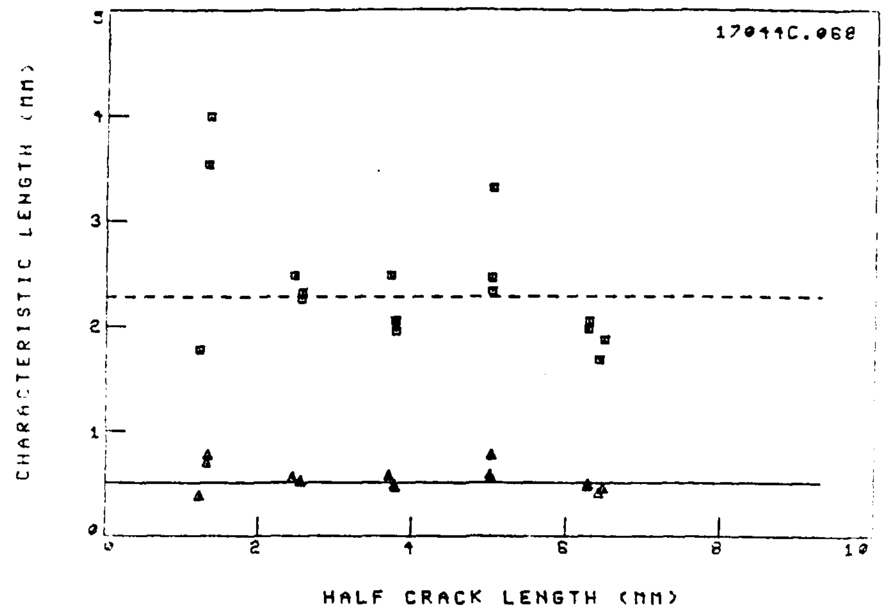

Figure 25. Characteristic dimensions (WN-fracture model) as a function of half crack length for graphite/epoxy $[0/90/\pm45]_s$ laminate (Δ —— "point stress" criterion, d_o = 0.51 mm; - - - "average stress" criterion, a_o = 2.26 mm) indicating that both can be considered as material constants.

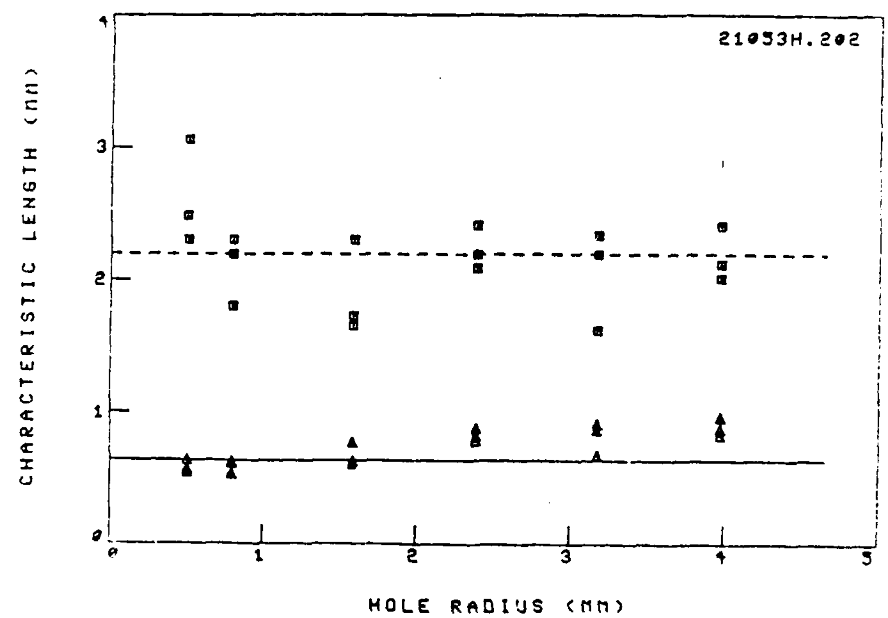

Figure 26. Characteristic dimensions (WN-fracture model) as a function of half crack length for boron/aluminum $[\pm45/0_2]_s$ laminate (Δ —— "point stress" criterion, d_o = 0.64 mm; - - - "average stress" criterion, a_o = 2.20 mm indicating that both can be considered as material constants.

V. DISCUSSION

- BOTH STRESS FAILURE CRITERIA ARE TWO-PARAMETER FRACTURE MODELS, I.E. σ_o AND d_o OR a_o.
- FOR ANY NEW MATERIAL SYSTEM THEY CAN BE DETERMINED EXPERIMENTALLY FROM TESTING UNNOTCHED AND NOTCHED SPECIMENS.
- MINIMUM OF TWO TESTS ARE REQUIRED, HOWEVER, SCATTER IN TEST RESULTS SHOULD BE TAKEN INTO ACCOUNT IN DETERMINING THE SUFFICIENT NUMBER OF TESTS REQUIRED.
- THE CHARACTERISTIC DISTANCES d_o AND a_o DO DEPEND ON THE SUBJECT LAMINATE.
- THEY MUST BE DETERMINED EXPERIMENTALLY A PRIORI FOR EACH MATERIAL SYSTEM AND LAMINATE CONFIGURATION INDEPENDENTLY.
- ONCE d_o AND a_o ARE KNOWN, BOTH WN-FRACTURE MODELS CAN BE APPLIED TO PREDICT THE TREND FOR THE NOTCHED STRENGTH AND THE CRITICAL STRESS INTENSITY FACTORS.
- WHEN THESE CHARACTERISTIC DIMENSIONS ARE PROPERLY DETERMINED, AN EXCELLENT AGREEMENT WITH EXPERIMENTS IS ESTABLISHED FOR ALL LAMINATE CONFIGURATIONS AND MATERIAL SYSTEMS, FIGURES 22-24.
- RESULTS INDICATE THAT d_o AND a_o ARE INDEPENDENT OF NOTCH SIZE, FIGURES 25-26.

K-FRACTURE MODEL
(CIRCULAR HOLES)

Modified WN "point-stress" criterion for laminates containing circular holes and having $K_T^\infty = 3.0$ (i.e. quasi-isotropic laminates). K-fracture model assumes that the characteristic distance, d_o, depends on hole radius, Figure 27.

Using the expression derived from WN "point-stress" criterion, Eq. (24):

(38) $$\sigma_N^\infty/\sigma_o = 2/(2 + \xi_1^2 + 3\xi_1^4) \qquad \text{where } \xi_1 = R/(R + d_o)$$

Solving for d_o:

(39) $$d_o = \sqrt{6}\, R\, \{-1 + [1-24(1-\sigma_o/\sigma_N^\infty)]^{1/2}\}^{-1/2} - R$$

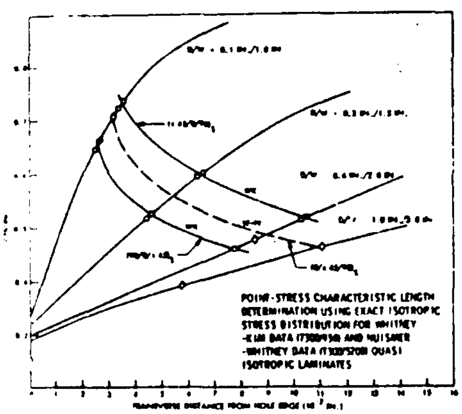

Figure 27. Graphical point-stress characteristic length determination using exact finite-width stress distribution and published data [6].

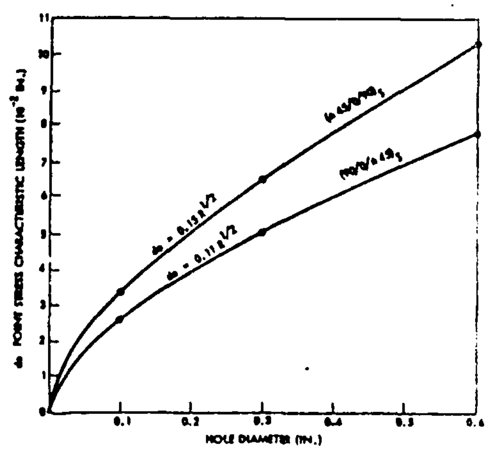

Figure 28. Plot of point-stress characteristic lengths from Figure 27 versus hole diameter showing parabolic relationship [6].

K-fracture model assumes that d_o is related parabolically to the hole radius, Figure 28, and through curve fitting determined that:

$$d_o = k_o R^{\frac{1}{2}} \tag{40}$$

Rewriting Eq. (38):

$$\sigma_N^\infty/\sigma_o = 2[2 + (1 + d_o R^{-1})^{-2} + 3(1 + d_o R^{-1})^{-4}]^{-1} \tag{41}$$

Substituting Eq. (40):

$$\sigma_N^\infty/\sigma_o = 2[2 + (1 + k_o R^{-\frac{1}{2}})^{-2} + 3(1 + k_o R^{-\frac{1}{2}})^{-4}]^{-1} \tag{42}$$

COMMENTS:

- The K-fracture model is a two parameter model, namely σ_o and d_o (or k_o).
- Values of d_o are determined for individual test data from Eq. (38).
- Values of k_o are determined through error analysis to best fit the experimental data.
- Linear regression technique can be applied for the case of $K_T^\infty = 3.0$.
- This model could also be extended to the WN "average-stress" criterion. However, it requires numerical integration of the stress distribution.
- This model could also be extended to laminates containing cracks, see discussion on PWG-fracture model.
- Experimental results obtained by Karlak [6] indicated a parabolic relationship between d_o and hole radius, Figure 29. This relationship was applied to Whitney-Kim data [31] and resulted in an excellent agreement, Figure 30.
- Comparison between notched strength data and prediction shows excellent agreement, Figure 31, also for the cases in which the characteristic dimension is relatively independent of hole radius, Figure 32.

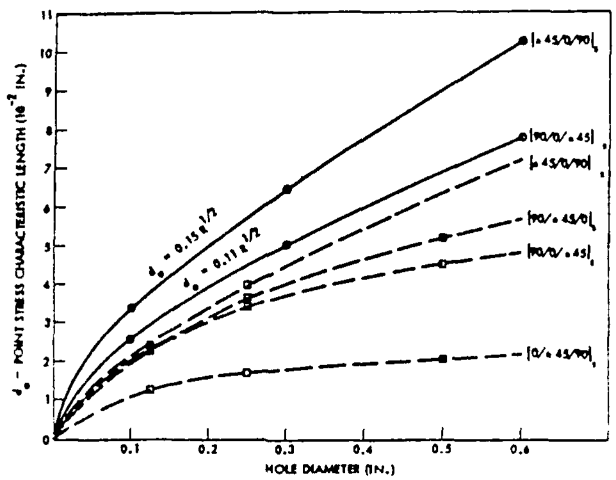

Figure 29. Tentative plot of point-stress characteristic lengths versus hole diameter [6].

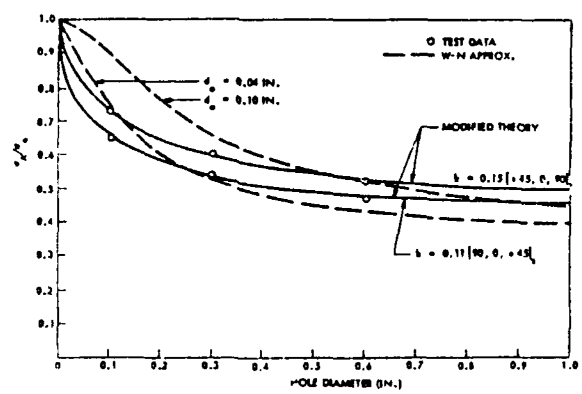

Figure 30. Comparison of original Whitney-Kim notched strength ratio based on constant point-stress characteristic length (dashed curves) and modification proposed here (solid curves) [6].

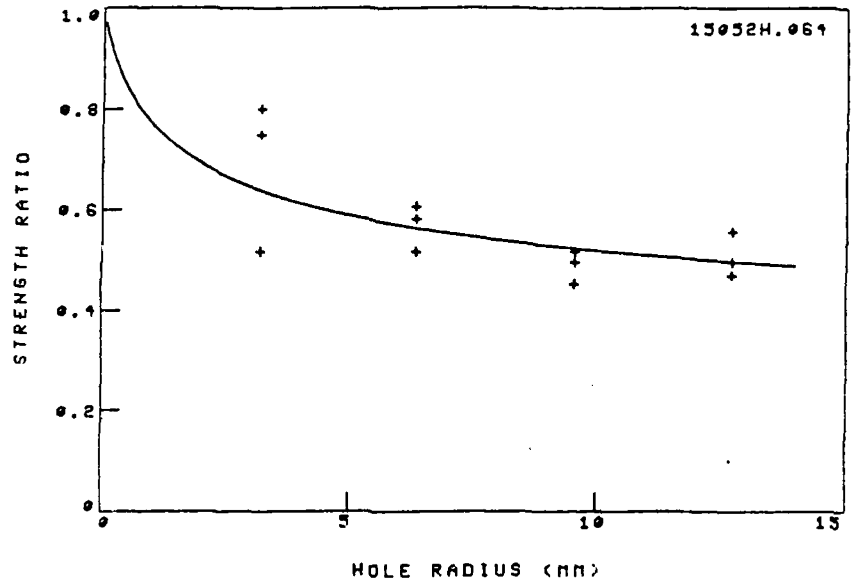

Figure 31. Comparison between experiments and prediction (K-fracture model) for graphite/epoxy $[0_2/\pm 45]_s$ laminate (k_o = 0.75).

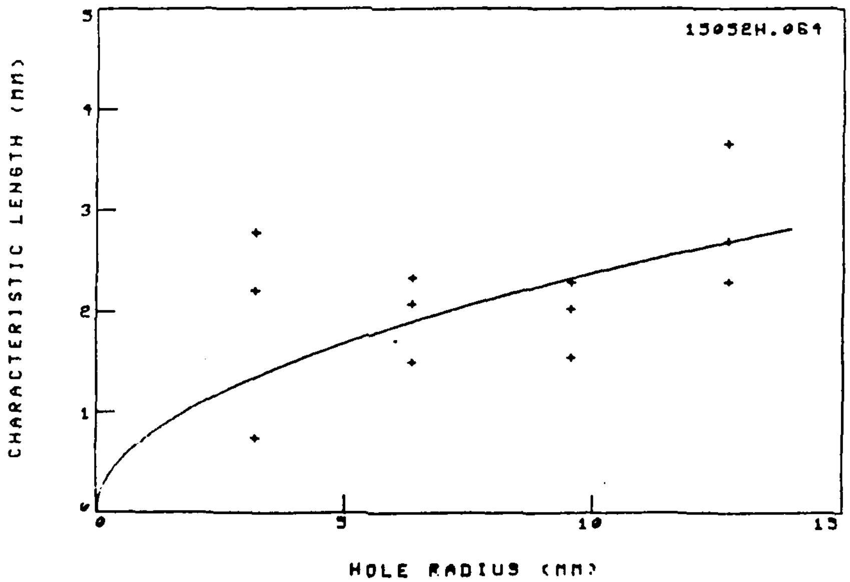

Figure 32. Characteristic distance, d_o, versus hole radius (K-fracture model) for graphite/epoxy $[0/\pm 45]_s$ laminate (k_o = 0.75).

PWG-FRACTURE MODEL

(CIRCULAR HOLE)

I. INTRODUCTION

- Modified WN-"point-stress" criterion for laminates containing circular holes ($K_T \neq 3.0$).
- It is assumed that the characteristic distance, d_o, depends on hole radius.
- An exponential relationship between d_o and hole radius is assumed.
- Notched strength-radius superposition principal is proposed which allows superposition of all laminates and materials onto a single master curve.
- For this purpose two radius shift parameters are defined which depend on the notch sensitivity of the subject laminate.
- Relative notch sensitivity is discussed.

II. NOTCHED STRENGTH PREDICTIONS:

Rewriting Eq. (15):

$$\sigma_y/\sigma^\infty = (1/2)\ \{2 + (R/x)^2 + 3(R/x)^4 - (K_T^\infty - 3)[5(R/x)^6 - 7(R/x)^8]\} \tag{43}$$

where

$$K_T^\infty = 1 + \{2[(E_y/E_x)^{1/2} - \nu_{yx} + E_y/G_{yx}\}^{1/2} \tag{44}$$

Assumption:

$$d_o \propto R^m \tag{45}$$

Introducing a notch sensitivity factor, C:

(46) $d_o = (R/R_o)^m/C$ R_o...reference notch radius introduced so that (R/R_o) is nondimensional.

Using the "point-stress" criterion, Eq. (13), together with Eqs. (43) and (46):

(47) $\sigma_N^\infty/\sigma_o = 2\,\{2 + (\lambda)^2 + 3(\lambda)^4 - (K_T^\infty-3)[5(\lambda)^6 - 7(\lambda)^8]\}^{-1}$

where

(48) $\lambda = [1 + R^{m-1}\,R_o^{-m}\,C^{-1}]^{-1}$

and R_o is a reference notch radius, for algebraic simplicity chosen equal to 1.0 in. Thus, PWG-fracture model is a three-parameter model (σ_o, C, m).

III. EFFECT OF PARAMETERS ON NOTCH SENSITIVITY:

- The higher the value of C, the more notch sensitive the material, Figure 33:
  - $C \to 0$: notch insensitivity
  - $C \to \infty$: $\sigma_N^\infty/\sigma_o = 1/K_T^\infty$

  for other values of m different notch sensitivity curves will be obtained.

- The exponential parameter is bounded between $0 < m < 1$, Figure 34:
  - $m = 0$: WN "point-stress" criterion is recovered
  - $m = 1$: notched strength is independent of hole radius
  - $R > 1.0$: notch sensitivity decreases with increasing radius (for $C = 10\ in^{-1}$). Therefore: PWG-fracture model is applicable for $R \leq 1.0$ inch. However: increasing C will shift the cross-over point to the right.

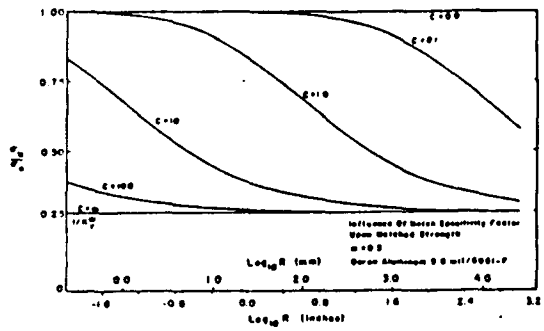

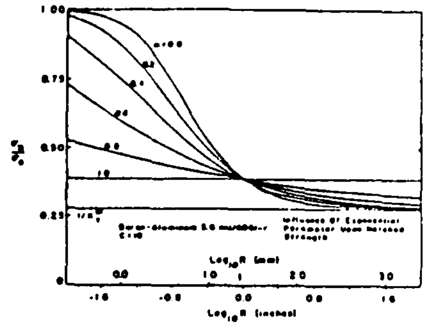

Figure 33. Influence of notch sensitivity factor upon notched strength [7].

Figure 34. Influence of exponential parameter upon notched strength [7].

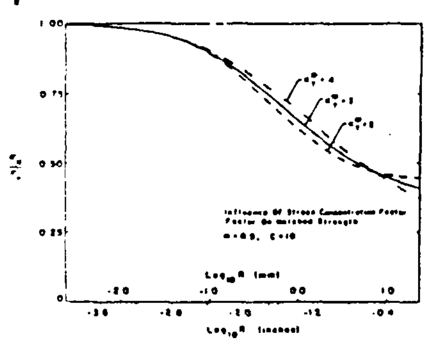

Figure 35. Influence of stress concentration factor on notched strength [7].

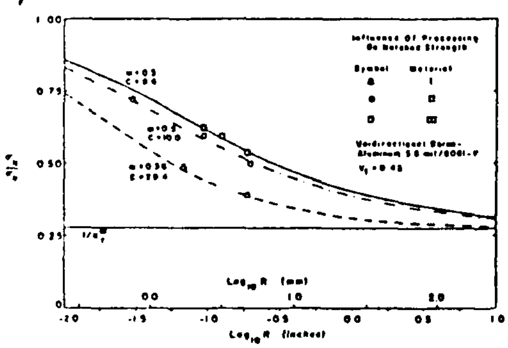

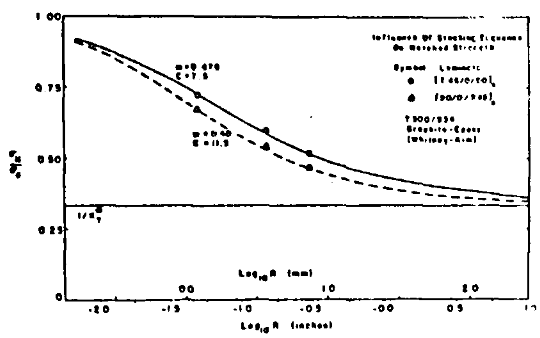

Figure 36. Influence of processing on notched strength [7].

Figure 37. Influence of stacking sequence on notched strength [7] (data taken from [31]).

- The stress concentration factor, K_T^∞, affects notch sensitivity, Figure 35:

  - K_T^∞ ranges in most cases between $2.0 < K_T^\infty < 6.0$

  - For $R < 1.0$ in, $K_T^\infty = 3.0$ (isotropic) is a good approximation (for $C = 10\ \text{in}^{-1}$ and $m = 0.5$).

- COMMENT: Note that the parameters C, m, and K_T^∞ are coupled. Consequently, the actual values of these parameters for a given set of notched strength data may not necessarily indicate the notch sensitivity of the subject material. A relative notch sensitivity parameter has been introduced, see Section V. Excellent agreement between prediction and experiments has been established by PWG [7], Figure 36 and 37. Similar data, Figures 38 and 39, also show very good agreement.

IV. NOTCHED STRENGTH-RADIUS SUPERPOSITION METHOD:

- To superimpose all notched strength data onto a single master curve which is defined by preselected values of C^* and m^*.

- For this purpose a radius shift parameter, a_{cm}, is defined as follows:

  A necessary and sufficient condition for the superposition of a point on the notched strength curve defined by C and m to a new point on a curve defined by C^* and m^* is that: $\lambda^* = \lambda$, i.e.

(48) $$(R^*)^{m^*-1} (R_o)^{-m^*} (C^*)^{-1} = (R)^{m-1} (R_o)^{-m} (C)^{-1}$$

Solving for R^*:

(49) $$R^* = (C^*/C)^{\alpha} (R_o)^{\beta} R^{a_m}$$

where: $\alpha = 1/(m^*-1)$

$\beta = (m^*-m)/(m^*-1)$

$a_m = (m-1)/(m^*-1)$

- Define:

(50) $$a_{cm} = (C^*/C)^{\alpha} (R_o)^{\beta} R^{a_m-1}$$

(51) $$R^* = a_{cm} R$$

R^*..."new" radius on the "master curve" defined by C^* and m^* which are selected arbitrarily.

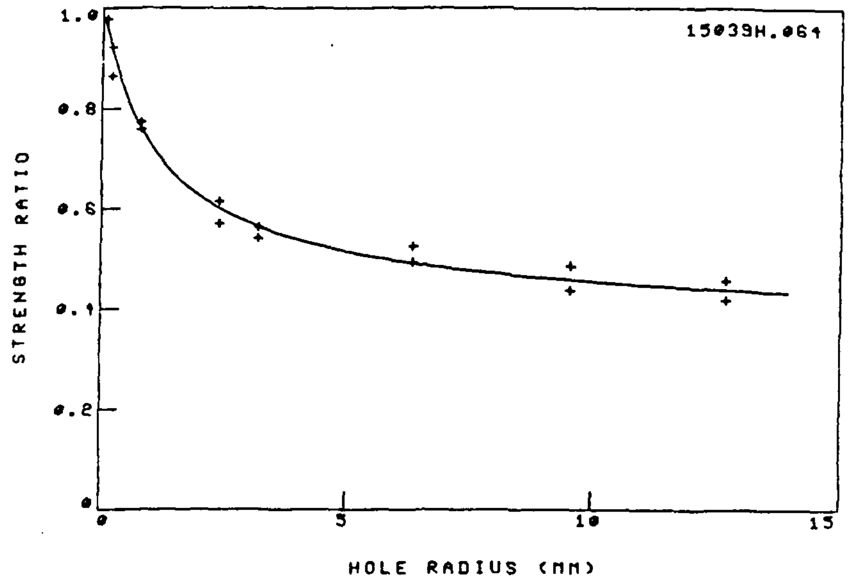

Figure 38. Comparison between experiments and prediction (PWG-fracture model for graphite/epoxy [0/±45/90]$_s$ laminate (m = 0.37, C = 0.45, R_{ns} = 1.43).

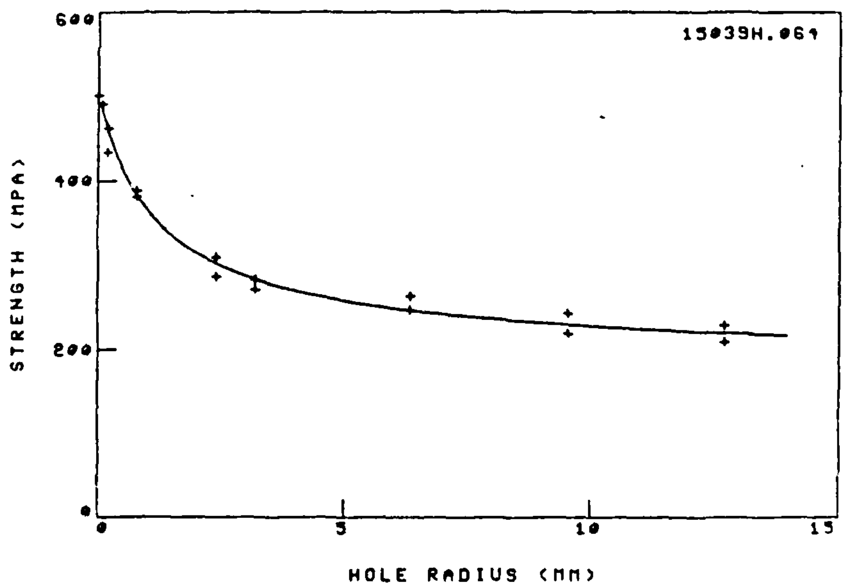

Figure 39. Comparison between experiments and prediction (PWG-fracture model) for graphite/epoxy [0/±45/90]$_s$ laminate (m = 0.37, C = 0.45, R_{ns} = 1.43).

• EFFECT OF PARAMETERS ON RADIUS SHIFT PARAMETER:

(Use $R_o = 1.0$ inch)

a. m = constant, K_T^{∞} = constant, Figure 40:

$\alpha = 1/(m^*-1)$, $\beta = 0$, $a_m = 1$

(52) $$R^* = (C^*/C)^{1/(m^*-1)}\ R$$

(53) $$a_c = (C^*/C)^{1/(m^*-1)} \quad \text{(definition)}$$

(54) $$R^* = a_c R$$

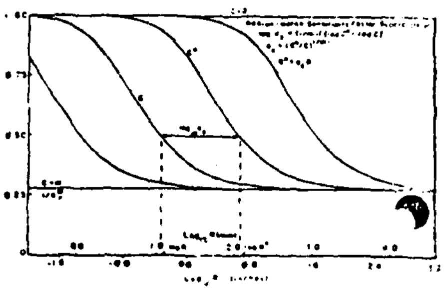

Figure 40. Radius-notch sensitivity factor superposition [8]

b. C = constant, K_T^{∞} = constant, Figure 41:

(55) $$R^* = R^{a_m}$$

(56) $$\mathrm{Log}_{10}\, R^* = a_m \log_{10} R$$

where

(57) $$a_m = (m-1)/(m^*-1)$$

Combining both cases:

(58) $$R^* = a_c R^{a_m}$$

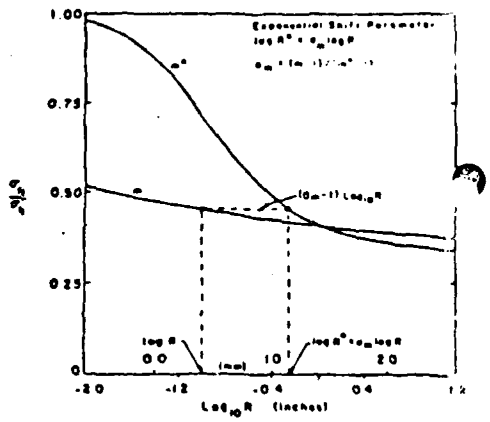

Figure 41: Exponential shift parameter [8].

Using the two radius shift parameters a_c and a_m a single σ_N^{∞} - R curve can be constructed for all laminate configurations and material system (providing they all have the same K_T^{∞}), e.g. Figures 42-43 and Table 1.

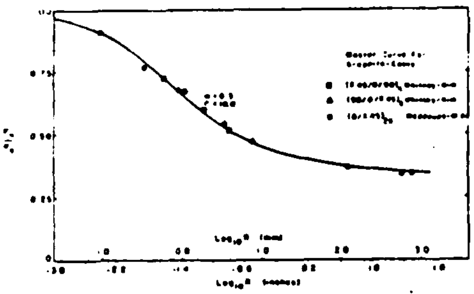

Figure 42. Master curve for graphite/epoxy [8]. Data taken from Ref. [3,31].

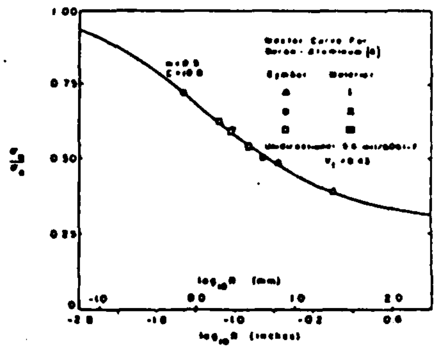

Figure 43. Master curve for boron/aluminum [8].

Data in Figures 42 and 43 are taken from Figures 36 and 37, respectively.

Table 1. Material Superposition Parameters [8]

Material	m	C $[\text{in.}^{-1}]$	a_m	a_c	K_T^{∞}
B/Al I $[0]_6$	0.36	29.4	1.28	8.64	3.607
B/Al II $[0]_6$	0.50	10.0	1.00	1.00	3.607
B/Al III $[0]_6$	0.50	8.6	1.00	0.74	3.607
T300/934 $[\pm45/0/90]_s$	0.48	7.5	1.04	0.56	3.000
T300/934 $[90/0/\pm45]_s$	0.40	11.5	1.20	1.32	3.000
Morganite II/4617 $[0/\pm45]_{2s}$	0.15	40.0	1.70	16.00	2.943

c. m = constant, C = constant (K_T is variable):

To superimpose all laminates of different orthotropy into a single master curve which correspond to $K_T^{*\infty} = 3.0$

From Eq. (47) for $K_T^{*\infty} = 3.0$

$$\sigma_N^{\infty}/\sigma_o = 2\{2 + \lambda^{*2} + 3\lambda^{*4}\}^{-1} \qquad \lambda^* \text{ (i.e. } R^*\text{) for } K_T^{*\infty} = 3.0 \tag{59}$$

$$(3\lambda^*)^4 + (\lambda^*)^2 + 2(1 - 1/S) = 0 \qquad \sigma_N^{\infty}/\sigma_o = S \tag{60}$$

$$\lambda^{*2} = \{-1 + [1 - 24(S-1)/S]^{1/2}\}/6 \tag{61}$$

Solving Eqs. (59) and (61) for R^*:

$$R^* = C^{1/(m-1)} \{[(-1 + \{1 + 24(1-S)/S\}^{1/2})/6]^{-1/2} - 1\}^{1/(m-1)} \tag{62}$$

Consequently, the strength data of any laminate configuration and material system can be superimposed into a common master curve of $K_T^{*\infty} = 3.0$ and having arbitrarily preselected values of C^* and m^*, Figure 44.

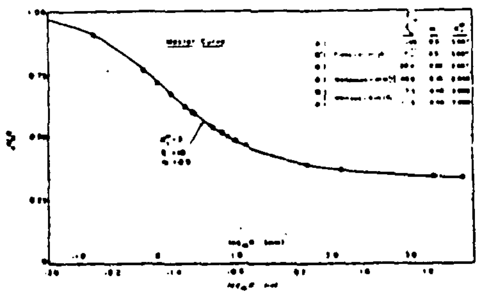

Figure 44. Master curve for all materials [8] (from data shown in Figures 42 and 43).

V. RELATIVE NOTCH SENSITIVITY:

To quantify the degree of relative notch sensitivity of the subject material, Figure 45.

As a reference condition, a notch insensitive material is chosen, i.e. $m^* = 0.0$, $C^* = 1.0 \text{ inch}^{-1}$:

(63) $R_{nS} = \log_{10}R^* - \log_{10}R$ (definition)

Using $R^* = a_{cm}R$ (Eq. (51))

(64) $\log_{10}R^* - \log_{10}R = \log_{10}a_{cm}$

(65) $R_{ns} = \log_{10}a_{cm}$

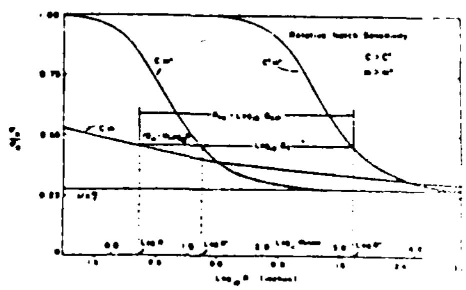

Figure 45 . Relative notch sensitivity parameter [8].

Using Eq. (50) with R = 0.1 inch (for algebraic simplicity), $m^* = 0.0$, $C^* = 1.0 \text{ inch}^{-1}$, $R_o = 1.0$ inch:

(66) $R_{ns} = m + \log_{10}C$

COMMENT: R_{ns} is defined for laminates having the same K_T^∞. When laminates of unequal orthotropy are involved, the degree of notch sensitivity should be determined from Eq. (47).

VI. DATA ANALYSES:

A computer program routine scans through all possible combinations of C and m and chooses the values which result in the smallest error between the expected data and the predictions according to Eq (47). A straight-forward linear regression program can e employed for the special case of laminates containing circular holes and having $K_T^\infty = 3.0$.

Values of the relative notch sensitivity, R_{ns}, for the six material systems discussed previously, Figures 42 and 43, are shown in Table 2 [8]. It should be recalled that R_{ns} is defined for material systems having the same K_T^{∞}, thus a comparison of the elastic notch sensitivity values can be made only among the three types of boron/aluminum or among the three graphite/epoxy laminates. Comparison between the R_{ns} values of the two material systems is meaningless since they have different K_T^{∞} values.

Table 2. Relative Notch Sensitivity [8]

Material	m	C [in.$^{-1}$]	R_{ns}	K_T^{∞}
B/Al III $[0°]_6$	0.50	8.6	1.43	3.607
B/Al II $[0°]_6$	0.50	10.0	1.50	3.607
B/Al I $[0°]_6$	0.36	29.4	1.83	3.607
T300/934 $[\pm 45/0/90]_s$	0.48	7.5	1.36	3.000
T300/934 $[90/0/\pm 45]_s$	0.40	11.5	1.46	3.000
Morganite II/4617 $[0/\pm 45]_{2s}$	0.15	40.0	1.75	2.943

Notched strength data were compared with prediction and an excellent agreement has been established, Figure 46. The master curve to which all notched strength data were shifted, Figure 46, was selected from Ref. [7], i.e. $m^*=0.5$ and $C^*=1.0$ inch$^{-1}=0.4$ mm^{-1}. Figure 47 shows the master curve defined by $m^*=0.5$, $C^*=0.4$ mm^{-1}, $K_T^{\infty *}=3.0$ and the shifted notched strength data of the different graphite/epoxy laminates containing circular holes which were analyzed in this review.

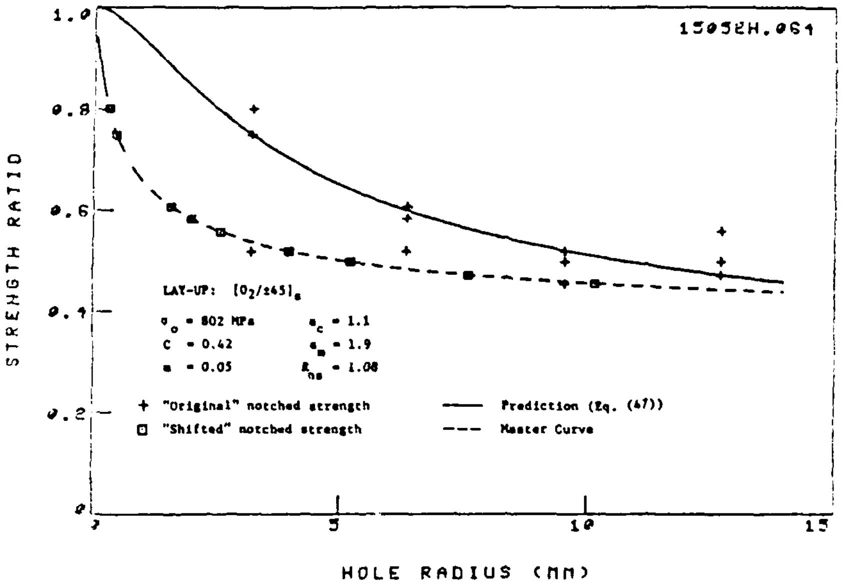

Figure 46. Notched strength versus hole radius predictions and master curve (PWG-fracture model) for graphite/epoxy $[0_2/\pm45]_s$ laminate.

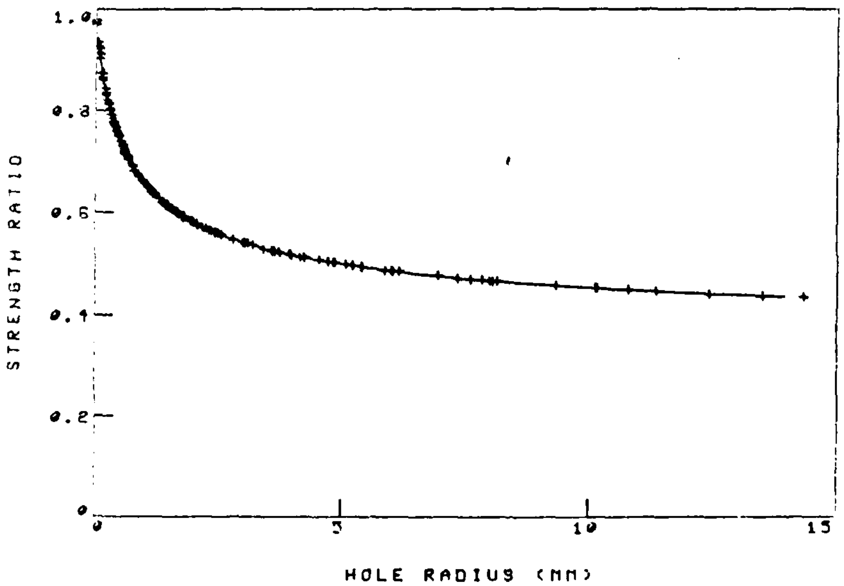

Figure 47. Master curve for all graphite/epoxy laminates containing circular holes.

PWG-FRACTURE MODEL
(STRAIGHT CRACKS)

The subsequent formulation is analogous to that developed by PWG for laminates containing circular holes.

I. NOTCHED STRENGTH PREDICTIONS:

From the exact elasticity solution, Eq. (21)

(67) $\sigma_y/\sigma^{\infty} = x(x^2 - c^2)^{-\frac{1}{2}} \qquad x > c$

Assumption:

(68) $d_o \propto c^m$

Introducing a crack notch sensitivity factor

(69) $d_o = (c/c_o)^m/K \qquad c_o$...reference half-crack length introduced so that (c/c_o) is nondimensional

Using the "point-stress" criterion, Eq. (27), together with Eq. (69)

(70) $\sigma_N^{\infty}/\sigma_o = (1 - \lambda_1^2)^{\frac{1}{2}}$

where

(71) $\lambda_1 = [1 + c^{m-1}\, c_o^{-m}\, K^{-1}]^{-1} \qquad$ (analogous to Eq. (48))

and c_o is a reference half-crack length, for algebraic simplicity chosen equal to 1.0 inch.

Thus, PWG-fracture model is a three-parameter model (σ_o, C, m).

Since:

$$d_o = c^m/K \qquad (72)$$

$$\log_{10} d_o = m \log_{10} c - \log_{10} K \qquad (73)$$ (see Figure 48)

Using $\sigma_y \Big|_{x=c+d_o} = \sigma_o$ together with Eq. (67):

$$\sigma_N^\infty/\sigma_o = \{1-[c/(c+d_o)]^2\}^{1/2} \qquad (74)$$

Solving for d_o:

$$d_o = c\{[1 - (\sigma_N^\infty/\sigma_o)^2]^{-1/2}-1 \qquad (75)$$

The values of K and m can be obtained by a least squares fit of the data. These can be used to predict the notched strength. From Eqs. (72) and (74):

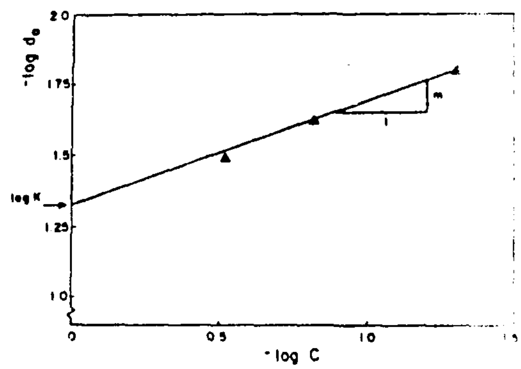

Figure 48. Relations between characteristic dimensions and the notch size for T300/934 $[90/0/\pm 45]_s$ [9]. (Data taken from [31]).

$$\sigma_N^\infty/\sigma_o = \{1 - (1 + c^{m-1} K^{-1})^{-2}\}^{1/2} \qquad (76)$$

The values of $K = 19.0$ inch^{-1} and $m = 0.4$ fit the data best, Figure 49.

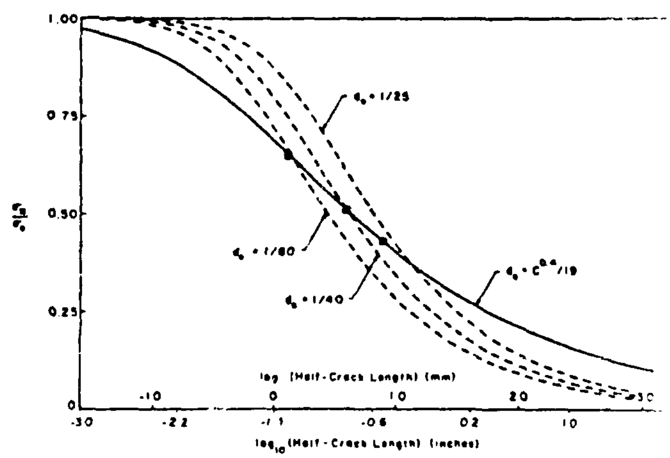

Figure 49. Inappropriateness of a constant characteristic dimension for the graphite/epoxy T300/934 $[90/0/\pm 45]_s$ material system [9]. (Data taken from Ref. [31].)

II. EFFECT OF PARAMETERS ON NOTCH SENSITIVITY:

- The higher the value of K, the more notch sensitive the material, Figure 50.

$K \rightarrow 0$: notch insensitivity

$K \rightarrow \infty$: zero strength of any finite cracks.

For other values of m, different notch sensitivity curves will be obtained.

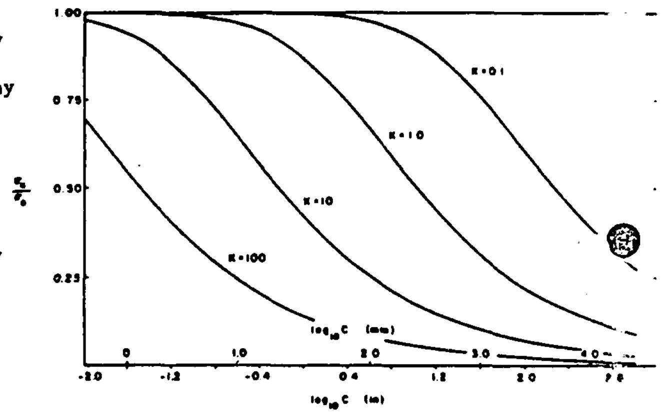

Figure 50. Influence of the constant K on the notched strength: m = 0.2 [9].

- The exponential parameter is bounded between $0 < m < 1$

$m = 0$: WN "point-stress" criterion is recovered

$m = 1$: notched strength is independent of crack length.

$c > 1.0$: notch sensitivity decreases with in- increasing crack length (for K=10).

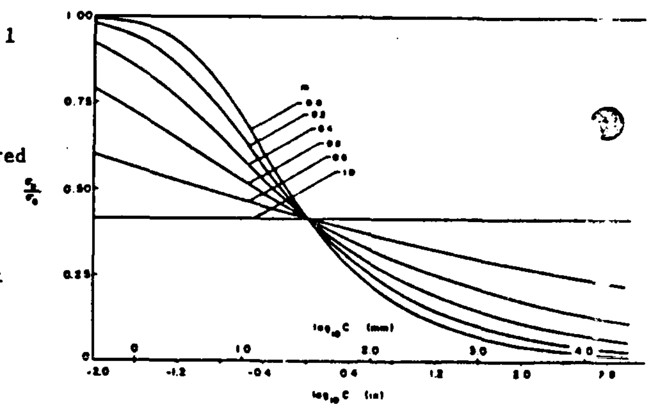

Figure 51. Influence of the constant m on the notched strength: K = 10 [9].

The higher the value of K the larger the crack length for which the cross-over occurs, Figure 51.

Notch sensitivity curves in linear scales are shown in Figures 52 and 53.

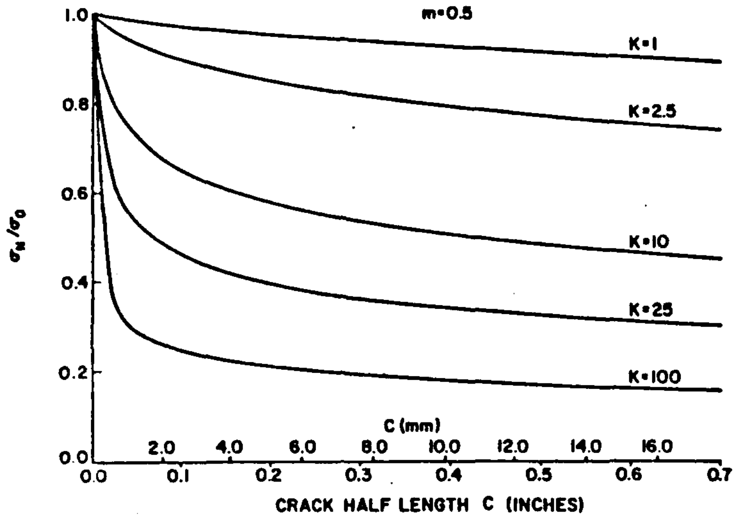

Figure 52. Effect of K on notched strength [32].

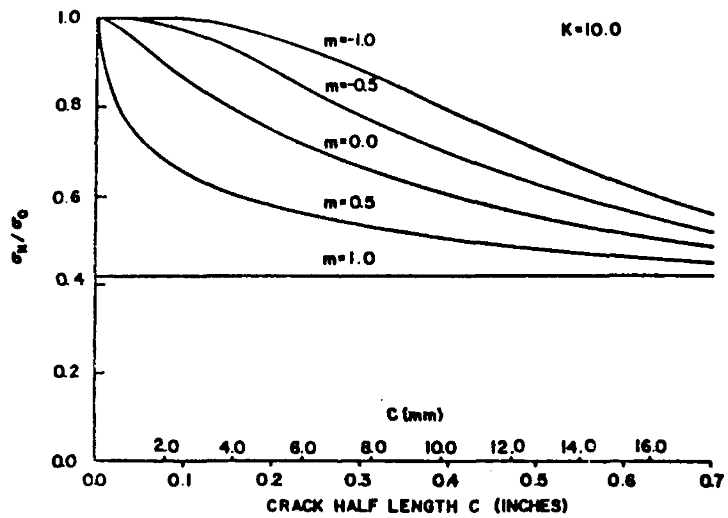

Figure 53. Effect of m on notched strength [32].

Comparisons between experiments and predictions indicate very good agreement for the case in which the characteristic dimension d_o is independent of crack length, Figures 54 and 55. Excellent agreement is also established however when d_o does depend on crack length, Figures 56 and 57.

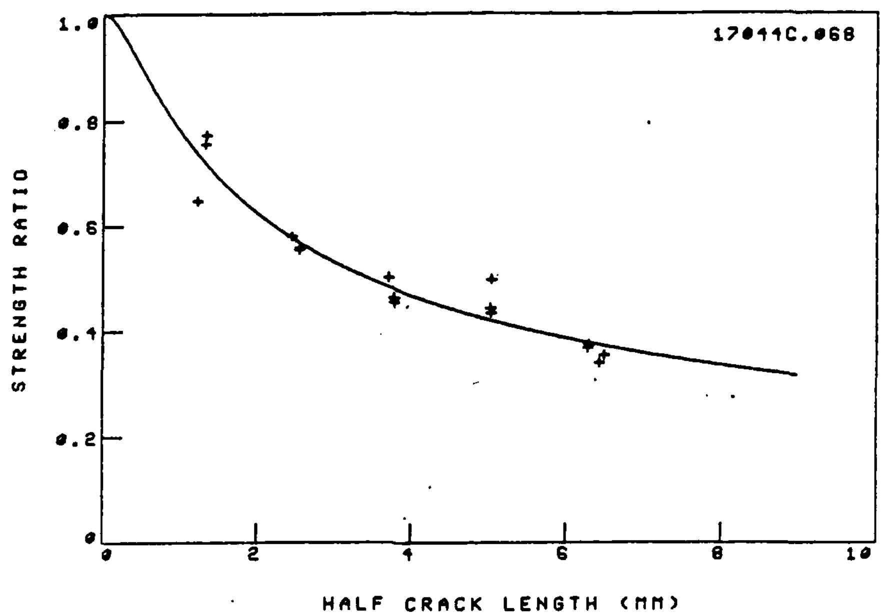

Figure 54. Comparison between experiments and prediction (PWG-fracture model) for graphite/epoxy $[0/90/\pm45]_s$ laminate (m = -0.1, K = 2.30, R_{ns} = 46.6).

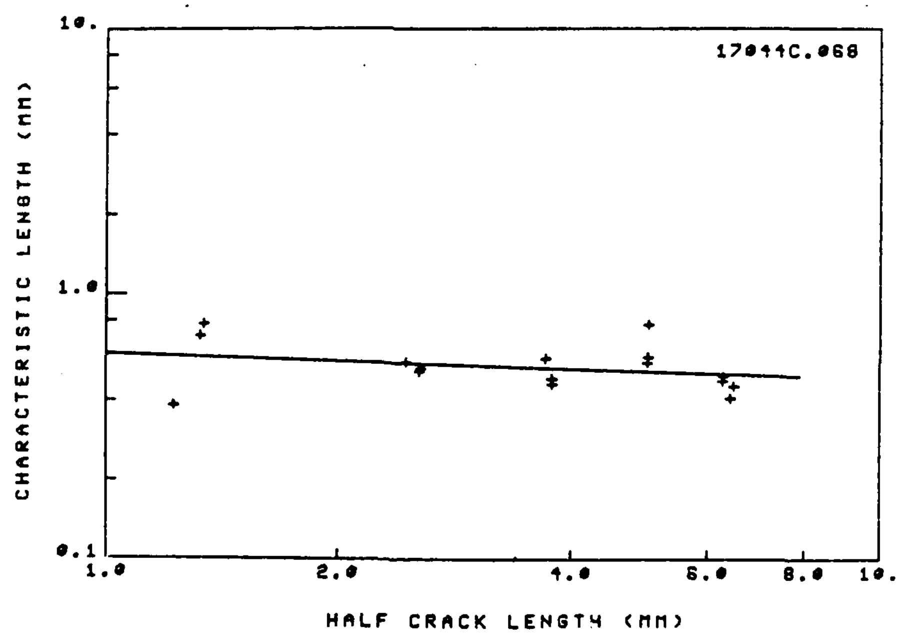

Figure 55. Characteristic dimensions (PWG-fracture model) as a function of half crack length for graphite/epoxy $[0/90/\pm45]_s$ laminate (m = -0.1, K = 2.30, R_{ns} = 46.6).

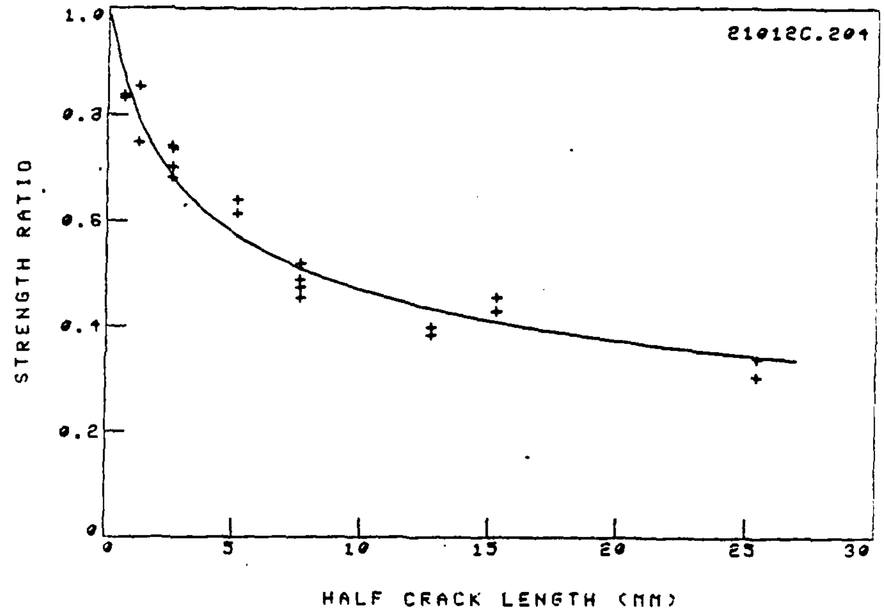

Figure 56. Comparison between experiments and prediction (PWG-fracture model) for boron/aluminum $[0/\pm45]_s$ laminate ($m = 0.23$, $K = 0.62$, $\hat{a}_{Km} = 26.9$).

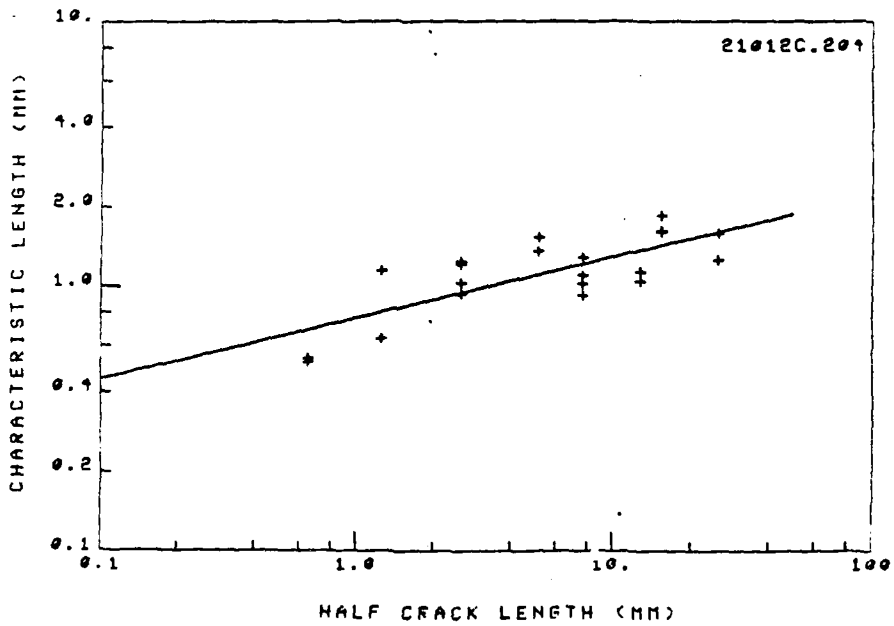

Figure 57. Characteristic dimension (PWG-fracture model) as a function of half crack length for boron/aluminum $[0/\pm45]_s$ laminate ($m = 0.23$, $K = 0.62$, $\hat{a}_{Km} = 26.9$).

COMMENT: Note that the parameters K and m are coupled. Consequently, the actual values of these parameters for a given set of notched strength data may not necessarily indicate the notch sensitivity of the subject material. A relative notch sensitivity parameter has been introduced.

III. NOTCHED STRENGTH - CRACK LENGTH SUPERPOSITION METHOD:

- To superimpose all notched strength data onto a single master curve which is defined by preselected values of K^* and m^*.

- For this purpose a crack length shift parameter, a_{Km}, is defined as follows:

A necessary and sufficient condition for superposition of a point on the notched strength curve defined by K and m to a new point on a curve defined by K^* and m^* is that: $\underline{\lambda_1^* = \lambda_1}$, i.e.

(77) $$(c^*)^{(m^*-1)} (c_o)^{-m^*} (K^*)^{-1} = (c)^{(m-1)} (c_o)^{-m} (K)^{-1}$$

solving for c^*:

(78) $$c^* = (K^*/K)^{\alpha} (c_o)^{\beta} (c)^{a_m}$$

where: $\alpha = 1/(m^*-1)$

$\beta = (m^*-m)/(m^*-1)$

$a_m = (m-1)/(m^*-1)$

Define:

(79) $$a_{Km} = (K^*/K)^{\alpha} (c_o)^{\beta} (c)^{a_m-1}$$

(80) $$c^* = a_{Km} c$$

c*..."new"half-crack length on the master curve defined by K^* and m^* which are selected arbitrarily.

. EFFECT OF PARAMETERS ON CRACK LENGTH SHIFT PARAMETER:

(Use c_o = 1.0 inch)

a. K = constant, Figure 58:

(81) $c' = c^{(m-1)/(m^*-1)}$

(82) $c' = c^{a_m}$

b. m = constant, Figure 58:

(83) $c^* = a_K c'$

(84) $a_K = (K^*/K)^{1/(m^*-1)}$

Combining Eqs. (82) and (83):

(85) $c^* = a_K c^{a_m}$

Analogous to the procedure shown for laminates containing circular holes.

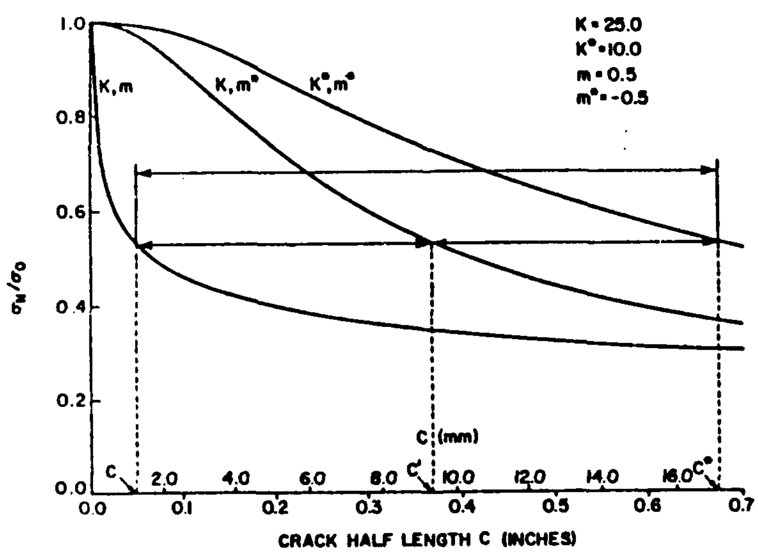

Figure 58. Superposition principle for composite material system [32].

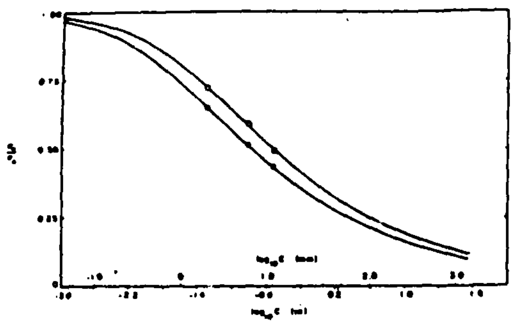

Figure 59. Data for graphite-epoxy T300/934 system: □ , $[\pm45/0/90]_s$, m=0.4, K=13.5; o, $[90/0/\pm45]_s$, m=0.4, K=19.0 [9] (data taken from Ref. [31]).

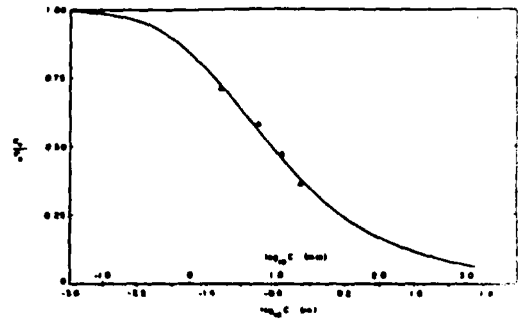

Figure 60. Data for glass-epoxy Scotchply 1002 material system: Δ, $[0/\pm45/90]_{2s}$, m=0.2, K=22.0 [9] (data taken from Ref. [53]).

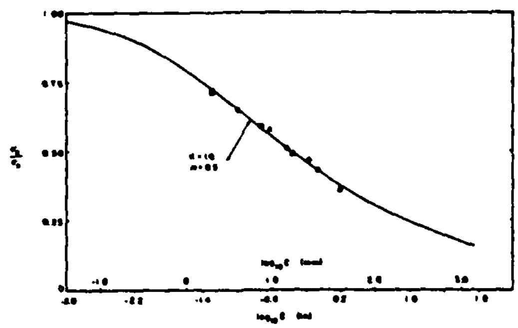

Figure 61. Slit notch master curve (-): □ , T300/934, $[\pm45/0/90]_s$, m=0.4, K=13.5; o, T300/934 $[90/0/\pm45]_s$, m=0.4, K=19.0; Δ, Scotchply 1002, $[0/\pm45/90]_{2s}$, m=0.2, K=22.0

PWG [9] analyzed notched strength data of graphite/epoxy and glass epoxy as shown in Figures 59 and 60, respectively. Using Eq. (79), the data for all three laminates were superimposed into a single master curve with pre-selected m*=0.5 and K*= 10 inch^{-1}, Figure 61, and an excellent agreement has been established.

Similarly, the "original" notched strength data of unidirectional boron/aluminum can be shifted to a pre-selected master curve (m*=0.5, K*= 10 inch^{-1}), Figure 62. The restuls of shifting the notched strength data of all boron/aluminum laminates containing straight cracks are shown in Figure 63.

IV. RELATIVE NOTCH SENSITIVITY

- To quantify the degree of notch sensitivity of the subject material, Figure 58.

- As a reference condition, a notch insensitive material is chosen, i.e. $m^* = 0.0$, $K^* = 1.0$ inch^{-1}:

- The relative notch sensitivity is obtained by calculating the crack length shift a_{Km} for a reference half-crack length of 0.1 inch.

(86) $\hat{a}_{Km} = a_{Km}$ ($m^* = 0.0$, $K^* = 1.0$ inch^{-1}, $c = 0.1$ inch, $c_o = 1.0$ inch)

Substituting Eq. (86) into Eq. (79) yields:

(87) $R_{ns} = \log_{10} \hat{a}_{Km} = m + \log_{10} K$ (analogous to Eq. (66))

Values of $\hat{a}_{Km}$ for the three material systems analyzed in Figures 59-60 are listed in Table 3.

Table 3: Generalized Notch Sensitivity Factor [9].

Material	Reference	m	K	$\hat{a}_{Km}$
Graphite/Epoxy T300/934 $[\pm45/0/90]_s$	31	0.4	13.5	33.9
Graphite/Epoxy T300/934 $[90/0/\pm45]_s$	31	0.4	19.0	47.7
Glass/Epoxy Scotchply 1002 $[0/\pm45/90]_{2s}$	5	0.2	22.0	34.9

V. DATA ANALYSES

A straightforward linear regression program can be employed from which the least squares fit of K and m is determined by using Eq. (73). The scatter in results is then illustrated as shown in Figures 55 and 57.

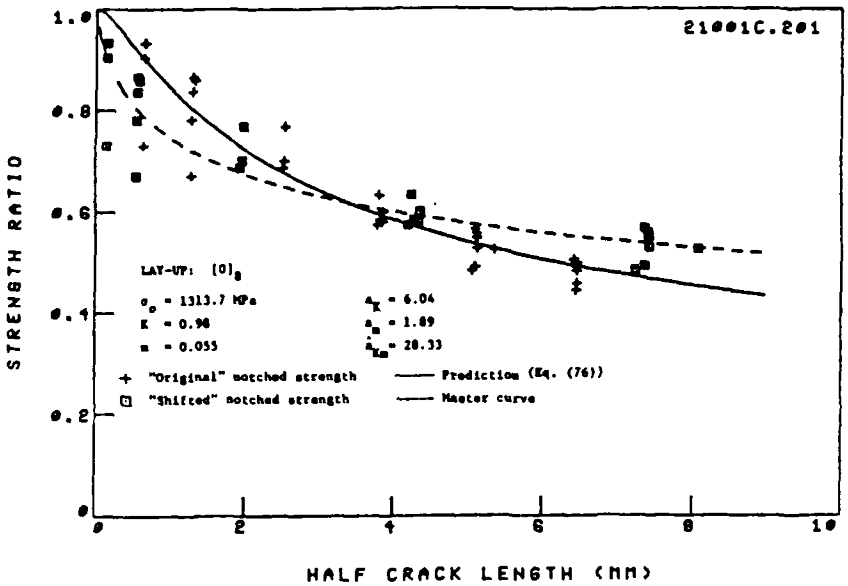

Figure 62. Notched strength versus crack length prediction and master curve (PWG-fracture model) for boron/aluminum $[0]_8$ laminate.

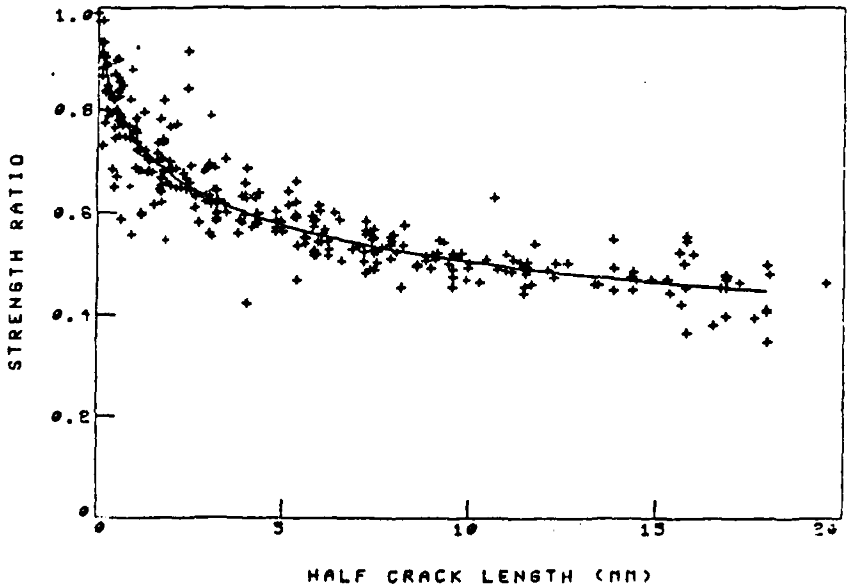

Figure 63. Master curve for all boron/aluminum laminates containing straight cracks.

MODIFIED PWG-FRACTURE MODEL

I. STRAIGHT CRACKS:

- To determine the threshold of notch sensitivity, i.e. the case in which the set of notched strength data results in $m < 0$.

- A new parameter is introduced, c_i^*, which represents the largest half-crack length for which no reduction in strength is noticeable, i.e. c_i^* is defined as the critical notch insensitive half-crack length.

(88) $c_c = c - c_i \qquad c > c_i$ $\qquad c_i$...notch insensitive half-crack length

c_c...corrected half crack length

Replacing c in Eq. (76) by c_c:

(89) $\sigma_N^\infty/\sigma_o = \{1 - (1 + c_c^{m-1}\,K^{-1})^{-2}\}^{\frac{1}{2}}$

i.e. shifting the σ_N^∞/σ_o versus c curve along the abscissa from $c = 0.0$ to $c = c_i$.

- Determine the combination of K, m, and c_i which results in the minimum least squares error between experiments and prediction (Eq. (89)). These values are defined as K_i^*, m_i^*, and c_k^*, Figure 64. The variations of K and m with c_i are shown in Figures 65 and 66, respectively. The values of K_i^* and m_i^* are based on the value of c_i^*.

Using the "critical corrected half-crack length" c_c^*:

(90) $c_c^* = c - c_i^* \qquad c > c_i^*$

to redefine the characteristic dimensions in terms of the critical parameters K_i^*, m_i^*, and c_c^*:

(91) $d_o^* = (c_c^*)^{m_i^*}/K_i^* \qquad c > c_i^*$ $\qquad$ analogous to Eq. (72)

$d_o = 0 \qquad c \leqslant c_i^*$

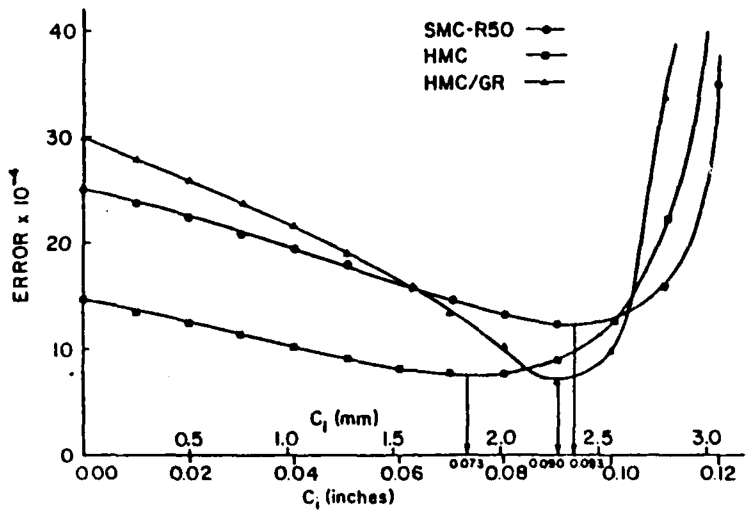

Figure 64. Error as a function of notch insensitive crack half length [32].

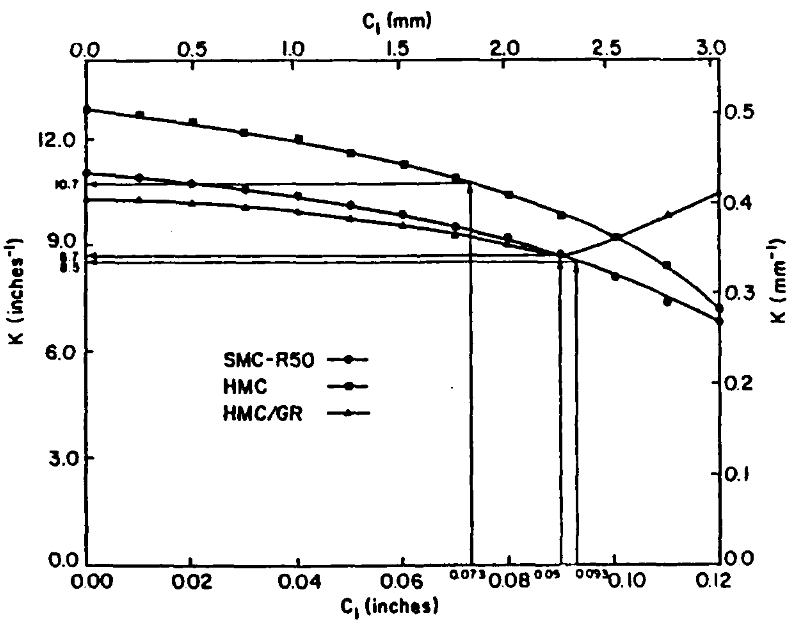

Figure 65. Crack notch sensitivity factor as a function of notch insensitive crack half length [32].

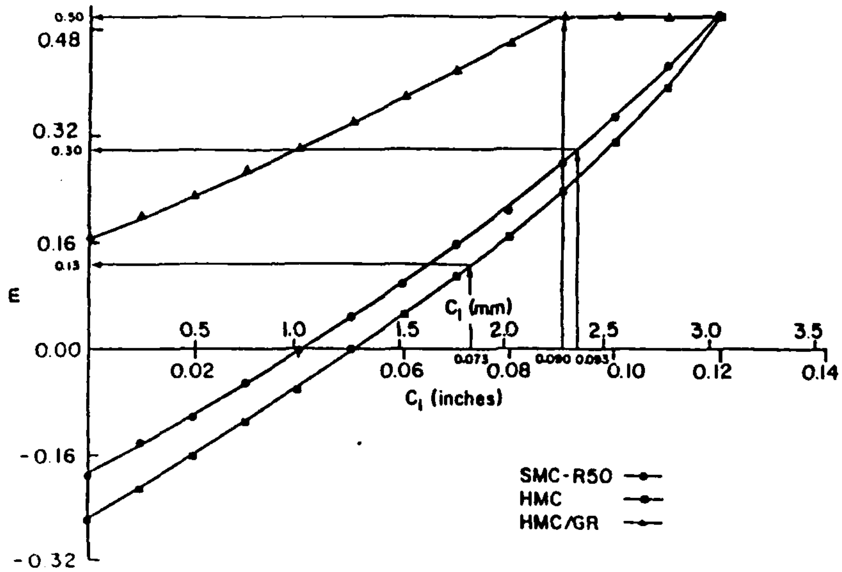

Figure 66. Exponential parameter as a function of notch insensitive crack half length [32].

Replacing K, m, and c_c in Eq. (89) by K_i^*, m_i^*, and c_c^*, respectively:

(92) $$\sigma_N^\infty/\sigma_o = \{1 - (1 + c_c^{*(m_i^*-1)} K_i^{*-1})^{-2}\}^{\frac{1}{2}} \qquad c > c_i^*$$

$$\sigma_N^\infty/\sigma_o = 1.0 \qquad c \leq c_i^*$$

analogous to Eq. (76)

- m_i^* is now always positive
- d_o^* increases with increasing half-crack length
- comparison between experiments and predictions is shown in Figures 67 and 68.
- The modification enables the determination of the size of the notch insensitive region.

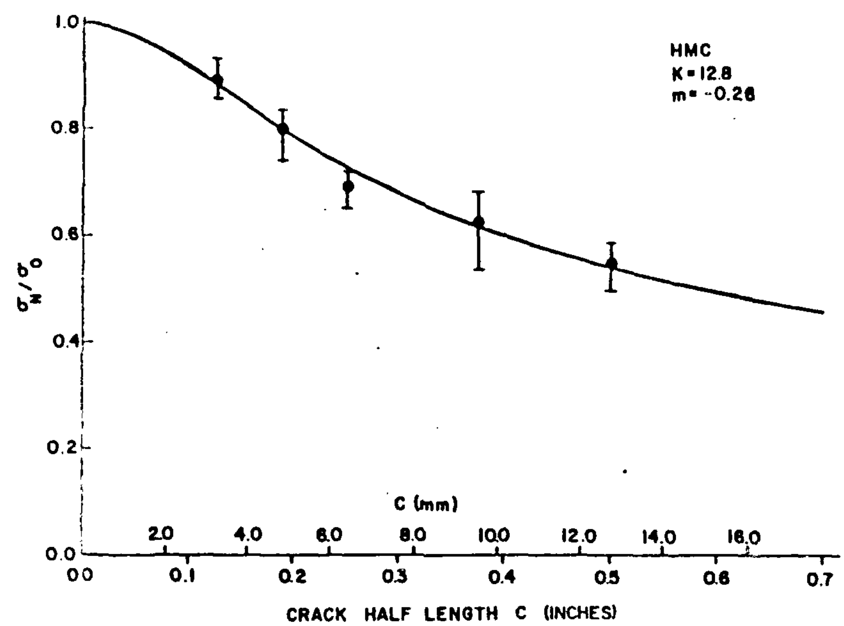

Figure 67. Notched strength of HMC as a function of crack half length [32].

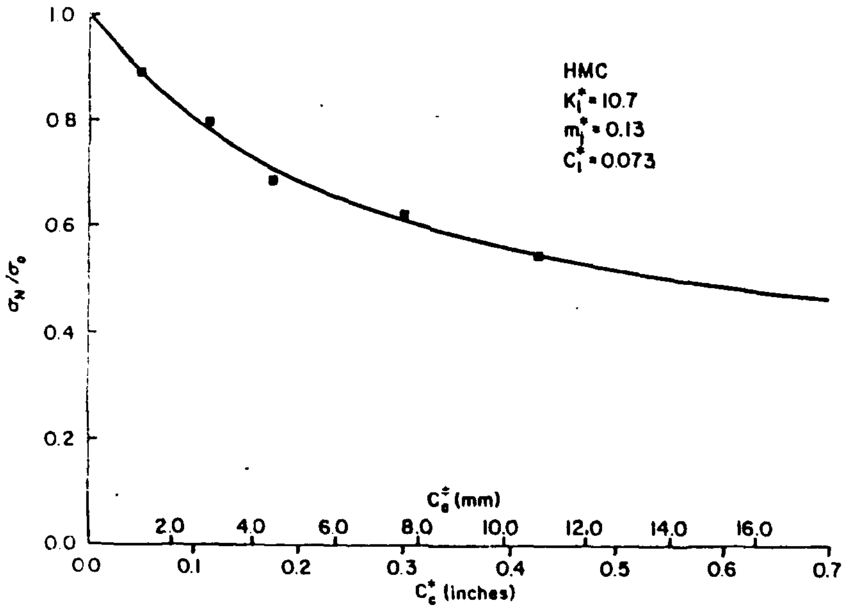

Figure 68. Notched strength of HMC as a function of critical corrected crack half length [32].

- PWG and WN fracture models do not account for a notch insensitive region (σ_N^∞/σ_o = 1.0 at c = 0.0)

- Modified PWG-fracture model does account for a notch insensitive region (σ_N^∞/σ_o = 1.0 at c = c_i^*), i.e. the σ_N^∞/σ_o axis is shifted to c_i^*. The values of K_i^* and m_i^* are calculated after eliminating the notch insensitive region.

- The modified PWG-fracture model is also applicable for the cases of m > 0, Figure 69.

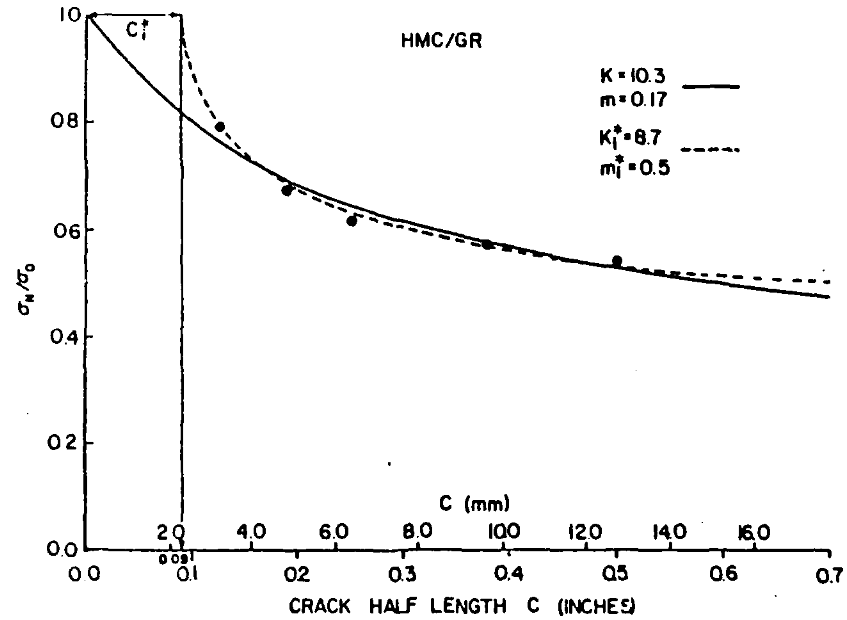

Figure 69. Notched strength of HMG/graphite as a function of crack half length for two values of K and m [32].

- The relative notch sensitivity factor becomes (see Eq. (87))

$$R^*_{nsi} = m^*_i + \log_{10} K^*_i \tag{93}$$

where the superposition method is applied in a similar manner to that previously described. However, the crack length shift would be applied from the K^*_i, m^*_i curve to the master curve of K^*, m^*, rather than from the initial K, m curve.

II. CIRCULAR HOLES:

The formulation of the modified PWG-fracture model for laminates containing circular holes is identical to that proposed for laminates containing straight cracks (Eqs. (88) to (93)).

$$R^*_c = R - R^*_i \qquad R > R^*_i \tag{94}$$

R^*_i...critical notch insensitive radius

R^*_c...critical corrected hole radius

$$d^*_o = (R^*_c/R_o)^{m^*_i}/C^*_i \qquad R > R^*_i \tag{95}$$

$$d^*_o = 0 \qquad R \leq R^*_i$$

Replacing C, m and R in Eq. (47) by C^*_i, m^*_i, and R^*_c, respectively:

$$\sigma^\infty_N/\sigma_o = 2\{2 + \lambda^2_i + 3\lambda^4_i - (K^\infty_T - 3)[5\lambda^6_i - 7\lambda^8_i]\}^{-1} \qquad R > R^*_i \tag{96}$$

$$\sigma^\infty_N/\sigma_o = 1.0 \qquad R \leq R^*_i$$

where

$$\lambda_i = [1 - (R^*_c)^{m^*_i - 1} (R_o)^{-m^*_i} (C^*_i)^{-1}]^{-1} \tag{97}$$

and:

$$R^*_{nsi} = m^*_i + \log_{10} C^*_i \qquad \text{(similar to that given by Eqs. (66) and (93))} \tag{98}$$

ML-FRACTURE MODEL
(CIRCULAR HOLES AND STRAIGHT CRACKS)

- The LEFM equation applied to homogeneous materials is:

(99) $\sigma_N^{\infty} = K_{IC}\sqrt{\pi c}$

in which the exponential ½ is the order of the mathematical stress singularity at the tip of the crack.

- ML-fracture model proposed that the fracture of composites is governed by:

(100) $\sigma_N = H_C(2c)^{-n}$

H_C...Composite Fracture Toughness [MPa (mm)^n], a property of the subject material

n..."The order of singularity of a crack with its tip at the interface of two different materials"

- The fracture model is based on stress analysis for the case of cracks at the interface of a bimaterial, i.e. matrix and fiber, Figure 70.

- The order of singularity is a function of the ratio of the shear moduli of the matrix and filament, μ_1/μ_2, and the two Poisson's ratios, ν_1 and ν_2, Table 4 [10,11].

From Eq. (100):

(101) $\log_{10}(\sigma_N^{\infty}/\sigma_o) = \log_{10}(H_C/\sigma_o) - n \log_{10}(2c)$

H_C and n are determined from a least squares fit using linear regression and results are plotted on a log $(\sigma_N^{\infty}/\sigma_o)$ versus log(2c/W) or log (2R/W) format, Figure 71.

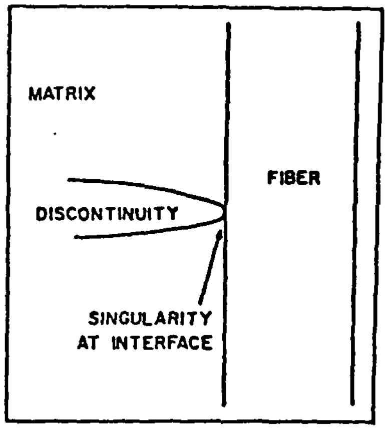

Figure 70. Positioning of discontinuity at matrix/fiber interface [33].

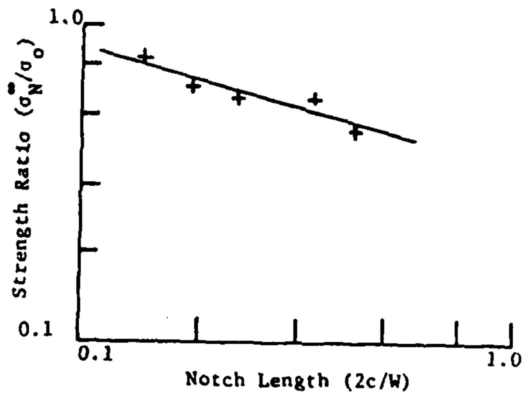

Figure 71. Schematic plot on log-log format of ML - fracture model.

Table 4. Order of Singularity [11]

μ_1/μ_2	ν_1	ν_2	n
0.01	0.30	0.20	0.250
0.01	0.35	0.20	0.269
0.25	0.30	0.15	0.263
0.25	0.30	0.20	0.262
0.25	0.30	0.25	0.261
0.25	0.35	0.20	0.280
0.50	0.30	0.20	0.280
0.50	0.35	0.20	0.297
0.10	0.30	0.20	0.310
0.158	0.30	0.20	0.339
0.20	0.30	0.20	0.357
0.10	0.33	0.20	0.319
0.158	0.33	0.20	0.347
0.20	0.33	0.20	0.364

Comparisons between prediction and experiments in logarithmic and linear scales are shown in Figures 72-73 for graphite/epoxy laminate containing a circular hole and in Figures 74-75 for boron/aluminum laminate containing a straight crack.

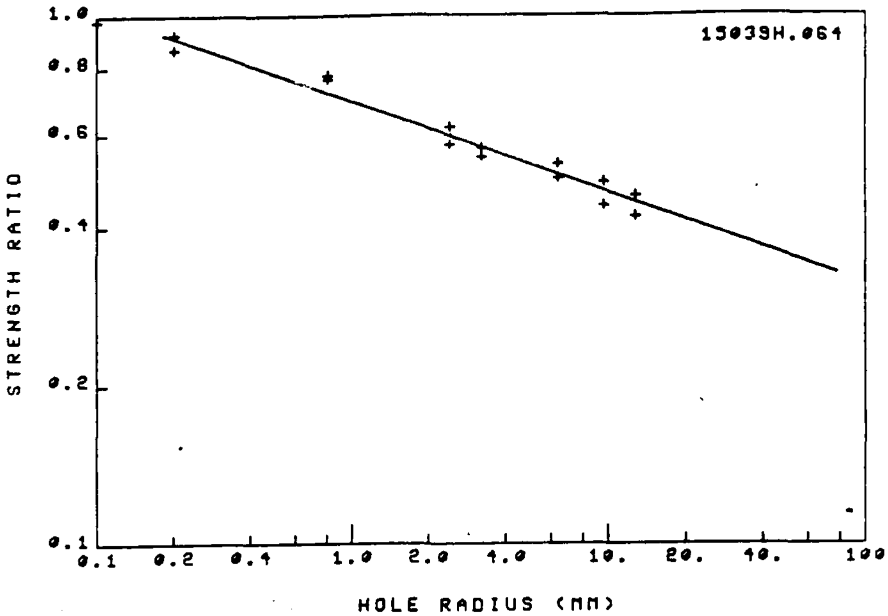

Figure 72. Comparison between experiments and prediction (ML-fracture model) for graphite/epoxy $[0/\pm45/90]_s$ laminate, shown on a logarithmic scale (n = 0.173, H_c/σ_o = 0.775).

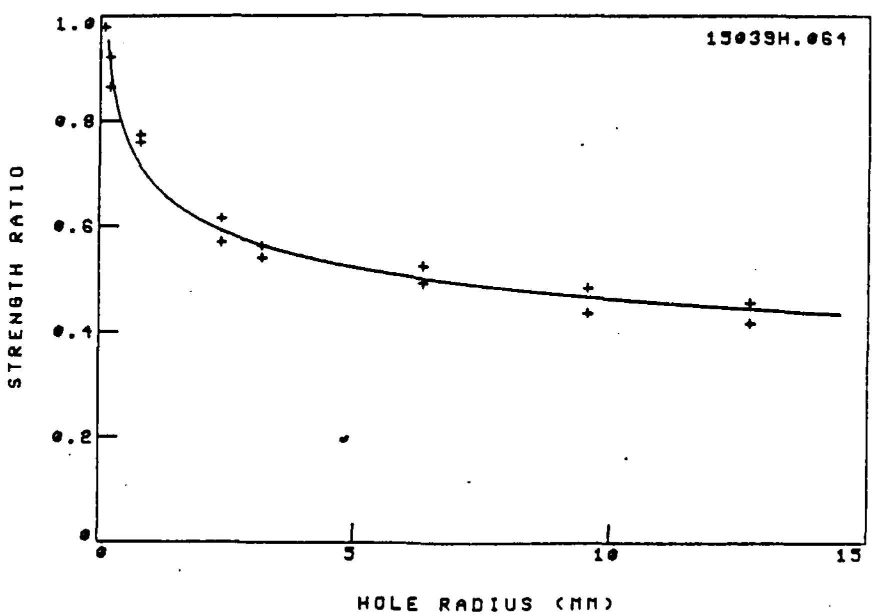

Figure 73. Comparison between experiments and prediction (ML-fracture model) for graphite/epoxy $[0/\pm45/90]_s$ laminate, shown on a linear scale (n = 0.173, H_c/σ_o = 0.775).

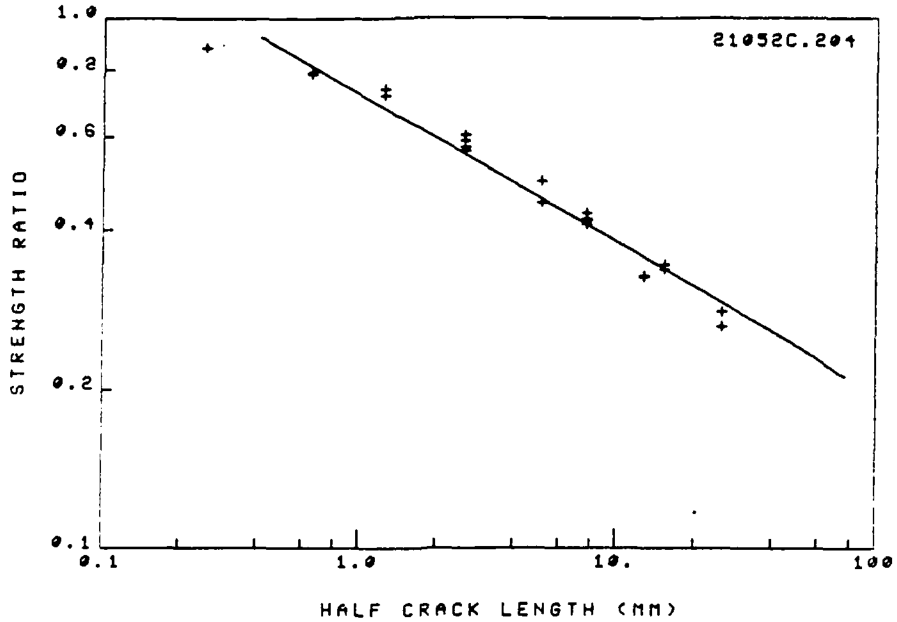

Figure 74. Comparison between experiments and prediction (ML-fracture model) for boron/aluminum $[0_2/\pm45]_s$ laminate, shown on a logarithmic scale ($n = 0.280$, $H_c/\sigma_o = 0.871$).

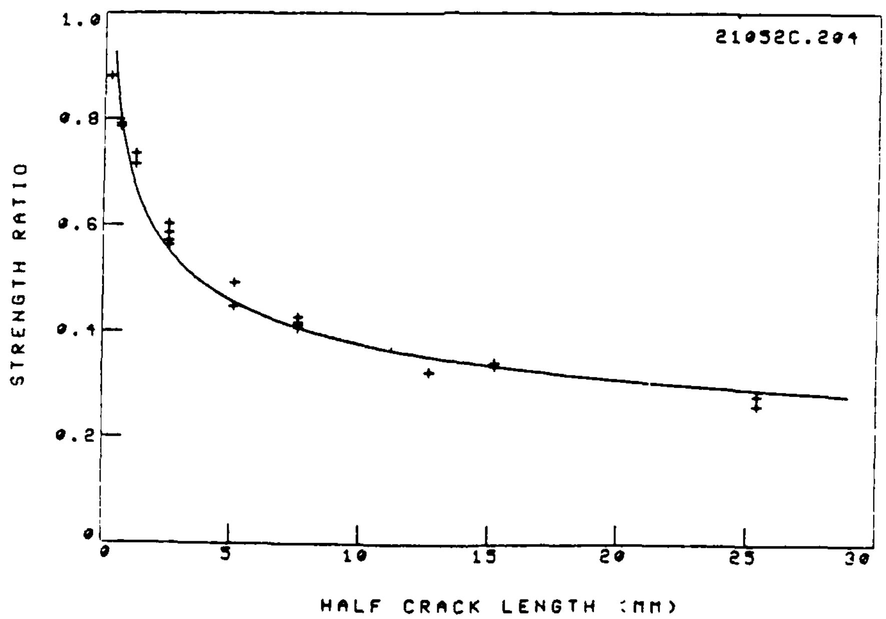

Figure 75. Comparison between experiments and prediction (ML-fracture model) for boron/aluminum $[0_2/\pm45]_s$ laminate, shown on a linear scale ($n = 0.280$, $H_c/\sigma_o = 0.871$).

PS-FRACTURE MODEL
(STRAIGHT CRACKS)

I. INTRODUCTION

DEVELOPED FOR LAMINATES WHICH EXHIBIT SIGNIFICANT NONLINEAR STRESS-STRAIN CURVES, e.g. $[\pm 45]_s$ Gr/Ep, B/Al, ETC.

- DATA ARE ANALYZED IN TERMS OF STRAIN RATHER THAN STRESS.
- A "GENERAL FRACTURE-TOUGHNESS PARAMETER", Q_C, IS PROPOSED.
- Q_C IS DERIVED ON THE BASIS OF FIBER FAILURE IN THE PRINCIPAL LOAD-CARRYING LAMINAE, I.E. IS INDEPENDENT OF LAMINATE ORIENTATION.
- THE RELATIONSHIP BETWEEN K_Q AND Q_C DEPENDS ONLY ON THE ELASTIC CONSTANTS OF THE LAMINATE.
- BASED UPON Q_C, THE CRITICAL STRESS AND STRAIN INTENSITY FACTORS AND NOTCHED STRENGTH OF INDIVIDUAL LAMINATES CAN BE CALCULATED.
- Q_C IS PROPORTIONAL TO THE ULTIMATE TENSILE STRAIN OF THE FIBERS.
- CONSEQUENTLY, THE CRITICAL STRESS INTENSITY FACTOR CAN BE PREDICTED SOLELY FROM THE ULTIMATE TENSILE STRENGTH OF THE UNNOTCHED LAMINATE.
- THE CRACK TIP DAMAGE ZONE SIZE CAN BE PREDICTED BASED UPON Q_C.
- PS-FRACTURE MODEL IS BASED UPON A STRAIN FAILURE CRITERION.

II. STRAIN FAILURE CRITERION

Stress and Strain Intensity Factors:

(102) $K = S\sqrt{\pi c\ \sec(\pi c/W)}$ (103) $K_\varepsilon = \varepsilon_o\sqrt{\pi c\ \sec(\pi c/W)}$

Applying Crack Tip Damage Zone Size:

(104) $K = S\sqrt{\pi(c+\rho)\ \sec(\pi c/W)}$ (105) $K_\varepsilon = \varepsilon_o\sqrt{\pi(c+\rho_\varepsilon)\ \sec(\pi c/W)}$

Critical Stress and Strain Intensity Factors:

(105) $K_Q = S_C\sqrt{\pi(c+\rho_C)\ \sec(\pi c/W)}$ (107) $K_{\varepsilon Q} = \varepsilon_{oC}\sqrt{\pi(c+\rho_{\varepsilon C})\ \sec(\pi c/W)}$

Critical Crack Tip Damage Zone Size:

(108) $\rho_C = \dfrac{(K_Q/F_{tu})^2}{\pi}$ (109) $\rho_{\varepsilon C} = \dfrac{(K_{\varepsilon Q}/\varepsilon_{tu})^2}{\pi}$

(110) $K_Q = K_{Qe}[1-K_{Qe}^2/(\pi c F_{tu}^2)]^{-1/2}$ (111) $K_{\varepsilon Q} = K_{\varepsilon Qe}[1-K_{\varepsilon Qe}^2/(\pi c\varepsilon_{tu}^2)]^{-1/2}$

Elastic Critical Stress and Strain Intensity Factors:

(112) $K_{Qe} = S_C\sqrt{\pi c\ \sec(\pi c/W)}$ (113) $K_{\varepsilon Qe} = \varepsilon_{oC}\sqrt{\pi c\ \sec(\pi c/W)}$

For Linear Elastic Material

(114) $\varepsilon_{oC} = S_C/E_y$ $\varepsilon_{tu} = F_{tu}/E_y$

$K_{eQ} = K_Q/E_y$ $\rho_{\varepsilon C} = \rho_C$

---

* Although the subject of finite width correction (FWC) factor is addressed in detail in the following Section, it has been incorporated into the PS-fracture model so that the formulation will be identical to that developed by Poe and Sova [12].

DEFINITIONS:

K, K_ε.....stress and strain intensity factors, respectively.

K_Q,$K_{\varepsilon Q}$....critical stress and strain intensity factors, respectively.

K_{Qe},$K_{\varepsilon Qe}$..elastic critical stress and strain intensity factors, respectively.

ρ, ρ_ε.....crack tip damage zone size for stress and strain, respectively.

ρ_C, $\rho_{\varepsilon C}$....critical crack tip damage zone size for stress and strain, respectively.

S, ε_o.....remote (far-field) stress and strain, respectively.

S_C, ε_{oC}...remote (far-field) stress and strain at failure, respectively.

F_{tu}, ε_{tu}..unnotched ultimate tensile stress and strain, respectively.

In order to apply a strain failure criterion, the strains at the notch tip are derived based on stress analysis [15] for an anisotropic and homogeneous laminate containing straight cracks. The singular stresses ahead of the crack tip for a specially orthotropic laminate subjected to model I loading are, (for θ = 0, Figure 76):

$$(115) \quad \begin{Bmatrix} \sigma_x \\ \sigma_y \\ \sigma_{xy} \end{Bmatrix} = \frac{K}{E_y\sqrt{2\pi r}} \begin{Bmatrix} (E_x E_y)^{\frac{1}{2}} \\ E_y \\ 0 \end{Bmatrix}$$

Due to symmetry, $_{xy} = 0$ and the strains are expressed by:

$$(116) \quad \begin{Bmatrix} \varepsilon_x \\ \varepsilon_y \\ \gamma_{xy} \end{Bmatrix} = \frac{K[\beta]}{E_y\sqrt{2\pi r}} \begin{Bmatrix} (E_x E_y)^{\frac{1}{2}} \\ E_y \\ 0 \end{Bmatrix}$$

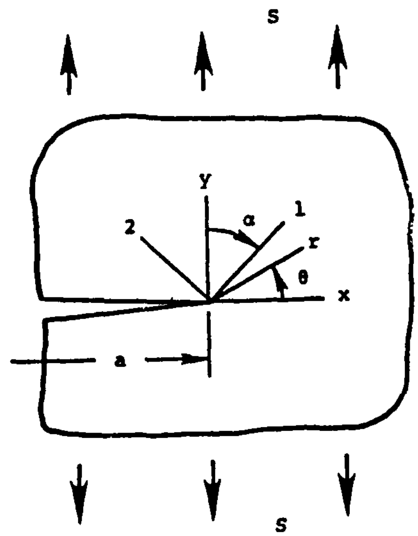

Figure 76. Laminate and principal laminae coordinates [12].

$$(117)\quad [\beta] = \begin{bmatrix} 1/E_x & -\nu_{yx}/E_y & 0 \\ -\nu_{yx}/E_y & 1/E_y & 0 \\ 0 & 0 & 1/G_{xy} \end{bmatrix}$$

Transforming the singular strains to the principal directions of the i^{th} lamina

$$(118)\quad \begin{Bmatrix} \varepsilon_1 \\ \varepsilon_2 \\ \frac{1}{2}\gamma_{12} \end{Bmatrix}_i = [T]_i \begin{Bmatrix} \varepsilon_x \\ \varepsilon_y \\ \gamma_{xy} \end{Bmatrix} \quad \text{where:} \quad (119)\quad [T] = \begin{bmatrix} \sin^2\alpha & \cos^2\alpha & \sin 2\alpha \\ \cos^2\alpha & \sin^2\alpha & -\sin 2\alpha \\ -\frac{1}{2}\sin 2\alpha & \frac{1}{2}\sin 2\alpha & -\cos 2\alpha \end{bmatrix}$$

Substituting Eq. (116) into Eq. (118)

$$(120)\quad \begin{Bmatrix} \varepsilon_1 \\ \varepsilon_2 \\ \frac{1}{2}\gamma_{12} \end{Bmatrix} = \frac{K}{E_y\sqrt{2\pi r}} \begin{Bmatrix} \zeta_1 \\ \zeta_2 \\ \zeta_{12} \end{Bmatrix}_i \quad \text{where:} \quad (121)\quad \begin{Bmatrix} \zeta_1 \\ \zeta_2 \\ \zeta_{12} \end{Bmatrix}_i = [T]_i[\beta] \begin{Bmatrix} (E_xE_y)^{\frac{1}{2}} \\ E_y \\ 0 \end{Bmatrix}$$

ASSUMPTION: "A laminate fails whenever the fiber strains reach a critical level in the principal load carrying laminae".

Thus: $\varepsilon_1 \sqrt{2\pi r}$ = CONSTANT (AT FAILURE)

i.e. Independent of Laminate Lay-Up

CONCLUSION: $K_Q(\zeta_1)_i/E_y$ = CONSTANT (at Failure, $K \rightarrow K_Q$)

(122) DEFINITION: $Q_C = K_Q(\zeta_1)_i/E_y$ "GENERAL FRACTURE-TOUGHNESS PARAMETER"

Special Case: Linear elastic material, $K_{\varepsilon Q} = K_Q/E_y$, thus:

$$(123)\quad Q_C = K_{\varepsilon Q}(\zeta_1)_i$$

The value of $(\zeta_1)_i$ has to be determined individually for each principal load-carrying lamina using Eq. (121), e.g.

(124) $\alpha = 0°$: $(\zeta_1)_i = 1 - \nu_{yx} \sqrt{E_x/E_y}$

(125) $\alpha = 45°$: $(\zeta_1)_i = \frac{1}{2}(1 - \nu_{yx}\sqrt{E_x/E_y})(1 + \sqrt{E_y/E_x})$

(126) $\alpha = \alpha$: $(\zeta_1)_i = (1 - \nu_{yx} \sqrt{E_x/E_y})(\sqrt{E_y/E_x} \cdot \sin^2\alpha + \cos^2\alpha)$

III. DATA ANALYSIS

A. The "General-Fracture Toughness Parameter":

Q_C can be calculated in three different ways, i.e.:

1. $Q_C = K_{\varepsilon Q}(\zeta_1)_i$ — $K_{\varepsilon Q}$ determined from Eq. (111), ε_{tu} and $\varepsilon_{\alpha C}$ are given
2. $Q_C = K_Q(\zeta_1)_i/E_y$ — K_Q determined from Eq. (110), F_{tu} and S_C are given
3. $Q_C = K_Q(\zeta_1)_i/E_{uy}$ — E_{uy}...ultimate secant modulus.

- Values of Q_C calculated from the first procedure are intermediate between the upper and lower values calculated from the second and third procedures, respectively, Figure 77 and Table 5.

- The latter two procedures yield equal values for linear materials.

- With increasing nonlinearity in the stress-strain curves the difference between the upper and lower bounds would be larger.

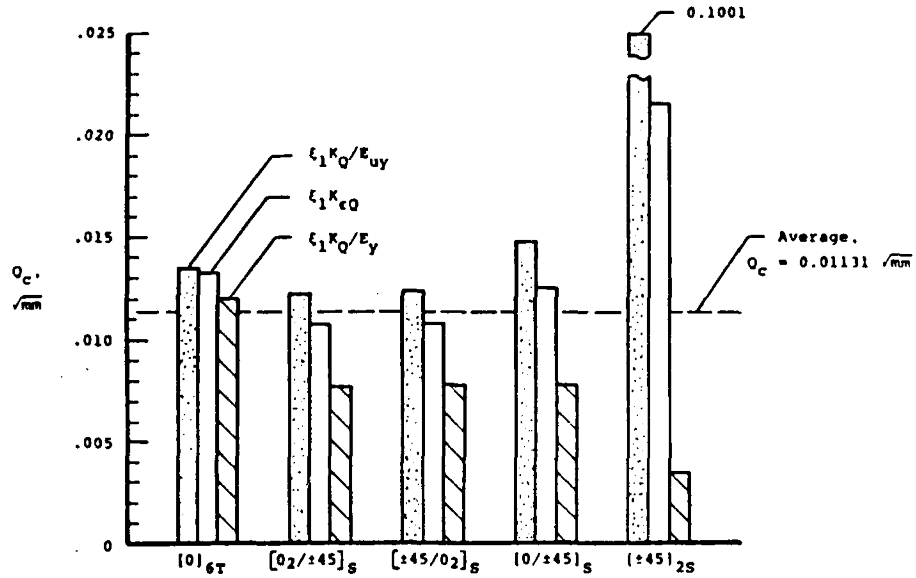

Figure 77. Values of the "General Fracture-Toughness Parameter" for Boron/Aluminum Laminates [12].

Table 5. "General Fracture-Toughness Parameter", Q_C, for Five Boron/Aluminum Laminates [12].

Laminate Orinetation	ζ_1	Q_C, $\sqrt{mm}$ calculated from - $\zeta_1 K_{\epsilon Q}$	$\zeta_1 K_Q/Ey$	$\zeta_1 K_Q/Euy$
$[0]_{6T}$	0.8409	0.01328	0.01200	0.01347
$[0_2/\pm45]_s$	0.7841	0.01068	0.00764	0.01223
$[\pm45/0_2]_s$	0.7806	0.01074	0.00771	0.01233
$[0/\pm45]_s$	0.7375	0.01250	0.00770	0.01477
$[\pm45]_{2s}$	0.6771	0.02156	0.00350	0.1001

B. Notched Strength Predictions:

The notched strength can be calculated in three ways all based on the assumption that Q_C for a given material system is constant.

1. $K_Q = Q_C E_y/\xi_1$ and apply Eq. (110) to calculate S_C.

2. $K_Q = Q_C E_{uy}/\xi_1$ and apply Eq. (110) to calculate S_C.

3. $K_{\varepsilon Q} = Q_C/\xi_1$ and apply Eq. (111) to calculated ε_{oC} and use the stress-strain equations,

- The predictions of notched strength using $K_{\varepsilon Q}$ values agree well with experiments, while those using K_Q with E_{uy} and E_y yield the upper and lower bounds, respectively, Figure 78.

- The difference between the upper and lower bounds predictions is largest for the $[\pm 45]_{2s}$ laminate, and generally increases with the percentage of the ±45° plies, Figure 78.

C. Critical Damage Zone Size:

- The critical crack tip damage zone sizes, ρ_C and $\rho_{\varepsilon C}$, can be calculated from Eqs. (108) and (109), respectively, when the values of K_Q and $K_{\varepsilon Q}$ are back-calculated from Eqs. (122) and (123), respectively using the average values of Q_C.

- Notched strength data analyzed in [40] for a variety of center-crack $[0_i/\pm 45_j/90_k]_s$ laminates (Gr/Ep, B/Ep, Gl/Ep, Gr/PI, B/Al, etc.) indicate that Q_C/ε_{tuf} is reasonably constant, i.e.:

(127) $$Q_C/\varepsilon_{tuf} \doteq 1.5\sqrt{mm}$$

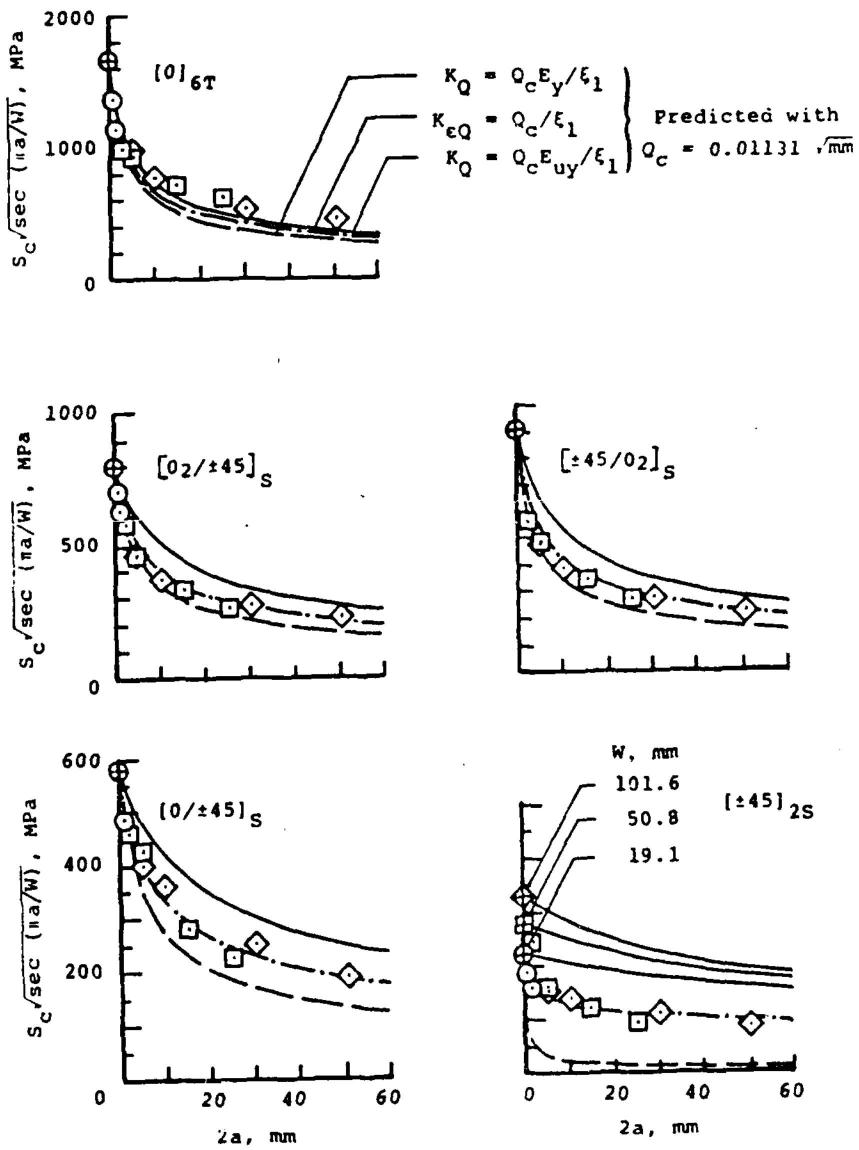

Figure 78. Measured and predicted strengths ("+" inside symbols indicates F_{tu}) [12].

provided that:

- Laminate failed predominantly by self-similar crack extension

- Neither delamination nor splitting in the 0° plies at the crack tip occurs.

- Crack tip damage zone size is small.

- Using Eqs. (109) and (123):

$$\rho_{\varepsilon C} = \frac{1}{\pi}\left(\frac{1.5\varepsilon_{tuf}}{\zeta_1\ \varepsilon_{tu}}\right)^2 . \tag{128}$$

i.e., critical damage zone size is not constant but depends on laminate orientation $(\zeta)_1$, and therefore on the laminate elastic constants.

- The critical fiber strain ahead of the crack tip in the load-carrying lamina is: $\varepsilon_1 = Q_C/\sqrt{2\pi r}$.

- Assuming that $\varepsilon_1 = \varepsilon_{tuf}$ at $r = d_o$ (WN-point stress criterion).

  Thus: $\sqrt{2\pi d_o} = Q_C/\varepsilon_{tuf}$.

  i.e. the characteristic distance in the "point stress" criterion of the WN-fracture model is proportional to the square of Q_C/ε_{tuf}.

- Since d_o varies significantly among the different Gr/Ep laminates analyzed (see WN-fracture model) having the same ε_{tuf} (=0.01) it should be expected that Q_C varies among the different laminates as well.
- However, if the conditions listed above are satisfied it could be expected that Q_C is independent of laminate configuration.

- For a given laminate, a constant value of Q_C, independent of crack length, results in an excellent agreement with experiments, Figures 79-80.

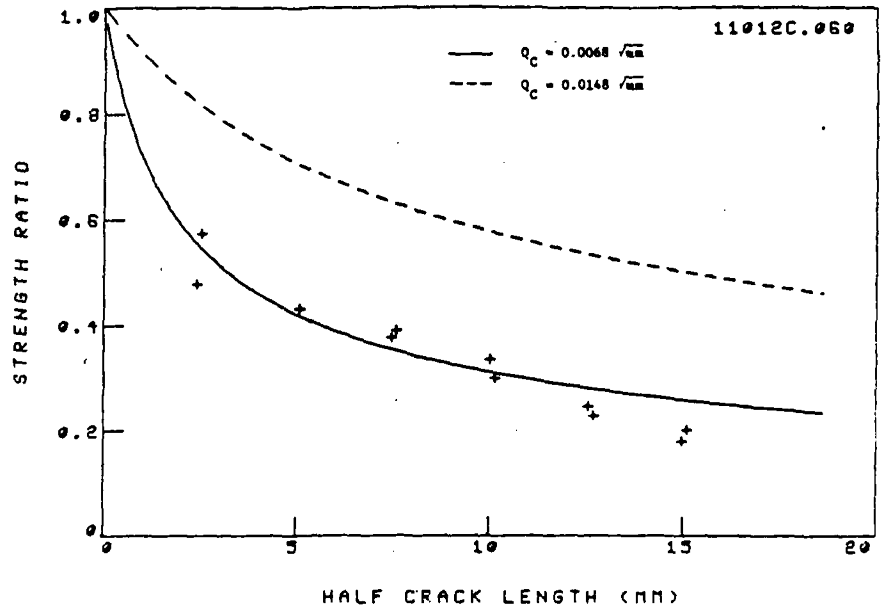

Figure 79. Notched strength versus crack length predictions (PS-fracture model) for graphite/epoxy $[0/\pm 45]_s$ laminate (solid line: Q_C of the subject laminate; dashed line: Q_C obtained from average of values given in Table 16).

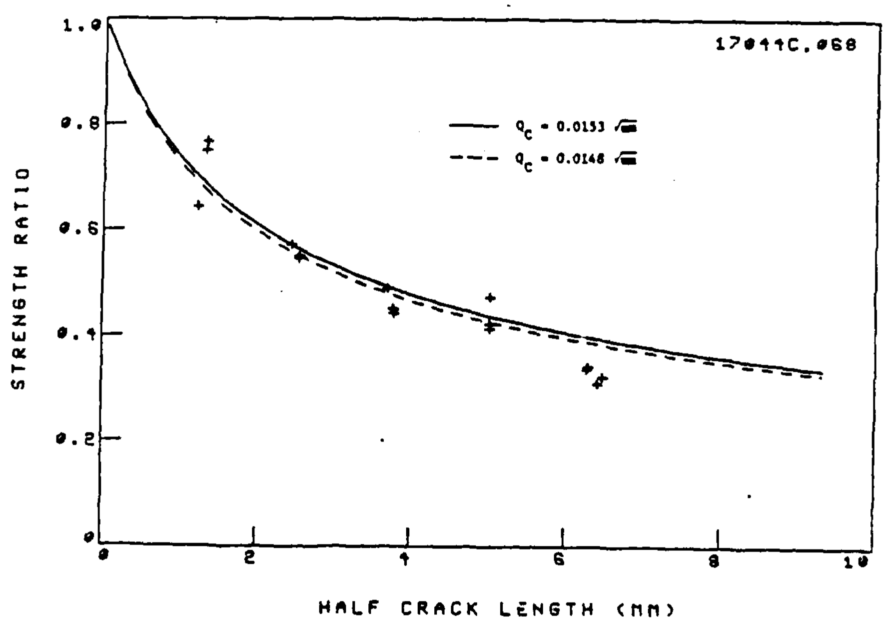

Figure 80. Notched strength versus crack length predictions (PS-fracture model) for graphite/epoxy $[0/90/\pm 45]_s$ laminate (solid line: Q_C of the subject laminate; dashed line: Q_C obtained from average of values given in Table 16).

D. Discussion:

- In order to fully apply the PS-fracture model the elastic constants (E_x, E_y, ν_{yx}), strengths (F_{tu}, S_C), strains (ε_{tu}, ε_{tuf}, ε_{oC}) and ultimate secant modulus (E_{uy}) must be known.

- Most experimental data published do not include several of these material properties, predominantly the values of E_{uy} and ε_{oC}.

- Consequently, only calculation procedure #2 (for calculating Q_C) and calculation procedure #1 (for calculating K_Q and S_C) can be employed.

- For most Gr/Ep laminates, this may be sufficient since their stress-strain curve is essentially linear to failure.

- Thus, from Eqs. (110), (112), and (122) [40]:

$$S_C \sqrt{\sec(\pi c/W)}/F_{tu} = \{1 + \pi c[\zeta_1 F_{tu}/Q_C E_y]^2\}^{-\frac{1}{2}} \qquad (129)$$

using $Q_C = 1.5\ \varepsilon_{tuf}$

$$S_C \sqrt{\sec(\pi c/W)}/F_{tu} = \{1 + \pi c[\zeta_1 F_{tu}/1.5\varepsilon_{tuf} E_y]^2\}^{-\frac{1}{2}} \qquad (130)$$

For linear stress strain curves; $F_{tu} = \varepsilon_{tuf} E_y$:

$$S_C \sqrt{\sec(\pi c/W)}/F_{tu} = [1 + \pi c(\xi_1/1.5)^2]^{-\frac{1}{2}} \qquad (131)$$

which yields the prediction of the notched-to-unnotched strength ratio for linear materials.

For nonlinear laminates, applying Eqs. (111), (113), and (123):

$$\varepsilon_{oC} \sqrt{\sec(\pi c/W)/\varepsilon_{tu}} = \{1 + \pi c[\zeta_1 \varepsilon_{tu}/1.5\varepsilon_{tuf}]^2\}^{\frac{1}{2}} \qquad (132)$$

and using the Ramberg-Osgood stress-strain equations or any polynomials yields the strength ratio.

FINITE WIDTH CORRECTION (FWC) FACTOR

I. ISOTROPIC FINITE WIDTH CORRECTION FACTOR

The previously described fracture models were formulated assuming the plates are of infinite width. For proper comparisons between the experimental results and predictions FWC should be applied, i.e.

(133) $$\sigma_N^{\infty} = Y\sigma_N$$

(134) $$K_Q = Y\sigma_N \sqrt{\pi c}$$

For plates containing circular holes [43]:

(135) $$Y = \frac{2 + (1 - 2R/W)^3}{3(1 - 2R/W)}$$

For plates containing center cracks:

Irwin's tangent formula [44]:

(136) $$Y = \sqrt{(W/\pi c)\ \tan(\pi c/W)}$$

Feddersen's secant formula [44]:

(137) $$Y = \sqrt{\sec(\pi c/W)}$$

2nd and 3rd degree polynomials [44]:

(138) $$Y = 1 - 0.1\ (2c/W) + (2c/W)^2$$

(139) $$Y = 1 + 0.1282(2c/W) - 0.2881(2c/W)^2 + 1.5254(2c/W)^3$$

etc.

II. ORTHOTROPIC FINITE WIDTH CORRECTION FACTOR

- There are several analytical methods to determine FWC, e.g.:
  - Boundary collocation solution [45]
  - Boundary integral equation [46]
  - Finite elements [47]

  etc.
- No closed-form solutions are available, and the FWC for orthotropic materials require numerical solutions.
- Therefore, the closed-form expressions available for isotropic materials are frequently used for orthotropic materials.
- Validity of the applicability of isotropic FWC factor to orthotropic materials is discussed below:

(140) $$H = Y_{(orthotropic)}/Y_{(isotropic)} = K_{I(orthotropic)}/K_{I(isotropic)}$$

- The larger *the length-to-width ratio* (L/W) *is, the* closer H approached 1.0 [47].
- When $L/W > 3.0$, the error for [0°] Gr/Ep is less than 2% [48].
- Local and global compliances of center notched [0°] B/Al and BSiC/Ti indicate that isotropic FWC factor (Eq. (139)) can be used [49].
- Values of H for a variety of Gr/Ep T300/5208 laminates were calculated in [50] for DEC and CCT specimens using the boundary integral formulation. ($2a/W = 0.1$ to 0.7, $L/W = 5.0$)
- H depends on specimen geometry, lay-up, and material properties, Figures 81 and 82

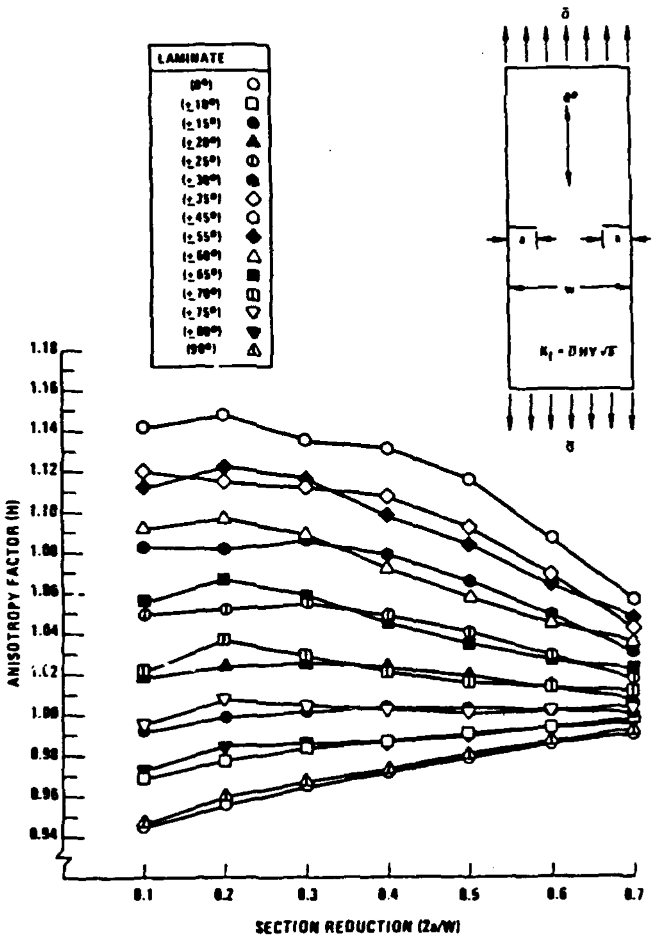

Figure 81. Anisotropy factor [illegible] sus net section reduction for double-edge [illegible] acked specimens [50].

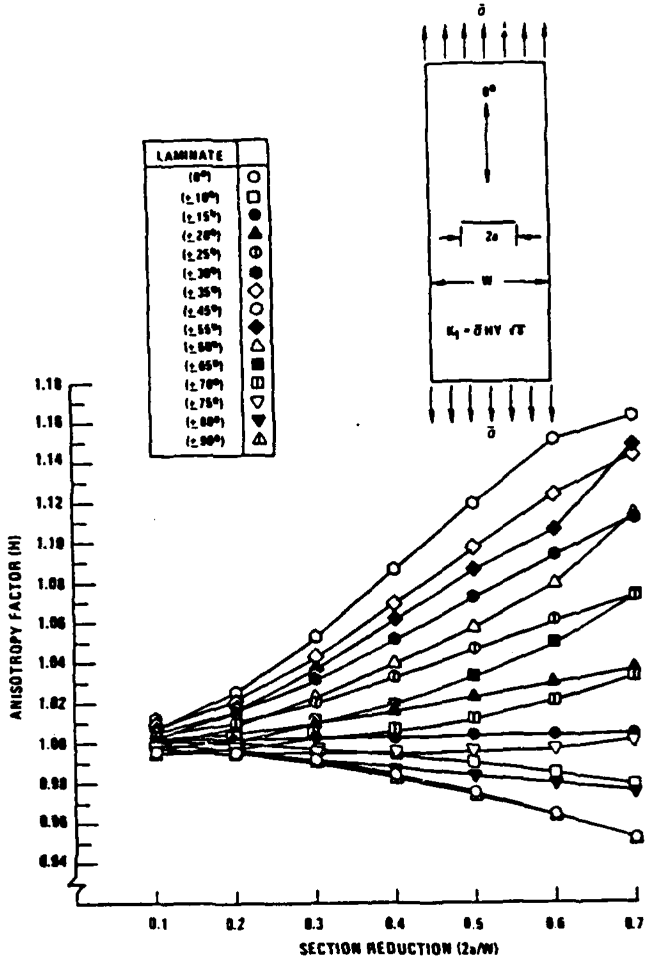

Figure [illegible]. Anisotropy factor versus net section reduction for center-cracked specimens [50].

- As the "free edge distance" becomes larger, H approaches unity, regardless of geometry and material.

- H is largest for $[\pm 45]_s$, decreases (symmetrically) for increasing and decreasing ply angle.

- A correlation between H and the in-plane shear modulus has been suggested, Figures 83 and 84 , [50].

- For all practical purposes $2c/W < 0.5$ for which $H < 1.12$.

- H is further reduced for multidirectional laminates, e.g. Table 6.

- H was calculated for four Gr/Ep laminates: $[90_2/\pm 45]_s$, $[90/\pm 45]_s$, $[0/\pm 45]_s$, and $[\pm 45]_s$, for laminates containing circular holes, center-cracks, and cracks emanating from circular and elliptical cutouts, all of various sizes [46].
  - For $[\pm 45]_{2s}$: $H \cong 1.06$ for $2c/W = 0.5$
  - For all other laminates $H \cong 1.02$ for $2c/W = 0.5$

- Consequently, in this work the isotropic FWC factors are used, i.e. Eqs. (135) and (139) for laminates containing circular holes and straight cracks, respectively. For PS-fracture model, Eq. (137) has been employed.

Table 6. Anisotropy factor in CCT specimens of mixed orthotropic laminates[a]

Laminate[b] \ 2c/W[c]	0.1	0.2	0.3	0.4	0.5	0.6	0.7
$[0/\pm 45]_s$[b]	1.002	1.006	1.012	1.019	1.028	1.037	1.045
$[0_4/\pm 45]_s$[b]	1.001	1.001	1.000	0.999	0.998	0.996	0.994

a. Data taken from Table 5 of [50]

b. HTS graphite/epoxy. Lamina properties are: $E_L = 144.8$ GPa, $E_T = 11.7$ GPa, $G_{LT} = 4.5$ GPa, $\nu_{LT} = 0.28$

c. Center-cracked tension specimens.

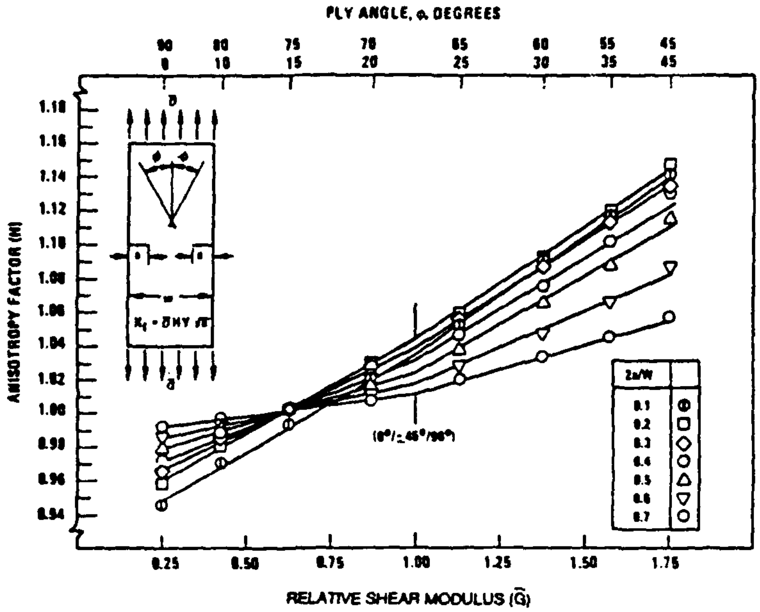

Figure 83. Anisotropy factor versus relative shear modulus for double-edge-cracked specimens [50].

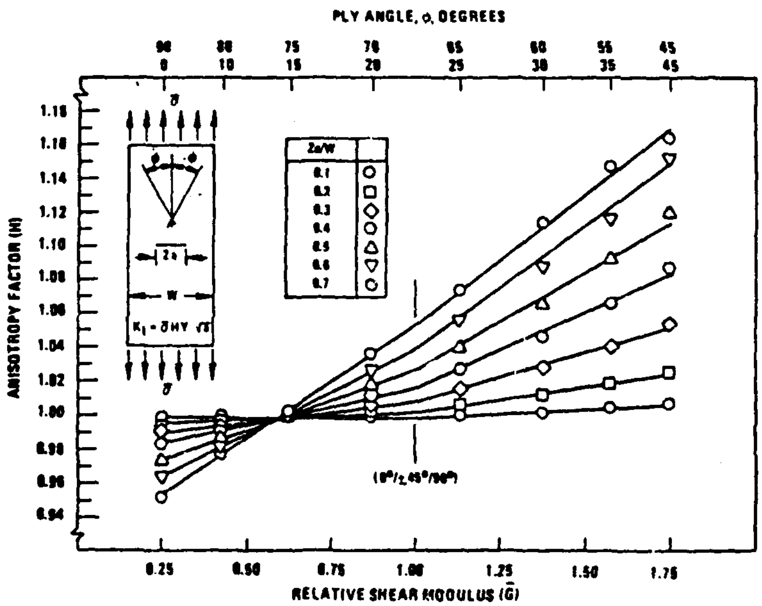

Figure 84. Anisotropy factor versus relative shear modulus for center-cracked specimens [50].

COMPARISON BETWEEN EXPERIMENTS AND PREDICTIONS

OBJECTIVES

- COLLECT AND REVIEW NOTCHED STRENGTH DATA OF Gr/Ep, B/Al, AND Gr/PI LAMINATES CONTAINING DISCONTINUITIES; i.e. Circular Holes, Center Cracks, and Impact Damage*.

- COMPARE NOTCHED STRENGTH DATA WITH THE FRACTURE MODEL PREDICTIONS.

- CORRELATE THE VARIOUS PARAMETERS ASSOCIATED WITH THE DIFFERENT FRACTURE MODELS WITH NOTCH SENSITIVITY OF COMPOSITE LAMINATES AND EVALUATE THEIR APPLICABILITY AS MEASURES OF NOTCH SENSITIVITY.

- ANALYZE THE EFFECT OF A VARIETY OF MATERIAL PARAMETERS ON NOTCH SENSITIVITY OF COMPOSITE LAMINATES.

- THE COMPARISONS AND CORRELATIONS AND THE SUBSEQUENT CONCLUSIONS ARE BASED ON A REVIEW OF**.
  - 2800 NOTCHED STRENGTH DATA
  - 20 MATERIAL SYSTEMS
  - 62 LAMINATE CONFIGURATIONS
  - ALL UNIAXIAL TENSILE LOADING IN AMBIENT CONDITIONS

* The system of data collection and a sample of the review procedure are shown in the following 7 pages.
** Material nomenclature, lay-ups, etc. are listed in the following pages.

DATA FILING SYSTEM

File Names

Each set of notched strength data collected from the literature was assigned a number for the purpose of storing the data in the computer in the form of data files. This number, or File Name, is comprised of nine digits which represent five types of information:

1. The first two digits represent the material system, as listed in Table 7.
2. The third digit represents the test temperature, as listed in Table 8.
3. The next two digits (fourth and fifth) represent the laminate configuration, or lay-up, as listed in Table 9.
4. The sixth digit represents the shape of the discontinuity, as listed in Table 10.
5. The last three digits represent the reference number from which the set of data was taken, as numbered in the list of references.

For example, File Name 110044H.056 represents:

1. Digits 11 - from Table 7; graphite/epoxy T300/5208.
2. Digit 0 - from Table 8; 21°C (70°F) - room temperature.
3. Digit 44 - from Table 9; $[0/90/\pm45]_s$ laminate.
4. Digit H - from Table 10; containing a circular hole.
5. Digits 056 - from the reference list; Reference No. 56.

Summary nomenclature of the file name is given below:

```
X X X X X X.X X X
|   | |   | |_________ Reference
|   | |   |__________ Discontinuity Shape
|   | |__________ Lay-Up
|   |__________ Test Temperature
|__________ Material System
```

The file name appears at the top of each Figure.

Table 7. File Name; Material System

Material System	File Name[a]
I. Graphite/Epoxy	
Not Available[b]	10
T300/5208	11
AS1/3501-6	12
T300/934	13
T300/934C	14
SP-286T300	15
AS/3501-5	16
AS/3501-6	17
II. Boron/Aluminum	
Not Available[b]	2X
5.6/6061F	21
8.0/1100F	22
5.6/2024F	23
4.0/6061F	24
4.2/6061F[c]	25
4.2/2024F[c]	26
5.7/6061F[c]	27
5.6/6061T6	28
5.6/2024T6	29
III. Graphite/Polyimide	
Not Available[b]	3X
Celion 6000/PMR-15	31

a. First two digits in File Name.

b. For cases in which constituents are not outlined in Publication.

c. BSiC/Al

Table 8. File Name; Test Temperature

Temperature °C	(°F)	File Name[a]
21	(70)[b]	O
10	(50)	A
38	(100)	B
66	(150)	C
93	(200)	D
121	(250)	E
149	(300)	F
177	(350)	G
204	(400)	H
232	(450)	I
260	(500)	J
288	(550)	K
315	(600)	L
343	(650)	M
371	(700)	N
399	(750)	O
427	(800)	P
-46	(-50)	Q
-73	(-100)	R
-101	(-150)	S
-129	(-200)	T
-157	(-250)	U
-184	(-300)	V
-212	(-350)	W

a. Third digit in File Name.

b. Room temperature.

Table 9. File Name ; Laminate Lay-Up

Lay Up	File Name[a]	Lay Up	File Name[a]
$[0]_n$	01	$[90_2/0]_s$	26
$[\pm15]_s$	02	$[+15/0/-15]_s$	27
$[\pm30]_s$	03	$[+30/0/-30]_s$	28
$[\pm45]_s$	04	$[+45/0/-45]_s$	29
$[\pm60]_s$	05	$[+60/0/-60]_s$	30
$[\pm75]_s$	06	$[+75/0/-75]_s$	31
$[\pm90]_n$	07	$[90/0/90]_s$	32
$[0/\pm5]_s$	08	$[0/\pm45]_{2s}$	33
$[0/\pm10]_s$	09	$[90/\pm45]_s$	34
$[0/\pm15]_s$	10	$[+45/0/-45/0]_s$	35
$[0/\pm30]_s$	11	$[0/90]_s$	36
$[0/\pm45]_s$	12	$[0/90]_{2s}$	37
$[0/\pm60]_s$	13	$[0/90]_{4s}$	38
$[0/\pm75]_s$	14	$[0/\pm45/90]_s$	39
$[0/\pm90_2]_s$	15	$[0/\pm45/90]_{2s}$	40
$[\pm5/0]_s$	16	$[\pm45/0/90]_s$	41
$[\pm10/0]_s$	17	$[90/0/\pm45]_s$	42
$[\pm15/0]_s$	18	$[90/\pm45/0]_s$	43
$[\pm20/0]_s$	19	$[0/90/\pm45]_s$	44
$[\pm25/0]_s$	20	$[\pm45/90/0]_s$	45
$[\pm30/0]_s$	21	$[\pm45/0/90]_{2s}$	46
$[\pm35/0]_s$.	22	$[90/0/\pm45]_{2s}$	47
$[\pm45/0]_s$	23	$[+45/0/-45/90]_{2s}$	48
$[\pm60/0]_s$	24	$[90/\pm45/0]_{2s}$	49
$[\pm75/0]_s$	25	$[0/90/\pm45]_{2s}$	50

Table 9. Continued

Lay Up	File Name[a]
$[+45/90/-45/0]_{2s}$	51
$[0_2/\pm45]_s$	52
$[\pm45/0_2]_s$	53
$[0/+45/90/-45]_{2s}$	54
$[90/-45/0/+45]_{2s}$	55
$[0/+45/90/-45]_s$	56
$[+45/0/-45/0]_s$	57
$[0/+45/-45/0]_s$	58
$[0/90/\pm45_2]_s$	59
$[0/\pm22]_s$	60
$[90/\pm22]_s$	61
$[0/\pm22/0]_s$	62

(a) Fourth and fifth digits in File Name.

Table 10. File Name: Notch Shape

Notch Shape	File Name[a]
Circular Center Hole	H
Straight Center Crack	C
Impact Damage (Central)	I
Circular Center Hole with Slits	S
Double Edge Notch[b]	D
Single Edge Notch[b]	E

(a) Sixth digit in File Name

(b) Not included in this report.

SAMPLE LITERATURE REVIEW

Reference [64]

Author: I.M. Daniel

Title: The Behavior of Uniaxially Loaded Graphite/Epoxy Plates with Holes.

Publication: in Proceedings of the First International Conference on Composite Materials (ICCM-I), Boston, U.S.A., 1978, pp. 1019-1034.

File Names: 15039H.064, 15052H.064

Materials: Graphite/Epoxy SP-286T300

Lay-Up: $[0/\pm45/90]_s$, $[0_2/\pm45]_s$

Dimensions: 560 x 127 x 1.05 mm (gage length = 408 mm)

Geometry: Circular Hole - 0.0, 0.2, 0.4, 1.6, 4.8, 6.4, 12.7, and 25.4 mm in diameter

Tabs: Glass/Epoxy, 3M 1007 Scotchply, $[0/90]_s$ laminate, 76 mm long.

No. of Tests: 2-3 tests per crack per laminate; total of 28 notched tests.

Test Conditions: Stroke control, 1 mm/min, friction grips, Riehle testing machine.

Measurements: Local (near crack region) strain, coating, and notched strength

Lamina Properties: Not available (taken from Ref. [58].

Stress Concentration Factor, K_T^∞:

$[0/\pm45/90]_s$: $K_T^\infty = 3.00$

$[0_2/\pm45]_s$: $K_T^\infty = 3.49$

Comments: 1. Unnotched strength for both laminates is not available. For $[0/\pm45/90]_s$ laminate the value given in Ref. [58] was taken for the data analysis of this report since it is of the same material system as that studied in this paper [64]. For $[0_2/\pm45]_s$ laminate the value given in Ref. [66] of 802 MPa is taken for the data analysis of this report.

2. References [65,66] provide additional details on test results.

Results and Conclusions:

The author investigated the deformation and failure of uniaxially loaded graphite/epoxy plates with holes and correlated the notched strength data with the "point stress" and "average stress" criteria of the WN-fracture model. The main conclusions are:

1. The "point stress" and "average stress" criteria satisfactorily described the strength reduction.
2. There is a critical hole diameter below which the laminates become notch-insensitive.
3. In the case of quasi-isotropic laminates, strength reduction was found to be independent of notch geometry, i.e. specimens with holes and cracks of the same size had nearly the same strength.
4. For $[0/\pm45/90]_s$ laminate: $a_o = 3.8$ mm $d_o = 1$ mm

   For $[0_2/\pm45]_s$ laminate: $a_o = 5$ mm

Table 11. Notched Strength Data Taken from Ref. [64]

15039H.064

GR/EP SP-286T300 [0/+45/-45/90]S 15039H.064

2R [mm]	2R/W	STRENGTH [MPa]	STRENGTH RATIO
0.00	0.00	502.0	1.000
0.20	0.00	491.5	0.979
0.40	0.00	434.0	0.865
0.40	0.00	463.0	0.922
1.60	0.01	387.9	0.773
1.60	0.01	380.9	0.759
4.80	0.04	285.6	0.570
4.80	0.04	308.5	0.615
6.40	0.05	281.3	0.562
6.40	0.05	270.3	0.540
12.70	0.10	260.2	0.524
12.70	0.10	244.4	0.492
19.10	0.15	213.6	0.436
19.10	0.15	237.0	0.484
25.40	0.20	199.7	0.416
25.40	0.20	218.8	0.456

15052H.064

GR/EP SP-286T300 [0/0/+45/-45]S 15052H.064

2R [mm]	2R/W	STRENGTH [MPa]	STRENGTH RATIO
0.00	0.00	802.0	1.000
6.40	0.05	640.3	0.800
6.40	0.05	598.4	0.748
6.40	0.05	412.9	0.516
12.70	0.10	480.8	0.606
12.70	0.10	461.0	0.581
12.70	0.10	409.6	0.516
19.10	0.15	387.2	0.495
19.10	0.15	403.7	0.516
19.10	0.15	353.1	0.451
25.40	0.20	379.2	0.495
25.40	0.20	359.2	0.469
25.40	0.20	425.2	0.555

RESULTS AND CONCLUSIONS

- VERY GOOD AGREEMENT BETWEEN ALL FRACTURE MODELS REVIEWED AND ALL EXPERIMENTAL NOTCHED STRENGTH DATA HAS BEEN ESTABLISHED.

- THE FRACTURE MODELS ARE ALL SEMI-EMPIRICAL, i.e. THEY CAN BE APPLIED PROVIDING THAT AT LEAST 2-3 (Depending Upon the Fracture Model) NOTCHED STRENGTH DATA ARE KNOWN A PRIORI.

- THE FRACTURE MODELS INCLUDE CERTAIN PARAMETERS WHICH ARE ASSUMED TO BE MATERIAL CONSTANTS, i.e. Independent of Specimen Geometry.

- THESE PARAMETERS STRONGLY DEPEND ON LAMINATE CONFIGURATION AND MATERIAL SYSTEM AS WELL AS ON THE VARIETY OF INTRINSIC AND EXTRINSIC VARIABLES.

- CONSEQUENTLY, THESE PARAMETERS MUST BE DETERMINED (EXPERIMENTALLY) FOR EACH LAMINATE CONFIGURATION AND MATERIAL SYSTEM INDEPENDENTLY.

- THE NUMBER OF TESTS THAT MUST BE CONDUCTED IN DETERMINING THE FRACTURE MODELS PARAMETERS DEPENDS UPON THE MODEL ITSELF AND THE LEVEL OF ACCURACY REQUIRED.

- IN THE FRACTURE MODELS REVIEWED THE ACTUAL PATTERN AND DETAILS OF THE NOTCH TIP DAMAGE ARE BY-PASSED BY SIMULATING THE DAMAGE AS SOME "EFFECTIVE" NOTCH TIP DAMAGE ZONE AND ASSUMING IT TO GROW IN A SELF-SIMILAR MANNER.

- THE VARIOUS PARAMETERS ASSOCIATED WITH THE DIFFERENT FRACTURE MODELS DEPEND ON A VARIETY OF INTRINSIC AND EXTRINSIC VARIABLES SUCH AS:

  - <u>INTRINSIC VARIABLES</u>
    - LAMINATE CONFIGURATION
    - STACKING SEQUENCE
    - CONSTITUENTS PROPERTIES
    - FIBER VOLUME FRACTION
    - FIBER-MATRIX INTERFACE
    - FABRICATION PROCEDURE
  - <u>EXTRINSIC VARIABLES</u>
    - LOADING FUNCTION
    - LOADING RATE
    - SPECIMEN GEOMETRY
    - SHAPE OF DISCONTINUITY
    - TEST TEMPERATURE
    - MOISTURE CONTENT

- HOWEVER, A COMPREHENSIVE EVALUATION OF THE EFFECT(S) OF THESE VARIABLES ON THE NOTCH SENSITIVITY OF COMPOSITE LAMINATES IS STILL LACKING, e.g. Effect(s) of matrix toughness, fiber strength, etc.

- ALSO, ANY COMPARISON OF NOTCH SENSITIVITY AMONG DIFFERENT LAMINATES OBTAINED FROM DIFFERENT SOURCES IS OF QUESTIONABLE VALUE, i.e.

  - Very few publications report fiber volume fraction, environmental test conditions, fabrication procedures, constituents (fibers) properties, etc

- VERY FEW WORKS ATTEMPT TO CORRELATE THE RECORDED NOTCH SENSITIVITY WITH THE OBSERVED FAILURE PROCESSES AND FAILURE MODES PRIOR TO CATASTROPHIC FRACTURE.

- SINCE THE APPLICABILITY OF THE FRACTURE MODELS REVIEWED DEPENDS ON THE FAILURE PROCESSES, e.g. delamination, splitting, size of damage zone, etc., ADDITIONAL ATTENTION TO THIS ISSUE IS WARRANTED.

- THERE IS NOW A GROWING DEMAND FOR LIGHT-WEIGHT COMPOSITES IN "PRIMARY" STRUCTURES. CONSEQUENTLY, A MORE THOROUGH UNDERSTANDING IS REQUIRED OF THE WAY IN WHICH PERTINENT LOADING, ENVIRONMENTAL AND MATERIAL PARAMETERS AFFECT STRENGTH, TOUGHNESS, FRACTURE BEHAVIOR, FATIGUE CHARACTERISTICS, IMPACT RESPONSE, ETC., OF COMPOSITE LAMINATES.

- PRACTICALLY ALL THE LAMINATES REVIEWED ARE HIGHLY NOTCH SENSITIVE. FOR MANY CASES, THE NOTCHED STRENGTH REDUCES BY AS MUCH AS 50% FOR NOTCH-LENGTH-TO-WIDTH RATIOS OF 0.2 ÷ 0.3.

- MOST OF THE EXPERIMENTAL STUDIES ON NOTCHED STRENGTH OF COMPOSITE LAMINATES ARE LIMITED TO TWO TYPES OF NOTCH GEOMETRIES: CIRCULAR HOLES AND STRAIGHT CRACKS, CENTRALLY LOCATED.

- THE MAJORITY OF THE NOTCHED STRENGTH DATA ON GRAPHITE/EPOXY ARE FOR LAMINATES CONTAINING CIRCULAR HOLES, WHILE FOR BORON/ALUMINUM MOST OF THE DATA ARE FOR LAMINATES CONTAINING STRAIGHT CRACKS.

EVALUATION OF RESULTS*

- EFFECT OF LAMINATE CONFIGURATION: The experimental notched strength data indicate that laminate lay-up strongly affects the notched strength and notch sensitivity of graphite/epoxy and boron/aluminum laminates, e.g. Figures 85-90 and Figures 91-92, respectively.

- EFFECT OF LAMINATE STACKING SEQUENCE: Most of the notched strength data indicate that laminate stacking sequence does affect the notch sensitivity of graphite/epoxy laminates, Figure 93, most probably resulting from differences in the failure processes. No sufficient data are available to draw any conclusions for boron/aluminum laminates, Figure 94.

- EFFECT OF NOTCH TIP RADIUS: It has been determined that notch tip radius (or shape of discontinuity)has little effect on notch sensitivity of graphite/epoxy, Figure 95, and boron/aluminum, Figure 96. This characteristic has frequently been cited in the literature [208,216,254-256], and it is attributed to the notch tip blunting during damage progression.

- EFFECT OF IMPACT DAMAGE: Both resin matrix and metal matrix composites are highly sensitive to impact damage, even when it is nonvisual damage. The lateral damage is the major cause of strength degradation. Results indicate that induced lateral damage can be presented as through-the-thickness straight cracks for post-impact residual strength predictions, Figures 97-98.

- EFFECT OF TEST TEMPERATURE: Very little data are available regarding the effect of temperature on the notch sensitivity of composite laminates. Results shown in Figures 99 -100 indicate that at elevated temperature boron/aluminum can become more notch sensitive, which might be due to strength degradation of the fibers.

---

* In the following discussion only the predicted notch sensitivity curves (WN-fracture model, "average stress" criterion) are plotted. The actual experimental data are excluded for the sake of clarity.

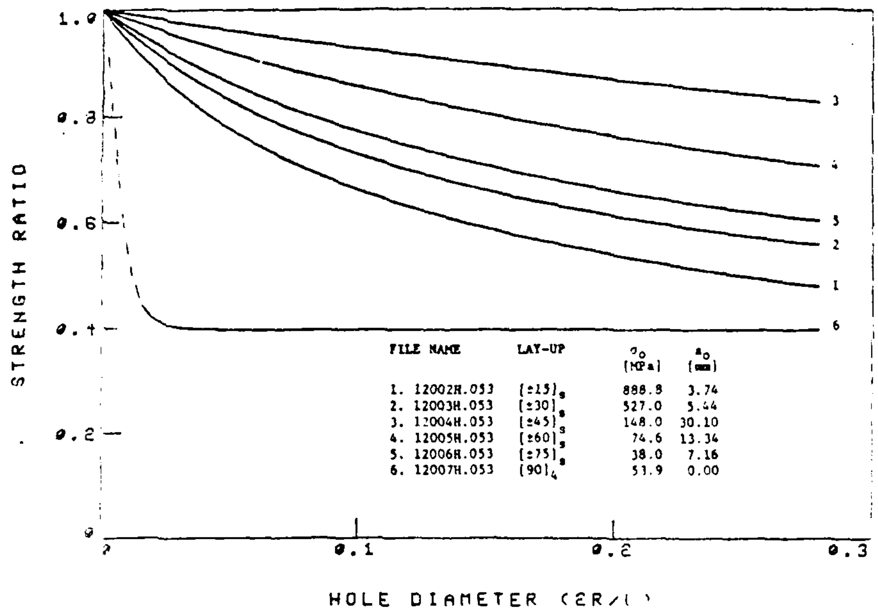

Figure 85. Notched strength versus hole diameter predictions (WN-fracture model, "average stress" criterion) for graphite/epoxy $[\pm\theta]_s$ laminates showing effect of angle on notch sensitivity.

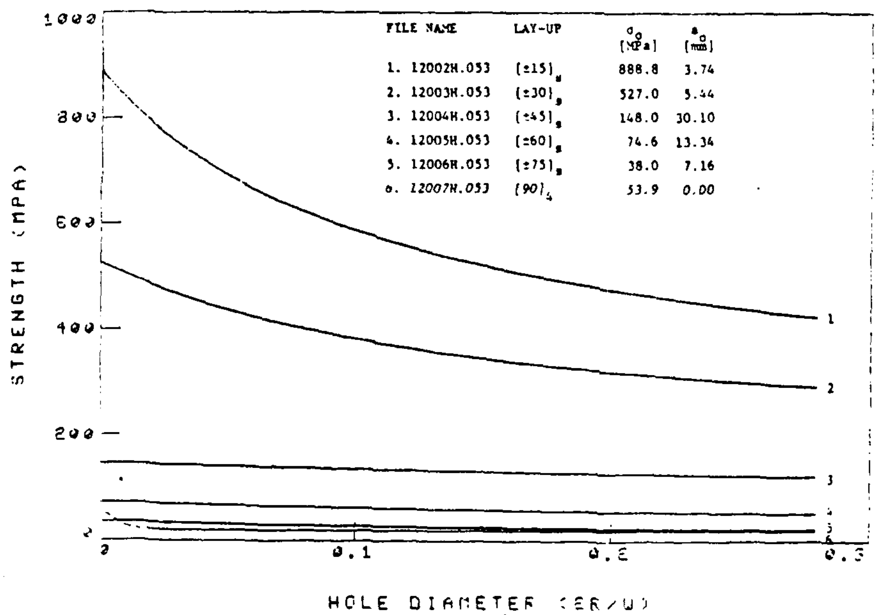

Figure 86. Notched strength versus hole diameter predictions (WN-fracture model, "average stress" criterion) for graphite/epoxy $[\pm\theta]_s$ laminates.

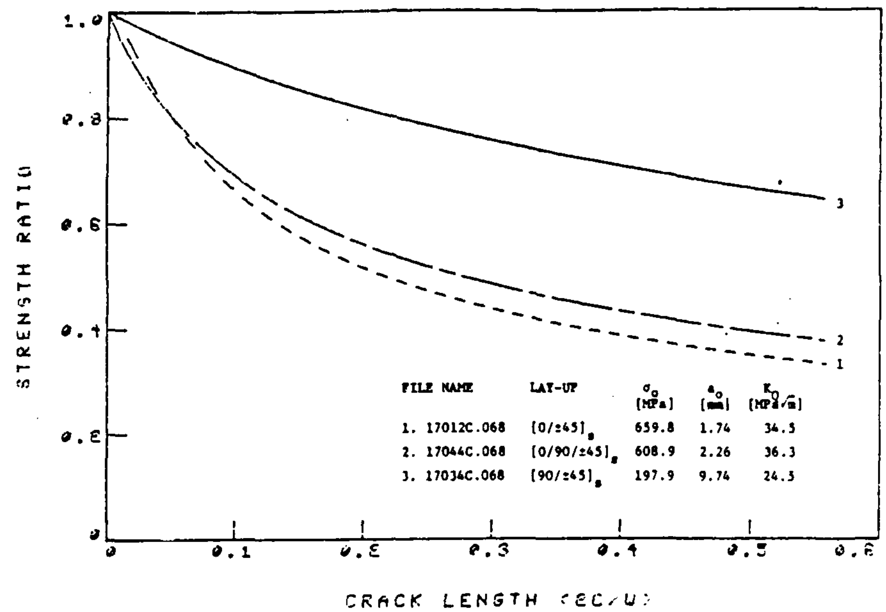

Figure 87. Notched strength versus crack length predictions (WN-fracture model, "average stress" criterion) for graphite/epoxy laminates.

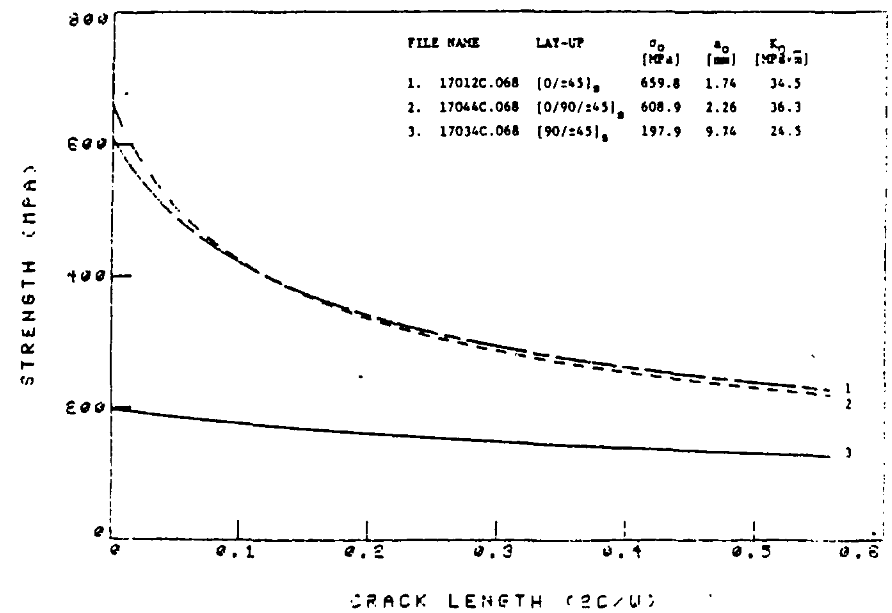

Figure 88. Notched strength versus crack length predictions (WN-fracture model, "average strength" criterion) for graphite/epoxy laminates.

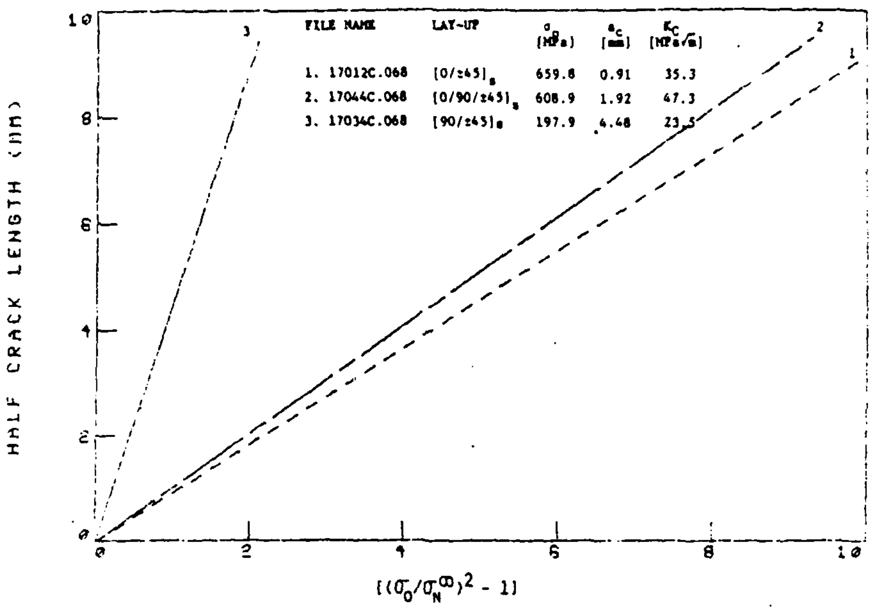

Figure 89. Best fit for a_c (WEK-fracture model) for graphite/epoxy laminates.

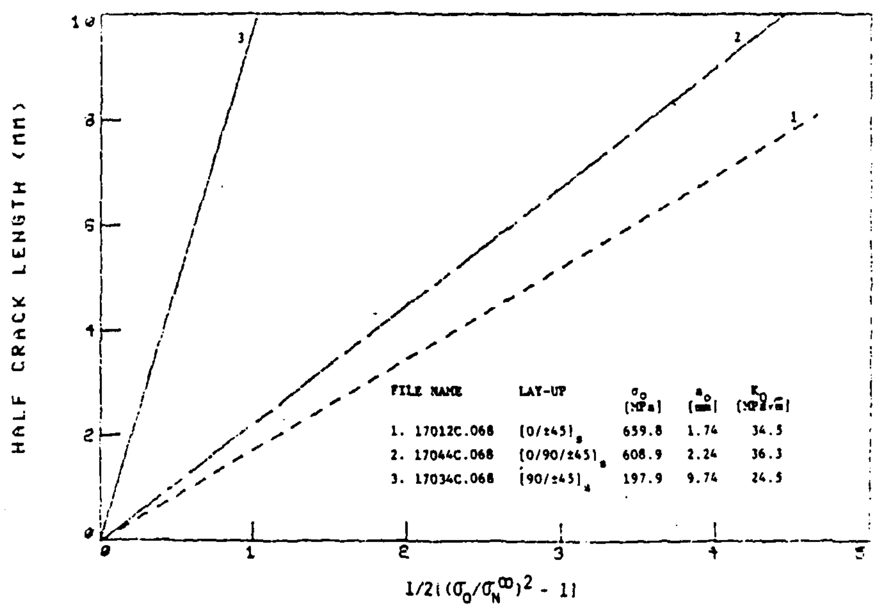

Figure 90. Best fit of a_o (WN-fracture model, "average stress criterion) for graphite/epoxy laminates.

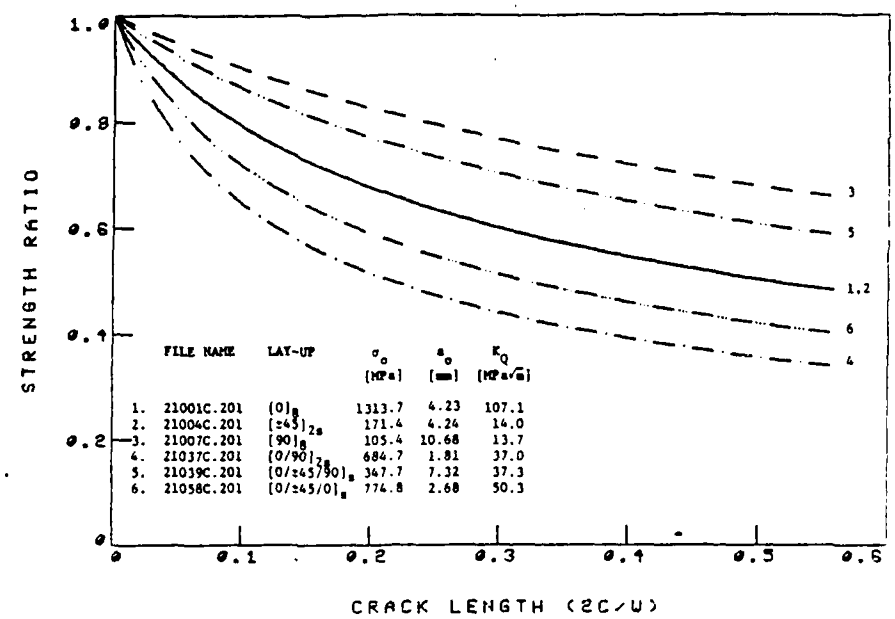

Figure 91. Notched strength versus crack length predictions (WN-fracture model, "average stress" criterion) for several 5.6 mil boron/aluminum 6061F laminates.

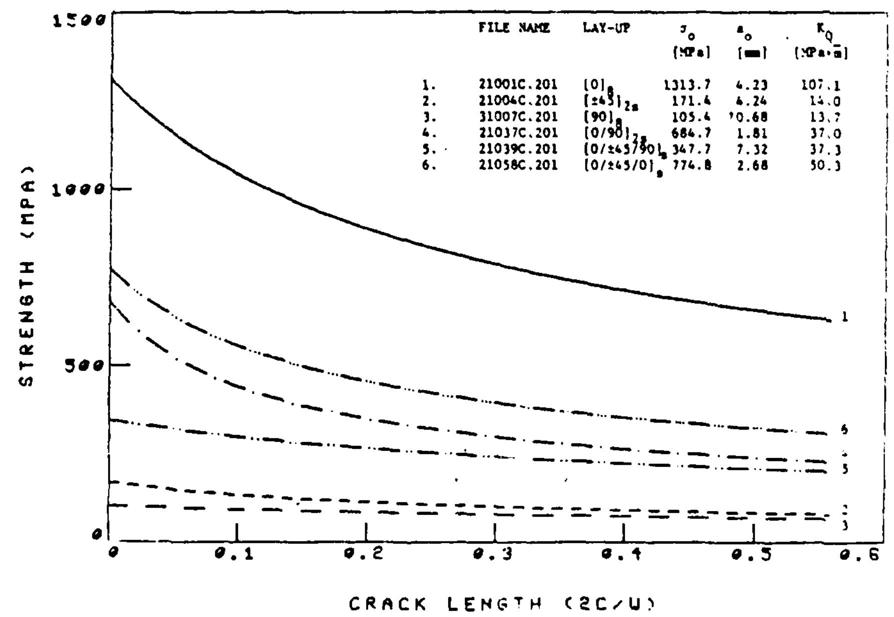

Figure 92. Notched strength versus crack length predictions (WN-fracture model, "average-stress" criterion) for several 5.6 mil boron/aluminum 6061F laminates.

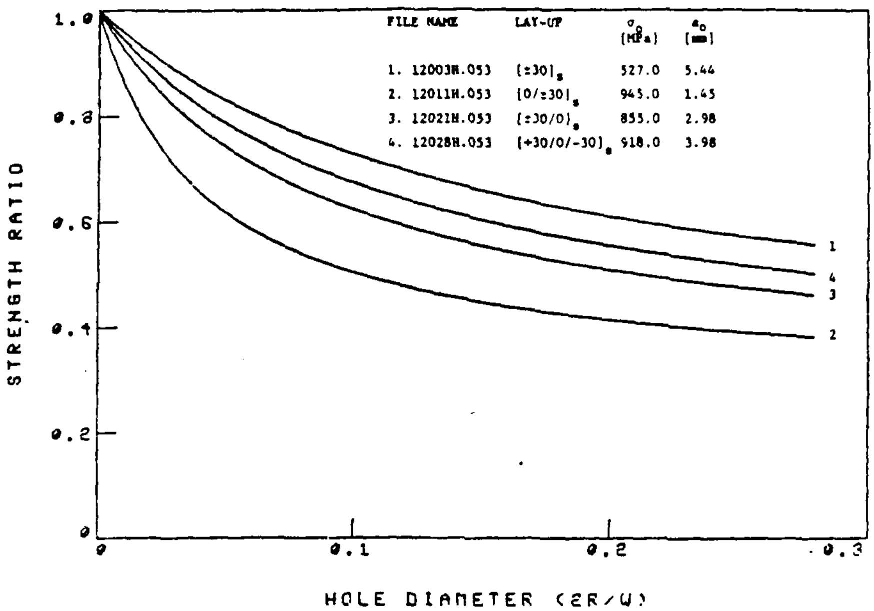

Figure 93. Notched strength versus hole diameter predictions (WN-fracture model, "average stress" criterion) for graphite/epoxy laminates showing effect of stacking sequence on notch sensitivity.

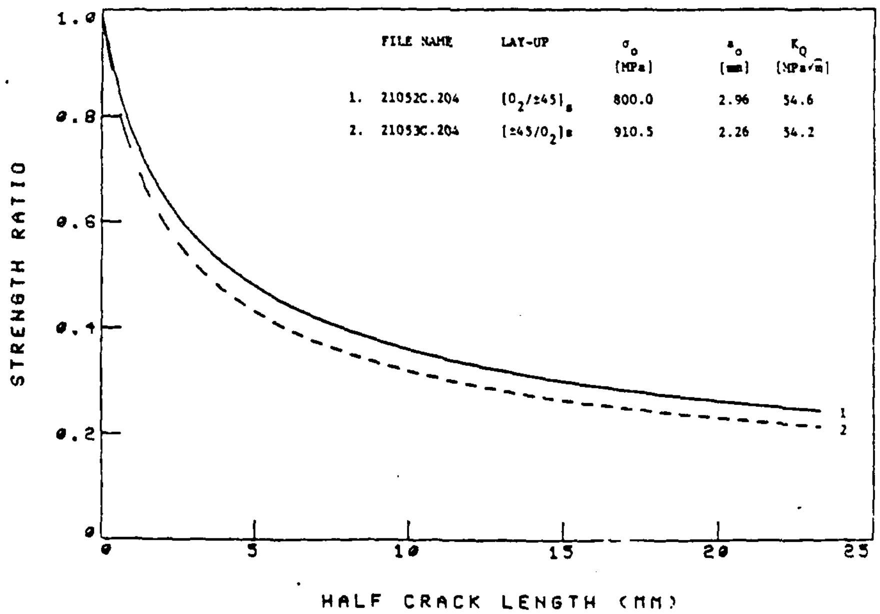

Figure 94. Effect of stacking sequence (WN-fracture model, "average-stress" criterion) on notched strength of boron/aluminum laminates containing straight cracks.

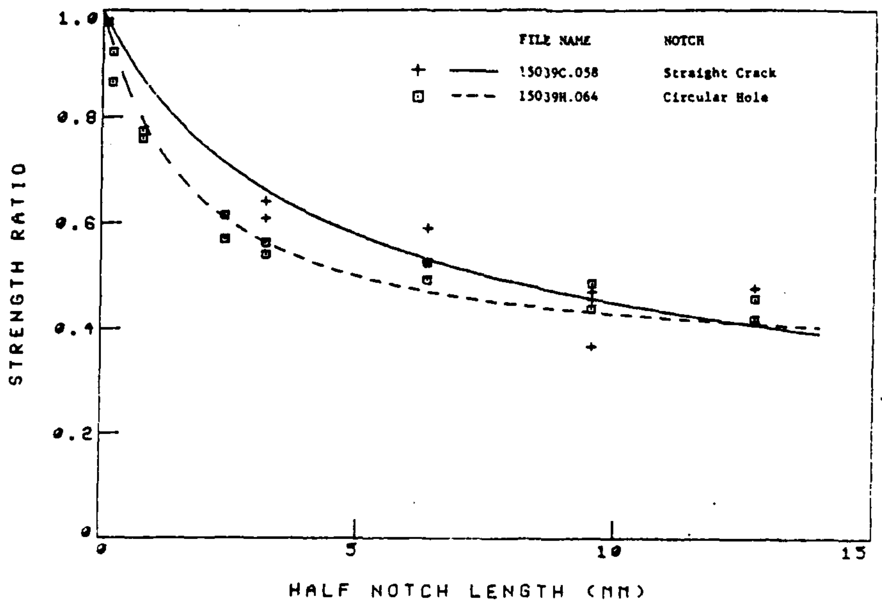

Figure 95. Notched strength versus notch length predictions (WN-fracture mod . "average stress" criterion) for graphite/epoxy $[0/\pm45/90]_s$ laminates containing circular holes and straight cracks.

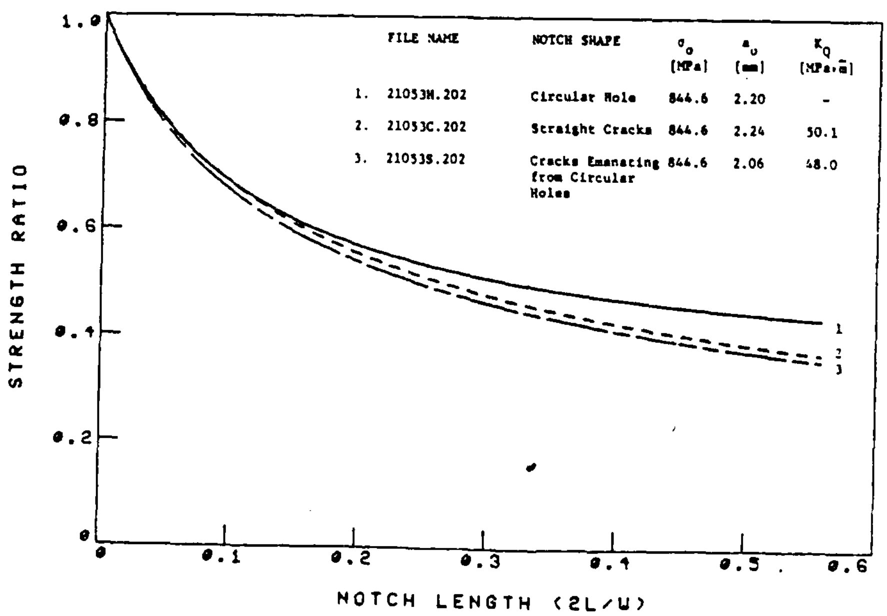

Figure 96. Effect of notch shape (WN-fracture model, "average-stress" criterion) on notched strength of boron/aluminum $[\pm45/0_2]_s$ laminates.

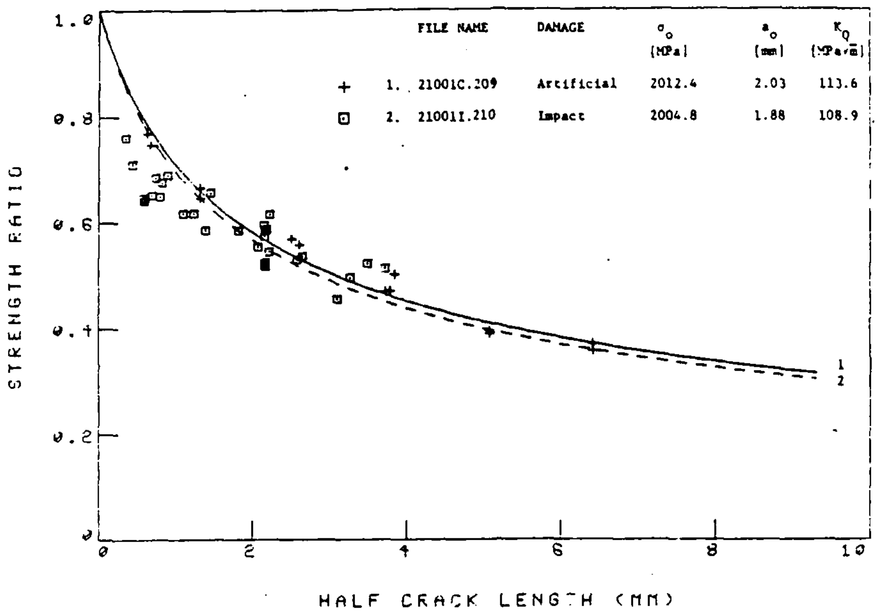

Figure 97. Residual tensile strength versus lateral damage size, due to impact and artificial damage (WN-fracture model, "average-stress" criterion) for boron/aluminum $[0]_8$ specimens.

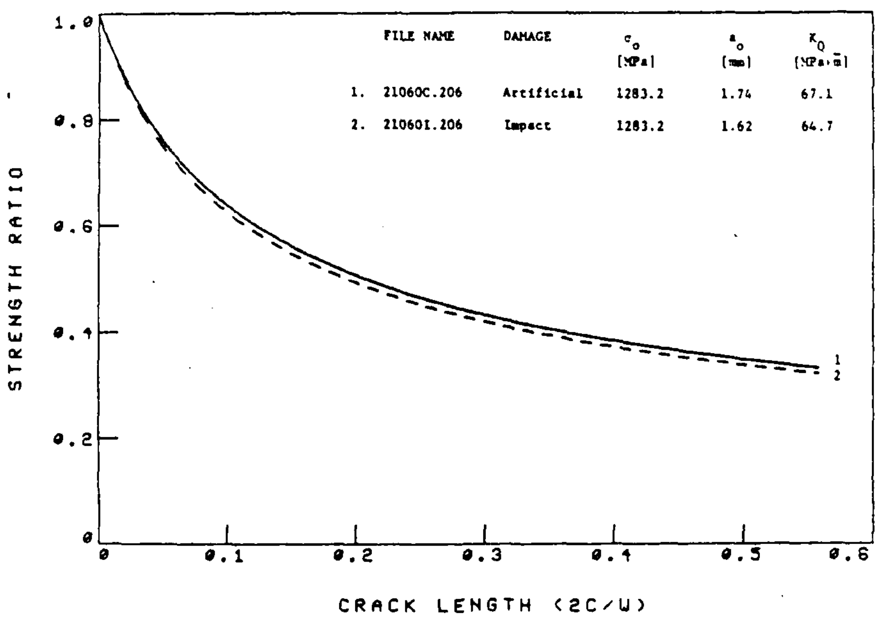

Figure 98. Residual tensile strength versus lateral damage size, due to impact and artificial damage (WN-fracture model, "average-stress" criterion) for boron/aluminum $[0/\pm22]_s$ laminates.

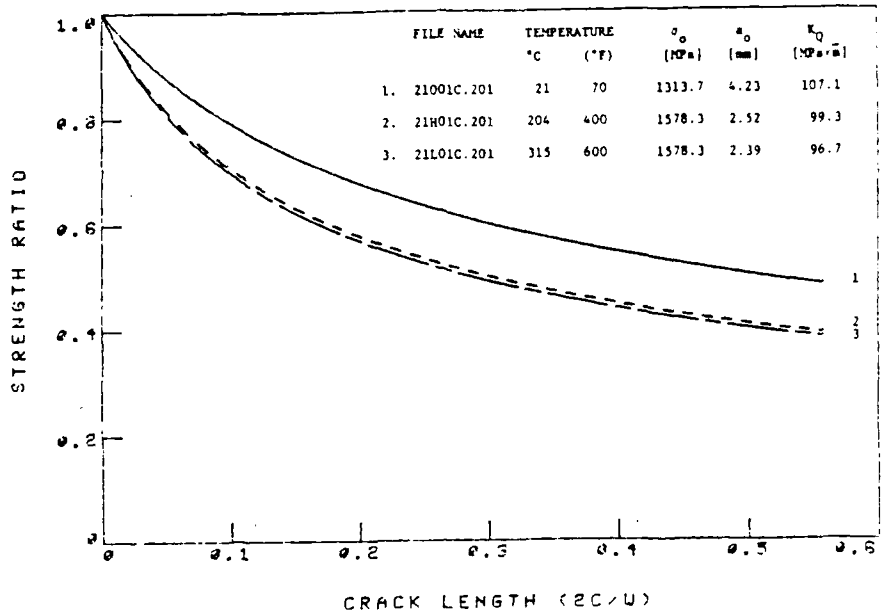

Figure 99. Effect of test temperature (WN-fracture model, "average-stress" criterion) on notched strength of boron/aluminum $[0]_8$ containing straight cracks.

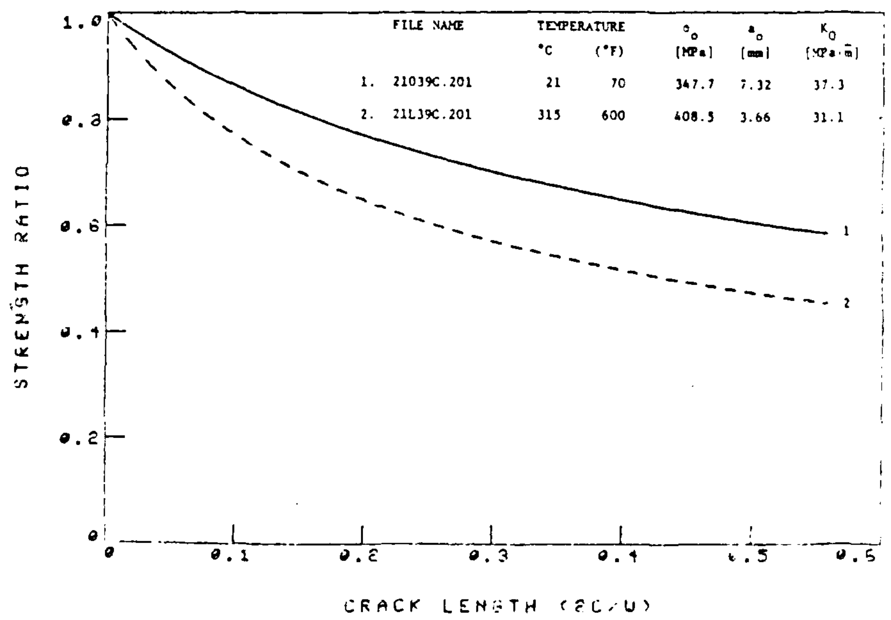

Figure 100. Effect of test temperature (WN-fracture model, "average-stress" criterion) on notched strength of boron/aluminum $[0/\pm45/90]_s$ laminates containing straight cracks.

AD-A168 005 DEVELOPMENT OF FRACTURE MECHANICS MAPS FOR COMPOSITE MATERIALS VOLUME 4(U) DEUTSCHE FORSCHUNGS- UND VERSUCHSANSTALT FUER LUFT- UND RAUMF.. H W BERGMANN 3/3

UNCLASSIFIED DEC 85 AFWAL-TR-85-4150-VOL-4 F/G 11/4 NL

END
DATE
FILMED
6-86

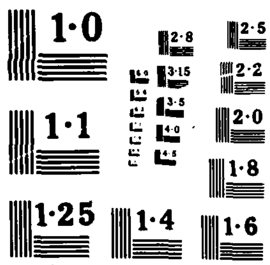
1·0
2·8
2·5
3·15
2·2
3·5
2·0
1·1
4·0
4·5
1·8
1·25
1·4
1·6

• EFFECT OF CONSTITUENTS: Significant differences in notch sensitivity (and notched strength) were obtained for a seemingly identical material system, Figure 101. These differences are attributable either to different fabrication procedures [209] or to differences in fiber strength, Figure 102. Improved notch sensitivity of unidirectional boron/aluminum can be achieved through a proper choice of constituents. Effect of constituents on notch sensitivity, Figure 103, indicates that the combination of large fiber diameter and ductile matrix leads to improved notch sensitivity characteristics. When two different aluminum alloys, e.g. 6061F and 2024F, are chosen as the matrix material, very little effect on notch sensitivity has been recorded, Figure 104. Effect of heat treatment and type of matrix, on notch sensitivity and deformation characteristics of boron/aluminum are reported in [229,234,238]. Similar systematic studies on graphite/epoxy are not conclusive.

• EFFECT OF LAMINATE CONFIGURATION ON FRACTURE MODEL PARAMETERS: The effect of lamination angle on the characteristic dimension, a_o, (WN-average stress criterion) for angle-ply $[\pm\theta]_{2s}$ laminates is shown in Figure 105, indicating that the largest value (i.e. the least notch sensitivity) occurs for $[\pm 45]_{2s}$ laminate. With the addition of a 0° ply (e.g. $[0/\pm\theta]_s$, $[\pm\theta/0]_s$, and $[+\theta/0/-\theta]_s$) the dependence of a_o on θ is reversed, i.e. the value of a_o is smallest for $\theta \approx 45°$, Figures 106-108, indicating the highest notch sensitivity for that angle. Similar results were obtained for a_c in the WEK-fracture model. No such correlation could be established between the PWG-fracture model parameters (i.e. a_c and a_m) and the angle θ of the four laminates. The effect of the angle θ on the relative notch sensitivity parameter, R_{ns}, is shown in Figures 109-110, indicating that it is independent of ply orientation for most cases. Similarly, no correlation between the ML-fracture model parameters, i.e. n and H_C/σ_o and the angle θ could be established, Figures 111-114.

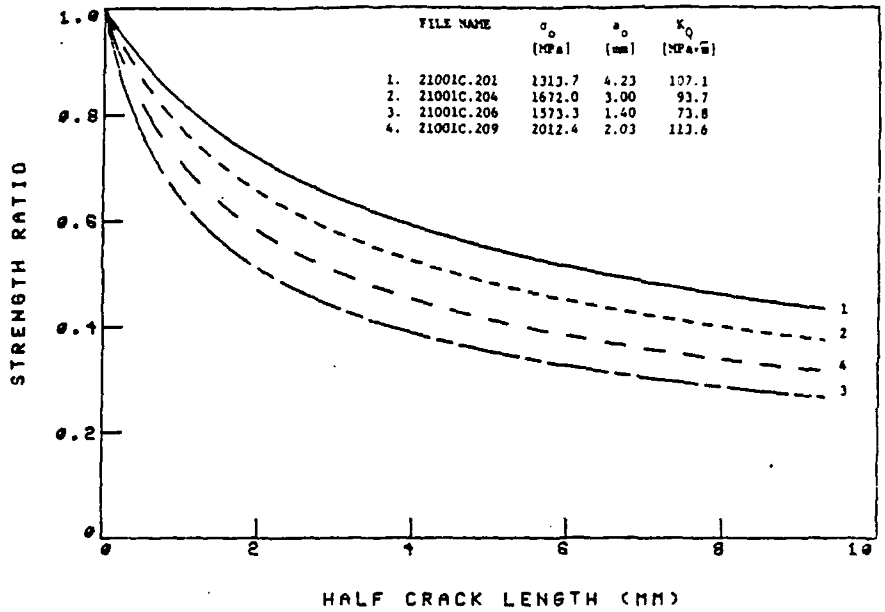

Figure 101. Notched strength versus crack length predictions (WN-fracture model, "average stress" criterion) for boron/aluminum $[0]_8$ laminates.

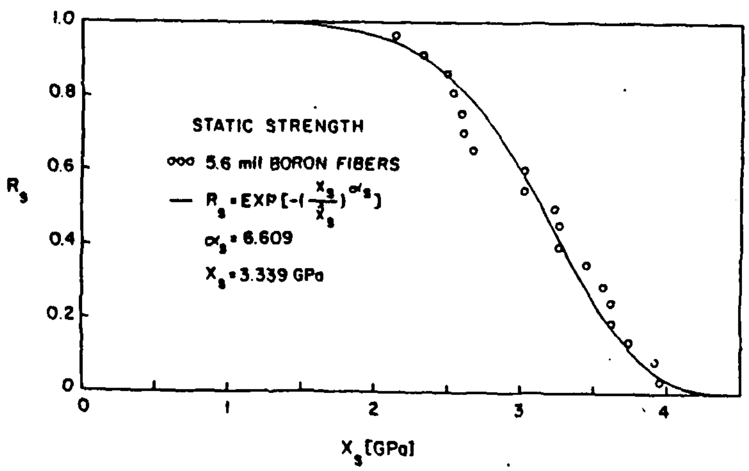

Figure 102. Static strength distribution of individual 5.6 mil diameter boron fibers [201].

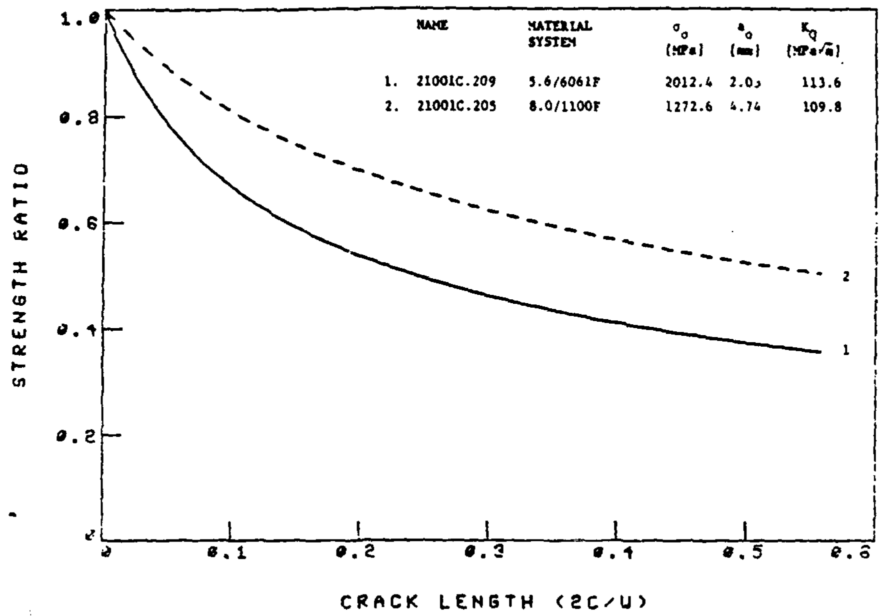

Figure 103. Notched strength versus crack length predictions (WN-fracture model), "average-stress" criterion) for unidirectional boron/aluminum with different constituents.

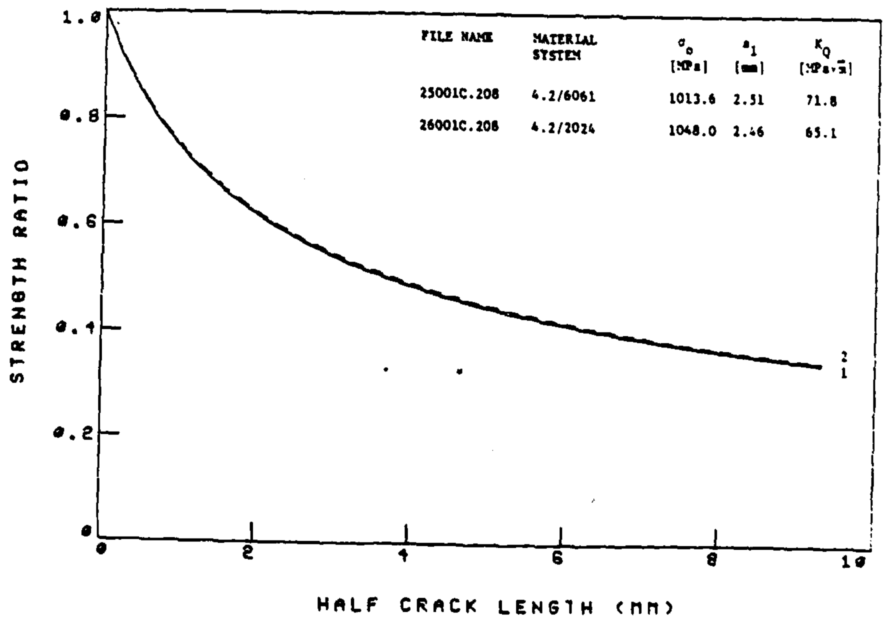

Figure 104. Notched strength versus crack length predictions (WN-fracture model, "average stress" criterion) for unidirectional borsic/aluminum with different aluminum matrices.

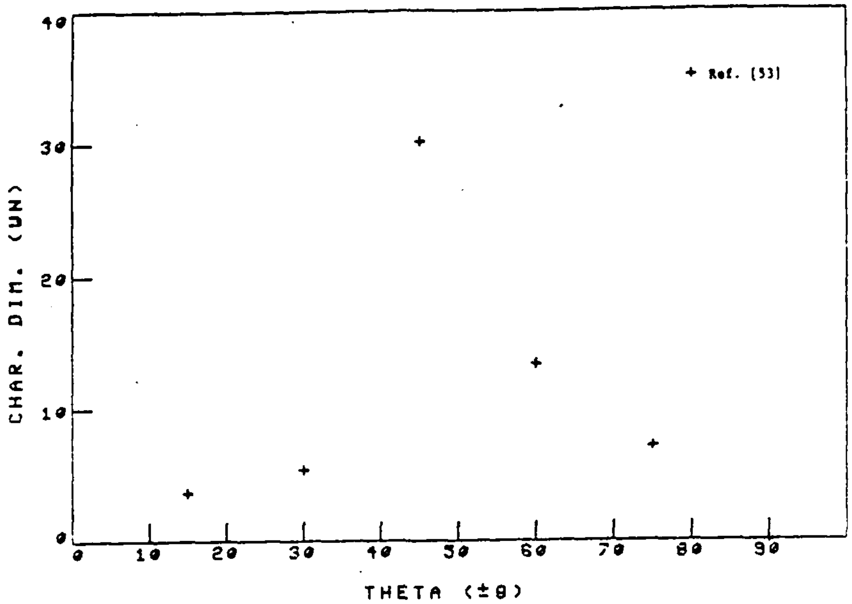

Figure 105. Experimental values of characteristic dimension, a_o, (WN-fracture model "average stress" criterion) as a function of angle for graphite/epoxy $[\pm\theta]_s$ laminates containing circular holes. Individual data are given in Table 11 and Appendix B.

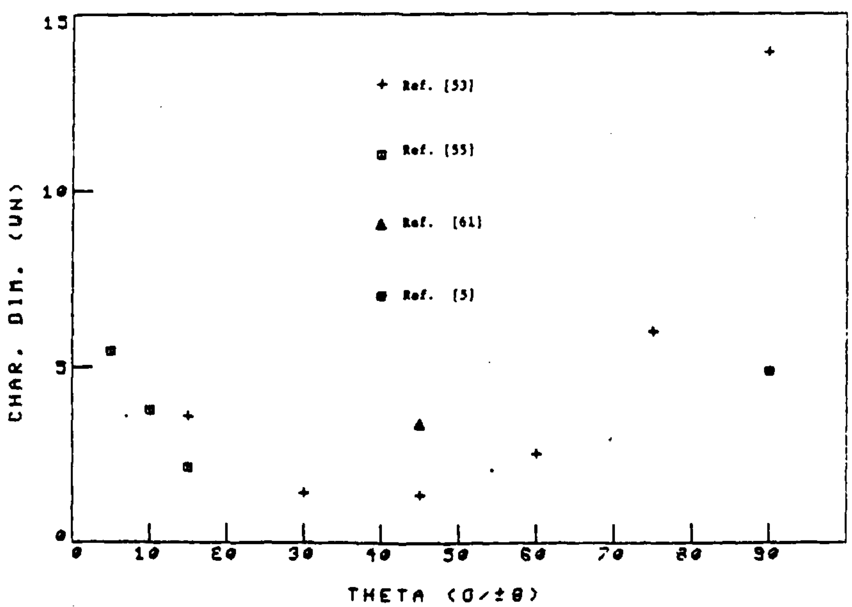

Figure 106. Experimental values of characteristic dimension, a_o, (WN-fracture model "average stress" criterion) as a function of angle for graphite/epoxy $[0/\pm\theta]_s$ laminates containing circular holes. Individual data are given in Table 11 and Appendix B.

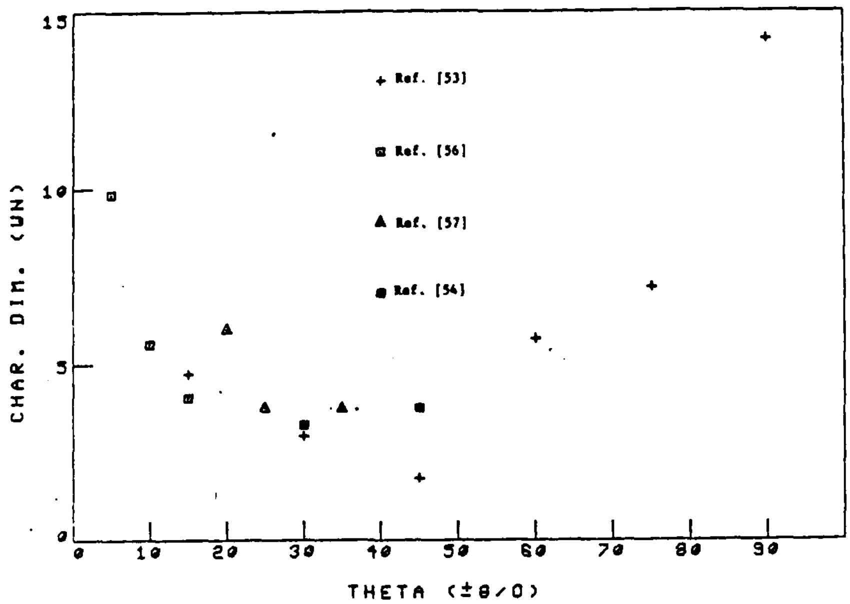

Figure 107. Experimental values of characteristic dimension, a_o, (WN-fracture model "average stress" criterion) as a function of angle for graphite/epoxy $[\pm\theta/0]_s$ laminates containing circular holes. Individual data are given in Table 11 and Appendix B.

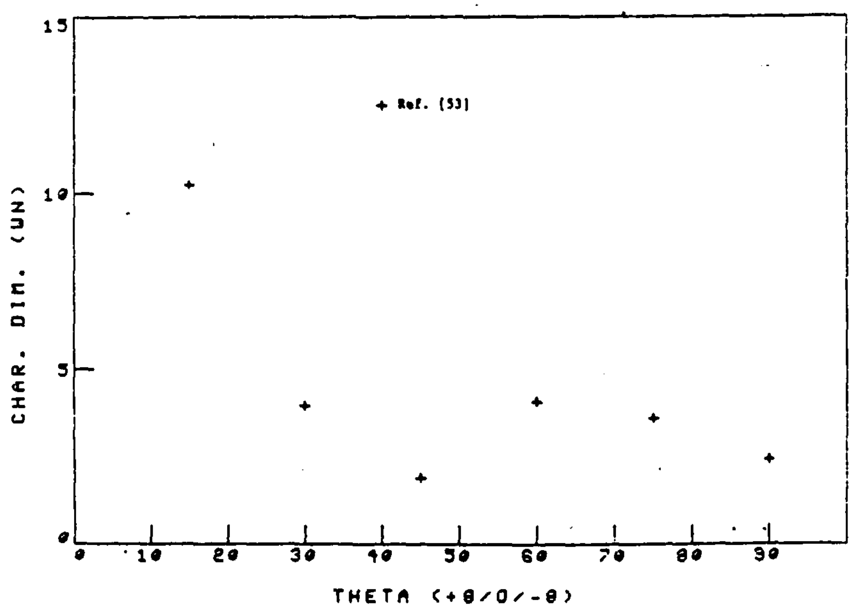

Figure 108. Experimental values of characteristic dimension, a_o, (WN-fracture model, "average stress" criterion) as a function of angle for graphite/epoxy $[+\theta/0/-\theta]_s$ laminates containing circular holes. Individual data are given in Table 11 and Appendix B.

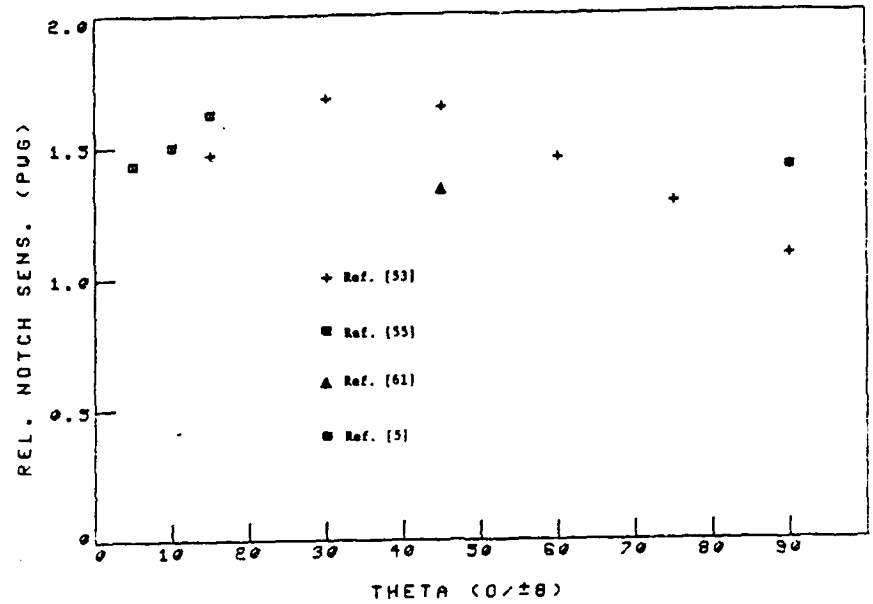

Figure 109. Experimental data of relative notch sensitivity, R_{ns}, (PWG-fracture model) as a function of angle for graphite/epoxy $[0/\pm\theta]_s$ laminates containing circular holes. Individual data are given in Table 13 and Appendix D.

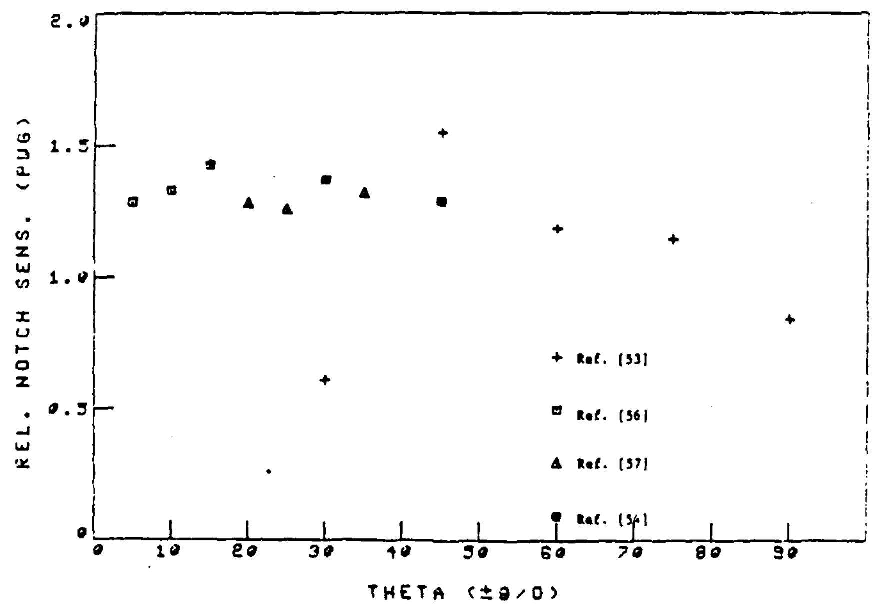

Figure 110. Experimental data of relative notch sensitivity, R_{ns}, (PWG-fracture model) as a function of angle for graphite/epoxy $(\pm\theta/0)_s$ laminates containing circular holes. Individual data are given in Table 13 and Appendix D.

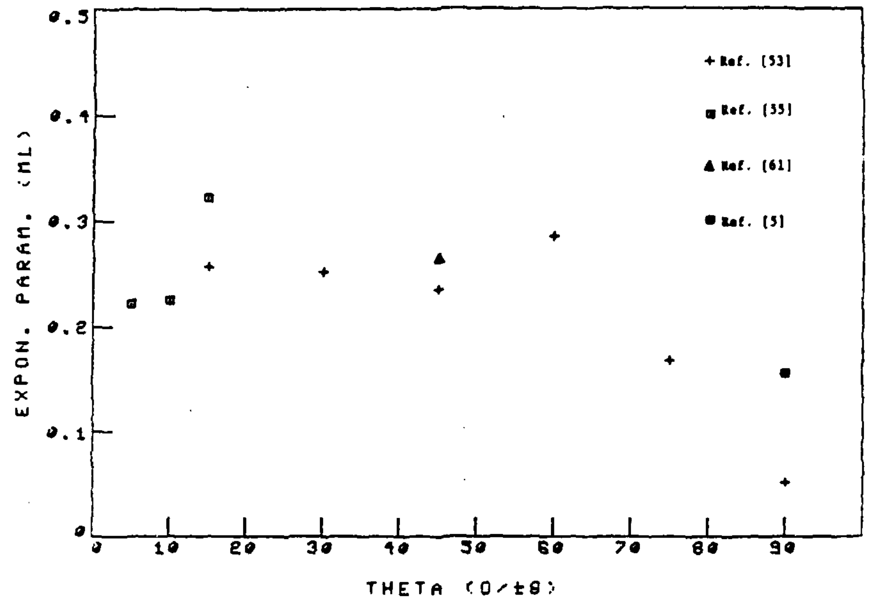

Figure 111. Experimental values of exponential parameter, n, (ML-fracture model) as a function of angle for graphite/epoxy [0/±θ]$_s$ laminates containing circular holes. Individual data are given in Table 14 and Appendix E.

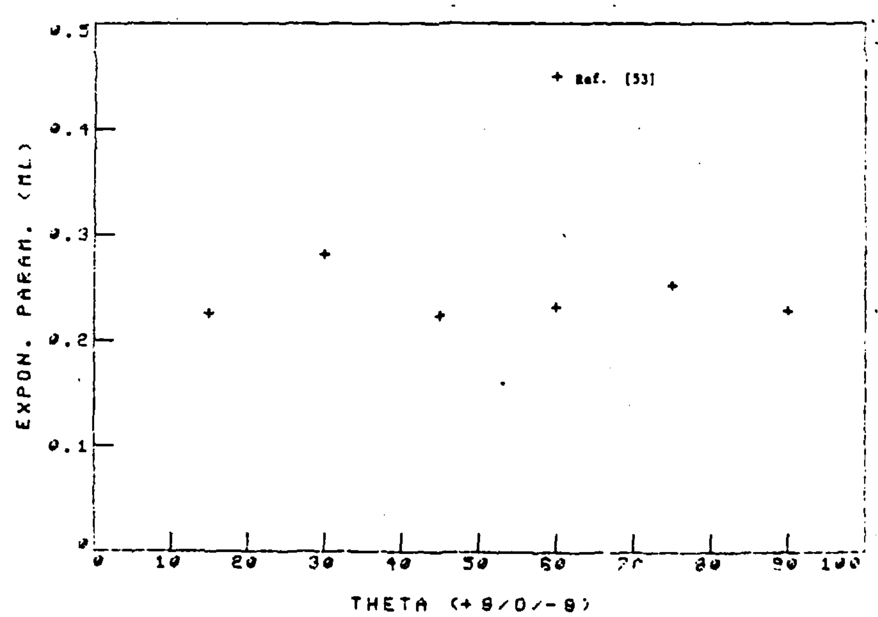

Figure 112. Experimental values of exponential parameter, n, (ML-fracture model) as a function of angle for graphite/epoxy [+θ/0/-θ]$_s$ laminates containing circular holes. Individual data are given in Table 14 and Appendix E.

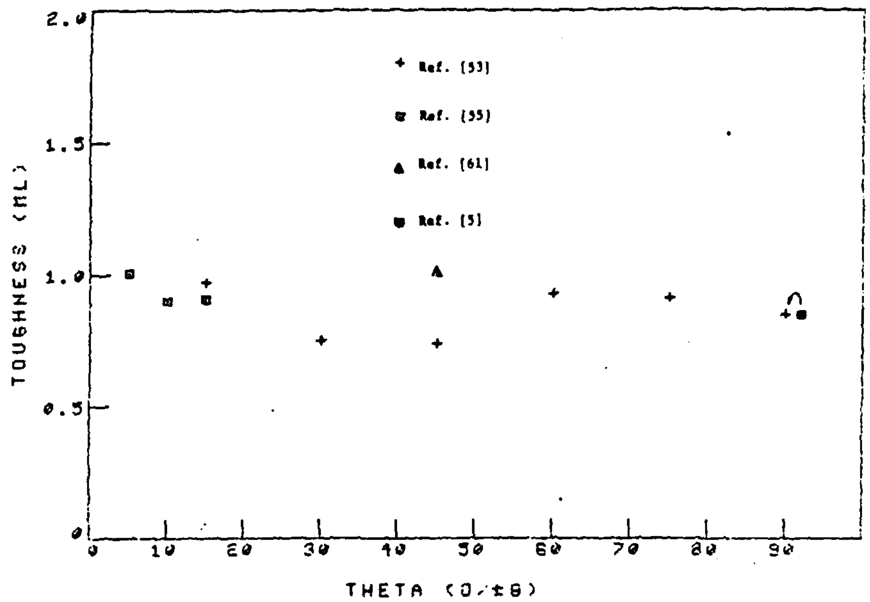

Figure 113. Experimental values of fracture toughness, K_c/σ_o, (ML-fracture model) as a function of angle for graphite/epoxy $[0/\pm\theta]_s$ laminates containing circular holes. Individual data are given in Table 14 and Appendix E.

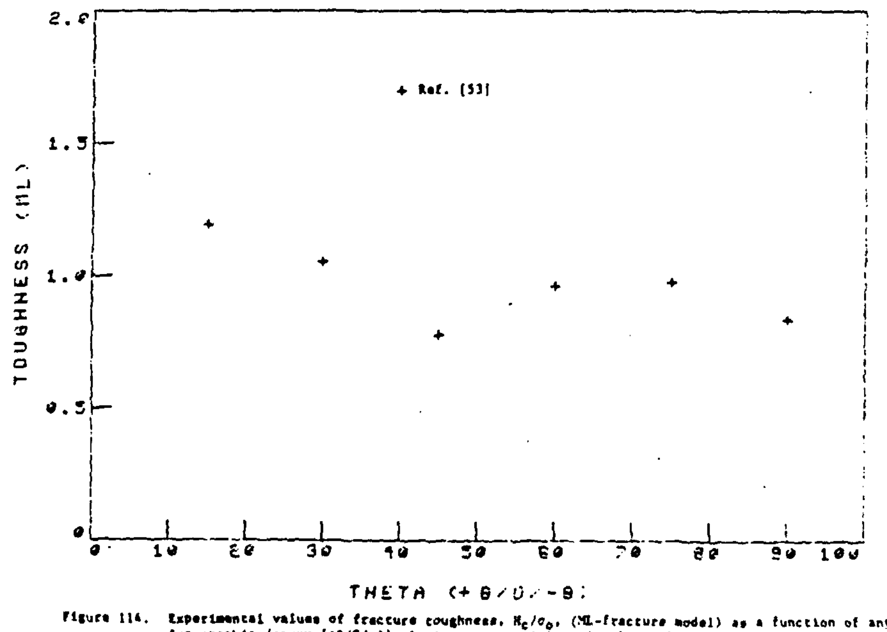

Figure 114. Experimental values of fracture toughness, K_c/σ_o, (ML-fracture model) as a function of angle for graphite/epoxy $[+\theta/0/-\theta]_s$ laminates containing circular holes. Individual data are given in Table 14 and Appendix E.

CORRELATION BETWEEN NOTCH SENSITIVITY AND FRACTURE MODEL PARAMETERS: The different fracture models reviewed in this report utilize a variety of parameters associated with each model and which must be determined experimentally. In all the models it is assumed that these parameters are constant, i.e. independent of notch size, and are to be considered as material parameters. It is of interest to identify which of these parameters can be correlated to the notch sensitivity of composite laminates containing circular holes and straight cracks. For this purpose, the ratio of notched to unnotched strength (σ_N^∞/σ_o) at a specific notch size has been recorded from the data such as those listed in Table 11, and it has been correlated with the various parameters associated with the different fracture models. The notch sizes for which σ_N^∞/σ_o was recorded are: $2R/W = 0.25$ for graphite/epoxy laminates containing holes; and $2c/W = 0.30$ for boron/aluminum laminates containing straight cracks. The correlation between the notched strength and the various parameters is shown in Figures 115 to 134. Each point in these Figures represents a set of notched strength data as shown for example in Table 11. Consequently, these Figures combined all the sets of notched strength data reviewed, irrespective of material system, constituents properties, fabrication procedures, laminate configuration, stacking sequence, specimen geometry, loading procedure, etc. Thus, significant scatter exists in the values of all the parameters and it is emphasized that conclusions regarding the presence or absence of correlation can only be qualitative, i.e. restricted to the specific specimen geometry, loading function, etc. which are analyzed in this study. It should be noted that although the results shown in Figures 115 to 134 are for a specific notch size (of $2R/W = 0.25$ and $2c/W = 0.3$), similar Figures and correlations are obtained for all other notch sizes.

a. WEK-fracture model (Figures 115-116): A correlation exists between notch sensitivity and a_c. The smaller a_c is, the more notch sensitive the subject material. This is to be expected from Eq. (11). The few exceptions are for the data depicted from Refs. [204] and [208] as indicated in Figure 116. The values of a_c for the laminates tested in [204] are based on approximately 20 notched strength data for each laminate. However, the data were obtained from three different specimen widths, 19.1 mm, 50.8 mm and 101.6 mm. It is possible therefore that lumping all notched strength data of the different laminates widths is the cause for this discrepancy. The data given in [208] are for 4.2 mil borsic/aluminum which is a different system from the 5.6 mil boron/aluminum laminates tested in most other sets of data.

b. WN-fracture model (Figures 117-120): A correlation exists between notch sensitivity and d_o, Figures 117-118, and a_o, Figures 119-120. The smaller the characteristic distances are, the more notch sensitive the subject material, as expected from Eqs. (23,27) and (25,31), respectively.

c. K-fracture model (no Figures): No correlation could be found between the notch sensitivity and k_o.

d. PWG-Fracture model (Figures 121-130): No correlation could be found between notch sensitivity and the various parameters, i.e. exponential parameters, m, Figures 121-122, the notch sensitivity factors C and K, Figures 123-124, the notch shift parameters, a_c and a_K, Figures 125-126, and the notch sensitivity factors, a_m, Figures 127-128. The only exception is in regard to the relative notch sensitivities R_{ns} and $\hat{a}_{Km}$, Figures 129-130, which show a clear correlation between their values and the notch sensitivity. The larger R_{ns} and $\hat{a}_{Km}$ are, the more notch sensitive the subject material is. This correlation is expected considering the definition of these two parameters given previously.

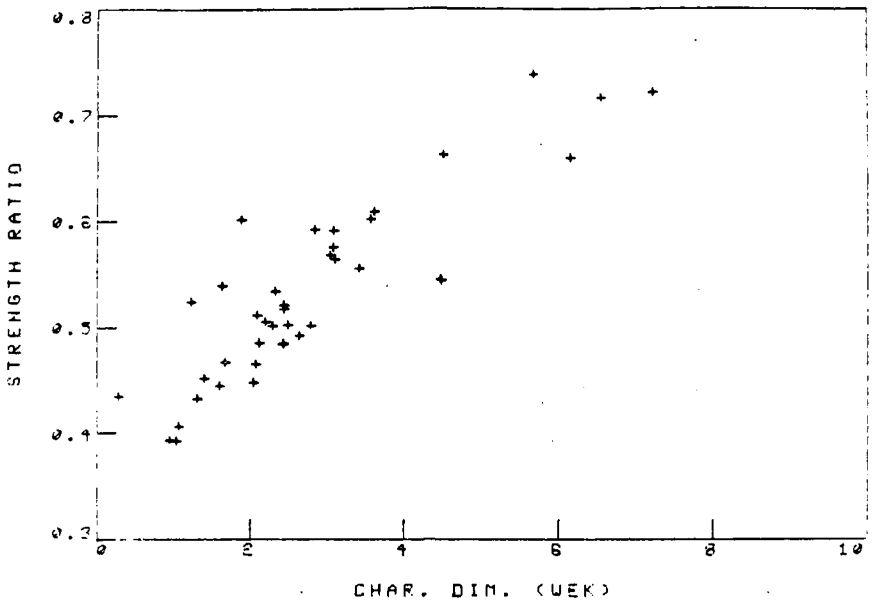

Figure 115. Correlation between notched strength ratio (for 2R/W = 0.25) and characteristic dimensions, a_c, (WEK-fracture model) for graphite/epoxy laminates containing circular holes.

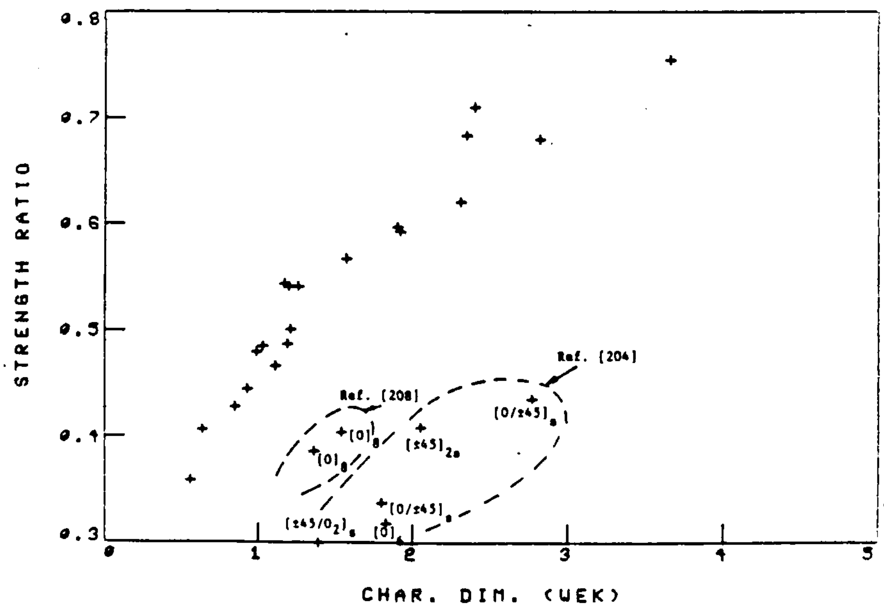

Figure 116. Correlation between notched strength ratio (for 2c/W = 0.3) and characteristic dimension, a_c, (WEK-fracture model) for boron/aluminum laminates containing straight cracks.

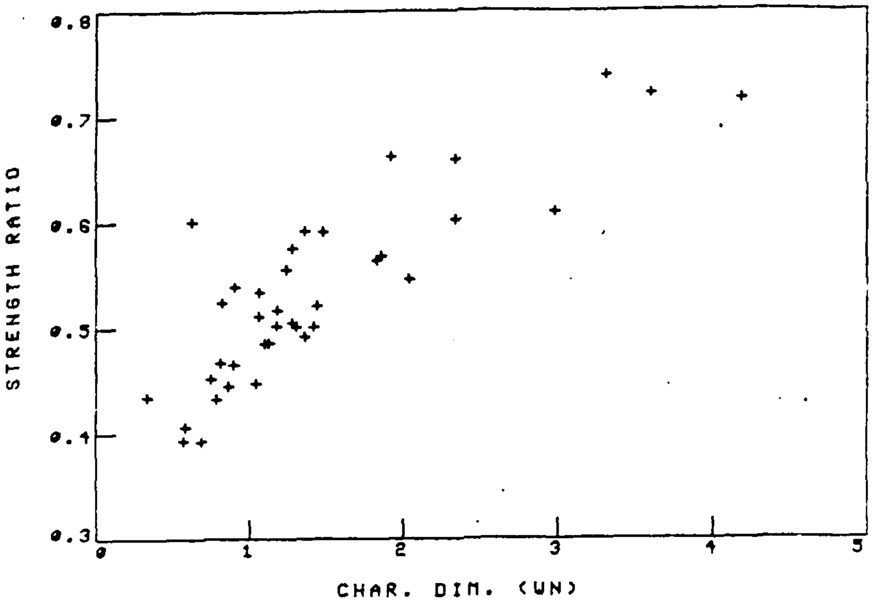

Figure 117. Correlation between notched strength ratio (for 2R/W = 0.25) and characteristic dimension, d_o, (WN-fracture model, "point stress" criterion) for graphite/epoxy laminates containing circular holes.

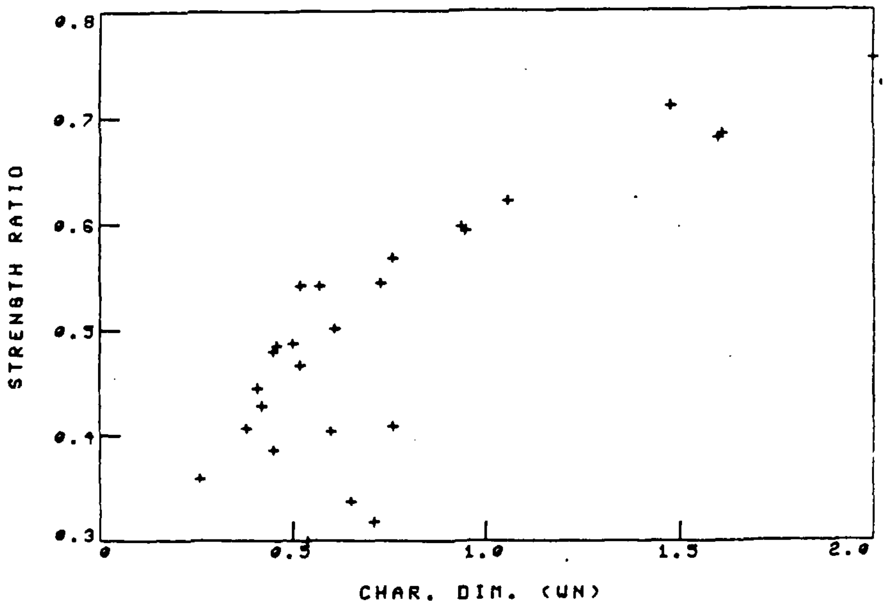

Figure 118. Correlation between notched strength ratio (for 2c/W = 0.3) and characteristic dimension, d_o, (WN-fracture model, "point-stress" criterion) for boron/aluminum laminates containing straight cracks.

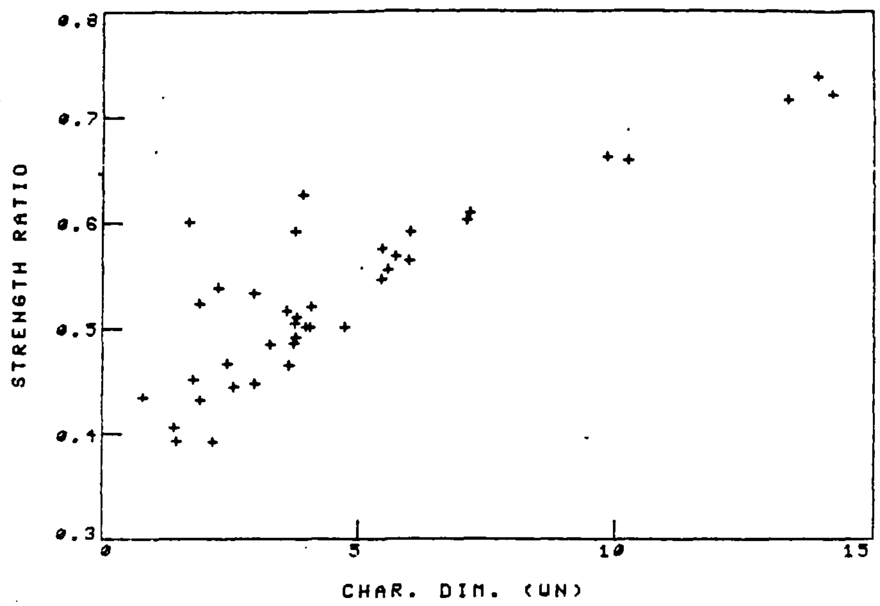

Figure 119. Correlation between notched strength ratio (for 2R/W = 0.25) and characteristic dimension, a_o. (WN-fracture model, "average stress" criterion) for graphite/epoxy laminates containing circular holes.

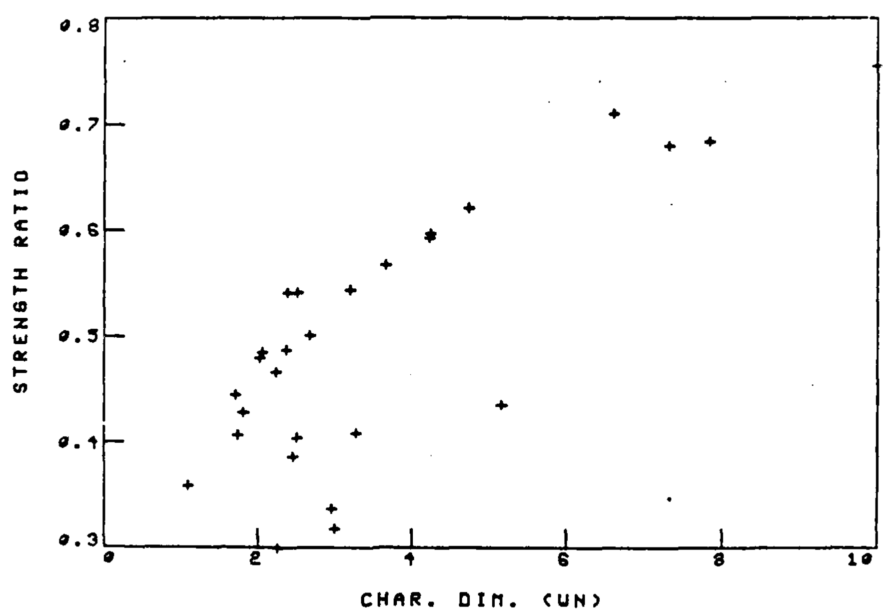

Figure 120. Correlation between notched strength ratio (for 2c/W = 0.3) and characteristic dimension, a_o, (WN-fracture model, "average-stress" criterion) for boron/aluminum laminates containing straight cracks.

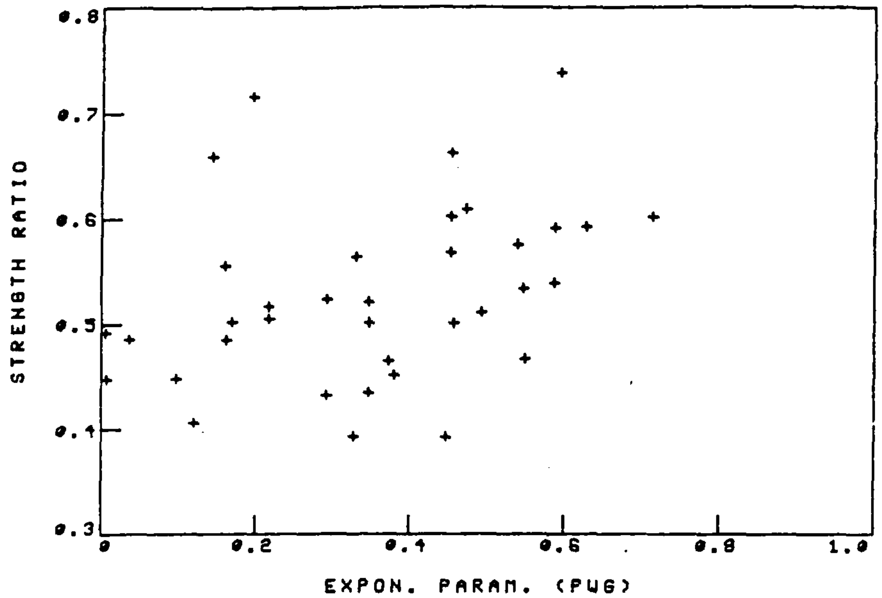

Figure 121. Correlation between notched strength ratio (for 2R/W = 0.25) and exponential parameter, m, (PWG-fracture model) for graphite/epoxy laminates containing circular holes.

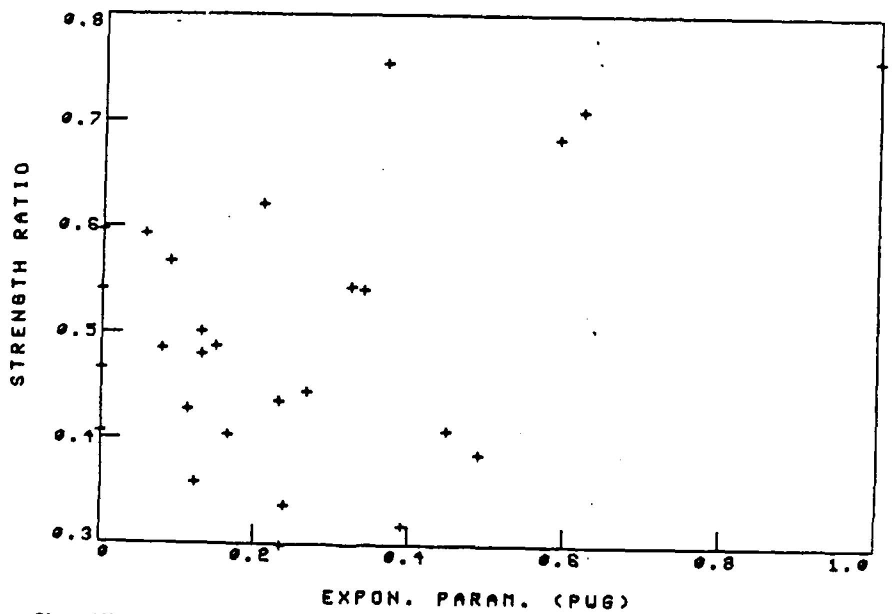

Figure 122. Correlation between notched strength ratio (for 2c/W = 0.3) and exponential parameter, m, (PWG-fracture model) for boron/aluminum laminates containing straight cracks).

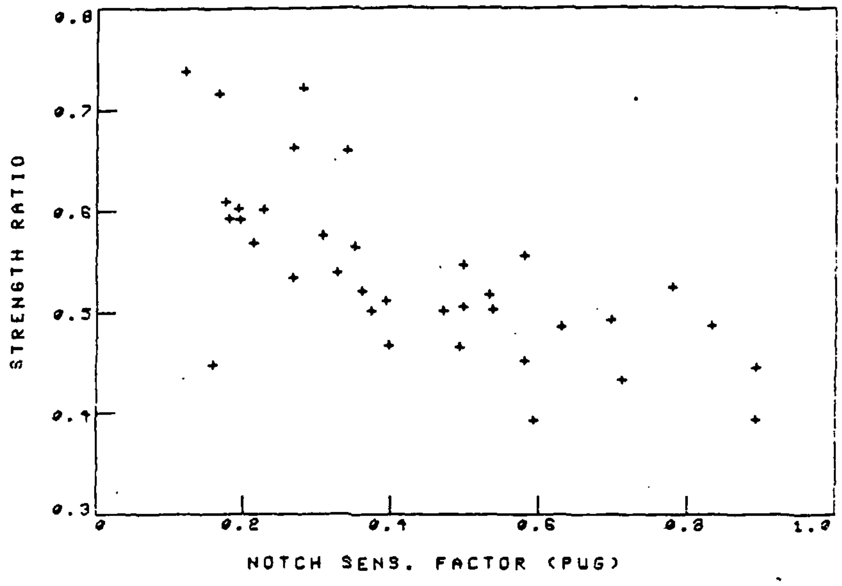

Figure 123. Correlation between notched strength ratio (for 2R/W = 0.25) and notch sensitivity factor, C, (PWG-fracture model) for graphite/epoxy laminates containing circular holes.

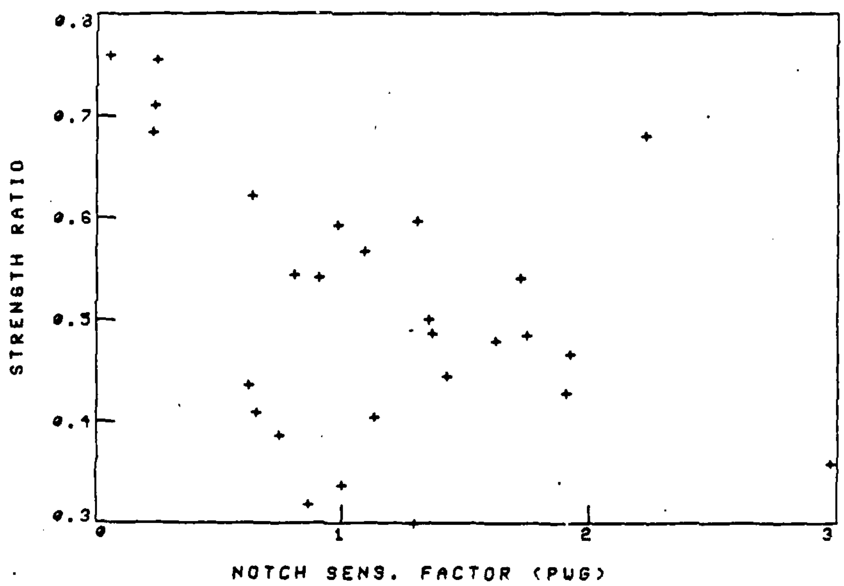

Figure 124. Correlation between notched strength ratio (for 2c/W = 0.3) and notch sensitivity factor, K, (PWG-fracture model) for boron/aluminum laminates containing straight cracks.

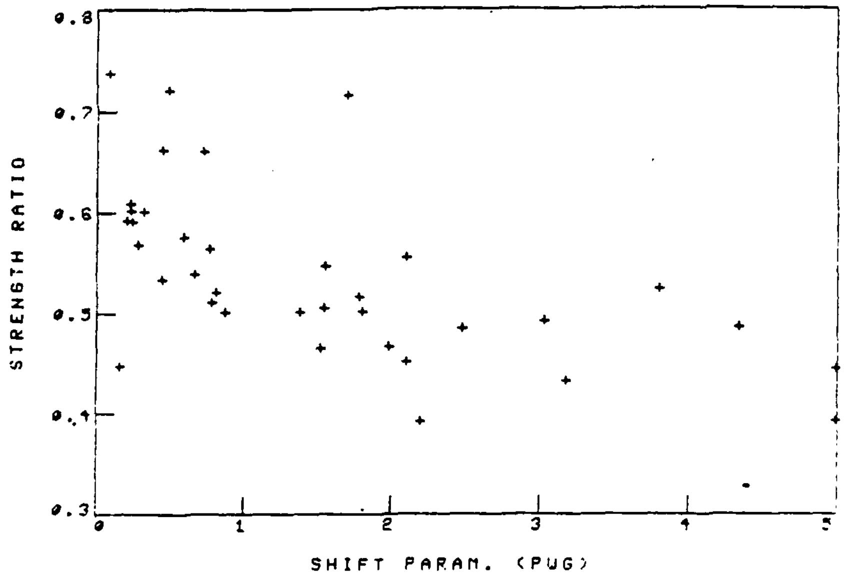

Figure 125. Correlation between notched strength ratio (for 2R/W = 0.25) and shift parameter, a_c. (PWG-fracture model) for graphite/epoxy laminates containing circular holes.

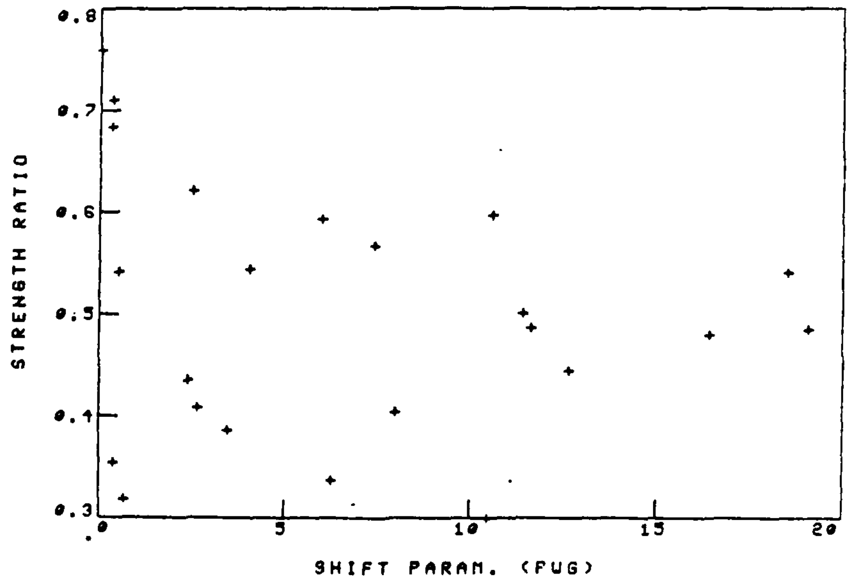

Figure 126. Correlation between notched strength ratio (for 2c/W = 0.3) and shift parameter, a_x. (PWG-fracture model) for boron/aluminum laminates containing straight cracks.

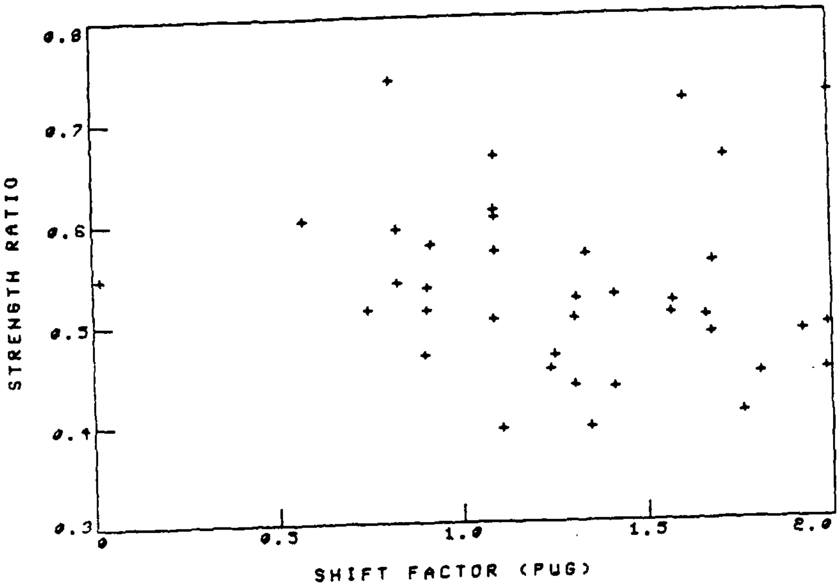

Figure 127. Correlation between notched strength ratio (for 2R/W = 0.25) and shift factor, a_m, (PWG-fracture model) for graphite/epoxy laminates containing circular holes.

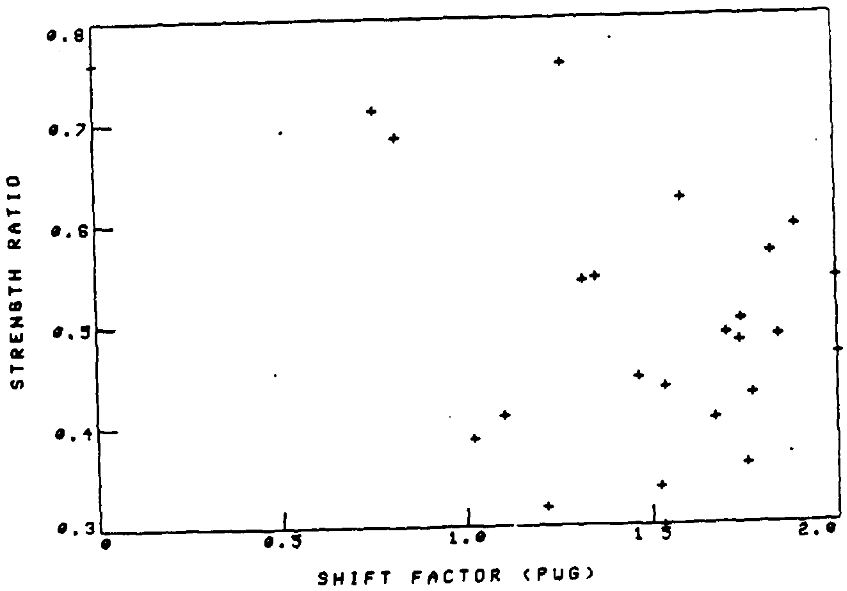

Figure 128. Correlation between notched strength ratio (for 2c/W = 0.3) and shift factor, a_m, (PWG-fracture model) for boron/aluminum laminates containing straight cracks.

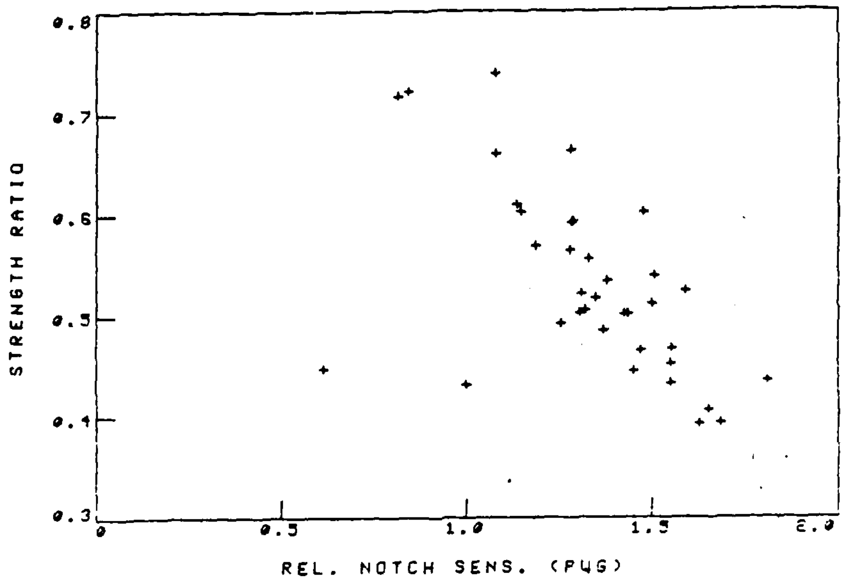

Figure 129. Correlation between notched strength ratio (for $2R/W = 0.25$) and relative notch sensitivity, R_{ns}, (PWG-fracture model) for graphite/epoxy laminates containing circular holes.

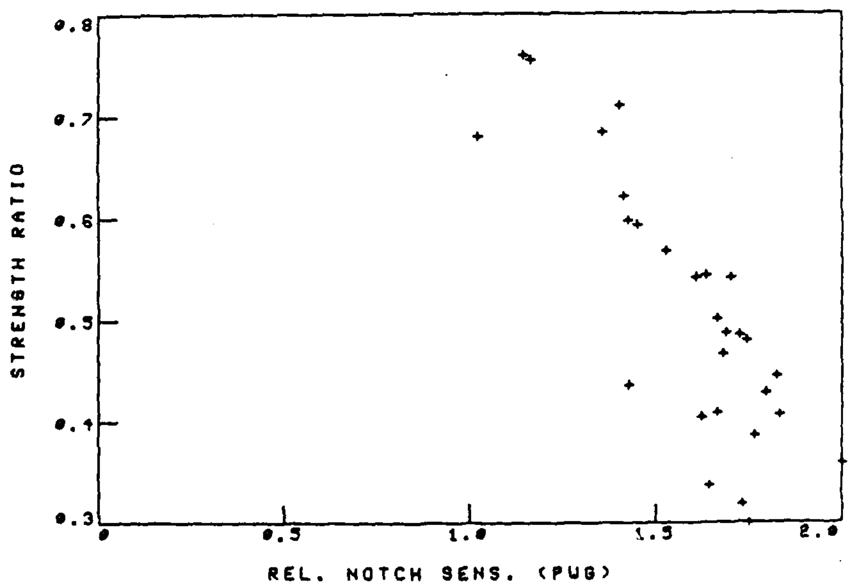

Figure 130. Correlation between notched strength ratio (for $2c/W = 0.3$) and relative notch sensitivity, R_{ns}, (PWG-fracture model) for boron/aluminum laminates containing straight cracks ($R_{ns} = \log_{10} \dot{a}_{Km}$).

The results shown in Figures 121-128 indicate that no correlation could be established between the various parameter (m, C, K, a_m, a_C, and a_x) and the notch sensitivity C and K of composite laminates containing either circular holes or straight cracks. Although the parameteric analysis shown in Figures 33 and 34 for holes and 50 and 51 for cracks indicate that there is a direct correlation between m, C, K, and notch sensitivity, i.e. larger values evidence higher notch sensitivity, it should be recalled that these parametric analyses were performed where only one of the parameters was a variable while the other parameter was held constant. As previously discussed, each laminate is characterized by a different pair of m ard C or m and K (for holes and cracks, respectively). For all practical purposes, no correlation can be made between their specific values for a given composite laminate and the notch sensitivity of that laminate. Similarly, no such correlation can be made with any of the other parameters associated with the PWG-fracture model, except the relative notch sensitivities R_{ns} and $\hat{a}_{Km}$.

e. <u>ML-Fracture model (Figures 131-134)</u>: *No correlation could be found* between the exponential parameter, n, and notch sensitivity, Figures 131-132. For laminates containing circular holes, most values are between 0.1 to 0.4; while for laminates containing straight cracks, the values range between 0.2 to 0.45, all with very large scatter. Neither could any correlation be found between the composite fracture toughness, H_C/σ_o, and notch sensitivity, Figures 133-134. The values of H_C/σ_o range between 0.8 to 1.2 for laminates containing both circular holes and straight cracks.

f. <u>Effect of Model Parameters Selection on Predictions (Figure 135)</u>: Finally, many studies address whether the constants associated with the different fracture models are independent of either material system or laminate configuration. The results shown previously clearly indicate that all the constants strongly depend

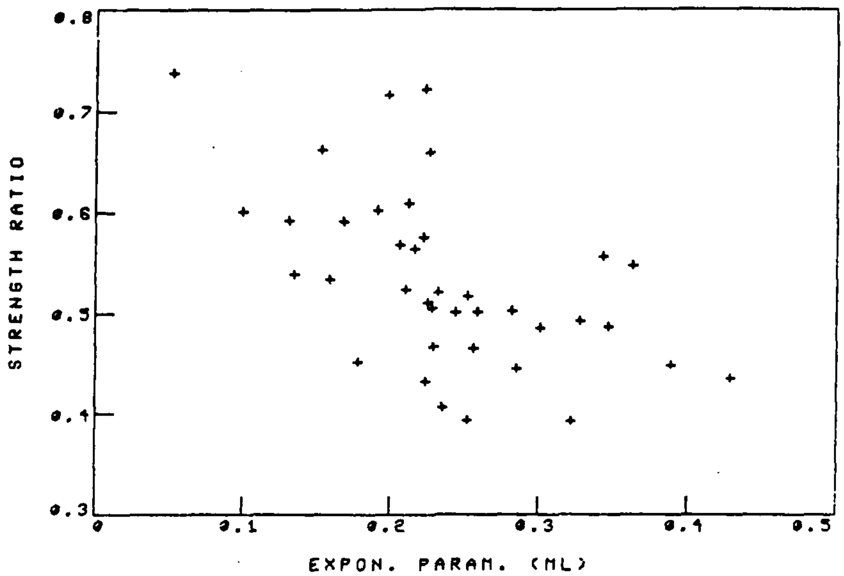

Figure 131. Correlation between notched strength ratio (for $2R/W = 0.25$) and exponential parameter, n, (ML-fracture model) for graphite/epoxy laminates containing circular holes.

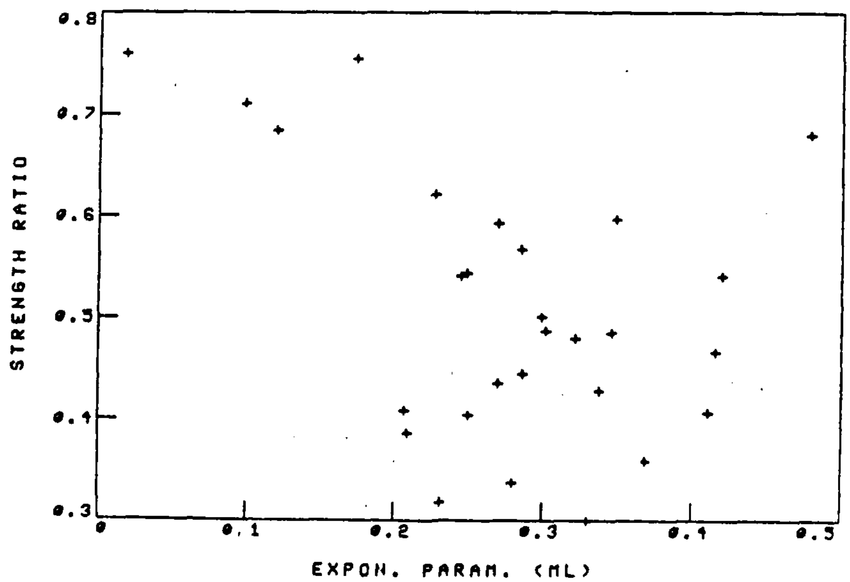

Figure 132. Correlation between notched strength ration (for $2c/W = 0.3$) and exponential parameter, n, (ML-fracture model) for boron/aluminum laminates containing straight cracks.

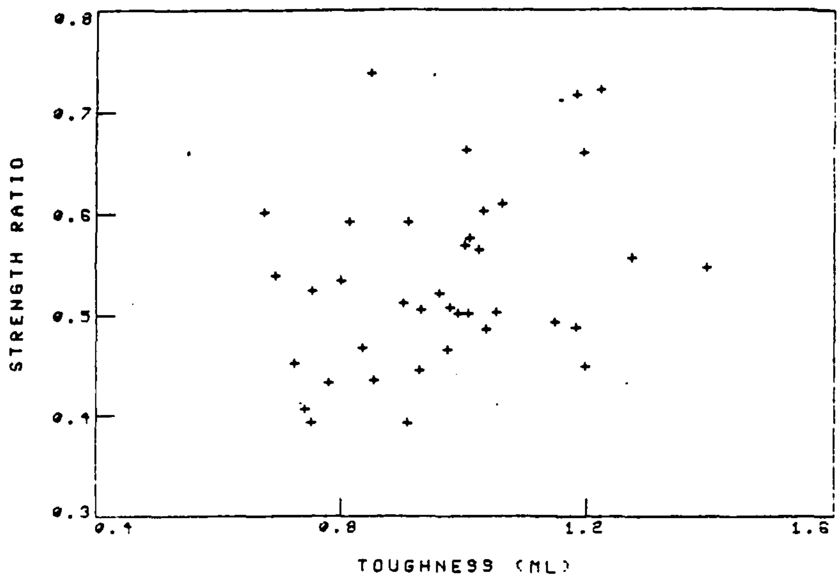

Figure 133. Correlation between notched strength ratio (for $2R/W = 0.25$) and composite fracture toughness, H_C/σ_o, (ML-fracture model) for graphite/epoxy laminates containing circular holes.

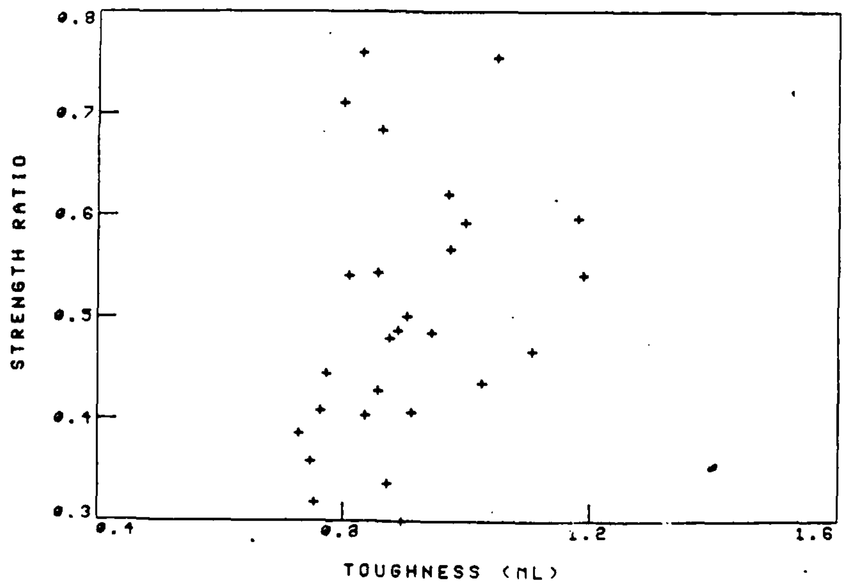

Figure 134. Correlation between notched strength ratio (for $2c/W = 0.3$) and composite fracture toughness, H_C/σ_o, (ML-fracture model) for boron/aluminum laminates containing straight cracks.

on laminate configuration as well as other factors such as fabrication procedures, fibers' properties, etc. Consequently, the applicability of a given fracture model parameter is restricted to the specific set of data for which it has been determined. Figure 135 shows a representative notched strength data of a $[0_2/\pm45]_s$ laminate compared with the WN-fracture model using relatively small and large values of d_o and a_o within the range of values listed previously. The characteristic distances, d_o and a_o, of the $[0_2/\pm45]_s$ laminate have intermediate values. The comparison clearly indicates the degree of error which can result by choosing arbitrary values for d_o and a_o and applying them to all laminate configurations of a given material system.

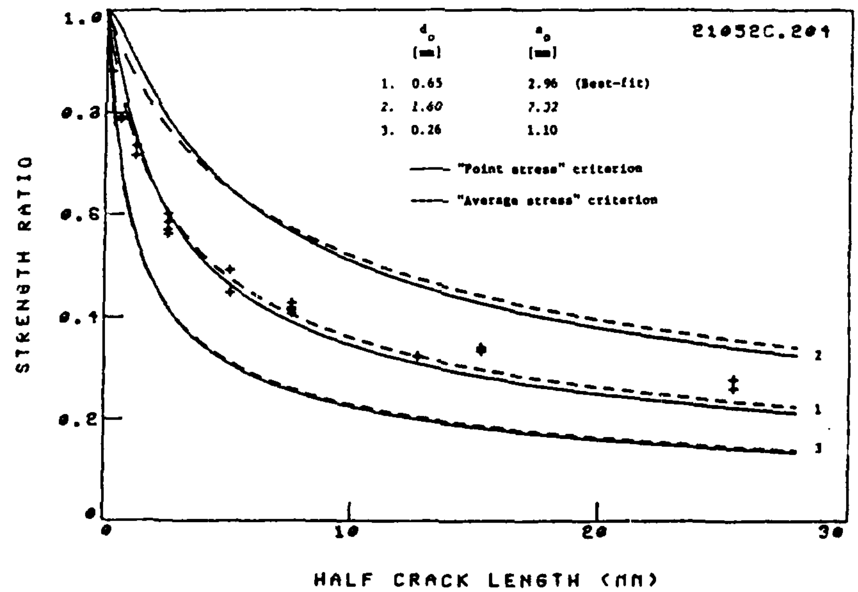

Figure 135. Effect of the characteristic dimensions (WN-fracture model) on notched strength of boron/aluminum laminates containing straight cracks.

NOMENCLATURE†

Symbol	Definition
A_{ij}	Orthotropic in-plane stiffnesses
a	Length of intense energy region (WEK-fracture model).
a_c	Crack tip damage zone size at failure (WEK-fracture model).
	Radius shift parameter for notch sensitivity factor (PWG-fracture model).
a_{cm}	Generalized radius shift parameter (PWG-fracture model).
a_K	Crack-length shift parameter for notch sensitivity factor (PWG-fracture model).
a_{Km}	Generalized crack-length shift parameter (PWG-fracture model).
$\hat{a}_{Km}$	Generalized notch sensitivity factor for cracks (PWG-fracture model).
a_m	Radius shift factor for exponential parameter (PWG-fracture model,
a_o	Characteristic dimensions (WN-fracture model; average stress criterion).
C	Radius notch sensitivity factor (PWG-fracture model).
C^*	Radius notch sensitivy factor on master curve (PWG-fracture model).
C^*_i	Critical hole notch sensitivity factor (PWG-fracture model).
c	Half crack length
c'	Shifted half crack length by a_K (PWG-fracture model).
c^*	shifted half crack length by a_{Km} (PWG-fracture model).
c_c	Corrected half crack length (PWG-fracture model).
c^*_c	Critical corrected half crack length (PWG-fracture model).

† Efforts were made in this report to use the same nomenclature which appeared in the papers reviewed. Therefore, in a few cases the same symbol may have different definitions or the same definition may have different symbols.

c_i	Notch insensitive half crack length (PWG-fracture model).
c_i^*	Critical notch insensitive half crack length (PWG-fracture model).
c_o	Reference half crack length (PWG-fracture model).
	Effective characteristic dimension (WN-fracture model).
d_o	Characteristic dimension (WN-fracture model, point stress criterion).
d_o^*	Critical characteristic dimension for holes and cracks (PWG-fracture model).
$\bar{d}_o$	Characteristic distance for "general fracture-toughness parameter"
E	Young's modulus
E_L	Longitudinal lamina stiffness
E_T	Transverse lamina stiffness
E_{uy}	Ultimate (secant) longitudinal laminate stiffness (PS-fracture model)
E_x	Effective transverse laminate stiffness
E_y	Effective longitudinal laminate stiffness
F_{tu}	Ultimate tensile strength of unnotched laminate (PS-fracture model).
G	Shear modulus
G_I	Energy release rate (mode I)
G_{LT}	Lamina in-plane shear modulus
G_{yx}	Effective in-plane laminate shear modulus
H_c	Composite fracture toughness (ML-fracture model).
K	Crack notch sensitivity factor (PWG-fracture model).
	Mode I stress-intensity factor (PS-fracture model).
K^*	Crack notch sensitivity factor on master curve (PWG-fracture model).

K_i^*	Critical crack notch sensitivity factor (PWG-fracture model).
K_I	Mode I stress-intensity factor
K_{IC}	Mode I fracture toughness
K_Q	Critical stress-intensity factor, fracture toughness
K_Q'	Modified critical stress-intensity factor (WN-fracture model).
K_{Qe}	Elastic critical stress-intensity factor (PS-fracture model).
K_ε	Strain-intensity factor (PS-fracture model).
$K_{\varepsilon Q}$	Critical strain-intensity factor (PS-fracture model).
$K_{\varepsilon Qe}$	Elastic critical strain-intensity factor (PS-fracture model).
K_T	Stress concentration factor for a finite width plate
K_T^∞	Stress concentration factor for an infinite plate
k_o	Proportionality constant (K-fracture model).
L	Length of specimen
m	Exponential parameter (PWG-fracture model).
m^*	Exponential parameter on master curve (PWG-fracture model).
m_i^*	Critical exponential parameter (PWG-fracture model).
n	Order of singularity, exponential parameter (ML-fracture model).
Q_c	General fracture-toughness parameter (PS-fracture model).
R	Hole radius
R^*	Shifted hole radius by a_{cm} (PWG-fracture model).
R_c^*	Critical corrected hole radius (PWG-fracture model).
R_i^*	Critical notch insensitive hole radius (PWG-fracture model).
R_{ns}	Relative notch sensitivity factor for holes and cracks (PWG-fracture model).

R^*_{nsi}	Critical relative notch sensitivity factor for holes (PWG-fracture model).
R_o	Reference hole radius (PWG-fracture model).
r, θ	Polar coordinates
S	Far-field applied stress (PS-fracture model).
	Non-dimensional strength at a given notch radius (PWG-fracture model).
S_c	Notched laminate strength (PS-fracture model).
$[T]$	Transformation matrix (PS-fracture model).
t	Laminate thickness
x	Coordinate measured from center of notch perpendicular to applied longitudinal stress
Y	Finite width correction factor
y	Coordinate measured from center of notch directed in the loading direction
W	Width of specimen
α	Fiber orientation angle
	$= 1/(m^*-1)$ (PWG-fracture model).
β	$= (m^*-m)/(m^*-1)$ (PWG-fracture model).
$[\beta]$	Matrix of constituents properties (PS-fracture model).
γ_{xy}	Shear strain (in laminate reference system).
γ_{12}	Shear strain (in laminae reference system).
ε_x, ε_y	Normal strains (in laminate reference system).
ε_1, ε_2	Normal strains (in laminae reference system).
ε_o	Far field strain of notched laminate (PS-fracture model).

ε_{oC}	Far field strain of notched laminate at failure (PS-fracture model).
ε_{tu}	Ultimate tensile strain of unnotched laminate (PS-fracture model).
ε_{tuf}	Ultimate tensile strain of fibers (PS-fracture model).
$\zeta_1, \zeta_2, \zeta_{12}$	Material constants (PS-fracture model).
θ	Angle (Figure 76)
λ	$= [1 + R^{m-1} R_o^{-1} C^{-1}]^{-1}$ (PWG-fracture model).
λ^*	$= \lambda$ on master curve defined by C^* and m^* (PWG-fracture model).
λ_1	$= [1 + c^{m-1} c_o^{-m} K^{-1})^{-1}$ (PWG-fracture model).
λ_1^*	$= \lambda_1$ on master curve defined by K^* and m^* (PWG-fracture model).
λ_i	$= [1+(R_c^*)^{(m_i^*-1)} (R_o)^{-m_i^*} (C_i^*)^{-1}]^{-1}$ (modified PWG-fracture model).
μ_1	Shear modulus of matrix
μ_2	shear modulus of filament
ν	Poisson's ratio
ν_1	Poisson's ratio of matrix
ν_2	Poisson's ratio of filament
ν_{yx}	Effective laminate major Poisson's ratio
ξ_1	$= R/(R+d_o)$ (WN-fracture model, "point stress" criterion for holes).
ξ_2	$= R/(R+a_o)$ (WN-fracture model, "average stress"criterion for holes).
ξ_3	$= c/(c+d_o)$ (WN-fracture model, "point stress" criterion for cracks).
ξ_4	$= c/(c+a_o)$ (WN-fracture model, "average stress" criterion for cracks).
ρ	Crack tip damage zone size in terms of stress (PS-fracture model).
ρ_C	Critical crack tip damage zone size in terms of stress (PS-fracture model).
ρ_ε	Crack tip damage zone size in terms of strain (PS-fracture model).

$\rho_{\varepsilon C}$	Critical crack tip damage zone size in terms of strain (PS-fracture model).
σ	Axial stress
σ^{∞}	Far-field longitudinal stress
σ_N	Notched tensile strength of a finite width plate
σ_N^{∞}	Notched tensile strength of an infinite plate
σ_o	Unnotched strength
σ_y	Normal stress component in the y-direction (loading direction)
$\sigma_x, \sigma_y, \sigma_{xy}$	Stress distributions in the laminate reference system (Figure 53)

Abbreviations

CRIT.	Critical
FWC	Finite Width Correction Factor
K	Karlak (-fracture model)
ML	Mar-Lin (-fracture model)
PS	Poe-Sova (-fracture model)
PWG	Pipes-Wetherhold-Gillespie (-fracture model)
SCF	Stress Concentration Factor
SIF	Stress Intensity Factor
WEK	Waddoups-Eisenmann-Kaminski (-fracture model)
WN	Whitney-Nuismer (-fracture model)

Units

GPa	Giga Pascal, 10^9 N/m^2
in	inch (= 25.4 mm)
KN	1000 Newton
lb	Pounds (= 4.448 Newton)
ksi	1000 lb/in^2 (= 6.894 MPa)

MPa	Mega Pascal, $10^6 N/m^2$ (= 0.145 ksi)
m	meter
mm	millimeter
N	Newton (= 0.2248 lb)
psi	lb/in^2

REFERENCES

1. M.F. Kanninen, E.F. Rybicki, and H.B. Brinson, "A Critical Look at Current Applications of Fracture Mechanics to the Failure of Fiber-Reinforced Composites", Composites, Jan. 1977, pp. 17-22.

2. E.M. Wu, "Fracture Mechanics of Anisotropic Plates", in Composite Materials Workshop, S.W. Tsai, J.C. Halpin and N.J. Pagano, Eds., Technomic Pub. Co., Inc., Stamford, Conn., 1968, pp. 20-43.

3. M.E. Waddoups, J.R. Eisenmann and B.E. Kaminski, "Macroscopic Fracture Mechanics of Advanced Composite Materials," J. Composite Materials, Vol. 5, 1971, pp. 446-454.

4. J.M. Whitney and R.J. Nuismer, "Stress Fracture Criteria for Laminated Composites Containing Stress Concentrations", J. Composite Materials, Vol. 8, 1974, pp. 253-265.

5. R.J. Nuismer and J.M. Whitney, "Uniaxial Failure of Composite Laminates Containing Stress Concentrations," in Fracture Mechanics of Composites, ASTM STP 593, American Society of Testing and Materials, 1975, pp. 117-142.

6. R.F. Karlak, "Hole Effects in a Related Series of Symmetrical Laminates", in Proceedings of Failure Modes in Composites, IV., The Metallurgical Society of AIME, Chicago, 1977, pp. 105-117.

7. R.B. Pipes, R.C. Wetherhold and J.W. Gillespie, Jr., "Notched Strength of Composite Materials, J. Composite Materials, Vol. 12, 1979, pp. 148-160.

8. R.B. Pipes, J.W. Gillespie, Jr., and R.C. Wetherhold, "Superposition of the Notched Strength of Composite Laminates," Polymer Engineering and Science, Vol. 19, No. 16, 1979, pp. 1151-1155.

9. R.B. Pipes, R.C. Wetherhold and J.W. Gillespie, Jr., "Macroscopic Fracture of Fibrous Composites", Materials Science and Engineering, Vol. 45, 1980, pp. 247-253.

10. K.Y. Lin, "Fracture of Filamentary Composite Materials", Ph.D. Dissertation, Department of Aeronautics and Astronautics, M.I.T., Cambridge, Mass., Jan. 1976.

11. J.W. Mar and K.Y. Lin, "Fracture Mechanics Correlation for Tensile Failure of Filamentary Composites with Holes", J. of Aircraft, Vol. 14, No. 7, July 1977, pp. 703-704.

12. C.C. Poe, Jr. and J.A. Sova, "Fracture Toughness of Boron/Aluminum Laminates with Various Proportions of 0° and ±45° Plies", NASA Technical Paper 1707, November 1980.

13. G.R. Irwin, "Fracture Dynamics", in Fracture of Metals, A.S.M., Cleveland, 1948.

14. O.L. Bowie, "Analysis of an Infinite Plate Containing Radial Cracks Originating from the Boundary of an Internal Circular Hole", Journal of Mathematics and Physics, Vol. 35, 1956, pp. 60-71.

15. P.C. Paris and G.C. Sih, "Stress Analysis of Cracks", in Fracture Toughness Testing and its Applications, ASTM STP 381, American Society of Testing and Materials, 1965, pp. 30-85.

16. A.A. Griffith, "The Phenomena of Rupture and Flow in Solids", Philosophical Transactions of the Royal Society, Vol. 221A, 1920, pp. 163-

17. S.P. Timoshenko and J.N. Goodier, "Theory of Elasticity", second edition, McGraw-Hill, New York, 1951, p. 78.

18. G.C. Sih, P.C. Paris and G.R. Irwin, "On Cracks in Rectilinearly Anisotropic Bodies", International Journal of Fracture Mechanics, Vol. 1, 1965, pp. 189-

19. E.M. Wu, "Application of Fracture Mechanics to Anisotropic Plates", Journal of Applied Mechanics, 1967, pp. 967-974.

20. S.G. Lekhnitskii, "Anisotropic Plates", Translated from the Second Russian Edition by S.W. Tsai and T. Cheron, Gordon and Breach, Science Publishers, Inc., New York, 1968.

21. H.J. Konish and J.M. Whitney, "Approximate Stresses in an Orthotropic Plate Containing a Circular Hole", Journal of Composite Materials, Vol. 9, 1975, pp. 157-166.

22. J.E. Ashton, J.C. Halpin and P.H. Petit, "Primer on Composite Materials: Analysis", Technomic Publishing Co., Stamford, Conn. 1969.

23. J.E. Ashton, and J.M. Whitney, "Theory of Laminated Plates", Technomic Publishing Co., Stamford, Conn., 1968.

24. R.M. Jones, "Mechanics of Composite Materials", Scripta Book Co., Washington, D.C., 1975.

25. B.D. Agarwal and L.J. Broutman, "Analysis and Performance of Fiber Composites", John Wiley & Sons, New York.

26. S.W. Tsai and H.T. Hahn, "Introduction to Composite Materials", Technomic Publishing Co., Westport, Conn., 1980.

27. S.G. Lekhnitskii, "Theory of Elasticity of an Anisotropic Body", Holden-Day, San Francisco, 1963.

28. H.J. Konish and T.A. Cruse, "The Determination of Fracture Strength in Orthotropic Graphite/Epoxy Laminates", in Composite Reliability, ASTM STP 580 American Society of Testing and Materials, 1974, pp. 490-503.

29. F.A. McClintock and G.R. Irwin, "Fracture Toughness Testing and Its Applications", in Fracture Toughness Testing, ASTM STP 381, American Society for Testing and Materials, 1965, pp. 84-113.

30. M.E. Waddoups and J.C. Halpin, Computers and Structures, Vol. 4, 1974

31. J.M. Whitney and R.Y. Kim, "Effect of Stacking Sequence on the Notched Strength of Composite Laminates", Air Force Materials Laboratory Technical Report, AFML-TR-76-177, November, 1977.

32. B.A. Yost, "Predicting the Notched Strength of Composite Materials", Delaware University Center for Composite Materials, Technical Report CCM-81-05, 1981.

33. J.W. Mar and P.A. Lagace, "Tensile Fracture of Graphite/Epoxy Laminates with Holes", in Proceedings of the Third International Conference on Composite Materials (ICCM-III), Paris, France, 1980, pp. 130-145.

34. D.N. Fenner, "Stress Singularities in Composite Materials with an Arbitrarily Oriented Crack Meeting an Interface", International Journal of Fracture, Vol. 12, 1975, pp. 705-721.

35. I.M. Daniel, "Biaxial Testing of Graphite/Epoxy Composites Containing Stress Concentrations", Mechanics of Composite Review, Air Force Material Laboratory and Air Force Office of Scientific Research Technical Report, October 1976, pp. 123-151.

36. R.W. Walter, R.W. Johnson, R.R. June and J.E. McCarthy, "Designing for Integrity in Long Life Composite Aircraft Structures," in Fatigue of Filamentary Composite Materials, ASTM STP 636, American Society for Testing and Materials, 1977, pp. 228-247.

37. K.Y. Lin, "Fracture of Filamentary Composite Materials", Ph.D. Dissertations, Department of Aeronautics and Astronautics, M.I.T., Cambridge, Mass., Jan. 1976.

38. J.M. Mar and K.Y. Lin, "Fracture of Boron/Aluminum Composites with Discontinuities", Journal of Composite Materials, Vol. 11, 1977, pp. 405-421.

39. J.A. Sova and C.C. Poe, Jr., "Tensile Stress-Strain Behavior of Boron/Aluminum Laminates", NASA TP-1177, 1978.

40. C.C. Poe, Jr., "A Unified Strain Criterion for Fracture of Fibrous Composite Laminates", Engineering Fracture Mechanics, Vol. 17, No. 2, 1983, pp. 153-171.

41. D.P. Garber, "Tensile Stress-Strain Behavior of Graphite/Epoxy Laminates", NASA CR 3592, 1982.

42. G. Caprino, J.C. Halpin and L. Nicolais, "Fracture Mechanics in Composite Materials", Composites, October 1979, pp. 223-227.

43. R.E. Peterson, "Stress Concentration Factors", John Wiley & Sons, New York, 1974.

44. W.F. Brown, Jr., and John E. Srawley, "Plane Strain Crack Toughness Testing of High Strength Metallic Materials", ASTM STP 410, American Society for Testing and Materials, 1966.

45. O.L. Bowie and C.E. Freeze, "Central Crack in Plane Orthotropic Rectangular Sheet", International Journal Fracture Mechanics, Vol. 8, No. 1, 1972, pp. 49-57.

46. T.A. Cruse and J.R. Osias, "Exploratory Development on Fracture Mechanics of Composite Materials", Air Force Materials Laboratory Technical Report, AFML-TR-74-111, April 1974.

47. S.N. Alturi, A.S. Kobayashi and M. Nakagaki, "A Finite Element Program for Fracture Mechanics Analysis of Composite Materials", in Fracture Mechanics of Composites, ASTM STP 593, American Society for Testing and Materials, 1975, pp. 86-98.

48. J. Mar, "Fracture and Fatigue in Bi-Materials", in Mechanics of Composite Review, Air Force Materials Laboratory and Air Force Office of Scientific Research Technical Report, October 1976, pp. 117-122.

49. J. Awerbuch and H.T. Hahn, "K-Calibration of Unidirectional Metal Matrix Composites", Journal Composite Materials, Vol. 12, 1978, pp. 222-237.

50. H.J. Konish, Jr., "Mode I Stress Intensity Factors for Symmetrically-Cracked Orthotropic Strips", in Fracture Mechanics of Composites, ASTM STP 593, American Society for Testing and Materials, 1975, pp. 99-116.

51. H.T. Hahn, "Fracture of Composite Materials", Linköping Institute of Technology, Department of Engineering Materials, Technical Report LiTh-IKP-R-256, August 1982.

52. J.F. Mandell, S.S. Wang and F.J. McGarry, "The Extension of Crack Tip Damage Zones in Fiber Reinforced Plastic Laminates", Journal Composite Materials, Vol. 9, 1975, pp. 266-287.

53. P.A. Lagace, "Static Tensile Fracture of Graphite/Epoxy", Ph.D. Dissertation, Department of Aeronautics and Astronautics, M.I.T., Cambridge, Mass., June 1980.

54. J.W. Mar and P.A. Lagace, "Tensile Fracture of Graphite/Epoxy Laminates with Holes", Proceedings of the Third International Conference on Composite Materials (ICCM-III), Paris, France, 1980, pp. 130-145.

55. J.I. Garcia, "Static Tensile Behavior of $[0]_6$, $[0/\pm5]_s$, $[0/\pm10]_s$, and $[0/\pm15]_s$ Graphite/Epoxy Laminates with Holes", Technology Laboratory for Advanced Composites, M.I.T. Department of Aeronautics and Astronautics, TELAC Report-80-7, June 1980.

56. J.I. Garcia, "Fracture of $[\pm5/0]_s$, $[\pm10/0]_s$, and $[\pm15/0]_s$, Graphite/Epoxy Coupons Under Tension", Technology Laboratory for Advanced Composites, M.I.T. Department of Aeronautics and Astronautics, TELAC Report-80-9, August 1980.

57. L.N. Hugh McManus, "Failure Modes in a Family of Graphite/Epoxy Laminates", Technology Laboratory for Advanced Composites, M.I.T. Department of Aeronautics and Astronautics, TELAC Report-81-8, May 1981.

58. I.M. Daniel, "Strain and Failure Analysis of Graphite/Epoxy Plates with Cracks", Experimental Mechanics, July 1978, pp. 246-252.

59. J.M. Whitney and R.Y. Kim, "Effect of Stacking Sequence on the Notched Strength of Laminated Composites", in Composite Materials: Testing and Design (Fourth Conference), ASTM STP 617, American Society for Testing and Materials, 1977, pp. 229-242.

60. D.H. Morris and H.T. Hahn, "Fracture Resistance Characterization of Graphite/Epoxy", in Composite Materials: Testing and Design (Fourth Conference), ASTM STP 617, American Society for Testing and Materials, 1977, pp. 5-17.

61. T.A. Cruse and J.R. Osias, "Exploratory Development on Fracture Mechanics of Composite Materials", Air Force Materials Laboratory Technical Report, AFML-TR-74-111, April 1974.

62. J.M. Whitney and R.Y. Kim, "High Temperature Tensile Strength of Graphite/Epoxy Laminates Containing Circular Holes", Journal Composite Materials, Vol. 10, 1976, pp. 319-324.

63. J.M. Kennedy, "Fracture Behavior of Hybrid Composite Laminates", AIAA/ASME/ASCE/AHS 24th Structures, Structural Dynamics and Materials Conference, AIAA Paper No.-83-0804-CP, Lake Tahoe, Nevada, May 2-4, 1983.

64. I.M. Daniel, "The Behavior of Uniaxially Loaded Graphite/Epoxy Plates with Holes", in Proceedings of the International Conference on Composite Materials (ICCM-II), Boston, USA, 1978, pp. 1019-1034.

65. I.M. Daniel, "Biaxial Testing of Graphite/Epoxy Composites Containing Stress Concentrations", Air Force Materials Laboratory Technical Report, AFML-TR-76-244, Part I, December 1976.

66. I.M. Daniel, "Biaxial Testing of Graphite/Epoxy Composites Containing Stress Concentrations - Part II", Air Force Materials Laboratory, AFML-TR-76-244, Part II, June 1977.

67. C.E. Harris and D.H. Morris, "A Characterization of the Fracture Behavior of Thick, Notched, Laminated Graphite/Epoxy Composites", VPISU Report No. VPI-E-83-31, Virginia Polytechnic Institute and State University, Blacksburg, Va., 1983.

68. J.Awerbuch, Unpublished data.

69. D.C. Phillips, "The Fracture Mechanics of Carbon Fiber Laminates", Journal Composite Materials, Vol. 8, 1974, pp. 130-141.

70. H.F. Brinson and Y.T. Yeow, "An Investigation of the Failure and Fracture Behavior of Graphite/Epoxy Laminates", UPISU Report No. VIP-E-75-23, Virginia Polytechnic Institute and State University, Blacksburg, Va., 1975.

71. D.H. Morris and H.T. Hahn, "Mixed Mode Fracture of Graphite/Epoxy Composites: Fracture Strength", Journal of Composite Materials, Vol. 11, 1977, pp. 124-138.

72. H.F. Brinson and Y.T. Yeow, "An Experimental Study of the Fracture Behavior of Laminated Graphite/Epoxy Composites", in Composite Materials: Testing and Design (Fourth Conference), ASTM STP 617, American Society for Testing and Materials, 1977, pp. 18-38.

73. T.R. Porter, "Evaluation of Flawed Composite Structure Under Static and Cyclic Loading", in Fatigue of Filamentary Composite Materials, ASTM STP 636, American Society for Testing and Materials, 1977, pp. 152-170.

74. Y.T. Yeow and H.F. Brinson, "A Study of Damage Zones or Characteristic Lengths as Related to the Fracture Behavior of Graphite/Epoxy Laminates", VPISU Report No. VPI-3-77-15, Virginia Polytechnic Institute and State University, Blacksburg, Va., 1977.

75. R.W. Walter and R.R. June, "Designing for Improved Fracture Strength in Advanced Composites", in the Proceedings of the Society for the Advancement of Material and Process Engineering, 23rd National SAMPE Symposium and Exhibition, Vol. 23, 1978, pp. 877-892.

76. R.T. Potter, "On the Mechanism of Tensile Fracture in Notched Fibre Reinforced Plastics", Proceedings of the Royal Society London, A., Vol. 361, 1978, pp. 325-341.

77. Y.T. Yeow, D.H. Morris and H.F. Brinson, "The Fracture Behavior of Graphite/Epoxy Laminates", Experimental Mechanics, January 1979, pp. 1-8.

78. R. Prabhakaran, "Tensile Fracture of Composites with Circular Holes", Journal of Materials Science and Engineering, Vol. 41, 1979, pp. 121-125.

79. R.Y. Kim, "Fracture of Composite Laminates by Three-Point Bend", Experimental Mechanics, February 1979, pp. 50-55.

80. Y.T. Yeow, D.H. Morris and H.F. Brinson, "A Correlative Study Between Analysis and Experiment on the Fracture Behavior of Graphite/Epoxy Laminates", VPISU Report No. VPI-E-77-20, Virginia Polytechnic Institute and State University, Blacksburg, Va., 1977. Also, Journal of Testing and Evaluation, Vol. 7, 1979, pp. 117-125.

81. C. Bathias, R. Esnault and J. Pellas, "Applications of Fracture Mechanics to Graphite Fibre-Reinforced Composites", Composites, July 1981, pp. 195-200.

82. S. Ochiai and P.W.M. Peters, "Tensile Fracture of Center-Notched Angle Ply $[0/\pm45/0]_s$ and $[0/90]_{2s}$ Graphite/Epoxy Composites", Journal Materials Science, Vol. 17, 1982, pp. 417-428.

83. S. Ochiai and P.W.M. Peters, "Effect of Notch Length, Specimen Thickness, Ply Thickness and Type of Defect on the Fracture Behaviour of Angle-Ply Graphite-Epoxy Composites", Journal Materials Science, Vol. 17, 1982, pp. 2324-2336.

84. G. Caprino, "On the Prediction of Residual Strength for Notched Laminate", Journal Materials Science, Vol. 18, 1983, pp. 2269-2273.

85. D.L. McDanels and R.A. Signorelli, "Effect of Fiber Diameter and Matrix Alloys on Impact-Resistant Boron/Aluminum Composites", NASA TN D-8204, November 1976.

86. K.M. Prewo, "Development of Impact Resistant Metal Matrix Composites", Air Force Materials Laboratory Technical Report, AFML-TR-75-216, March 1976.

87. M.G. Bader, J.E. Bailey and I. Bell, "The Effect of Matrix Interface Strength on the Impact and Fracture Properties of Carbon-Fibre-Reinforced Epoxy Resin Composites", Journal Applied Physics, 1973, pp. 572-586.

88. R.J. Palmer, "Investigation of the Effect of Resin Materials on Impact Damage to Graphite/Epoxy Composites", NASA CR-165677, March 1981.

89. J.G. Williams and M.D. Rhodes, "The Effect of Resin on the Impact Damage Tolerance of Graphite-Epoxy Laminates", NASA TM-83213, October 1981.

90. P.E. Hertzberg, B.W. Smith and A.G. Miller, "Effect of Matrix Resin on the Impact Fracture Characteristics of Graphite-Epoxy Laminates", NASA CR-165784, January 1982.

91. D.L. McDanels and R.A. Signorelli, "Effect of Angleplying and Matrix Enhancement on Impact-Resistant Boron/Aluminum Composites", NASA TN D-8205, October 1976.

201. M. Madhukar, "Fracture Behavior of Boron/Aluminum Laminates at Room and Elevated Temperatures", Ph.D. Dissertation, Drexel University, to be published.

202. J.W. Mar and K.Y. Lin, "Fracture of Boron/Aluminum Composites with Discontinuities", Journal Composite Materials, Vol. 11, 1977, pp. 405-421.

203. J. Awerbuch, "Fracture Behavior of Center Notched Boron/Aluminum Laminate", to be published.

204. C.C. Poe, Jr., and J.A. Sova, "Fracture Toughness of Boron/Aluminum Laminates with Various Proportions of 0° and ±45° Plies", NASA Technical Paper 1707, November 1980.

205. J. Awerbuch, "Effect of Constituents on the Fracture Behavior of Unidirectional Boron/Aluminum", to be published.

206. D.D. Dailey, "Prediction of Fracture Toughness for Specially Orthotropic Composite Laminates", M.Sc. Dissertation, School of Engineering, Air Force Institute of Technology (AFIT), December 1974.

207. M.A. Wright, D. Welch, and J. Jollay, "The Fracture of Boron Fiber Reinforced 6061 Aluminum Alloy", in Proceedings of First USA-USSR Symposium on Fracture of Composite Materials, G.C. Sih and V.P. Tamuzs Eds., Riga,USSR, Sept. 4-7, 1978, Sijthoff & Noordhoff, 1979, pp. 221-238.

208. K.G. Kreider, L. Dardi and K. Prewo, "Metal Matrix Composite Technology", Air Force Materials Laboratory Technical Report, AFML-TR-71-204, December 1971.

209. J. Awerbuch and H.T. Hahn, "Crack-Tip Damage and Fracture Toughness of Boron/Aluminum Composites", Journal Composite Materials, Vol. 13, 1979, pp. 82-107.

210. J. Awerbuch and H.T. Hahn, "Hard Object Impact Damage of Metal Matrix Composites", Journal Composite Materials, Vol. 10, 1976, pp. 231-257.

211. R.C. Jones, "Fractography of Aluminum-Boron Composites", Composite Materials: Testing and Design (First Conference), ASTM STP 460, American Society for Testing and Materials, 1969, pp. 512-527.

212. R.C. Jones and J.L. Christian, "Analysis of an Improved Boron/Aluminum Composite", Composite Materials: Testing and Design (Second Conference), ASTM STP 497, American Society for Testing and Materials, 1972, pp. 439-468.

213. J.H. Steele and H.W. Herring, "Tensile Fracture of Unidirectional B-Al Composite", Failure Modes in Composites, I.J. Toth, Ed., The Metallurgical Society of the AIME, Vol. I, New York, New York, 1972, pp. 343-356.

214. W.R. Hoover and R.E. Allred, "The Toughness of Borsic-Aluminum Composites With Weak Fiber Matrix Bonds", Failure Modes in Composites, I.J. Toth, Ed., The Metallurgical Society of the AIME, Vol. I, New York, New York, 1972, pp. 311-326.

215. J.R. Hancock and G.D. Swanson, "Toughness of Filamentary Boron/Aluminum Composites", Composite Materials: Testing and Design (Second Conference), ASTM STP 497, American Society for Testing and Materials, 1972, pp. 299-310.

216. K.G. Kreider and L. Dardi, "Fracture Toughness of Composites", Failure Modes in Composites, I.J. Toth, Ed., The Metallurgical Society of the AIME, Vol. I, New York, New York, 19[illegible], pp. 193-220.

217. K.M. Prewo, "The Notched Tensile Behavior of Metal Matrix Composites", Composite Materials: Testing and Design (Third Conference), ASTM STP 546, American Society for Testing and Materials, 1974, pp. 507-522.

218. J.P. Waszczak, "Applicability of Linear Elastic Fracture Mechanics to 5.6-mil Boron/6061 Aluminum", J. Aircraft, Vol. 13, No. 10, 1976, pp. 770-777.

219. W.R. Hoover, "Crack Initiation in B-Al Composites", Journal Composite Materials, Vol. 10, 1976, pp. 106-117.

220. J. Awerbuch and H.T. Hahn, "Fracture Behavior of Metal Matrix Composites", in Proceedings of the 14th Annual SES Meeting, 1977, pp. 343-350.

221. J.W. Mar and K.Y. Lin, "Fracture Mechanics Correlation for Tensile Failure of Filamentary Composites With Holes", J. of Aircraft, Vol. 14, No. 7, July 1977, pp. 703-704.

222. C.T. Sun and K.M. Prewo, "The Fracture Toughness of Boron Aluminum Composites", J. Composite Materials, Vol. II, 1977, pp. 164-175.

223. K.M. Prewo, "The Effect of Ply Lay-Up Sequence on the Fracture Toughness of Boron Aluminum", J. Composite Materials, Vol. 12, 1978, pp. 40-52.

224. J. Awerbuch and H.T. Hahn, "K-Calibration of Unidirectional Metal Matrix Composites", J. Composite Materials, Vol. 12, 1978, pp. 222-237.

225. P. Peters, "Fracture Mechanical Investigations on Unidirectional Boron-Aluminum and Boron-Epoxy Composites", Journal Composite Materials, Vol. 12, 1978, pp. 250-261.

226. P.W.M. Peters, "The Effect of Matrix Shear Deformation and Cracking on the Toughness of Boron/Aluminum", in Proceedings of the Third International Conference on Composite Materials (ICCM III), Paris, France, 1980, pp. 1153-1164.

227. E.D. Reedy, Jr., "On the Specimen Dependence of Unidirectional Boron/Aluminum Fracture Toughness", Journal Composite Materials, Vol. 14, 1980, pp. 118-131.

228. E.D. Reedy, Jr., "Analysis of Center-Notched Monolayers With Application to Boron/Aluminum Composites", Journal Mechanics and Physics of Solids, Vol. 28, 1980, pp. 265-286.

229. E.D. Reedy, Jr., "Notched Unidirectional Boron/Aluminum: Effect of Matrix Properties", Journal Composite Materials, Vol. 16, 1982, pp. 495-509.

230. W.F. Jones, "Experimental Determination of Internal Damage Growth in Unidirectional Boron/Aluminum Composites", Ph.D. Dissertation, Clemson University, August 1982.

231. W.S. Johnson, C.A. Bigelow, and Y.A. Bakei-El-Din, "Experimental and Analytical Investigation of the Fracture Processes of Boron/Aluminum Laminates Containing Notches", NASA TP-2187, 1983.

232. E.D. Reedy, Jr., "Fracture of Notched, Unidirectional Boron/Aluminum: Experiment and Analysis", In the Proceedings of ASME-AMD Symposium on Mechanics of Composite Materials, G.J. Dvorak, Ed., Boston, MA, November 13-18, 1983, pp. 157-170.

233. W.F. Jones and J.G. Goree, "Fracture Behavior of Unidirectional Boron/Aluminum Composite Laminates" in the Proceedings of ASME-AMD Symposium on Mechanics of Composite Materials, G.J. Dvorak, Ed., Boston, MA, November 13-18, 1983, pp. 171-177.

234. J.G. Goree and W.F. Jones, "Fracture Behavior of Unidirectional Boron/Aluminum Composite Laminates", NASA CR-3753, 1983.

235. L.R. Dharani, W.F. Jones, and L.G. Goree, "Mathematical Modeling of Damage in Unidirectional Composites", Engineering Fracture Mechanics, Vol. 17, 1983, pp. 555-573.

236. J.E. Alexander and R.G. Carlson, "Failure Processes in Metal Matrix Composites", AFML-TR-73-290, Air Force Materials Laboratory, 1973.

237. M.A. Wright and F.A. Iannuzzi, "The Failure of Notched Specimens of Boron-Fiber Reinforced 6061 Aluminum Alloy", Failure Modes in Composites, J.N. Fleck and R.L. Mehan, Eds., The Metallurgical Society of the AIME, Vol. II, New York, New York, 1974, pp. 68-94.

238. E.D. Reedy, Jr., "Large Strain Shear Response of Unidirectional Boron/Aluminum", Proceedings of the Joint Japan Society of Mechanical Engineers/Society for Experimental Stress Analysis Conference on Experimental Mechanics, Hawaii, May 22-30, 1982.

239. K.M. Prewo and K.G. Kreider, "High Strength Boron and Borsic Fiber Reinforced Aluminum Composites", J. Composite Materials, Vol. 6, July 1972, pp. 338-357.

240. K.M. Prewo and K.G. Kreider, "The Transverse Tensile Properties of Boron Fiber Reinforced Aluminum Matrix Composites", Metallurgical Transactions, Vol. 3, 1972, pp. 2201-2211.

241. I.J. Toth, "An Exploratory Investigation of the Time Dependent Mechanical Behavior of Composite Materials", AFML-TR-69-9, Air Force Materials Laboratory, April 1969.

242. G.D. Menke and I.J. Toth, "The Time Dependent Mechanical Behavior of Metal Matrix Composites", AFML-TR-71-102, Air Force Materials Laboratory, Sept. 1971.

243. K.M. Prewo and K.G. Kreider, "Fatigue Failure Mechanism in Boron Aluminum", Failure Modes in Composites, I.J. Toth, Ed., The Metallurgical Society of the AIME, Vol. I, New York, New York, 1972, pp. 395-413.

244. I. Leddet and A.R. Bunsell, "Fatigue Damage in Boron Aluminum", in Composite Materials: Testing and Design (Fifth Conference), ASTM STP 674, S.W. Tsai, Ed., American Society for Testing and Materials, 1979, pp. 581-596.

245. C.T. Herakovich, J.G. Davis, Jr. and C.N. Viswanatharns, "Tensile and Compressive Behavior of Borsic/Aluminum", Composite Materials: Testing and Design (Fourth Conference), ASTM STP 617, American Society for Testing and Materials, 1977, pp. 344-357.

246. C.T. Herakovich, J.M. Kennedy and D.R. Tenney, "Effect of Cyclic Loading and Temper Condition on the Tensile Behavior of Boron-Aluminum", Proceedings of Conference: Environmental Degradation of Engineering Materials, College of Engineering, Virginia Tech., 1977, pp. 331-343.

247. J.M. Kennedy, C.T. Kerakovich, and D.R. Tenney, "Influence of Temper Conditions on the Nonlinear Stress-Strain Behavior of Boron-Aluminum", VPISU Report No. VIP-E-77-18, Virginia Polytechnic Institute and State University, Blacksburg, VA, 1977.

248. K.M. Prewo, "Exploratory Development of Low-Cost Primary Fabrication Processes for Boron-Aluminum Composites", AFML-TR-74-40 Air Force Materials Laboratory, March 1974.

249. E.L. Foster, Jr., "Technology Development of Metal Matrix Composites for DOD Application Requirements", Proceedings of First MMC Workshop, Institute of Defense Analysis, Paper P-1144, September 1975.

250. A.R. Robertson, "Manufacturing Methods for Metal Matrix Structural Components", AFML-TR-76-140, Air Force Materials Laboratory, August 1976.

251. D.L. McDanels and R.A. Signorelli, "Effect of Fiber Diameter and Matrix Alloys on Impact-Resistant Boron/Aluminum Composites", NASA-TN D-8204.

252. K.M. Prewo, "Development of Impact Resistant Metal Matrix Composites", AFML-TR-75-216. Air Force Materials Laboratory, March, 1976.

253. D.L. McDanels and R.A. Signorelli, "Effect of Angle Plying and Matrix Enhancement on Impact-Resistant Boron/Aluminum Composites", NASA TN D-8205, October 1976.

254. J.M. Grandemange and K.N. Street, "The Effect of Notch Root Radius and Thickness on the Static Fracture Toughness of B-Al Composites", in Proceedings of the 1975 International Conference on Composite Materials, Vol. 2, 1975, pp. 1019-1050.

255. W.F. Jones, "Uni-Directional Composite Laminate With Circular and Rectangular Cut-Outs", M.S. Thesis, Clemson University, 1981.

301. J. Awerbuch and S. Ghaffari, "Deformation Characteristics and Failure Modes of Notched Graphite Polyimide Composites at Room and Elevated Temperatures", to be published.

302. D.P. Garber, D.H. Morris, and R.A. Everrett, Jr., "Elastic Properties and Fracture Behavior of Graphite/Polyimide Composites at Extreme Temperatures", in Composites for Extreme Environment, ASTM STP 768, American Society for Testing and Materials, 1982, pp. 73-91.

303. T.T. Serafini, P. Delvigs and G.R. Lightsey, "Thermally Stable Polyimides from Solutions of Monomeric Reactants", J. of Appl. Polymer Science, Vol. 16, 1972, pp. 905-915.

304. T.T. Serafini, "Processable High Temperature Resistant Polymer Matrix Materials", Proc. of the 1975 International Conference on Composite Materials (ICCM), 1975, pp. 202-220.

305. T.T. Serafini and P. Delvigs, "PMR Polyimides Prepeg with Improved Tack Characteristics", Proc. of the 1978 International Conference on Composite Materials, (ICCM), 1978, pp. 1320-1329.

306. P. Delvigs, T.T. Serafini and G.R. Lightsey, "Addition-Type Polyimides from Solutions of Monomeric Reactants", 17th National SAMPE Symposium and Exhibition SAMPE, Vol. 17, 1978, pp. III-B-7-1-III-B-7-15.

307. T.L. St. Clair and R.A. Jewell, "LARC-160: A New 550°F Polyimide Laminating Resin", 8th National SAMPE Technical Conference, Vol. 8, 1977, pp. 82-93.

308. I. Petker and B.A. Stern, "Microstructure, the Interface, and the Structural Performance to 700°F of Graphite/Polyimide Composite", Proc. of the 23rd National SAMPE Symposium and Exhibition, SAMPE, Vol. 23, 1978, pp. 75-790.

309. T.L. St. Clair and R.A. Jewell, "Solventless LARC-160 Polyimide Matrix Resin", Proc. of the 23rd National SAMPE Symposium and Exhibition, Vol. 23, SAMPE, 1978, pp. 520-527.

310. J.S. Jones, "Graphite/Polyimide Composite Materials Systems for Potential Space Shuttle Use", 21st National SAMPE Symposium and Exhibition, SAMPE, Vol. 21, 1976, pp. 438-458.

311. I. Petker, "Polyimide Resins in Advanced Composites - A Current Assessment", 21st National SAMPE Symposium and Exhibition, SAMPE, Vol. 21, 1976, pp. 37-49.

312. R.D. Vannuci, "Effect of Processing Parameters on Autoclaved PMR Polyimide Composites", Proc. 9th National SAMPE Technical Conference, Vol. 9, 1977, pp. 177-199.

313. T.T. Serafini, P. Delvigs, and R.D. Vannuci, "In Situ Polymerization of Monomers for High-Performance Poly (Phenylguinoxaline)/Graphite Fiber Composites", J. of Appl. Polymer Sci., Vol. 17, 1973, pp. 3235-3238.

314. P. Delvigs, L.C. Hsu, and T.T. Serafini, "The Synthesis of Novel Polyimide Precursor", J. of Polymer Sci. B, Vol. 8, 1970, pp. 29-35.

315. W.E. Winters and T.T. Serafini, "PMR Polyimides - Precessable High Temperature Composite Matrix Resins", 20th National SAMPE Symposium and Exhibition, SAMPE, Vol. 20, 1975, pp. 629-643.

316. H.H. Gibbs, "The Aging Characteristics of NR-150 Polyimide Binder System", 7th National SAMPE Technical Conference, Vol. 7, 1975, pp. 244-259.

317. H.H. Gibbs, "NR-150 Polyimide Binders - A New Approach to High Performance Composites", 17th National SAMPE Symposium and Exhibition. SAMPE, Vol. 17, 1972, pp. III-B-6-1-III-B-6-9.

318. D.F. Sims, D.N. Weed, and P.H. Francis, "Experimental Evaluation of Polyimide Composite Materials", Proc. of the 1978 International Conference on Composite Materials, (ICCM), 1978, pp. 91-99.

319. I.M. Daniel and T. Liber, "Lamination Residual Stresses in Fiber Composites", NASA CR-134826, 1975.

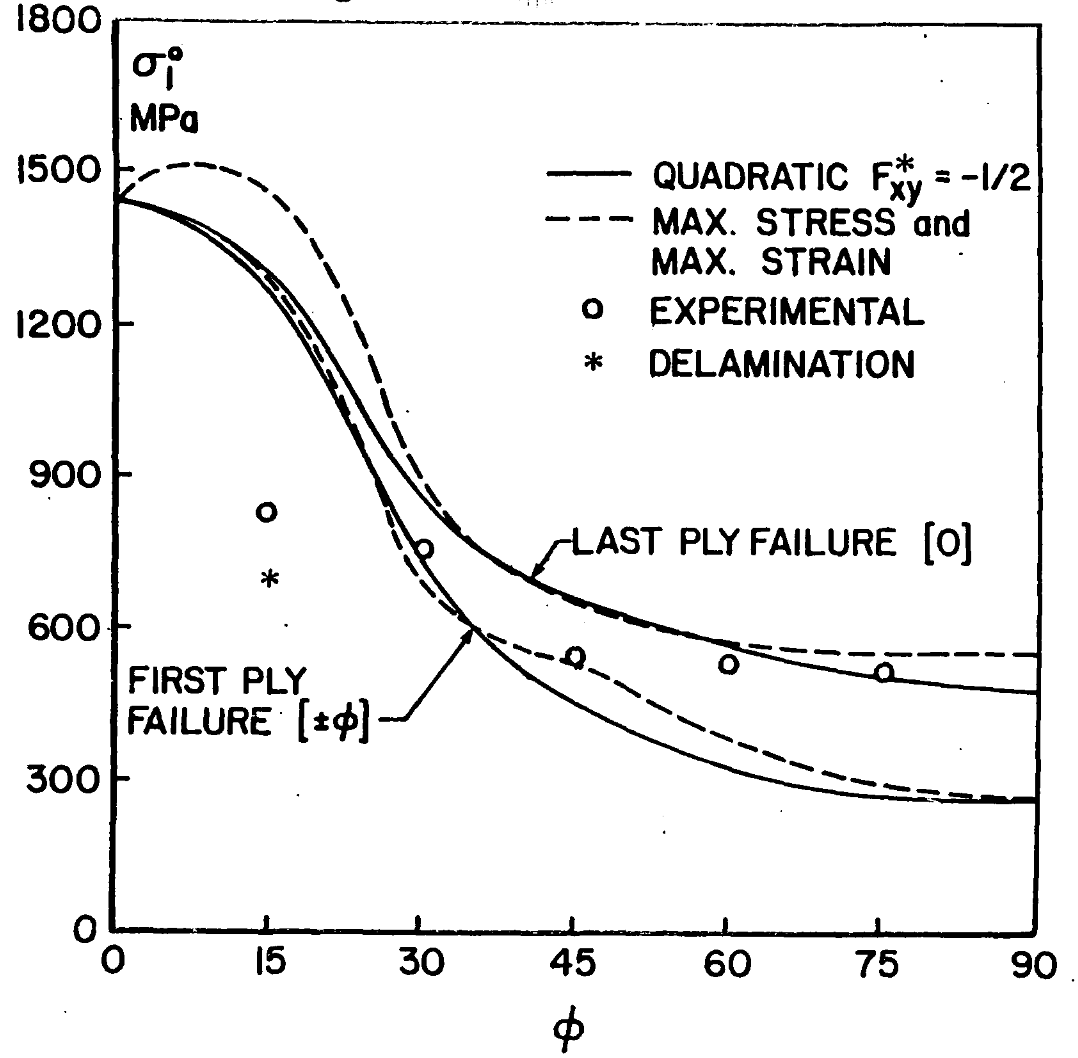

σ_1° MPa
1800
1500
1200
900
600
300
0
0
15
30
45
60
75
90
ϕ
QUADRATIC $F_{xy}^{*} = -1/2$
MAX. STRESS and MAX. STRAIN
EXPERIMENTAL
DELAMINATION
LAST PLY FAILURE [0]
FIRST PLY FAILURE [±ϕ]

and at points B and B_1 at the ends of the diameter perpendicular to the forces

$$\sigma_\theta = p(1 + n). \qquad (39.14)$$

One of these values will be the largest absolute value for the entire plate but it is impossible to know beforehand which one without know-

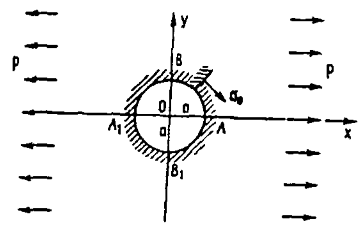

Fig. 79

ing the elastic constants. It could happen that the largest stress will not be at points B and B_1, but will instead be the compressive stress at points A and A_1.

The circular opening becomes elliptic under deformation with semi-axes a' and b' equal to

$$\left.\begin{aligned} a' &= a\left[1 + \frac{p}{E_1}(1 + n)\right], \\ b' &= a\left(1 - \frac{p}{\sqrt{E_1 E_2}}\right). \end{aligned}\right\} \qquad (39.15)$$

Fig. 80 shows the changes of σ_θ along the opening contour in a plate subjected to tension in direction x, the Young's modulus for which is the greatest (i.e., along the external layer).

At points A and A_1

$$\sigma_\theta = -0{\cdot}71p; \qquad (39.16)$$

and at points B and B_1

$$\sigma_\theta = 5{\cdot}45p. \qquad (39.17)$$

Points at which $\sigma_\theta = 0$ occur at angles $\theta = \pm 27°, \pm 153°$.

Fig. 81 shows the stress distribution in a plywood plate subjected to tension in direction x, the Young's modulus of which is the smallest (i.e., transverse to external layer).

At points A and A_1

$$\sigma_\theta = -1{\cdot}41p; \qquad (39.18)$$

and at points B and B_1

$$\sigma_\theta = 4{\cdot}15p. \qquad (39.19)$$

The stress become zero at points where $\theta = \pm 22°30', \pm 157°30'$.

The concentration factor ($K = 4{\cdot}15$) in this case is smaller than in the case of tension applied lengthwise to the external layer ($K = 5{\cdot}45$).

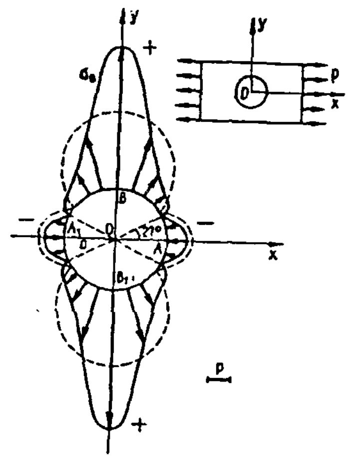

Fig. 80

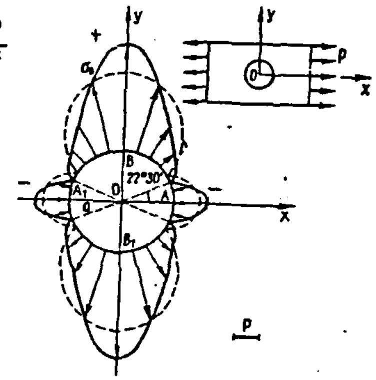

Fig. 81

As compared with the first case, the difference between the highest tensile stress and the highest compressive stress is not excessive when tension is applied transversely to the external layer. The ratio of the greatest tensile stress to the greatest compressive stress is approximately 7·7 in the first case and 2·95 in the second case, i.e., almost the same as in an isotropic plate.

For a plate stretched in the direction of the y-axis $\left(\varphi = \frac{\pi}{2}\right)$, we obtain from (39.10)

$$\sigma_\theta = p\frac{E_\theta}{E_1}k[(k + n)\cos^2\theta - \sin^2\theta]. \qquad (39.20)$$

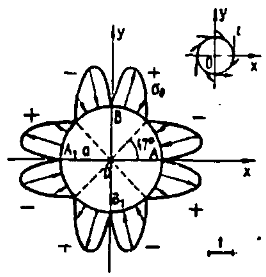

Fig. 76

and changes its values eight times. Its maximum surpasses that of t and is equal approximately to $1{\cdot}5t$.

3. *Tension at an angle to a principal direction.* For a plate subjected to tension by forces p which are applied at a considerable distance from the opening and which are acting with an angle φ in relation to the principal direction, we obtain (Fig. 77):

E_θ

$$\sigma_\theta = p\frac{E_\theta}{E_1}\{[-\cos^2\varphi + (k+n)\sin^2\varphi]\,k\cos^2\theta$$

$$+ [(1+n)\cos^2\varphi - k\sin^2\varphi]\sin^2\theta$$

$$- n(1+k+n)\sin\varphi\cos\varphi\sin\theta\cos\theta\}. \qquad (39.10)$$

For isotropic plates

$$\sigma_\theta = p[1 - 2\cos 2(\theta - \varphi)]. \qquad (39.11)$$

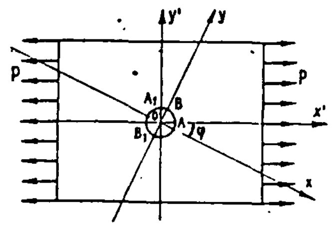

Fig. 77

The stress distribution in an orthotropic plate will not be symmetric with respect to the line parallel or perpendicular to the acting force. It will be symmetric only with respect to the center of the opening. The largest stress will not be at the ends of the diameter normal to the acting forces, but will be at other points.

Fig. 78 shows the stress changes at the opening edge in plywood subjected to tension by forces applied at 45° with respect to the principal

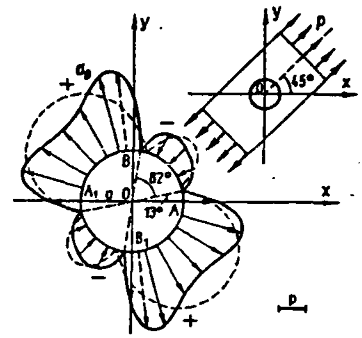

Fig. 78

directions (the x-axis runs along the fibers of the external layer). The greatest stress amounts to $3{\cdot}3p$, as compared with $\sigma_{max} = 3p$ in an isotropic plate. The stress concentration factor in the case of an orthotropic plate ($K = 3{\cdot}3$) differs little from the factor for an isotropic plate ($K = 3$). The stress equals zero at four points: $\theta = 13°, 82°, 193°$ and 262°.

4. *Tension in the principal direction* (Fig. 79). When $\varphi = 0$ we obtain from (39.10)

$$\sigma_\theta = p\frac{E_\theta}{E_1}[-k\cos^2\theta + (1+n)\sin^2\theta]. \qquad (39.12)$$

The stress distribution will be symmetrical with respect to both principal directions x and y. At points A and A_1 on the ends of the diameter parallel to the forces

$$\sigma_\theta = -\frac{p}{k}, \qquad (39.13)$$

APPENDIX I

Growth of Delaminations under Fatigue Loading

R. Prinz

DFVLR
Institut für Strukturmechanik
Braunschweig

AGARD

ADVISORY GROUP FOR AEROSPACE RESEARCH & DEVELOPMENT

7 RUE ANCELLE 92200 NEUILLY SUR SEINE FRANCE

Paper Reprinted from
Conference Proceedings No. 355

CHARACTERIZATION, ANALYSIS AND SIGNIFICANCE OF DEFECTS IN COMPOSITE MATERIALS

NORTH ATLANTIC TREATY ORGANIZATION

GROWTH OF DELAMINATIONS UNDER FATIGUE LOADING.

by

R.Prinz
Deutsche Forschungs- und Versuchsanstalt
für Luft- und Raumfahrt e.V.
Institut für Strukturmechanik
D-3300 Braunschweig-Flughafen
Germany

SUMMARY

In order to determine the nature of failure mechanisms a number of fatigue tests were performed. The test specimens partly have artificial delaminations between different layers of the multidirectional laminates made from T300/914C prepregs. For better understanding of the strength degradation in fatigue a damage model, based on the delamination propagation, starting from the free eages between the plies of a multidirectional laminate,has been developed. These defects propagate due to interlaminar stresses up to an area, which is critical in the case of tension-compression fatigue against buckling or shearing of parts of the delaminated test specimen.

LIST OF SYMBOLS

- $[A]$ Extensional stiffness matrix, KN/mm
- A_{11} Stiffness of the laminate in x-direction, KN/mm
- a Strip delamination size, crack length, mm
- a_0 Platic zone at the crack tip, mm
- da/dN Delamination growth rate, mm/cycle
- $[B]$ Coupling stiffness matrix, KN
- b Width of the specimen, mm
- c_i Displacement at the edge of the specimen in z-direction, mm
- c_m Measured value of the crack opening displacement at the edge of the specimen, mm
- $[D]$ Bending stiffness matrix, KN/mm
- d Laminate thickness, mm
- E_L Modulus of a lamina in fiber direction, KN mm^2
- E_T Modulus of a lamina in transverse direction, KN/mm^2
- G_{LT} Lamina shear modulus, KN/mm^2
- h Lamina thickness, mm
- k Plate curvature, 1/mm
- M Resultand moment, acting on the laminate Nmm/mm
- N Resultand force, acting on the laminate, N/mm
- N Number of load cycles
- R Stress ratio, $R = \sigma_x^l / \sigma_x^u$
- w_i Displacement in z-direction, mm
- x,y,z *Cartesian coordinates*
- δ Phase lag
- ε_x^0 Midplane strain
- ν_{ij}, ν_{LT} Poission's ratio
- $\rho^{(1)} \rho^{(2)}$ Curvature of delaminated parts (1) and (2), 1/mm
- σ_a Stress amplitude, N/mm^2
- σ_{ii} Calculated lamina normal stress, i= 1,2,3, N/mm^2
- σ_{ij} Calculated lamina shear stress i,j= 1,2,3, N/mm^2
- $\sigma_x \sigma_y \sigma_z$ Laminate normal stress in x-, y-, and z-direction
- σ_x^y Yield stress, N/mm^2
- σ_x^f Axial strength, N/mm^2

subscript

- c Critical
- d Damaged
- f Failure by static loading
- F Fatigue failure
- L Longitudinal
- T Transverse
- R Residual

superscript

- u,l upper, lower
- y Yield
- (1)(2) Portion 1, 2

1 INTRODUCTION

In the failure analysis of composite laminates, one of the most serious problem has been the propagation of interlaminar cracking, commonly known as delamination. Delaminations may be formed during manufacture due to incomplete curing or the introduction of foreign particle; they may result from impact damage; and they may result from interlaminar stresses existing at discontinuities or at the stress-free edges of a loaded composite structure. This mode of failure is a major cause for the deterioration of laminate structural properties, including its strength, stiffness, reliability and durability. Furthermore, delaminations may grow under increasing load or cyclic loading. Delamination growth redistributes the stress in plies of a laminate, and may influence residual stiffness, residual strength and fatigue life expecially under compressive fatigue loads. Hence, a fatigue analysis for composite laminates should take in to account the presence and the growth of delaminations.

The exact formation and growth mechanisms of interlaminar cracking in laminates are not well unterstood. The general belief is that a certain distribution of small interface flaws with a size in the order of the fiber diameter exist in laminates prior to loading. Under a critical loading condition, which include thermal (curing) stresses, swelling stresses of moist laminates and external loadings, some flaws would grow and coalesce with each other, forming a single crack of macroscopic proportion. Such an event would constitute the onset, or the initiation of the macro-crack.

In a fiber composite laminate made of $[0/\pm45/90]_s$ stacking sequence the damage development under tension load usuallystarts with the appearence of matrix cracks in the off-axis 90°-plies transverse to the load direction. As tension load or load cycles increase, the matrix cracks in the off-axis plies grow up to the adjacent layer and a characteristic pattern of matrix cracks forms as shown in Fig. 1., see intem 1. A stable pattern of regularly spaced matrix cracks develops in each off-axis ply predictable by a simple one dimensional model [1] . Riefsnider named this pattern the characteristic damage state (CDS) for matrix cracking. Where the matrix cracks terminate, local interface cracks frequently form at the ply boundaries. For the purpose of illustration a $[0,90]_s$ laminate is presented in Fig. 1. During the cyclic loading localized delaminations develops in the boundary between the 0°-and 90°-layer (see item No. 2) mainly at the edges of the specimen, but in the interior also (see for example item No. 3) [2], [3] .

Early investigators focused mainly on experimental and analytical work of free edge induced delamination in laboratory test specimens. A bibliography of this work is contained in Ref. [4] . After one has an understanding of the stress distribution near a free edge by finite element calculations, the next step in treating the delamination problem is to explain the mechanism and the criterion for the edge delamination. One of the most promising techniques for characterizing delamination growth is based on the strain energy release rate G during delamination growth. Measured critical values of G have been used to predict the onset and the growth of edge delaminations in composite laminates [5] , [6].

In the present study a technique was developed to characterize the onset and growth of delaminations in composite laminates. First, the damage that developed in unnotched $[0_2/+45/0_2/-45/0/90]_s$ graphite-epoxy laminates under static and cyclic tension and compression loading was determined by nondestructive test methods. During test loading crack opening displacement was monitored to relate delamination-crack opening with delamination size. Next, stress distribution generated from a finite element analysis was correlated with observed damage. The resulting test data and analysis were used to derive a closed-form equation for the edge crack opening assoziated with the delamination growth. Finally a correlation between delamination size and residual compression strength of fatigued specimens was established.

2. MATERIAL AND TEST EQUIPMENT

Laminates of $[0_2/+45/0_2/-45/0/90]_s$ stacking sequence were fabricated from 914C/T300B graphite/epoxy prepreg tape in a computer-controlled autoclave according to the manufacturers recommended cure procedure. Nominal fiber volume of the laminate was 60% + 2%. The sixteen-ply laminate had an average ply thickness of 0,125 mm. The 380 by 380 mm panels were bonded with fiberglass tabs of 1,0 mm thickness for the clamping reinforcement. These panals were cut by a diamond saw to specimens of different size depicted in Fig.2. Some of the type II specimens had teflon tabs or an inflation agent embeded between the boundaries of different layers. The coupons were stored and tested under laboratory conditions (21± 1°C and 50± 5% relative humidity) 3 to 6 months after fabrication. Some specimens were stored in a climatic chamber for different times to obtain different moisture distributions and moisture contents.

All tests were conducted on a closed-loop Schenck hydraulic testing machine. For displacement measurements strain-gauge transducers (SGT) were mounted on the specimens. To prevent slippage, a fast drying glue was applied on the transducer mounts where touched the specimen.

For measurement of the transverse contraction and transverse crack opening displacement (COD) on some specimens we used the DFVLR-MDR-Transducer (magnetic field depending resistor) [7] . The mounting of the transducer on the test specimen is shown in Fig. 3.

After each step-loading or after certain load cycles, the specimen was removed from the tester and delamination size measurements (C-scan) were made by an ultrasonic testing unit with a narrow waveband emitter [8] . For an exact ajustment of the specimens in the testing machine, the end of the specimens and the clamping device contain fitting holes. Dye-penetrant-enhanced radiography was not used because of the unknown influence of the penetrant fluid on the crack propagation. A Philips SEM 505 scanning eletron microscope was used to study and document the topographic features of the delaminated specimen fracture surfaces. [9] Prior SEM examination, gold was sputtered onto the fracture surface to obtain optimum resolution of the topografic features and to minimize static charging by the SEM beam.

3. OBSERVATION OF DELAMINATION GROWTH

During both quasi-static tension tests and constant amplitude tension-tension fatigue tests on $[0_2/+45/0_2/-45/0/90]_s$ laminates the same type of damage developed. First a few isolated transverse cracks formed in the 90°-plies. As these cracks grew in transverse direction the crack spacing decreased by forming new transverse cracks. These were followed almost by the onset of small delaminations along the edge at the transverse crack tip as seen in Fig. 4. The length of the small delaminations grew up to the interconnection with an other delamination during increasing static load or load cycles. Finally the delamination grew much more rapidly along the length of the specimen. In all cases delaminations on both sides of the specimen extended along the entire specimen length between the grips.

To illustrate the growth of the delamination a few ultrasonic C-scans were made on type II test specimen containing teflon circles implants between both of the 90-degree layers in the central position. Fig. 5 shows 4 C-scans of a stepwise tension loaded specimen. The rigth hand C-scan was made after final failure. This specimen fractured on the lower side with a V-shaped delamination inside the measurement area. Delamination started at a stress of about [illegible] N/mm² at both edges in the boundary between the 0-degree and 90-degree layer and grew slowly. Because of the clamping effect the delamination shape was twisted. There was no delamination growth during tension loading starting from the implants. In the same way a test specimen with an artificial blowing agent delamination degradated during static tension loading. Fig. 6. The internal delamination started from the sharp crack tips of the artificial blowing agent delamination and grew very slowly. The specimen failed at a ultimate strength of 1090 N/mm² after 30% of 90-degree layer were delaminated. There is [illegible] significant difference between the ultimate strength of artificial delaminated and no delaminated specimens. The load at edge delamination onset as well as the load at delamination the entire length and the ultimate load depend upon the moisture content and moisture profile of the specimen. Fig. 7. The tests were conducted in all cases at a temperature of [illegible]°C.

By way of contrast during compressive loading delamination started from the implants as shown in Fig. [illegible]. [illegible] delamination was observed up to the failure load at the edges of the specimen but a small growing of the central delamination was observed.

There are no basic differences in delamination growth between static tension test on one hand and tension-tension fatigue test on the other hand. Compared to these behavior in tension-compression fatigue test delaminations appeared between both the 90 degree and [illegible] layers as well as between the 45-degree and 0 degree layers. Fig. 9 shows the delamination opening of a specimen, which was loaded in tension-compression by a stress amplitude of [illegible] N/mm² with a stress ratio R = -1. After 30.000 cycles at the upper [illegible] state of σ_x^o = [illegible]00 N/mm² the delaminated crack between the 0-degree and 90 degree layer was opened. The crack opening size is about 0,1 mm. Fig. 9a. The same delaminated crack is shown in Fig. 9b after unlaoding to a stress of 0 N/mm². At this loading the size of crack opening is 0,02 mm because of the curing stress. Under compressive stress of σ_x = -500 N/mm² delaminations were observed between the 45 - degree and 0-degree layers. Fig. 9c.

The delamination progress in the cycling test with a stress ratio R = σ_x^u/σ_x^o = -1 is shown in Fig. 10 ([illegible] load, with $\sigma_x^o = -\sigma_x^u$ = 400 N/mm²) by the aid of C-scans which were taken after various numbers of cycles until the test piece finally fractured. The [illegible] of the edge delaminations in the 90° layers shows up clearly after [illegible].000 cycles [illegible] also the increase in delamination area at both the test piece edge and at the artificial delamination as well as at the natural delaminations which happened to be present. [illegible] delaminations were also examined with a microscope. It was seen that delaminations occurs in the interface between the 0-degree and the 45-degree layers also.

In the next illustrations is shown the planimetered area of the delamination propagation during fatigue tests. Fig. 11 and Fig. 12. Both specimen with embeded teflon tabs or inflation agent were tested with a stress ratio R = -1 and an upper stress of σ_x^o = 400 N/mm². The growth of the different delamination modes were planimetered as the number of load cycles incrased.

4. DELAMINATION GROWTH MODEL

The monitoring and the accurate description of the state of damage as a function of static loading and time or fatigue loading is required for successful development of procedures for predicting the residual strength and fatigue life of composite structures. Most of the available nondestructive test (NDT) methods, as for example penetrant enhanced X-ray radiography or ultrasonic C-scanning, require interruptions of testing. One have to remove the specimens out of the testing machine or at least to stop the test. The state of damage in composites can be measured indirect without interruption during testing by the measurement of the change of compliance. [5] One of the most promising techniques for characterizing delamination growth is based on the rate of strain energy released, G, with delamination growth. Measured critical G values have been used in sophisticated analyses [6] to predict the onset of edge delaminations in unnotched composite laminates.

In our present study, a technique was developed, employing the simple line-plasticity model (Dugdale-Barenblatt model).

First, during quasi-static tension loadings and during fatigue tests the transverse deformation in the thickness direction at the edge of the specimen was measured by a special home-made displacement - transducer. Next, stress distribution generated from a finite element analysis was correlated with the observed damage. Then, test data and analyses were used to derive a closed-form equation for the characterization of the delamination onset, and the delamination growth in relation to the crack opening displacement of the delamination (COD).

4.1 MEASUREMENT OF CRACK OPENING DISPLACEMENT

For the measurement of transverse deformation in thickness direction of the specimen we used the DFVLR-MDR-Transducer (Magnetic field depending resistor). The mounting of the transducer on the test specimen is shown in Fig. 3. Three halve-circle small springs of small bending stiffness were glued in the presented form at the specimen. The transducer was mounted by a vessel with two incorporated helical springs which supported

... opposite edge of the test specimen. The tests were ... and constant amplitude tension-tension fatigue. Fig. 1... The quasi-static loading was interrupted by unloading-loading ... crack opening displacement due to curing stresses after ... I like ... first test results of a very extensive test serie.

... static tension test was run at a constant load rate of 1 ... N/mm^2/ ... stress of σ_x = 758 N/mm^2. The stress-deformation recorded ... hand side the nonlinear lateral contraction of the specimen ... thickness- ... The maximum contraction was measured as c_m = -6μm. ... there was a creep deformation in z-direction. After about 10 minutes the ... 1μm was positiv. Then the specimen was unloaded. ... relax from c_m = +3,7μm to +3,5μm . After 1 minute the specimen was loaded ... after 1 minute more, at a total test time of 20 minutes, ... crack starts as seen in Fig. 15a. The crack opening displacement ... to ... grew during constant loading with decreasing rate ... During this period the stress-deformation response ... unloa- ... specimen was recorded at various intervals as seen in ... test was interrupted for 18 hours. Then the test started ... with ... σ_x =758 N/mm^2. After 20 minutes more the stress was increased ... σ_x =826 N/mm^2 for 3 hours. After this time the growth ... about ... opening displacement c_m = 16...μm. The size of the delamination ... Then the specimen was carefully cutted into two parts ... electron microscope (SEM) the distance between the crack tip ... edge. ... amplitude tension-tension tests the stress-deformation response ... measured at various load cycle intervals. Fig. ... shows a typical ... The first cycle starts with the increasing of the ... -650 N/mm^2 at a stress rate of 1 KN/min. From this ... the ... loading starts with an upper stress of σ_x^o ... N/mm^2 and the ... of ... (stress ratio R = 0,1). The stress-deformation response during the first ... and at various load cycle intervals seems to be equal to that ... the quasi-static test. From the beginning of cycle loading the ... ne- ... of the edge turn to positive values as shown in Fig. 17. ... displacement increased during the total loading time, but ... 20 load cycles and increased for higher load cycles. After ... there was a small mistake in the load control which ... At 12100 load cycles the stress amplitude was raised to ... cycles the measured crack opening displacement remain ... the free edge delamination was formed, lay in between ... load ... presents the load history and the displacement history of the ... different states of the damage. The sinusoidal cycling lateral displacement ... by the magnitude of the amplitude 1/2 c_a, the mean value ... the ... the stress cycling and the displacement response. At the first state ... amounts to δ_1 =180°. At the second state II the phase ... load cycles to δ_1=0° at 2203 cycles. Between these ... oscillations (the lateral displacement oscillation and the ... oscillation (both of the same frequency) superimpose themselves ... δ_1=180°. Therefore the amplitude of the measured displacement ... is ... II is the birth of the first small interlaminar cracks, which ... of the specimen from the tip of the transverse cracks ... -ply ... As observed with the stereo microscope those small interlaminar ... another during increasing load cycles. The union of the interlaminar ... called "free edge delamination", effected the increasing of the amplitude ... of the displacement as seen in Fig. 18 at the state III. The transition ... 3000 and 3010 load cycles. The size of the delamination was monitored ... The distance between the crack tip of delamination and the edge ... was measured by SEM.

... ANALYSIS

... quantitative predictions of the onset and growth of delaminations ... finite ... ADINA was used. Because delaminations form in unnotched laminates ... interlaminar stresses that develop at the edges, a quasi-three-dimensional ... analysis was performed. Some detailes of the analysis are described in [10]. ... system is shown in Figure 19. Only 1/4 of the section needs to be analysed ... symmetry. This quarter includes 8 layers and half the width of the test ... was set at 5 mm under the assumption that the edge stresses would fall off ...

... are illustrated in the following pictures. Figure 20 shows the deformation ... of the test piece section under a tensile loading of σ_x = 1 KN/mm^2. On the ... hand side picture edge , the displacements of the section in the ... are indicated. All originally level surfaces exhibit distortions, in the ... of the edge under tensile stressing; these distortions indicate the presence ... stresses at the edges. The distribution of tensile stress σ_{11} in the ... layers of the laminate resulting from an applied tensile stress σ_x agree ... which would also be obtained from the layer theory. Figure 21. The ... the 0° layers, which carry the main portion of the load, are ...% higher ... applied mean tensile load, and do not change markedly towards the edge of the ... The stresses σ_{22} arising as a result of the lateral deformation in the ... are in equilibrium with each other and fall off to zero at the edge, as ... from Fig. 22. Contrary to this, the peeling stresses σ_{33} in the 30° layer,

Fig. 23 start from zero in the middle of the test piece in the compressive stress area. They then pass through zero at about 0.2 mm from the edge and display a stress peak right on the edge between the 90°-and the 0°-layer, the height of which cannot be calculated exactly by use of finite element methods. An investigation conducted in the Institut on the effect of the mesh size of the elements,[10] assuming a linear law of elasticity, indicates that the peeling stress at this point and at the edge between the 45° layers and the 0° layers,albeit here as compressive stress σ_{33} under applied stress σ_x becomes infinitely high as the edge is approached. The same conclusion is also valid for the shear stresses σ_{13} , which are illustrated in Fig. 24 whereas the shear stresses σ_{12} and σ_{23} within and between the individual layers on Fig. 25 and Fig.26 fall off to zero at the edge. Of course the manufacture-induced intrinsic stresses between the individual layers are included in the investigation. With the aid of the distribution described of the secondary stresses σ_{33} and σ_{13} at the edge of a multilayer laminate, the crack initiation and the crack propagation already described which are observed in static testing or in fatigue testing on an undamaged test piece can be very well explained. As in fracture mechanics it may be assumed that no infinitely high stresses are generated in a real material (in this case the matrix resin between the fiber layers) because of plastic deformation. I will deal with the possiblitiy of using fracture mechanics method on delamination propagation at a later point.

Calculations were also carried out on test pieces with a delamination crack on the edge between the 90°-layers. The peeling stress σ_{33} and the shear stress σ_{13} at the crack tip are of the same order compared with the corresponding edge effect stresses. These stress distributions and the deformation of the cross-section showed reasonable correlation with the observed damage that developed. Indeed, examining σ_{33} and interlaminar shear stress distributions are helpfull in identifying likely delamination sites. However the calculation of interlaminar stress distributions by finite element analysis are very expensive. It is only useful for special cases of modelling damage growth qualitatively because the magnitude of calculated peak stresses at the edge varied with mesh size. Therefore, an alternative approach based upon the yield stress criterion was used to predict the delamination size.

CALCULATION OF THE DELAMINATION OPENING DISPLACEMENT

As known from the results of finite element calculations there exists a stress concentration at the edge of the considered multilayered laminate in the interface between the 90-degree and the 0-degree plies. The behavior of the matrix material in the presence of this stress concentration in interface can be estimated under the assumption, that the extend of the nonlinear stress-strain behavior is limited on a small plastic zone around the stress concentration.

In viscoelastic materials cracks can form and propagate with very low velocities and accelerate slowly [11] . Therefore, estimation of the crack tip velocity and the crack length at any time become necessary to estimate the lifetime of a structure.

A linear elastic stress analysis shows that stresses at the 90-0-degree-interface and at a crack tip become unbounded.[10] . However, materials exhibit a yield stress σ_Y^I above which they deform plastically, and thus there must be a plastic zone around the stress concentration which limits the size of any stresses. One can model this plastic behavior in a simple line-plasticity model (Dugdale-Barenblatt model).

To analyse the crack opening displacement c of the delamination (CODD) as a function of strip delamination size a and of the axial stress σ_x of the laminate

(1) $c = f(a, \sigma_x)$

A simple model was used. Considering a free edge strip delamination of the size a the measured value of the crack opening displacement c_m consists of (see Fig. 27)

(2) $c_m = c_1 + c_2 + c_3 + c_4 = c + c_3$,

c_1 is the displacement due to different transverse contractions ν_{12} of the single layers in both unbalanced (unsymmetric) delaminated strip induced curvature. c_2 means the displacement due to curing stresses induced curvature;c_3 the displacement due to transverse contraction ν_{13} and c_4 the displacement due to yield stress at the vicinity of the crack tip.
To calculate the displacement c_1,parts of the general constitutive equations for the laminate (see for example [12])

(3) $$\begin{Bmatrix} N \\ M \end{Bmatrix} = \begin{Bmatrix} A & B \\ B & D \end{Bmatrix} \cdot \begin{Bmatrix} \varepsilon \\ k \end{Bmatrix}$$

[illegible] used, where N and M are the resultant forces and moments acting on the laminate. [illegible] are called the extensional stiffness matrix, coupling stiffness matrix and [illegible] stiffness matrix, respectively. ε_x^o is called the midplane strain and k the plate [illegible]. This curvature can be expressed for the y-direction as

$$k_y = -\frac{\partial^2 w}{\partial y^2}$$

[illegible] coupling terms of the general constitutive equations (3) for this case are

$$M_y = B_{12}\,\varepsilon_x^o + D_{22}\,k_y$$

where the moment $M_y = 0$. Combining Eqs. (4) and (5) and integration leads to

$$w_1^{(1)} = \frac{B_{12}^{(1)}\varepsilon_x^o}{D_{22}^{(1)}}\;\frac{(a+a_o)^2}{2}$$

$$w_1^{(2)} = -\frac{B_{12}^{(2)}\varepsilon_x^o}{D_{22}^{(2)}}\;\frac{(a+a_o)^2}{2}$$

where the subscripts denote the coordinate axis and the superscripts (1) and (2) denote [illegible] delaminated parts of the specimen. Therefore the displacement due to different transverse contraction is:

$$c_1 = w_1^{(1)} + w_1^{(2)} = \frac{\varepsilon_x^o}{2}\,(a+a_o)^2\left(\frac{B_{12}^{(1)}}{D_{22}^{(1)}} - \frac{B_{12}^{(2)}}{D_{22}^{(2)}}\right)$$

[illegible] displacement c_2 due to curing stresses induced curvature can be expressed as

$$c_2 = \frac{1}{2}\,(\varrho^{(1)}+\varrho^{(2)})\,(a+a_o)^2$$

where $\varrho^{(1)}$ and $\varrho^{(2)}$ are the individual curvatures of the delaminated parts of the specimen. [illegible] transverse contraction of the whole laminate is

$$c_3 = \varepsilon_x^o\,\nu_{13}\,(d^{(1)}+d^{(2)}) = \varepsilon_x^o\,\nu_{13}\,d$$

where $d = d^{(1)} + d^{(2)}$ is the thickness of the specimen. At least the displacement [illegible] to constant yield stress σ_z^y can be estimated like a clamped beam with partly uniform [illegible] distribution of the length a_o as

$$c_4 = \left(\frac{1}{D_{22}^{(1)}} + \frac{1}{D_{22}^{(2)}}\right)\sigma_z^y\,\frac{a_o^4}{8}\left(1 + \frac{3a}{4a_o}\right)$$

[illegible] Eqs. 8 to 11 into Eq. 2 yields

$$c_m = \left[\left(\frac{B_{12}^{(1)}}{D_{22}^{(1)}} - \frac{B_{12}^{(2)}}{D_{22}^{(2)}}\right)\frac{(a+a_o)^2}{2} - \nu_{13}\,d\right]\frac{\sigma_x}{A_{11}} + \frac{1}{2}\,(\varrho^{(1)}+\varrho^{(2)})\,(a+a_o)^2 - \left(\frac{1}{D_{22}^{(1)}} + \frac{1}{D_{22}^{(2)}}\right)\left(1 + \frac{4}{3}\,\frac{a}{a_o}\right)\frac{a_o^4}{8}\,\sigma_z^y$$

[illegible] $\varepsilon_x^o = \sigma_x / A_{11}$.

[illegible] 12 all the properties are known exept the length of the plastic zone a_o. Assuming [illegible] a_o is a material property, we can estimate the value of a_o by the measurement of c_m [illegible] test specimen at delamination onset stress σ_x . In this case the crack length [illegible] 0 and therefore from Eq. 12

$$a_o = f\,(c_m,\sigma_x).$$

[illegible] the tested laminates of the stacking sequence $[0\ /{+45}/0\ /{-45}/0/90]_s$ fabricated from [illegible] graphite epoxy prepreg tape the amount of calculated plastic zone is $a_o = 0{,}5$ mm. [illegible] effective modulus properties of each unidirectional ply used for calculation are

$$E_L = 150\ \text{kN/mm}^2, \qquad E_T = 10.000\ \text{kN/mm}^2$$
$$G_{LT} = 5\ \text{kN/mm}^2 \ \text{and}\ \nu_{LT} = 0{,}30\ .$$

[illegible] these properties the extensional stiffness A_{11} , the coupling stiffnesses $B_{12}^{(1)}$ and $B_{12}^{(2)}$, [illegible] bending stiffnesses $D_{22}^{(1)}$ and $D_{22}^{(2)}$ and the curvatures due to curing stresses $\varrho^{(1)}$ and $\varrho^{(2)}$ were calculated by using classical lamination theory for both delaminated parts.

For our example these properties are

A_{11} = 107,261 KN/mm	
$B^{(1)}_{12}$ = 3,6765 KN	$B^{(2)}_{12}$ = -0,1739 KN
$D^{(1)}_{22}$ = 4,5380 KN/mm	$D^{(2)}_{22}$ = 0,9136 KN/mm
$\varrho^{(1)}$ = 0,003936 1/mm	$\varrho^{(2)}$ = 0,000956 1/mm
σ^{1}_{f} = 0,06 KN/mm²	σ_{x} = 0,758 KN/mm²

The curvatures ϱ were estimated for a difference of temperature ΔT = 100 K between test temperature and glass transition point. The strip delamination size a was calculated by the Eq.12 as a function of the crack opening displacement c_m. The results were compared with the size of edge delamination for different delamination states on several test pieces. Therefore delamination sizes were observed by C-scans and by a scanning elektron microscope (SEM) after ending the test and cutting the specimen transverse to the load direction. A comparison made between the measured and the calculated stress-displacement curves at different delamination states is shown in Fig.28 for a quasi-static-test and in Fig. 29 for a fatigue test. The estimation was carried out under the assumption, that $\bar{a}_0$ (in the place of a_0 at Eq. 12) is growing linear with the increasing stress σ_x up to the critical stress σ_{xc} of the delamination onset. ($\bar{a}_0 = a_0\sigma_x/\sigma_{xc}$). A good correlation was achieved for the measured and calculated stress-displacement curves.

We are still working on the formulation of delamination growth as a funktion of time t, a = f (σ_x, t) and a = f (σ_0, R, N, t) , and on the problem of strain energie release rate associated with the delamination growth also in relation to the change of specimen axial compliance. [5] .

The objective is to combine the degradation due to growing delamination size in tension-compression cycling with the residual compressive strength of fatigued and partly buckled specimens.

5. FATIGUE AND RESIDUAL STRENGTH MODEL

During quasi-static compressive testing or fatigue testing with considerable amplitudes of compressive stress, failure occurs by the buckling or kinking of individual fibers, fiber bundles or fiber layers which are more or less supported by the matrix resin. The supportive effect is reduced as the delamination progresses, under both tensile and compressive loading. Fracture occurs finally when a portion of the cross-section buckles and the remaining cross-section is no longer sufficient for the transmission of the applied loading. The effect of the antibuckling support which holds the test piece either over the entire area, or on a center line, or on the 2 edges of the gauge area, must be taken into consideration. Whilst the delamination state of a test piece in multi-layered CFRP has no substantial influence on the residual tensile strength or on the tensile fatigue strength, test pieces with delaminations are especially sensitive to compressive loading.

If the delamination state of a multi-layered test piece during cyclic loading is to be described , a formulation from fracture mechanics may be used for the purpose [13 , 14] .The growth of crack length (or in this case the delamination size a)with increasing number of cycles N is shown by

$$(14) \quad \frac{da}{dN} = g\,\bar{\sigma}^{\varkappa}\,a^{m}$$

where $\bar{\sigma}$ is a reference stress in the vicinity of the delamination crack tip; g, $\varkappa$ and m are constants to be determined empirically. By integration and insertion of limits for N = 0 with a = a_e and for N = N_d with a = a_d the number of loading cycles N is obtained which corresponds to the delamination size a_d:

$$(15) \quad N_d = \left(a_d^{(1-m)} - a_e^{(1-m)}\right) / (1-m)\,g\,\bar{\sigma}^{\varkappa}$$

Now we assume that the test piece fractures due to compressive loading when the delamination size a reaches a critical value [15] . As shown in Appendix A the critical delamination size a for a cyclic loaded specimen can be expressed as

$$(16) \quad a_d = \left(1 - \frac{\sigma_c}{\sigma_f}\right) \frac{A}{h}\,\frac{E}{E_i}$$

where σ_c is the critical compressive stress, σ_f the compressive strength of the virginal specimen, A the cross section, h the thickness of delamination strips, E the modulus of the non delaminated and E_i the modulus of the delaminated cross section. In the case of fatigue failure the specimen will fracture after N load cycles at the compressive cycling stress amplitude $\sigma_F = \sigma^{1}_{c}$ when the critical delamination size $a_d = a_F$ is reached.

$$(17) \quad a_F = \left(1 - \frac{\sigma_F}{\sigma_f}\right) \frac{A}{h}\,\frac{E}{E_i}$$

In the case of residual strength test of a fatigued specimen,after N_R load cycles the critical damage size $a_d = a_R$ can be expressed by

$$(18) \quad a_R = \left(1 - \frac{\sigma_R}{\sigma_f}\right) \frac{A}{h}\,\frac{E}{E_i}$$

where σ_R is the residual strength. The damage state D can be formulated as a function of dimensionless number of load cycles.

$$(19)\quad D = f\left(\frac{N_R}{N_F}\right).$$

Substituting N_R and N_F by Eqs. 15, 17 and 18 yields

$$(20)\quad D = f\left(\frac{\sigma_t - \sigma_R}{\sigma_t - \sigma_F}\right)^{1-m}.$$

For our further considerations we will use the simple expression for the damage state due to delamination

$$(21)\quad D = \left(\frac{\sigma_t - \sigma_R}{\sigma_t - \sigma_F}\right)^{1-m}.$$

The validity of this formula was controlled by fatigue tests.

6. FATIGUE TESTS AND RESIDUAL STRENGTH.

Fatigue tests were carried out on type I specimens with a gauge length of 15 mm to determine the number of load cycles to fracture under constant stress amplitude with the stress ratios of R = -1.0 and R = 0.1. The results are illustrated in Fig. 30. The specimens were supported over their entire area against structural buckling. In order to determine the damage state of the test pieces, additional specimens were subjected to fatigue loads at R = -.1.0. After certain number of cycles N the residual strength were checked. The results of the residual strength tests are plotted versus the number of loading cycles N_R in Fig. 31. The residual compressive strength falls off continuously with the approach to the number of cycles to fracture N_F, down to the fatigue stress σ_F. The residual tensile strength shows no significant change in comparison with the static strength.

The illustration of residual strength investigation in this form is very complex. In Fig.32 the damage state D of the test specimens is shown with reference to the progress of delamination. Since the test results are naturally scattered, the equation (21) was expanded by a number of terms which take account of this scattering.

$$(22)\quad D = \alpha + (1-\alpha)\left(\beta\,\frac{\sigma_t - \sigma_R}{\sigma_t - \sigma_F}\right)^{1-m}$$

where $\alpha = \alpha_1 + \bar{\alpha}$
and α_1 = statistical scatter for a given failure probability P based on static strength.
$\bar{\alpha}$ = average damage of a virginal test piece with a failure probability of 50%,
β = statistical scatter for a given survival probability $P_{\ddot{U}}$ based on the load cycles to failure.

The corresponding scatter distributions and curves of equal survival probability $P_{\ddot{u}}$ = 90%, 50% and 10% are shown in Fig. 32. The damage D to be determined in the residual strength investigations is calculated from equation (20) and entered into Fig. 32. The exponents m determined from the test results as m = 0,45. As can be deduced from Fig. 32, the delamination progress can be described satisfactorily with the aid of equations (17), (18) an (21), taking account of the scattering of the test results.

7. SUMMARY

In the present study a technique was developed to characterize the onset and the growth of edge delaminations in multidirectional composite laminates. The delamination that formed under static and cyclic loading in the interface between the layers of the laminates was determined by ultrasonic C-scans. During test loading the transverse contraction and the transverse crack opening displacement due to peeling stresses were monitored. The observed onset of delaminations was correlated with the stress distribution generated from a finite element analysis. The test data and the analysis were used to derive a closed-form equation for the delamination size assoziated with the onset of cracks and the crack opening displacement. Those defects progated slowly owing to interlaminar stresses up to an area, which is critical against buckling of parts of the delaminated test specimen in the case of tension-compression fatigue. A correlation between delamination size and residual compression strength of fatigued specimens was derived.

REFERENCES

[1] Masters J. E. : Reifsnider, K.L. — An Investigation of Cumulative Damage Development in Quasi-Isotropic Graphite/Epoxy Laminates. In: Damage in Composite Materials. ASTM STP 775, (1982), pp. 40-62

[2] Buczek, M.B. : Herakowich, C.T — Finite Element Models for Predicting Crack Growth Characteristics in Composite Materials. Virginia Polytechnic Institute and State University, Blacksburg, USA, VPI-E-29, Oct. 1982, 131 p.

[3] Schulte, K : Reifsnider, K.L Stinchkomb, W.W. — Entstehen und Ausbreiten von Ermüdungsschädigung in CFK. 18. AVK-Jahrestagung, 5.-7. Oktober 1982 in Freudenstadt, Seite 29-1 bis 29.8.

[4] Rybicki, E.F. : Schmueser, D.W. Fox, J. — Energie Release Rate Approach for Stable Crack growth in the Free-Edge Delamination Problem. J. Composite Materials 11 (1977), pp. 470 - 487

[5] O'Brien, T.K. : — Characterization of Delamination Onset and Growth in a Composite Laminate. In: Damage in Composite Materials, ASTM STP 775, 1982, pp. 140-167

[6] Crossmann, F.W. : Wang, A.S. D — The Dependence of Transverse Cracking and Delamination on Ply Thickness in Graphite/Epoxy Laminates. In: Damage in Composite Materials, ASTM STP 775 (1982), pp. 118-139

[7] Charvat, R. : Prinz, R. — Messwertaufnehmer. German Patent No. P 32 247 57.5, Europa-Patent Nr. (Transducer based on magnetic field depending resistor bridge-MDR-Transducer)

[8] Hillger, W. : Schütze, R. — Non-Destructive Testing of CFRP-Laminates. In: Damage Mechanics of Fiber-Reinforced Composite Materials. ESA-TT-758 (Dez. 1982) pp. 9-46

[9] Prinz, R. : Schmidt, K — Analyse delaminierter Bruchflächen multidirektional aufgebauter Probestäbe aus CFK nach statischer oder Schwingbeanspruchung. DFVLR-IB 131-83/10, 1983, 15 Seiten, 1 Tafel, 26 Bilder, Anhang 7 Bilder

[10] Rohwer, K. : — Stresses and Deformations in Laminated Test Specimens of Carbon Fiber Reinforced Composits. DFVLR-FB 82-15 (1982) 82p.

[11] Bernstorff, B.-S. v. : Crack Growth in Viscoelastic Materials under Varying Load Histories. SM. Report 80-4, California Institute of Technology, Pasadena, Cal., USA, March 1980, 50 p.

[12] Agarwal, B.D. : Broutman, L.J. — Analysis and Performance of Fiber Composites. John Wiley & Sons, New York, Toronto 1980, 355 p.

[13] Barsom, J.M. : — The Dependence of Fatigue Crack Propagation on Strain Energy Release Rate and Crack Opening Displacement. In: Damage Tolerance in Aircraft Structures, ASTM STP 486, 1971, pp. 1-15.

[14] Ratwani, M. M.: Kan, H.P — Compression Fatigue Analysis of Fiber Composites. American Institute of Aeronautics and Astronautics, Inc. 1980, Report 80-0707, pp. 279-284

[15] Whitcomb, J.D: — Aproximate Analysis of Postbuckled Through-Width Delaminations. Composites Techn. Rev. 4 (1982) 3, pp 71-77

[16] Gerard, G. : Becker, H — Handbook of Structural Stability Part. I-Buckling of Flat Plates. NACA TN 3781, 1957, 102 p, esp. Fig. 14

[17] Bhattacharya, A.B.: — Note on the Postbuckling Analysis of Cross-Ply Laminated Plates with Elastically Restrained Edges and Initial Curvatures. J. Struct. Mech. 10 (1982-83) 3 pp 359-372

APPENDIX A

A delamination propagation model under peeling stresses σ_{33} (mode I condition) may be expressed in a form similar to a crack propagation model in metals and is given by the Eq. 14. Let the initial defect characterized by a delamination size $a_o = 0$ and the size a_d after a number of loading cycles N_d. The integration of Eq. 14 yields

(A1) $N_d = a_d^{1-m}/(1-m)g\bar{\sigma}^2$

Assuming the edge delaminations a_i in the multilayer composite develope symmetrical from the edges to the center plane of the specimen as shown in Fig. A1. Than we may define the delaminated area $A^* = \sum_{i=1}^{n} a_i h_i$ and the non-delaminated area $\bar{A} = A - A^*$, where $A = b\,d$ means the total cross section. The load distribution on both parts of the cross-section is

(A2) $P_A = \sum_{i=1}^{n} P_{A_i^*} + P_{\bar{A}}$

It was observed in tension-compression fatigue tests and residual strength tests that parts of the cross section failed by buckling. The buckling load of the delaminated section i which buckles at first can be expressed by [15], [16]

(A3) $P_i = k_i A_i^* \frac{\pi^2 E_i}{12(1-\nu_{LT}^2)} \left(\frac{h_i}{a_i}\right)^2 \; ; \; \sigma_i = k_i \frac{\pi^2 E_i}{12(1-\nu_{LT}^2)} \left(\frac{h_i}{a_i}\right)^2$

where k_i is the compressive buckling coefficient for flat plates with one single supported edge and three clamped edges as shown in Fig. A 2 [16]. The value of the buckling coefficient is $2{,}0 > k_i > 1{,}2$[1]. During fatigue loading the delamination will grow up to the delamination size a_c. Than the strip becomes instable. It will be assumed that the postbuckling load of the delaminated strip remain constant and equal the buckling load during increasing strain (see Fig. A3 and [17]). With increasing number of load cycles the delamination growth will continue and the buckling load will decraese after Eq. (A3). See Fig. A4. When a certain part of all delaminated strips become instable the remaining non-delaminated cross section will faile because of exceeding its static strength (or the failure strain). Those considerations are transferable on the behavior of a delaminated laminate on residual strength test.
The residual strength at a certain number of load cycle N can be expressed from Eq. (A2)

(A4) $\sigma_N = \sum_{i=1}^{n} \sigma_{A_i^*} \frac{a_i h_i}{A} + \sigma_{\bar{A}} \left(1 - \frac{\sum a_i h_i}{A}\right)$

where $\sigma_{A_i^*} = P_i / a_i h_i$ and P_i are the buckling loads after Eq. (A3). To form a very simple relationship between residual strength and delamination size we assume that $h_i = h = \text{const}$, $\sum_{i=1}^{n} a_i h_i = a_N h$ (where a_N the delamination state after N number of load cycles). $\sigma_{A_i^*} = E_i \cdot \varepsilon$ and $\sigma_{\bar{A}} = E \cdot \varepsilon$. With regard to buckling stress and the above simplifications the residual strength yields

(A5) $\sigma_N = \sigma_f \left[\frac{E_1}{E} \frac{1}{A} \left(\frac{2h^3}{\varepsilon_f a_N} - a_N h\right) + 1\right]$

where $k_1 = 2$ was used. Assuming $(\sigma_N/\sigma_f - 1)^2 A^2/4h^2 > 2h^2/\varepsilon_f$ the critical delamination size can be expressed for the residual strength and for the failure load cycle as
$a_R = \left(1 - \frac{\sigma_R}{\sigma_f}\right) \frac{A}{h} \frac{E}{E_1}$ and $a_F = \left(1 - \frac{\sigma_F}{\sigma_f}\right) \frac{A}{h} \frac{E}{E_1}$ respectively. (see Eqs. (16) to (18)).

[1] for $l/a_i > 2$

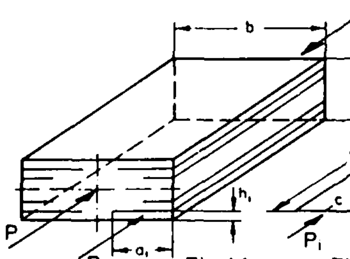

Fig A1

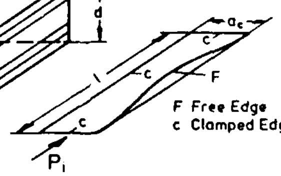

Fig. A2

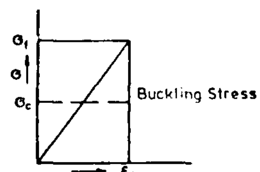

Fig A3

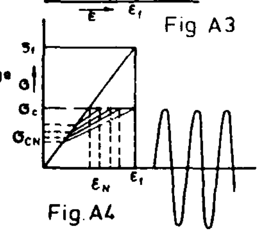

Fig. A4

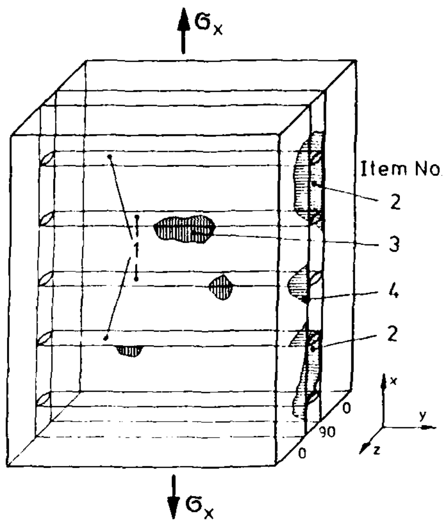

Fig. 1 Characteristic pattern of matrix cracks and delamination onset in the interlaminar plane between the 0-degree and the 90-degree-layers

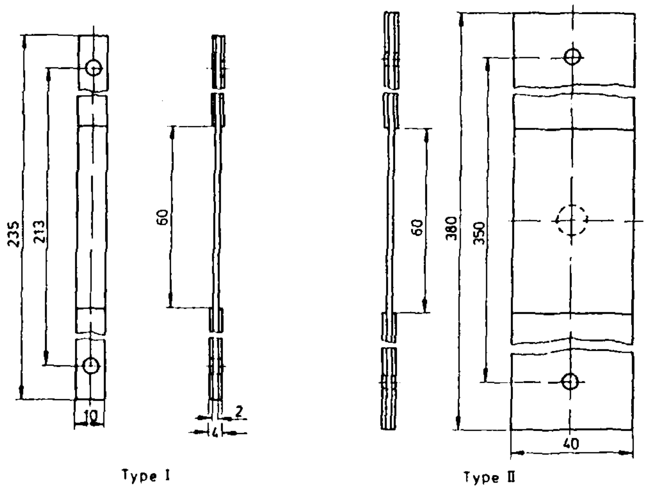

Fig. 2 Types of test specimens

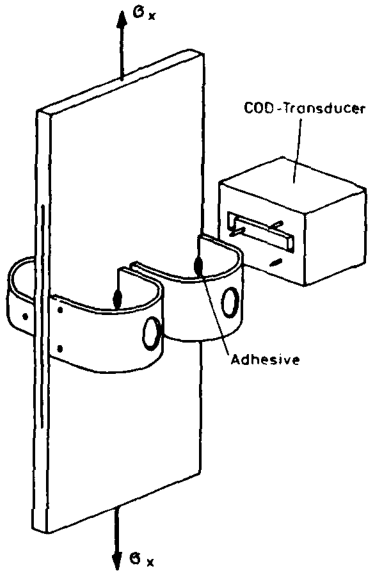

Fig. 3 Mounting of the MDR-COD transducer

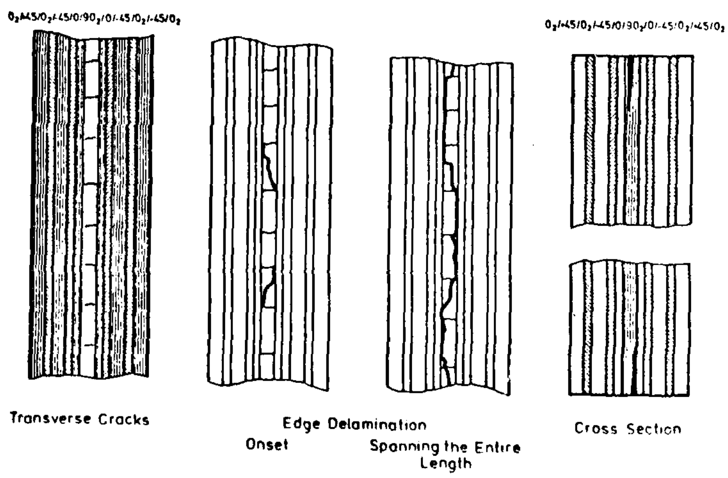

Fig. 4 Formation of edge delaminations during increasing tension load or increasing load cycles

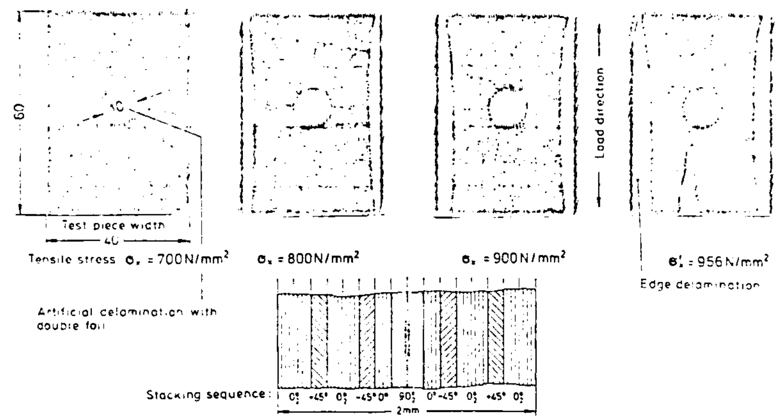

Fig. 5 State of delaminations under step-wise tensile loading to fracture. Ultrasonic C-scans of the test specimen containing teflon circles implants

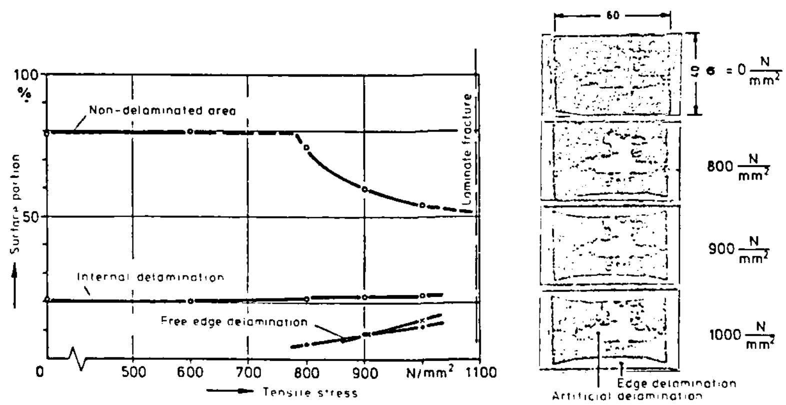

Fig. 6 Growth of the edge delaminations and of the artificial inflation agent delamination under increasing tensile loading

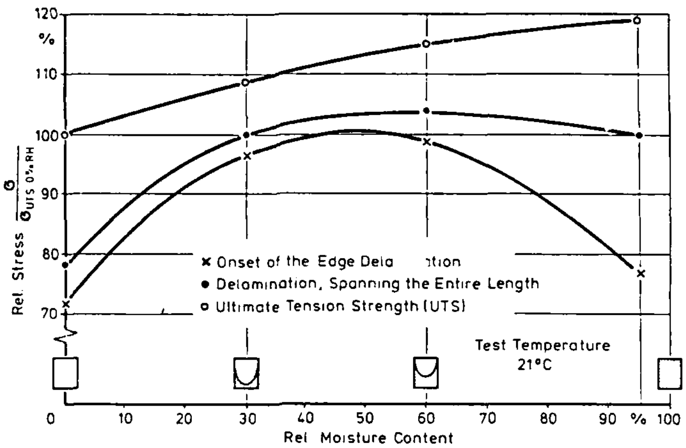

Fig. 7 The influence of moisture profile and moisture content on the formation of free edge delamination during tensile tests

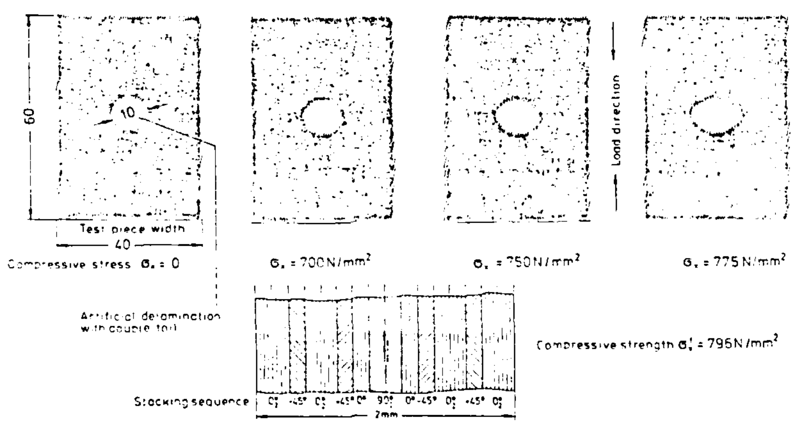

Fig. 8 Growth of artificial delamination under step-by-step compressive loading. Ultrasonic C-scans of a test specimen containing teflon circles implants

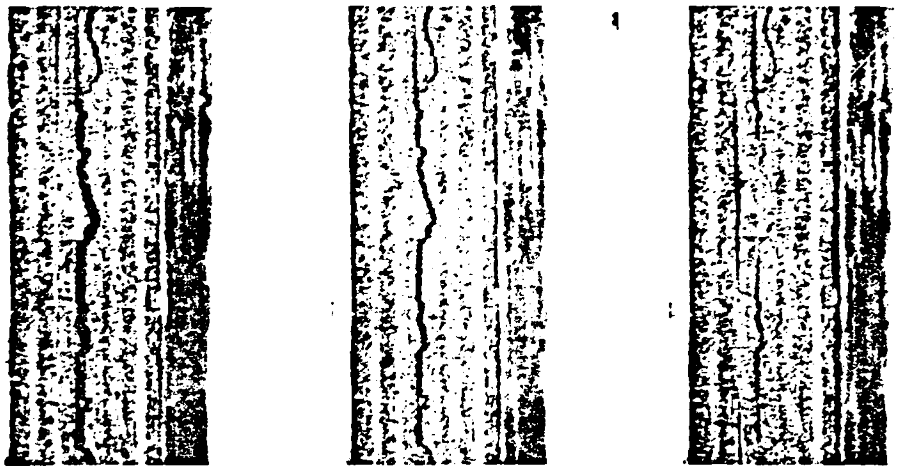

Crack opening, photographed under a stress of

σ_x^u = -500 N/mm² σ_x = 0 N/mm² σ_x^l = 500 N/mm²

Fig. 9 Crack types resulting from edge effects after 3.10^4 load cycles. Stress amplitude $\sigma_a = \pm$ 500 N/mm², Stress ratio R =-1.

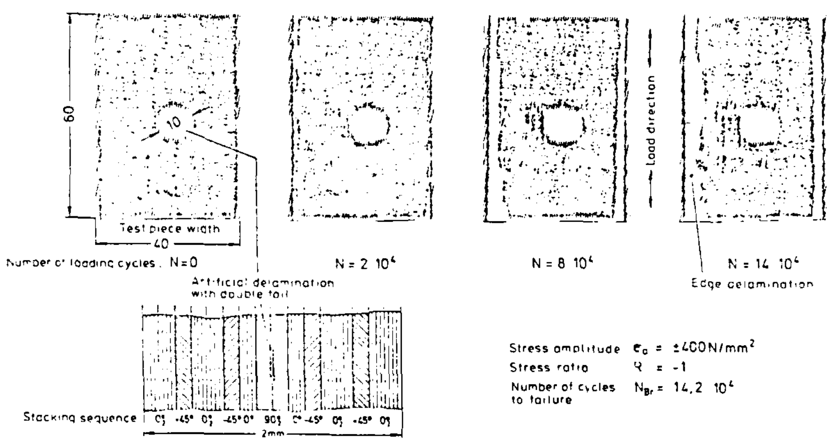

Fig. 10 Delamination states on increasing numbers of tension-compression loading cycles. Ultrasonic C-scans of a test specimen containing teflon circles implants

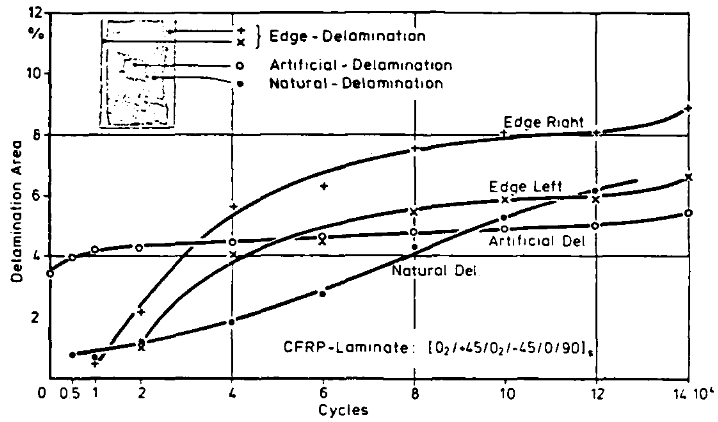

Fig. 11 Propagation of different types of delaminations during tension-compression fatigue loading. $\sigma_a = \pm 400$ N/mm², R = -1

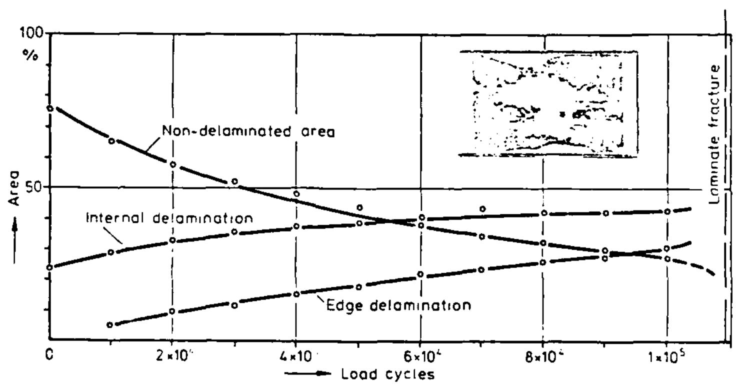

Fig. 12 Propagation of delaminations during tension-compression fatigue loading. $\sigma_a = \pm 400$ N/mm², R = -1

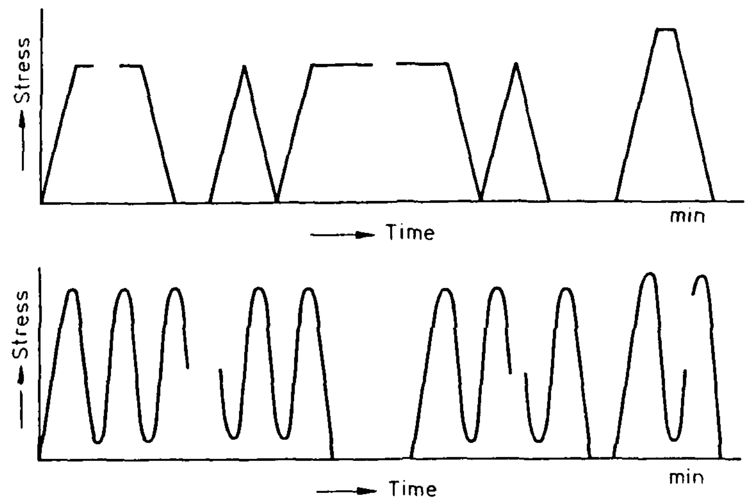

Fig. 13 Load-time-functions for the quasi-static and the cyclic loading tests

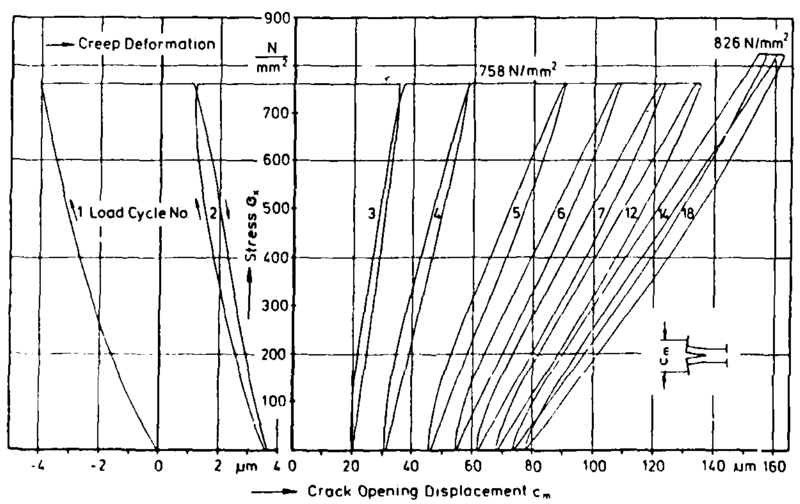

Fig. 14 Displacement c_m as a function of tensile stress for different sizes of delaminations

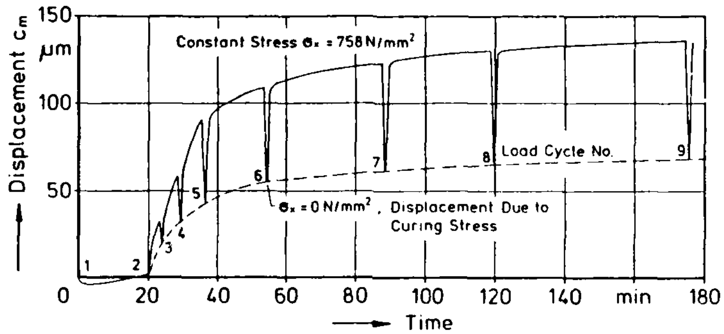

Fig. 15a

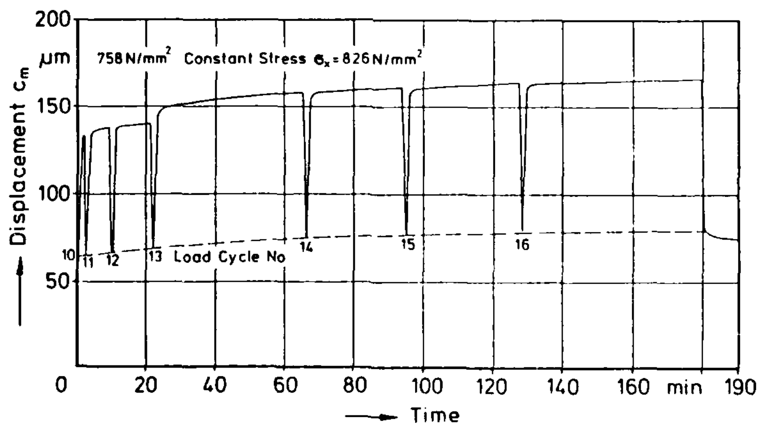

Fig. 15b

Fig. 15 Displacement c_m during constant stress as the function of time

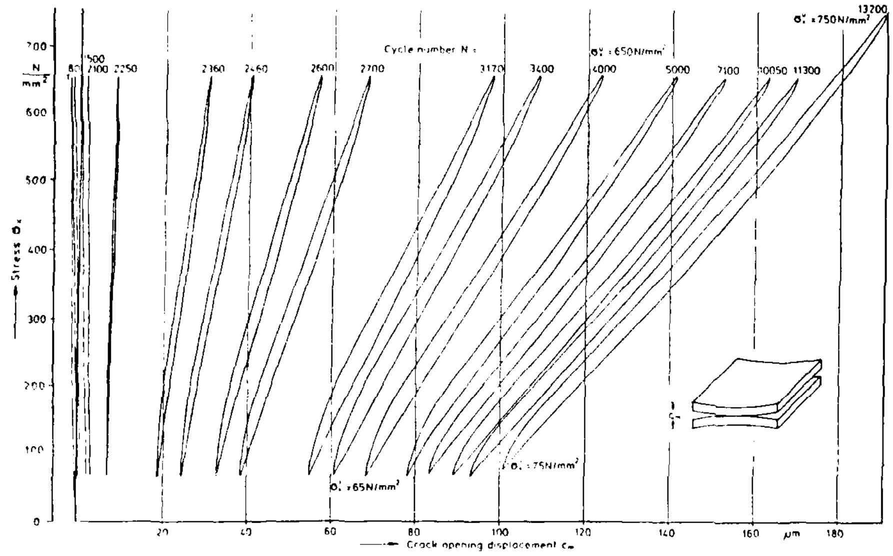

Fig. 16 Typical stress-displacement response for various numbers of load cycles in tension-tension fatigue test

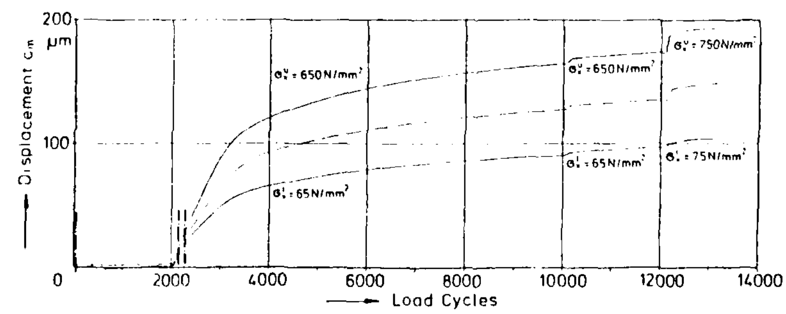

Fig. 17 Envelope of displacement c_m at the upper and the lower stress during tension-tension fatigue test

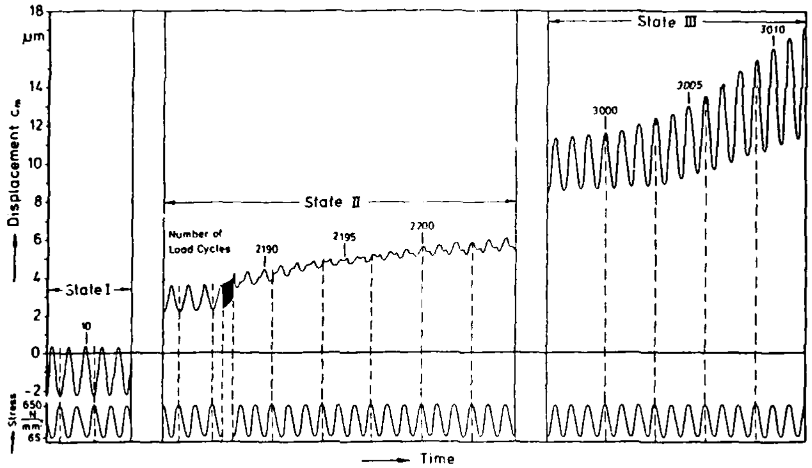

Fig. 18 Load cycling and displacement response for three various states during fatigue test
State I : Creep phase. State II: Onset of delamination
State III : Growth of delamination

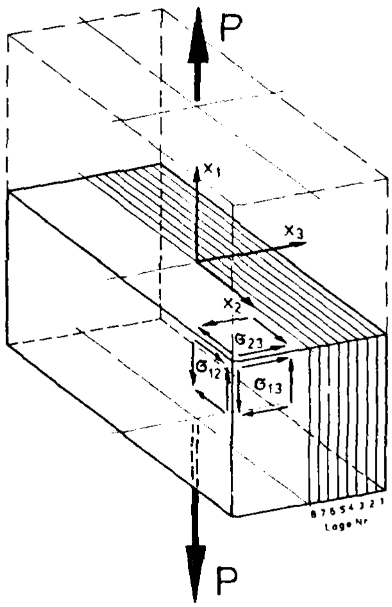

Fig. 19 Coordinate System

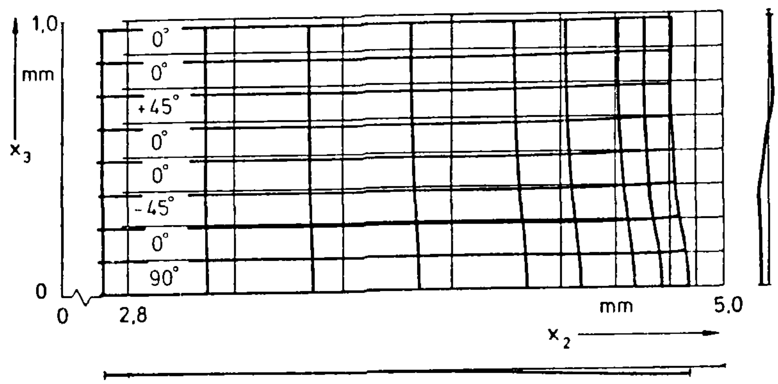

Fig. 20 Deformations of the cross-section resulting from loading of σ_x = 1000 N/mm²

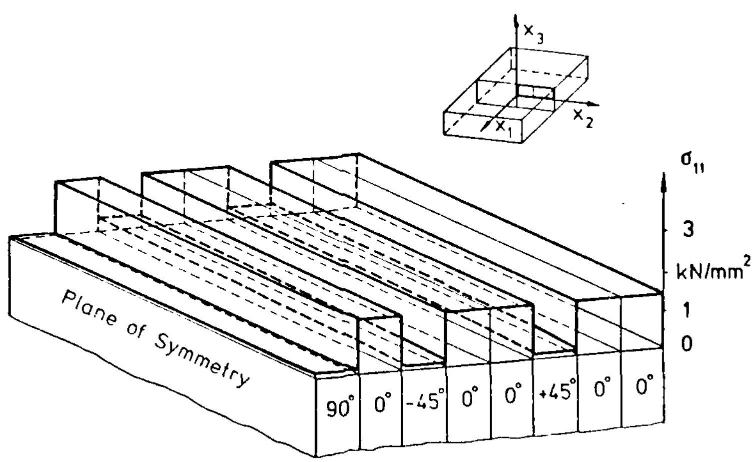

Fig. 21 Normal stresses σ_{11} in the individual layers resulting from longitudinal stress σ_x = 1000 N/mm²

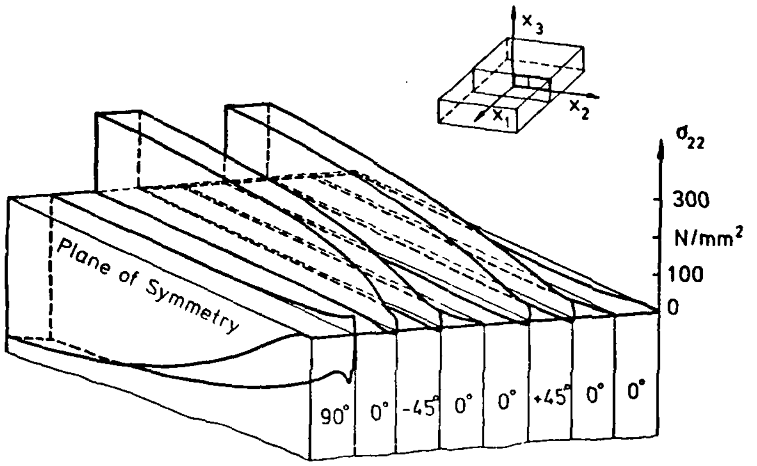

Fig. 22 Transverse stresses σ_{22} in the individual layers resulting from longitudinal stress σ_x = 1000 N/mm²

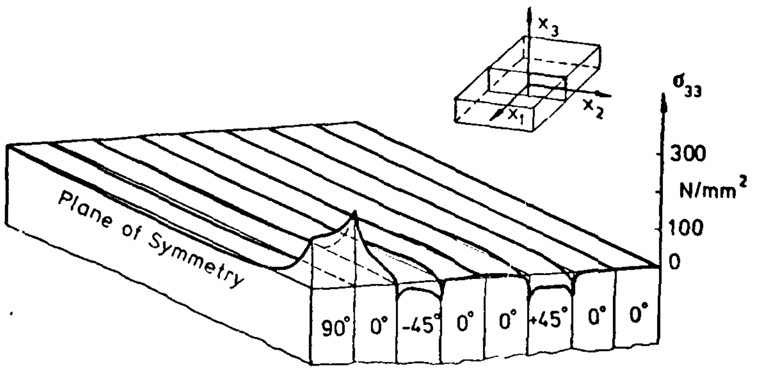

Fig. 23 Transverse stresses σ_{33} in the individual layers resulting from longitudinal stress σ_x = 1000 N/mm²

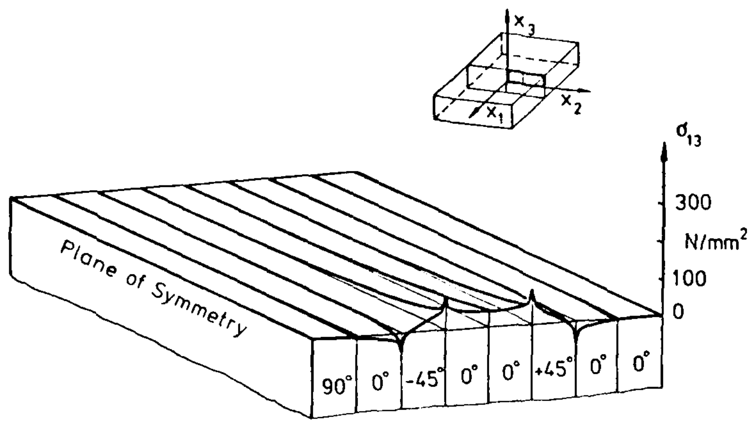

Fig. 24 Shear stresses σ_{13} in the individual layers resulting from longitudinal stress σ_x = 1000 N/mm²

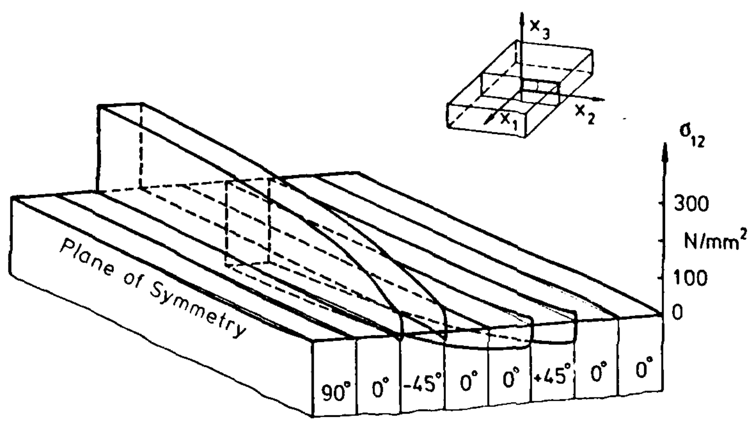

Fig. 25 Shear stress σ_{12} in the individual layers resulting from longitudinal stress σ_x = 1000 N/mm²

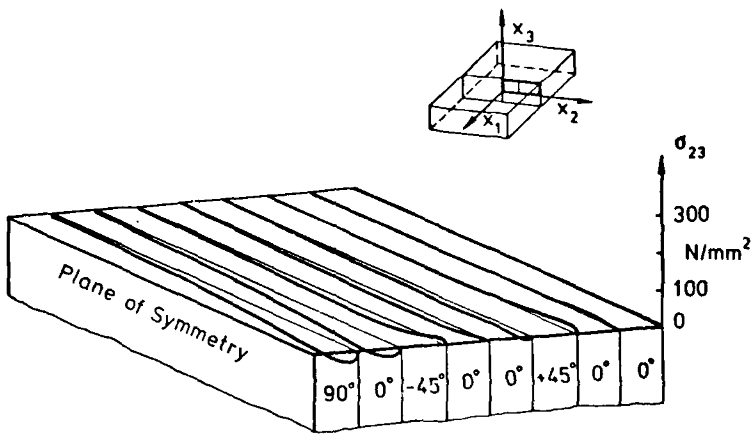

Fig. 26 Shear stresses σ_{23} in the individual layers resulting from longitudinal stress σ_x = 1000 N/mm²

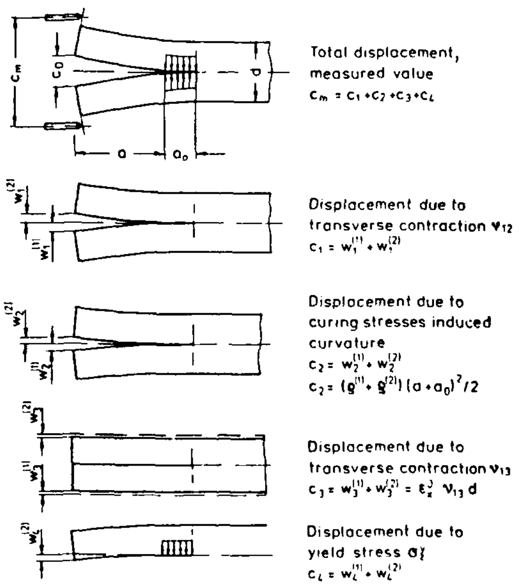

Fig. 27 Composition of the displacement c_m.

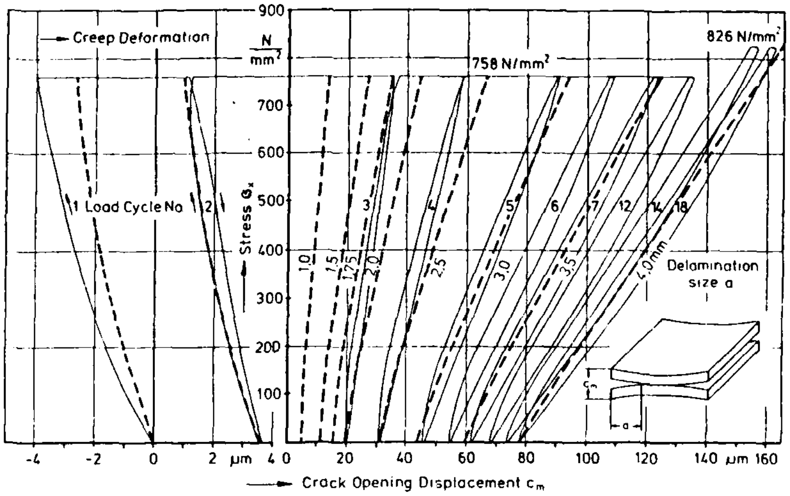

Fig. 28 Measured and calculated stress-displacement response for the quasi-static test. Calculated curves ---

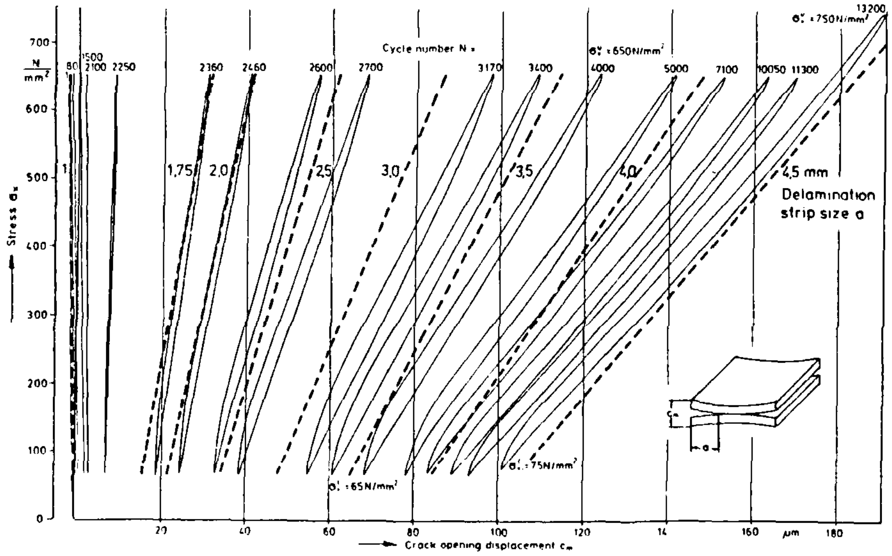

Fig. 29 Measured and calculated stress-displacement response. Calculated curves ---

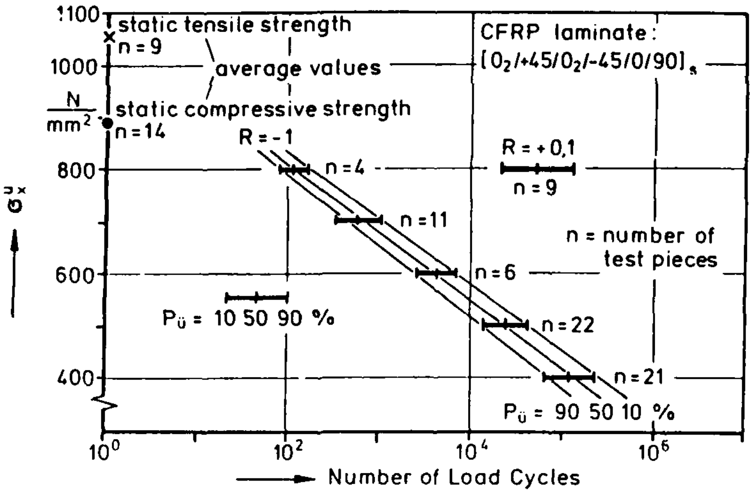

Fig. 30 Fatigue strength diagram for graphite/epoxy laminates.
Stress ratio R = -1 and R = 0.1

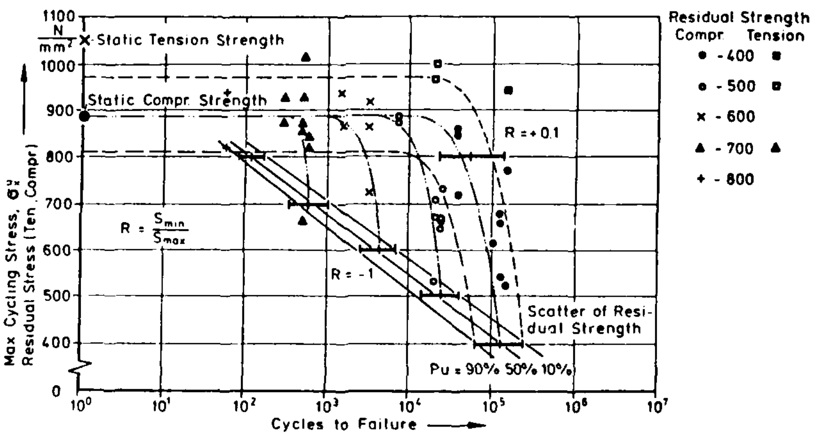

Fig. 31 S-N-curve and residual strength after cyclic loading.

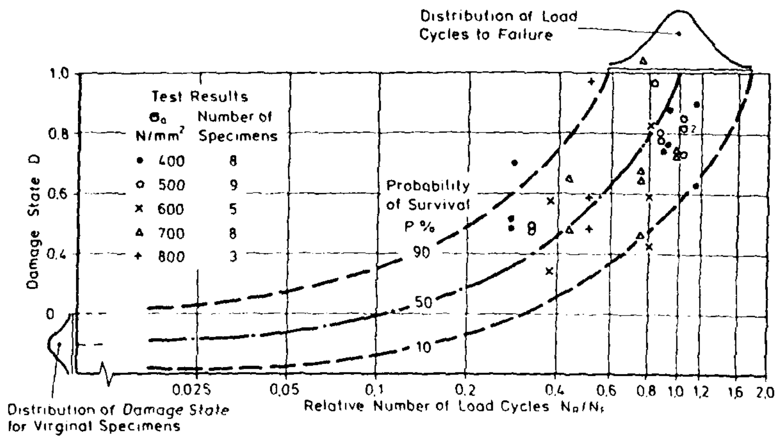

Fig. 32 Damage state D determinated from compressive residual strength after fatigue cycling.

APPENDIX K

Zur Auswahl eines CFK-Mehrschichten-
laminats für Versuche im Zugbereich

von

Dr.-Ing.K. Rohwer

Institut für Strukturmechanik,Braunschweig

DEUTSCHE FORSCHUNGS- UND VERSUCHSANSTALT FÜR LUFT- UND
RAUMFAHRT E.V., INSTITUT FÜR STRUKTURMECHANIK

Interner Bericht
IB 131-82/01

Zur Auswahl eines CFK-Mehrschichtenlaminats für Versuche im Zugbereich.

Braunschweig, Januar 1982

Der Bericht umfaßt:
19 Seiten mit
3 Tabellen und
8 Bildern

Der Bearbeiter:
Rohwer
(Dr.-Ing.K. Rohwer)

Gliederung Seite

1. Aufgabenstellung

Strukturen aus kohlefaserverstärktem Kunststoff (CFK) werden in der überwiegenden Mehrzahl aus mehreren Schichten mit unterschiedlicher Faserrichtung lamelliert, um das Tragvermögen des Werkstoffes möglichst gut zu nutzen. Ein Hindernis für eine umfassende Anwendung dieses vielversprechenden Materials auch in Primärstrukturen ist die immer noch unzureichende Kenntnis des Versagensvorgangs unter mechanischer Belastung und bei der Wirkung unterschiedlicher Temperatur- und Feuchteeinflüsse. Für die Erweiterung des Wissensstandes sind unter anderem Laborversuche an Probestäben aus Mehrschichtenlaminaten erforderlich.

Bei Versuchen an solchen Probestäben unter axialer Zugbelastung haben Pagano und Pipes [1], [2] ein Delaminieren entlang des freien Randes beobachtet. Sie führten dieses Phänomen auf das Auftreten interlaminarer Schälspannungen σ_{33} zurück. Andere Untersuchungen von Puppo und Evensen [3], Pipes und Pagano [4] und Rybicki [5] haben hohe interlaminare Schubspannungen σ_{13} an den freien Rändern von Proben mit Winkellagen ergeben. Art und Größe der Randspannungen sind von dem gewählten Lagenaufbau abhängig. Es ist daher möglich, durch eine günstige Wahl der Schichtenfolge die Randspannungen zu reduzieren und damit das Auftreten von Delaminationen einzuschränken. Delaminationen können die Übertragbarkeit der Meßergebnisse auf das Verhalten großflächiger Strukturen, bei denen freie Ränder nur eine untergeordnete Rolle spielen, erschweren. Für eine Reihe von anstehenden Zugversuchen an Mehrschichtenverbunden aus CFK soll deshalb im folgenden ein Lagenaufbau mit möglichst geringer Delaminationsgefahr ausgewählt werden.

2. Überlegungen zur Auswahl

2.1 Einschränkende Voraussetzungen

Die herzustellenden Proben sollen 380 mm lang und mindestens 10 mm breit sein und aus 16 Schichten zu je 0,125 mm Dicke bestehen. Eine Einschränkung für den Lagenaufbau besteht in der Forderung nach Symmetrie und Ausgeglichenheit, d.h.: jede der beiden symmetrischen Laminathälften soll die gleiche Anzahl von Winkellagen mit Faserrichtungen von $+\Theta$ und von $-\Theta$ enthalten.

Die Einhaltung dieser Forderung bewirkt die Entkopplung der Verformungen. Unter axialer Zugbelastung wird daher die Achse des Zugstabes gerade bleiben.

Die Belastung der Probe soll an beiden Enden durch Klemmbacken übertragen werden. Damit die für CFK recht hohen Kräfte auch eingeleitet werden können, müssen die Fasern der beiden außen liegenden Schichten in Längsrichtung ($\Theta = 0°$) orientiert sein.

Unter den genannten Voraussetzungen kann man noch über die Faserrichtungen von sieben Schichten entscheiden; dabei muß allerdings die Forderung nach Ausgeglichenheit beachtet werden.

2.2 Anzahl der möglichen Komplexionen

Die durch ihre Reihenfolge unterschiedlichen Komplexionen von n Schichten heißt Permutation P_n. Die Anzahl aller möglichen Permutationen ergibt sich zu

$$P_n = n!$$

Für n = 7 erhält man

$$P_7 = 7! = 5040 .$$

Nun wird in der praktischen Anwendung aber kaum ein Laminat mit sieben verschiedenen Faserrichtungen hergestellt werden. Einige Lagen werden gleiche Orientierung aufweisen. Tritt unter den n Elementen α mal das Element a, β mal das Element b u.s.w. auf, dann ergibt sich die Gesaamtzahl der Permutationen zu

$$P_n = \frac{n!}{\alpha!\ \beta! \cdots} .$$

Um die Zahl der möglichen Permutationen zu verringern, wird in einer ersten Wahl vorgegeben, daß das Laminat je eine +45°-, eine -45°- und eine 90°-Schicht sowie 4 (+1) 0°-Schichten aufweisen soll. Damit ergibt sich

$$P_{7,1} = 7!/4! = 5 \cdot 6 \cdot 7 = 210 .$$

In einer zweiten Wahl wird die 90°-Schicht durch eine zusätzliche 0°-Schicht ersetzt, so daß

$$P_{7,2} = \frac{7!}{5!} = 6 \cdot 7 = 42 \, .$$

Auch diese Zahl ist für eine systematische Analyse noch zu groß.

Die große Anzahl möglicher Komplexionen verdeutlicht die Anpassungsfähigkeit von geschichteten Faserverbundstrukturen, stellt aber auch eine Schwierigkeit bei der Wahl eines günstigen Schichtaufbaues dar. Man kann nur intuitiv wenige auswählen und diese miteinander vergleichen.

2.3 Bewertungskriterium

Angestrebt wird ein Laminat, für das die Gefahr einer Randdelamination unter Zugbeanspruchung möglichst gering sein soll. Am freien Rand treten Spannungen σ_{11}, σ_{33} und σ_{13} auf. Es wird angenommen, daß nur die beiden letztgenannten Komponenten die Delamination beeinflussen.

Finite-Element-Rechnungen haben ergeben, daß die größten interlaminaren Schub- und Schälspannungen an den Randpunkten auftreten, an denen die Faserrichtung wechselt. Andererseits weisen Konvergenztests [6] darauf hin, daß die Spannungen hier unendlich groß werden. Das resultiert aus der Fiktion einer unendlichen Elastizität der Werkstoffe. Reales Material baut in der Regel die Spannungsspitzen durch nichtlineares Materialverhalten ab. Allerdings muß damit gerechnet werden, daß an den Stellen, an denen man Spannungsspitzen berechnet, d.h. also wo die Faserrichtung wechselt, eine Delamination initiiert werden kann.

Die berechneten Spannungen an den Randpunkten sind nicht verwendbar. Stattdessen wird vorgeschlagen, entlang der Schichtgrenze nach innen zu gehen und die dem Rand am nächsten gelegenen verläßlichen Spannungswerte für die Beurteilung der Rißgefährdung heranzuziehen. Um einen Vergleich anstellen zu können, müssen die so bestimmten interlaminaren Schubspannungen σ_{13} und Schälspannungen σ_{33} zu einem Einzelwert verknüpft werden.

In Anlehnung an v. Mieses' Kriterium wird als Vergleichswert

$$\sigma_v = \operatorname{sign}(\sigma_{33}) \sqrt{\sigma_{33}^2 + 3(\sigma_{13})^2}$$

gewählt. Je größer σ_v ist, umso größer wird die Delaminationsgefahr eingeschätzt.

3. Falluntersuchung

3.1 Berechnete Laminate

Aus der Vielzahl möglicher Schichtaufbauten sind die folgenden vier ausgewählt worden:

1) $[0_2, +45, 0_2, -45, 0, 90]_s$

2) $[0_5, +45, -45, 90]_s$

3) $[0_2, 90, 0_2, +45, 0, -45]_s$

4) $[0_2, +45, 0_2, -45, 0_2]_s$

Zur Berechnung der Spannungen unter Axiallast wurde die in [6] beschriebene Elementteilung benutzt. Ergebnisse für die ersten drei Laminate sind in den Bildern 1 bis 6 dargestellt. Man erkennt, daß das Laminat 2 wegen gleichzeitig hoher Schub- und Schälspannungen am Übergang zwischen der 90°- und der -45°-Schicht ungeeignet ist. Es wird daher von vornherein ausgeschaltet.

Die Bilder 7 und 8 zeigen jeweils einen Vergleich der Randspannungen zwischen den Laminaten 3 und 1, sowie 4 und 1. Im Laminat 4 fällt der sehr geringe Schälspannungsanteil auf.

3.2 Bewertung

Eine Analyse der berechneten Spannungswerte entlang der Schichtgrenzen zeigt, daß bereits der nächstinnere Wert, eine Elementbreite = (1/256)·Laminatdicke $\approx 7.8 \cdot 10^{-3}$ mm vom Rand entfernt, als verläßlich angesehen werden kann. Die Genauigkeit kann da-durch kontrolliert werden, daß die Spannungen nicht über die Schichtgrenzen hinweg gemittelt wurden. Sie muß aus Gleichgewichtsgründen übereinstimmen. Für das benutzt Weggrößenverfahren charakterisieren daher die relativen Spannungsdifferenzen den Fehler in den Ergebnissen.

Die Tabellen 1, 2 und 3 enthalten die berechneten Spannungswerte an den Schichtgrenzen. Als Fehler wurde jeweils die absolute Spannungsdifferenz auf den absoluten Mittelwert bezogen. Die fast überall gute Genauigkeit schon in sehr geringem Abstand vom Rand wird auf die Verwendung von Elementen mit quadratischen Ansatz zurückgeführt. Die Tabellen enthalten außerdem noch den jeweiligen Vergleichswert σ_v .

4. Entscheidung

Das Laminat 1 weist in der 90°-Schicht einen Wert von $\sigma_v = 0{,}12353$ auf. Vorausgegangene Versuche haben auch gezeigt, daß dort die Delamination einfällt. Das Laminat 4 hat zwischen zwei 0°-Schichten einen σ_v-Wert von 0,06134, liegt daher erheblich günstiger. Das Laminat 3 hat einen maximalen σ_v-Wert von nur 0.04442. Dieser Wert liegt im Gegensatz zum Laminat 4 an einer Schichtgrenze, wo die Faserrichtung wechselt. Das könnte einen ungünstigen Einfluß haben. Da andererseits das Laminat 4 wegen der fehlenden 90°-Schicht und der damit sehr geringen Quersteifigkeit weniger praxisnah ist, wird für die Versuche das Laminat 3 ausgewählt.

5. Schrifttum

[1] N.J. Pagano and R.B. Pipes, Some observations on the interlaminar strength of composite laminates, Int. J. mech. Sci., 15 (1973) pp. 679-688.

[2] N.J. Pagano, On the calculation of interlaminar normal stresses in composite laminate, J. Composite Materials, 8 (1974) pp. 65-81.

[3] A.H. Puppo and H.A. Evensen, Interlaminar shear in laminated composites under generalized plane stress, J.Composite Materials, 4 (1970) pp. 204-220.

[4] R.B. Pipes and N.J. Pagano, Interlaminar stresses in composite laminates under uniform axial extension, J. Composite Materials, 4 (1970) pp. 538-548.

[5] E.F. Rybicki, Approximate three-dimensional solution for symmetric laminates under inplane loading, J. Composite Materials, 5 (1971) pp. 354-360.

[6] K. Rohwer, On the determination of edge stresses in layerd composites.
DFVLR, Institut für Strukturmechanik, Interner Bericht IB 131-81/12

Faser-richtung	σ_{33} [kN/mm²] (rel. Fehler)	σ_{13} [kN/mm²] (rel. Fehler)	$\sigma_v = \text{sign}(\sigma_{33})\sqrt{\sigma_{33}^2 + 3(\sigma_{13})^2}$
0°			
0°	0.00078 (0,2%)	0.00592 (0,0%)	0.01029
+45°	-0.02682 (3,2%)	0.03613 (0,4%)	-0.06809
0°	-0.02672 (3,2%)	-0.07231 (0,2%)	-0.12806
0°	0.00512 (0,0%)	-0.04698 (0,0%)	0.08154
-45°	-0.01427 (5,5%)	-0.07202 (0,2%)	-0.12555
0°	-0.00054 (133,7%)	0.03351 (0,4%)	-0.05804
90°	0.10237 (1,3%)	0.00625 (0,0%)	0.10294
90°	0.12353 (-)	0 (-)	0.12353

Tabelle 1 : Vergleichswerte σ_v für das Laminat 1 infolge Axiallast $\bar{\sigma}_{11}$ = 1 KN/mm²

Faser-richtung	σ_{33} [kN/mm²] (rel. Fehler)	σ_{13} [kN/mm²] (rel. Fehler)	$\sigma_v = \text{sign}(\sigma_{33})\sqrt{\sigma_{33}^2 + 3(\sigma_{13})^2}$
0°			
0°	0.00127 (1,2%)	0.00104 (0,0%)	0.00221
90°	0.04036 (2,3%)	0.00233 (0,0%)	0.04056
0°	0.04373 (2,2%)	0.00448 (0,0%)	0.04442
0°	-0.00962 (0,1%)	0.00937 (0,0%)	-0.01887
+45°	-0.05945 (1,7%)	0.04143 (0,6%)	-0.09318
0°	-0.06939 (1,5%)	-0.08303 (0,2%)	-0.15968
-45°	-0.07541 (1,4%)	-0.08400 (0,3%)	-0.16387
-45°	-0.08455 (-)	0 (-)	-0.08455

Tabelle 2 : Vergleichswerte σ_v für das Laminat 3 infolge Axiallast $\bar{\sigma}_{11}$ = 1 KN/mm²

Faser-richtung	σ_{33} [kN/mm^2] (rel. Fehler)	σ_{13} [kN/mm^2] (rel. Fehler)	$\sigma_v = \mathrm{sign}(\sigma_{33})\sqrt{\sigma_{33}^2 + 3(\sigma_{13})^2}$
0°			
	0.00176 (0.4%)	0.00565 (0.0%)	0.00994
0°			
	-0.01819 (4.0%)	0.03244 (0.4%)	-0.05905
+45°			
	-0.01701 (4.2%)	-0.05770 (0.2%)	-0.10138
0°			
	0.00658 (0.0%)	-0.03521 (0.0%)	0.06134
0°			
	-0.01396 (4.9%)	-0.05745 (0.2%)	-0.10048
-45°			
	-0.01179 (5.8%)	0.03183 (0.4%)	0.05637
0°			
	0.01274 (0.0%)	0.00561 (0.0%)	0.01602
0°			
0°	0.01528 (-)	0 (-)	0.01528

Tabelle 3 : Vergleichswerte σ_v für das Laminat 4 infolge Axiallast $\bar{\sigma}_{11}$ = 1 KN/mm^2

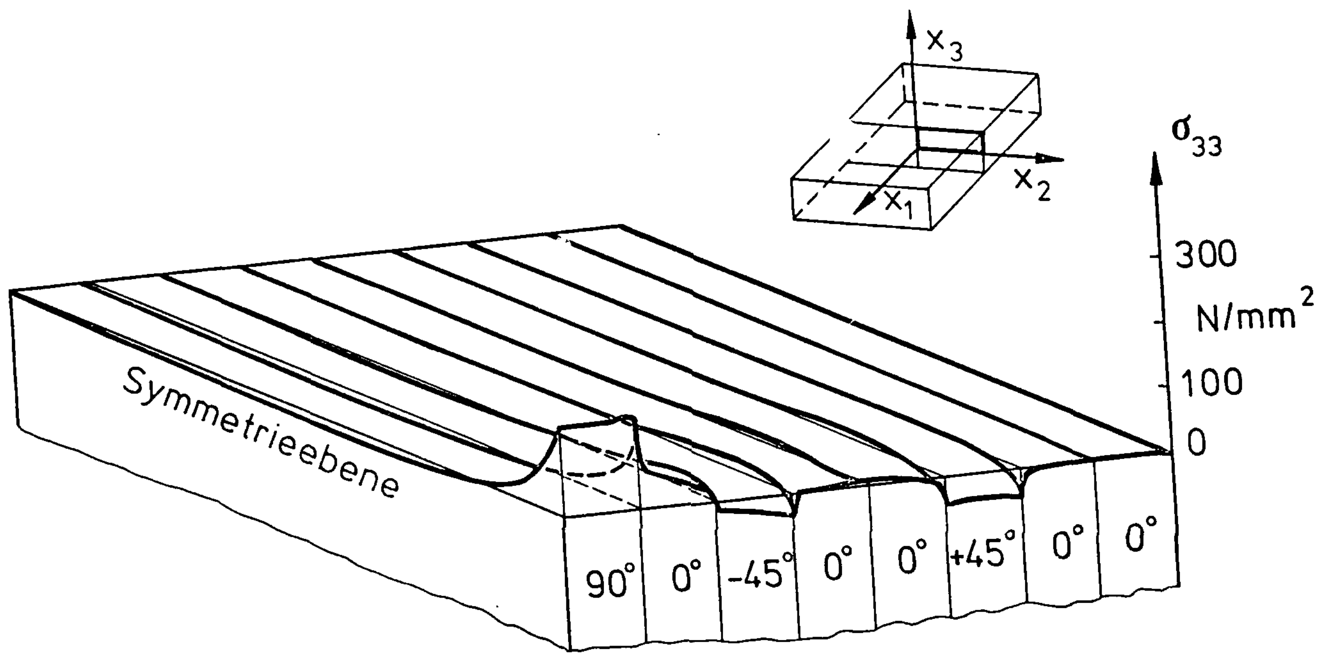

Bild 1: Schälspannung σ_{33} infolge Axiallast $\bar{\sigma}_{11} = 1\,kN/mm^2$

DFVLR 131/R-0184

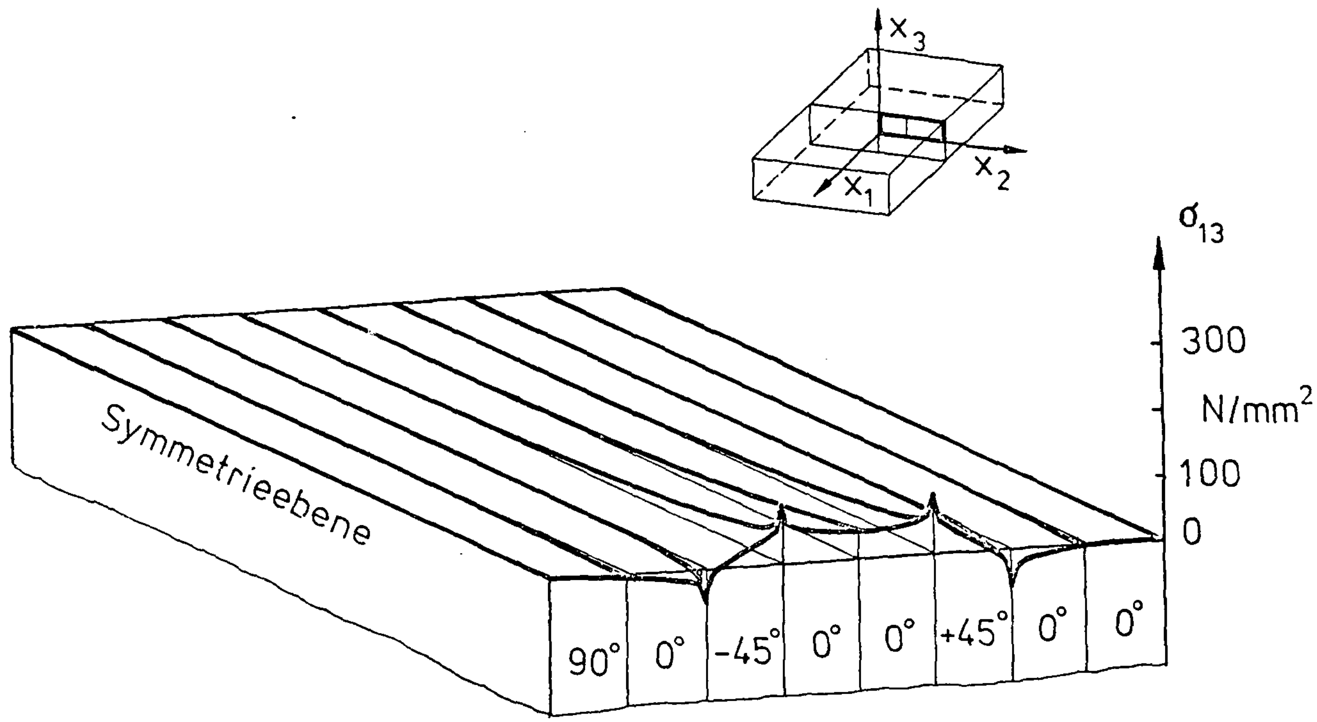

Bild 2: Schubspannung σ_{13} infolge Axiallast $\bar{\sigma}_{11} = 1\ \mathrm{kN/mm^2}$

DFVLR 131/R-0185

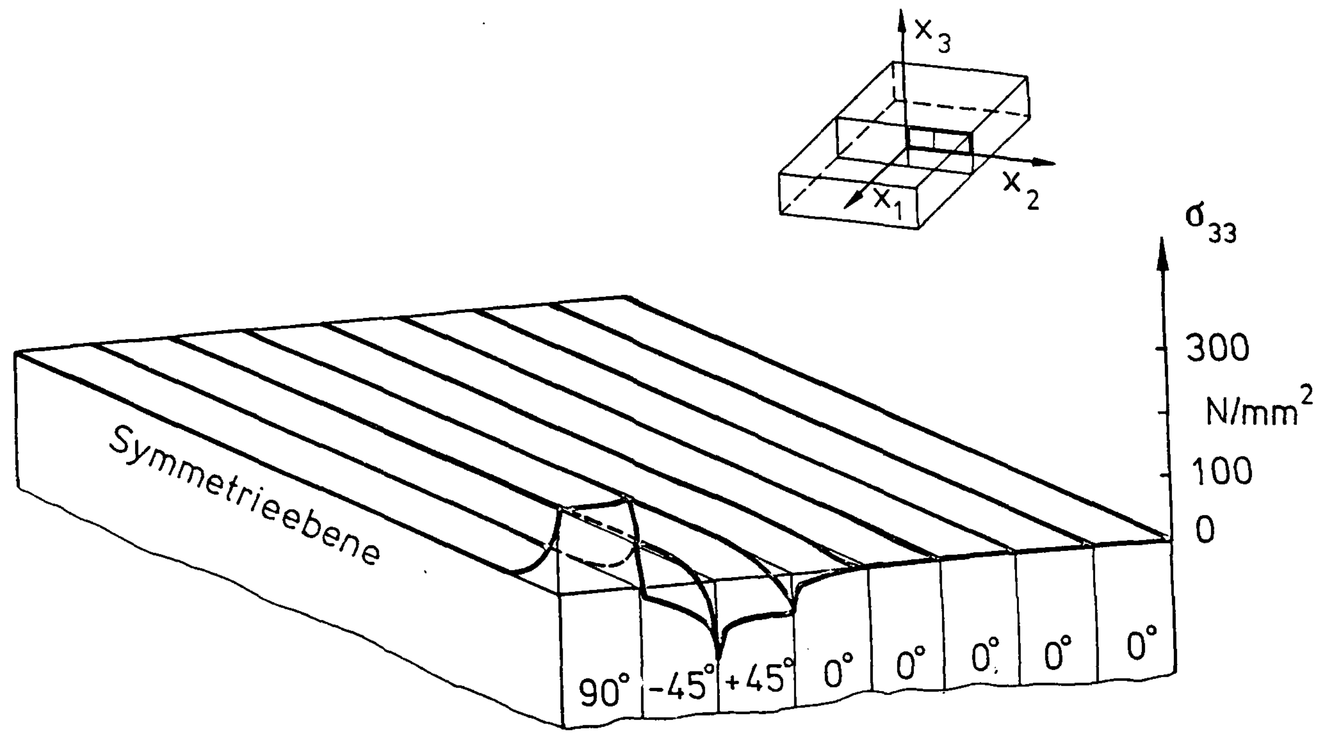

Bild 3: Schälspannung σ_{33} infolge Axiallast $\bar{\sigma}_{11} = 1\ \mathrm{kN/mm^2}$

DFVLR 131/R-0186

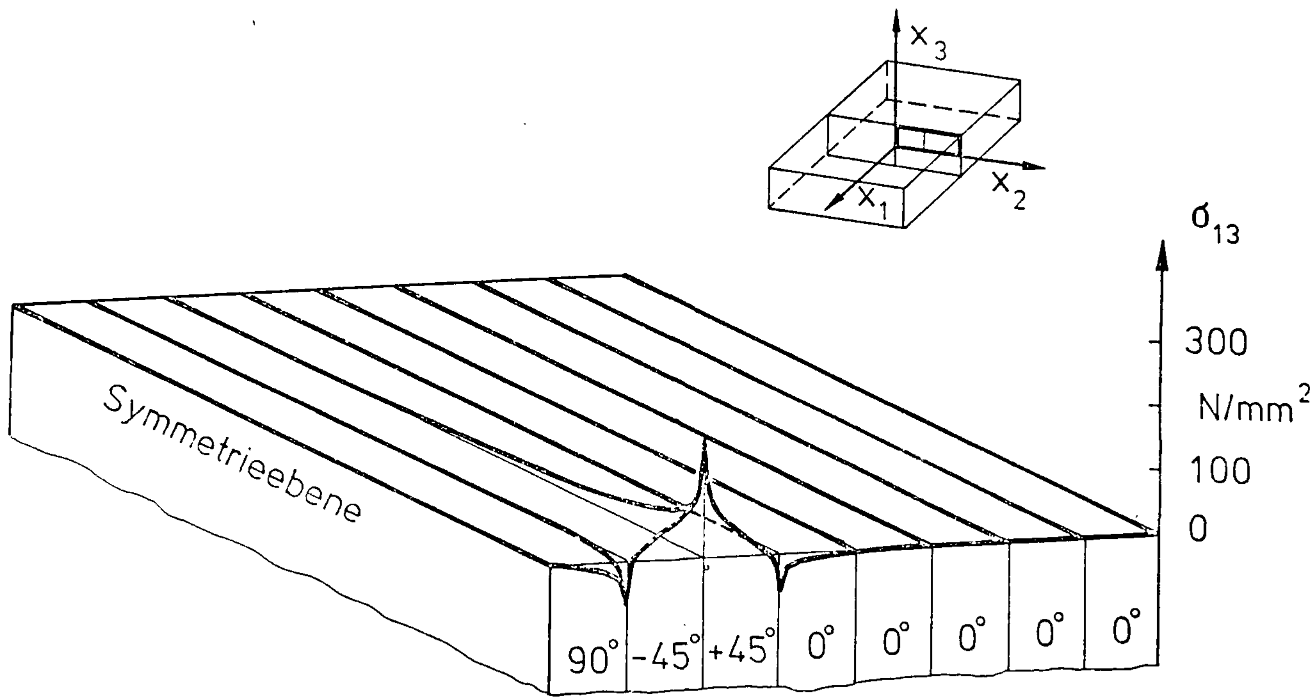

Bild 4: Schubspannung σ_{13} infolge Axiallast $\bar{\sigma}_{11} = 1\ kN/mm^2$

DFVLR 131/R-0187

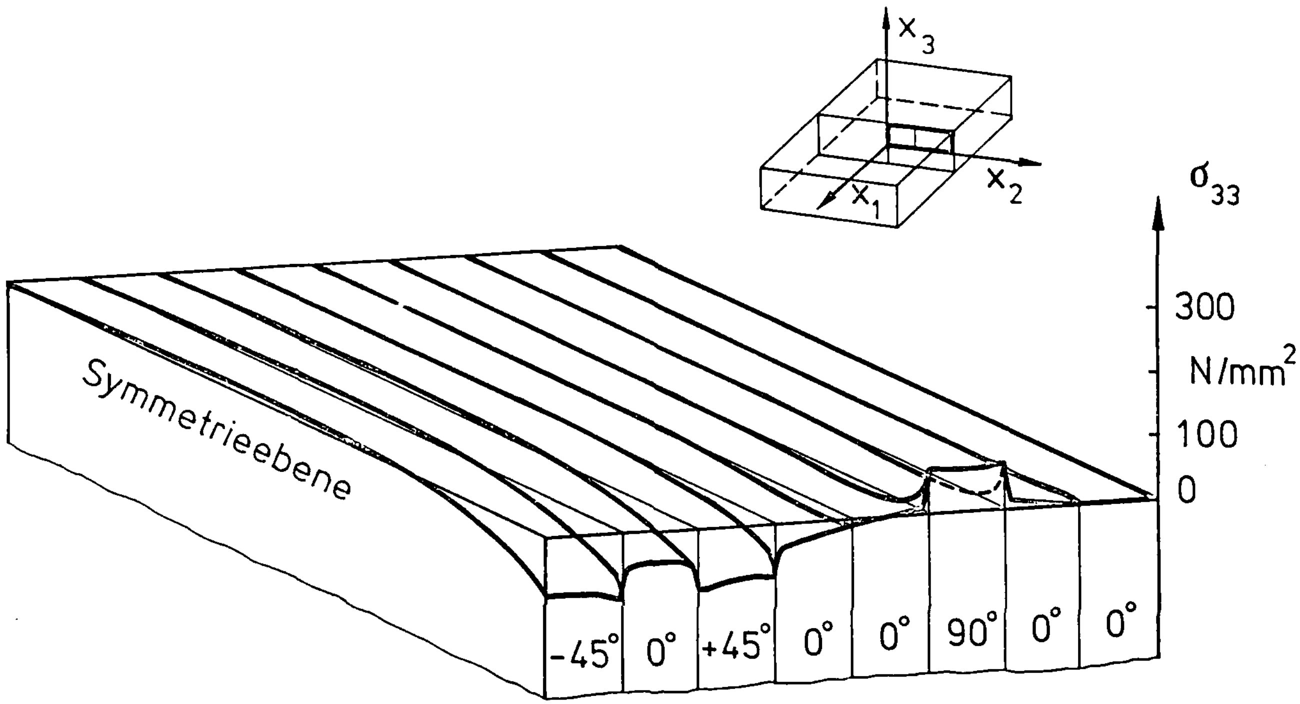

Bild 5: Schälspannung σ_{33} infolge Axiallast $\bar{\sigma}_{11} = 1\ kN/mm^2$

DFVLR 131/R-0188

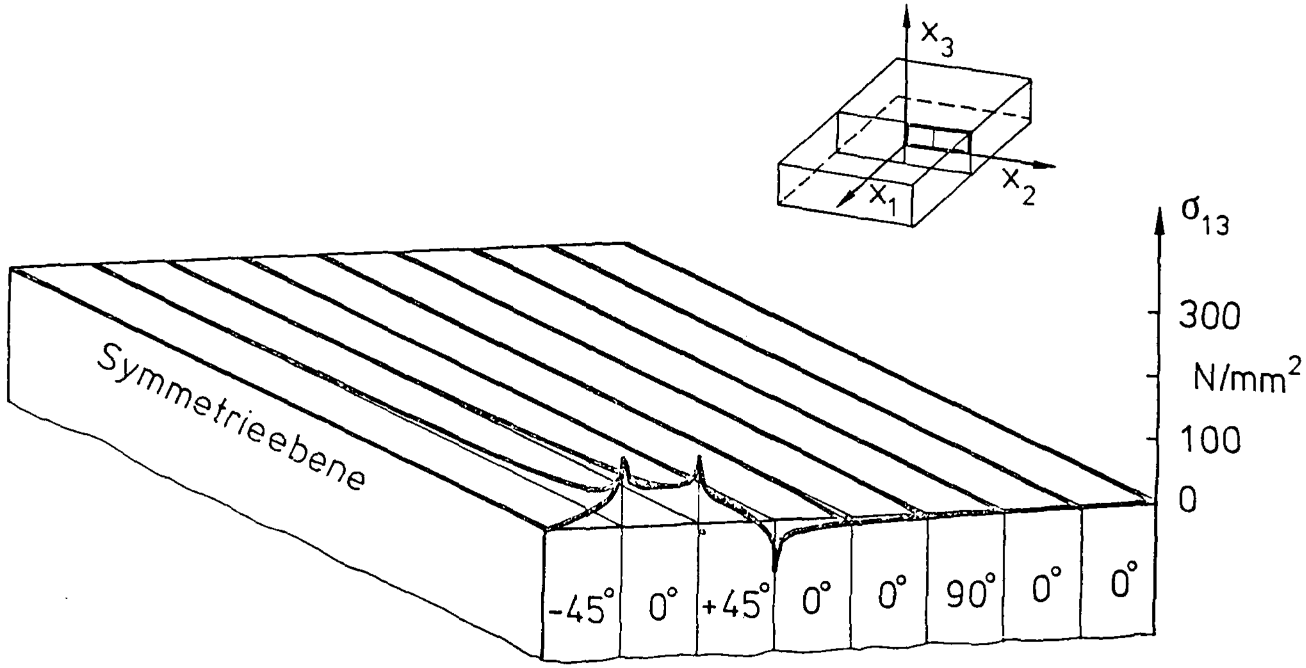

Bild 6: Schubspannung σ_{13} infolge Axiallast $\bar{\sigma}_{11} = 1\ kN/mm^2$

DFVLR 131/R-0189

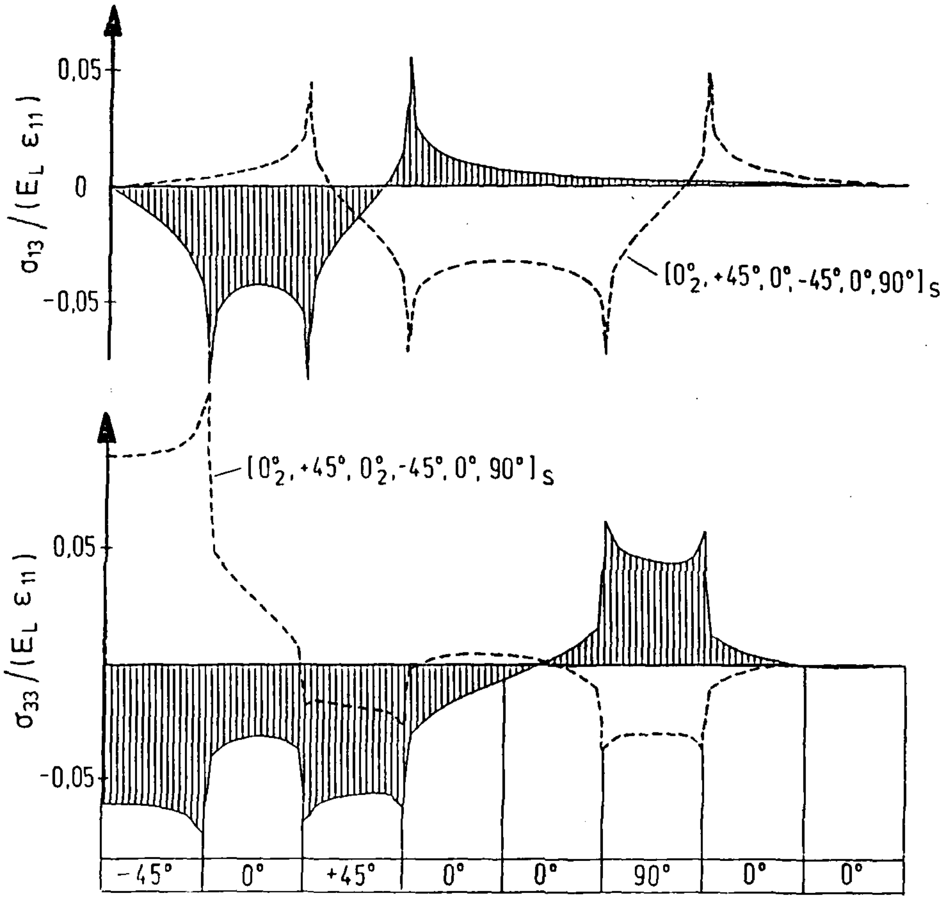

Bild 7: Randspannungen σ_{13} und σ_{33} unter Axiallast für das Laminat: $[\,0^\circ_2, 90^\circ, 0^\circ_2, +45^\circ, 0^\circ, -45^\circ\,]_s$

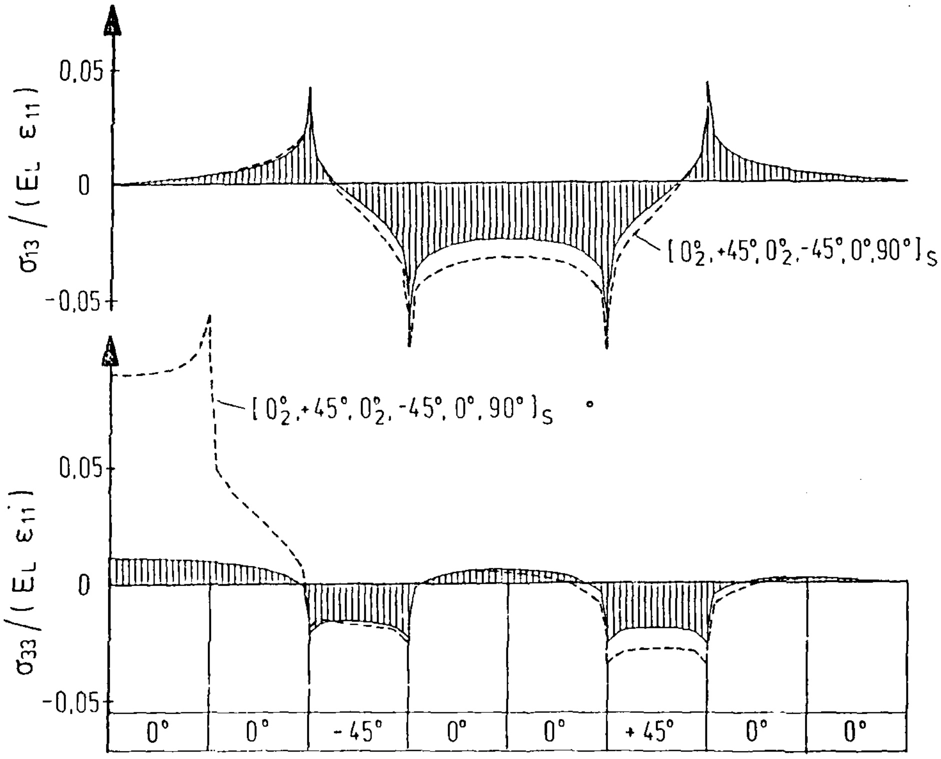

Bild 8: Randspannungen σ_{13} und σ_{33} unter Axiallast für das Laminat $[0^\circ_2, +45^\circ, 0^\circ_2, -45^\circ, 0^\circ_2]_s$

END

DATE

FILMED

6-86

DTIC